NASA Contractor Report 3982

NASA-CR-3982 19880014352

Full Potential Methods for Analysis/Design of Complex Aerospace Configurations

Vijaya Shankar, Kuo-Yen Szema,
and Ellwood Bonner

CONTRACT NAS1-15820
MAY 1986

~~NOTICE~~

~~FOR EARLY DOMESTIC DISSEMINATION~~

~~Because of its significant early commercial potential,~~ this information, which has been developed under a U.S. Government program, is being disseminated within the United States in advance of general publication. This information may be duplicated and used by the recipient with the express limitation that it not be published. Release of this information to other domestic parties by the recipient shall be made subject to these limitations.

Foreign release may be made only with prior NASA approval and appropriate export licenses. This legend shall be marked on any reproduction of this information in whole or in part.

~~Date for general release~~ April 30, 1988

NASA

NASA Contractor Report 3982

Full Potential Methods for Analysis/Design of Complex Aerospace Configurations

Vijaya Shankar, Kuo-Yen Szema,
and Ellwood Bonner
Rockwell International Corporation
Los Angeles, California

Prepared for
Langley Research Center
under Contract NAS1-15820

National Aeronautics
and Space Administration

**Scientific and Technical
Information Branch**

1986

FOREWORD

This final report was prepared by the Rockwell International Science Center, Thousand Oaks, CA for the Langley Research Center, National Aeronautics and Space Administration, Hampton, VA. The work was performed under Contract No. NAS1-15820, "Development of Full Potential Analysis Aero Prediction Technology for Hypersonic Configuration Design." Mr. Noel Talcott and Mr. Kenneth Jones were the Project Monitors on this contract.

Mr. E. Bonner of the Los Angeles Division, Rockwell International, was the Program Manager; Drs. V. Shankar and K.-Y. Szema of the Rockwell International Science Center were the Principal Investigators.

SUMMARY

The steady form of the full potential equation, in conservation form, is employed to analyze and design a wide variety of complex aerodynamic shapes. The nonlinear method is based on the theory of characteristic signal propagation coupled with novel flux biasing concepts and body–fitted mapping procedures. The resulting code is vectorized for the CRAY–XMP and the VPS–32 supercomputers.

Use of the full potential nonlinear theory is demonstrated for a single–point supersonic wing design and a multipoint design for transonic maneuver/supersonic cruise/maneuver conditions. Achievement of high aerodynamic efficiency through numerical design is verified by wind tunnel tests. Other studies reported here include analyses of a canard/wing/ nacelle fighter geometry.

CONTENTS

ILLUSTRATIONS

ILLUSTRATIONS (Continued)

1.0 INTRODUCTION

Development of supersonic/hypersonic configurations has traditionally relied on linearized methods and hypersonic impact theory. These approaches can treat complex geometries with minimum response time and cost, providing wide data coverage in terms of Mach number, angle of attack, trim deflection, yaw angle, etc. Shortcomings are present, however, in both the impact and the linearized methods. For the former, interference between surface elements is totally ignored in implementations such as classical Newtonian, tangent wedge and cone theories. Crossflow interactions and stagnation point singularities are also implicitly disregarded. In the latter, shocks, vorticity, and entropy wakes and layers are excluded. Furthermore, superposition of elementary solutions such as those for thickness and angle of attack freely used in linear models are, strictly speaking, invalid at supersonic/hypersonic speeds.

Modern vehicle concepts such as the Advanced Tactical Fighter (ATF) attempt to achieve an effective compromise between the transonic maneuver and supersonic cruise/ maneuver conditions. Multiple design considerations of this type impose stringent constraints on the aerodynamic shape of the vehicle to achieve high buffet-free lift performance with reduced trim drag. The analysis and design of these modern vehicle shapes is a tremendous challenge, requiring increasingly sophisticated nonlinear methods ranging from the full potential theory to the Navier-Stokes equations.

Full potential approximations include enough physics of the flow to allow realistic optimization and permit consideration of mutual interference of highly integrated, closely coupled arrangements to provide improvements to aerodynamic efficiencies achievable using linear methodology. This approach, in conjunction with the use of modern high-speed computers, achieves the objective of economic computational design that is responsive to conceptual aircraft development efforts.

This report presents a state-of-the-art technique to solve the steady form of the full potential equation employing several novel concepts such as 1) flux biasing for capturing shocks, 2) implicit approximate factorization scheme for computational efficiency, 3) wake treatment, 4) numerical mapping for treatment of complex geometries, and 5) vector coding for supercomputers. The steady form of the full potential equation is mainly used for treating predominantly supersonic flows with embedded subsonic regions, while the unsteady full potential equation is employed to treat blunt–nosed configurations, transonic Mach number flows and time–accurate unsteady simulations (oscillating wings). A unified full potential method[1] is currently under development which can handle flows across the Mach number range (subsonic, transonic, supersonic), including the supersonic marching technique[2–6] as a special case.

This report demonstrates the use of this full potential nonlinear aerodynamic prediction methodology to treat a wide variety of complex configurations, including a single point and a multipoint design of advanced fighter wings. Results shown include geometries with canard, nacelle and vertical tail.

In designing a fighter wing, linear theory[7,8] is used to establish candidate optimum thickness and zero drag–due–to–lift twist, camber and variable camber deflections at supersonic speeds. Nonlinear potential flow analyses are employed to capture embedded shock waves at transonic[9,10] and supersonic conditions[2–6] and then subsequently weaken the wave system through parametric redesign. Boundary layer analysis[11] follows the inviscid design/analysis to assess the flow quality of the nonlinear potential design. The extent of trailing edge separation in particular is evaluated. The general approach is schematically indicated in Fig. 1 and represents a summary of the numerical design experience at Rockwell covering the HiMAT, forward swept wing, SAAB and Air Force/Navy Research Technology contract studies.

The full potential code employed in this paper is operational on several computer systems, such as the CYBER 176 and VAX serial machines and the CRAY–XMP and VPS–32 supercomputers. Analysis of a complete fighter–like configuration requires 500 seconds on the CYBER 176 and about 20–35 seconds on the VPS–32 or CRAY–XMP class machines. The execution time required to run a case depends on the number of marching plane calculations and on the number of grid points at each marching plane. A typical fighter calculation may involve 400 marching planes to cover the entire length of the configuration with an average of 75 × 20 grid points per plane.

A brief description of the full potential methodology is presented here for completeness. More details can be found in Refs. 1 through 6 and 9.

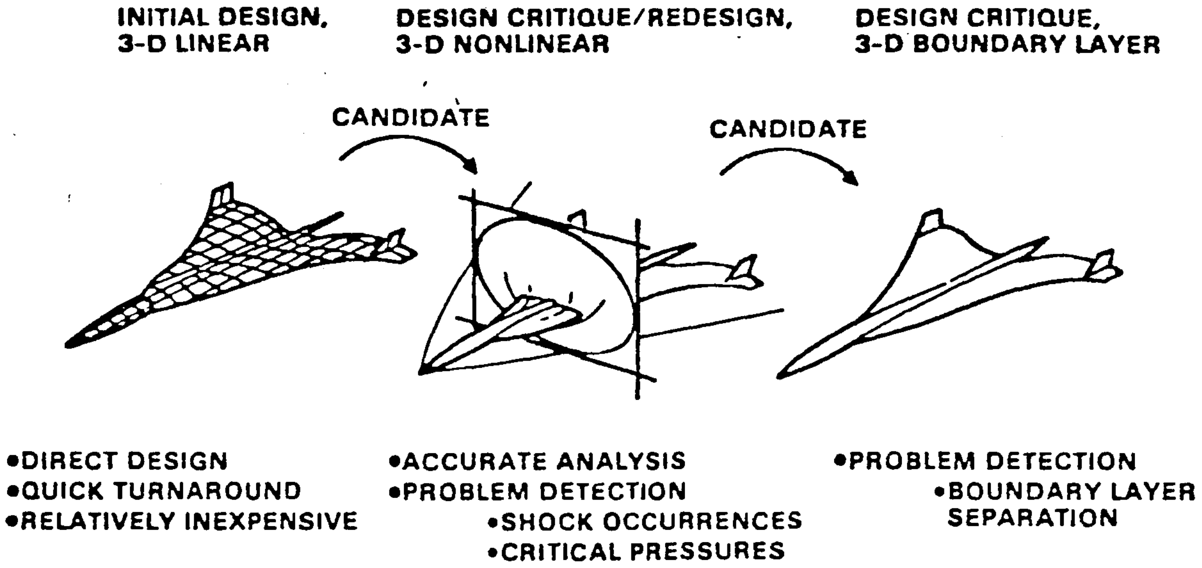

Fig. 1. Numerical design approach.

2.0 METHODOLOGY

As mentioned earlier, the steady form of the full potential equation is used for treating predominantly supersonic flows with pockets of subsonic regions.

2.1 Treatment of the Steady Equation

The steady, conservative full potential equation cast in an arbitrary coordinate system defined by $\varsigma = \varsigma(x, y, z)$, $\eta = \eta(x, y, z)$ and $\xi = \xi(x, y, z)$ can be written as

$$\left(\rho\frac{U}{J}\right)_{\varsigma} + \left(\rho\frac{V}{J}\right)_{\eta} \left(\rho\frac{W}{J}\right)_{\xi} = 0 \quad , \tag{1}$$

where the density ρ is given by

$$\rho = \left[1 - \left(\frac{\gamma - 1}{2}\right) M_{\infty}^{2} \left(U\phi_{\varsigma} + V\phi_{\eta} + W\phi_{\xi} - 1\right)\right]^{1/(\gamma-1)} \quad . \tag{2}$$

The nature of Eq. (1) can be analyzed by studying the eigenvalue system of Eq. (1) combined with the irrotationality condition in the (ς, η) and (ς, ξ) planes. A detailed discussion on this and the nomenclature can be found in Ref. 4. Therefore, only the final results are presented here.

1. At a grid point, the marching direction ς is hyperbolic $\left(a_{11} - (U^2/a^2)\right) < 0$ and the total velocity q is supersonic, $q > a$. This point will use the algorithm of Ref. 3. The quantity a_{11} is $\left(\varsigma_x^2 + \varsigma_y^2 + \varsigma_z^2\right)$.

2. At a grid point, the marching direction ς is elliptic $\left(a_{11} - (U^2/a^2)\right) > 0$, but the total velocity q is supersonic, $q > a$. This point will be treated by a transonic operator with a built-in density biasing based on the magnitude of $\left[1 - (a^2/q^2)\right]$. This case is termed Marching Subsonic Region (MSR).

3. At a grid point, the direction ς is elliptic $\left(a_{11} - (U^2/a^2)\right) > 0$ and the total velocity q is subsonic, $q < a$. This point will be treated by a subsonic central-differenced operator. This case is called Total Subsonic Region (TSR).

Figure 2 shows the schematic of a fuselage–canopy forebody geometry with an embedded MSR and TSR present in the supersonic flow. To solve this problem, the marching scheme of Ref. 3 is used when $\left[a_{11} - (U^2/a^2)\right]$ is positive. First, march from the nose up to the plane denoted by (A–B) in Fig. 2 using the method of Ref. 3. Then, between (A–B) and (C–D), which bound the subsonic bubble (MSR and TSR), use a relaxation scheme and iterate until the subsonic bubble is fully captured. Then, resume the marching scheme from the plane (C–D) downstream of the body. For blunt-nosed configurations, the unsteady method of Ref. 9 is used to generate the starting blunt body solution.

<u>Treatment of $\partial/\partial\varsigma\,(\rho\frac{U}{J})$ Term</u>

At a grid point $(i+1, j, k)$, the derivative in the marching direction ς is given by

$$\frac{\partial}{\partial\varsigma}\left(\rho\frac{U}{J}\right) = \underset{\substack{\downarrow\\ \text{supersonic}}}{\theta_i \frac{\overleftarrow{\partial}}{\partial\varsigma}\left(\rho\frac{U}{J}\right)_{i+1}} + \underset{\substack{\downarrow\\ \text{marching subsonic}}}{(1-\theta_{i+1})\frac{\overrightarrow{\partial}}{\partial\varsigma}\left(\tilde{\rho}\frac{U}{J}\right)_{i+1}} \quad , \tag{3}$$

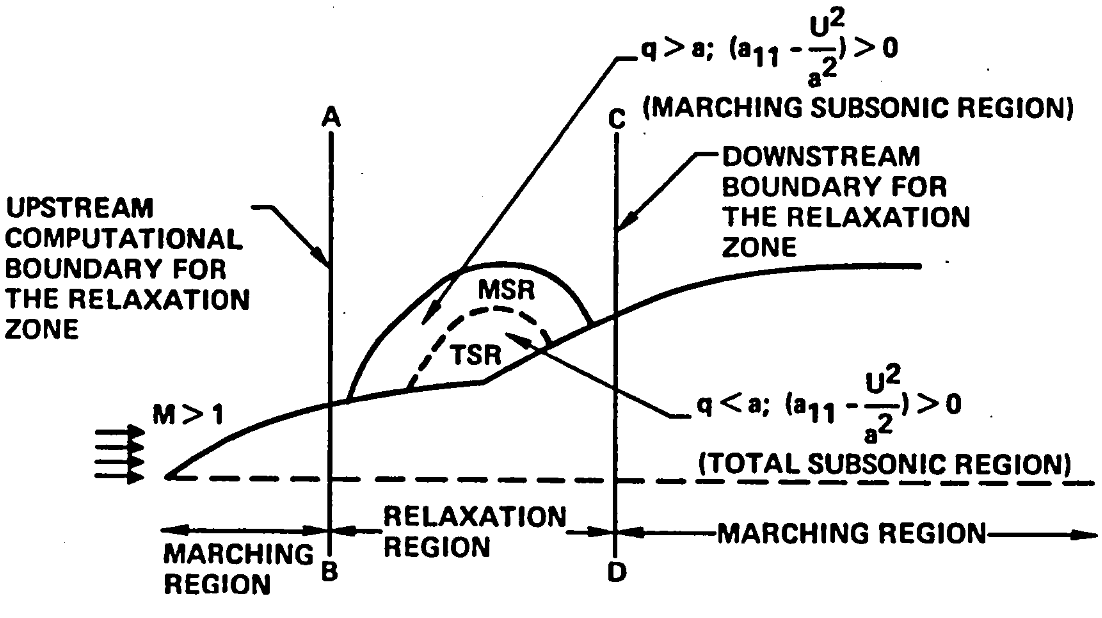

Fig. 2. Embedded subsonic bubble in a supersonic flow.

where

$\overleftarrow{\partial}$ refers to backward differencing

$\overrightarrow{\partial}$ refers to forward differencing

$\theta_i = 1$ if $\left[a_{11} - (U^2/a^2)\right] < 0$ (supersonic with respect to ς)

$= 0$ if $\left[a_{11} - (U^2/a^2)\right] > 0$ (subsonic with respect to ς)

and $i + 1$ is the current marching plane.

The first term in Eq. (3) corresponds to the supersonic marching operator and the second term is the subsonic operator. By using a local linearization procedure, Eq. (3) can be expressed in terms of ϕ only. The supersonic operator is given by

$$\begin{aligned} \frac{\overleftarrow{\partial}}{\partial\varsigma}\left(\rho\frac{U}{J}\right)_{i+1} &\doteq \frac{\overleftarrow{\partial}}{\partial\varsigma}\rho_i\Bigg[\left(a_{11} - \frac{U^2}{a^2}\right)\frac{\overleftarrow{\partial}}{\partial\varsigma}\Delta\phi \\ &\qquad + \left(a_{12} - \frac{UV}{a^2}\right)\frac{\partial}{\partial\eta}\Delta\phi + \left(a_{13} - \frac{UW}{a^2}\right)\frac{\partial}{\partial\xi}\Delta\phi + U_i\Bigg] \\ \Delta\phi &= (\phi_{i+1} - \phi_i) \end{aligned} \tag{4}$$

and the subsonic relaxation operator is given by

$$\frac{\overrightarrow{\partial}}{\partial\varsigma}\left(\tilde{\rho}\frac{U}{J}\right)_{i+1} \doteq \frac{\overrightarrow{\partial}}{\partial\varsigma}\left[\frac{\tilde{\rho}^{n+1}_{i+1}}{J}(a_{11}\,\overleftarrow{\phi}_{\varsigma} + a_{12}\phi_\eta + a_{13}\phi_\xi)_{i+1}\right] \quad , \tag{5}$$

where

$$\tilde{\rho}^{n+1}_{i+1} = \rho^n_{i+1} - \nu\left(\rho^n_{i+1} - \rho^n_i\right) \quad , \quad \text{for } U > 0$$

$$\nu = \max\left(0, 1 - \frac{a^2}{q^2}\right) \quad .$$

The superscript $(n + 1)$ denotes the current relaxation cycle for a subsonic bubble calculation.

Treatment of $\partial/\partial\eta\,(\rho\frac{V}{J})$ Term

$$\frac{\partial}{\partial\eta}\left(\rho\frac{V}{J}\right)=\theta_{i+1}\frac{\overleftarrow{\partial}}{\partial\eta}\left(\bar{\rho}\frac{V}{J}\right)_{j+1/2}+\left(1-\theta_{i+1}\right)\frac{\overleftarrow{\partial}}{\partial\eta}\left(\overset{\approx}{\rho}\,\frac{V}{J}\right)_{j+1/2}\quad . \tag{6}$$

supersonic marching subsonic

When $\theta_{i+1}=1$, that is, the point is supersonic with respect to ς, only the first term in Eq. (6) is used and the biased density $\bar{\rho}$ is defined by (for $V>0$)

$$\bar{\rho}_{j+1/2}=\left(1-\bar{\nu}_{j+1/2}\right)\rho^*_{j+1/2}+\frac{1}{2}\bar{\nu}_{j+1/2}\left(\rho^*_j+\rho^*_{j-1}\right)\quad , \tag{7}$$

where $\bar{\nu}=\max\left[0,1-a_{22}(a^2/V^2)\right]$.

In Eq. (7), the evaluation of ρ^* depends on whether the flow is conical or nonconical. For conical flows, all ρ^* quantities are evaluated at the i^{th} plane. For nonconical flows, at each nonconical marching plane, initially ρ^* is set to be the value at the i^{th} plane and then subsequently iterated to convergence by setting ρ^* to the previous iterated value of ρ at the current $i+1$ plane.

When the point is elliptic in the marching direction, the density biasing $\overset{\approx}{\rho}$ is based on $\overset{\approx}{\nu}=\max\left[0,1-(a^2/q^2)\right]$.

Combining the various terms of Eq. (1) as represented by Eqs. (3)–(7) together with the terms arising from $[\rho(W/J)_\xi]$ will result in a fully implicit model. This is solved using an approximate factorization implicit scheme[4]. Details on the initial and boundary conditions, wake treatment, and geometry and grid setup can be found in Ref. 5.

For treatment of complex geometries, the body-fitted coordinate system $(\tau,\varsigma,\eta,\xi)$ is generated using the procedure outlined in Ref. 12.

2.2 Treatment of Combined Yaw and Angle of Attack

A complete analysis of an aircraft configuration must address the vehicle's performance under angle of attack (α) and sideslip (β) flight conditions. For asymmetric configurations, a similar problem exists in that the flow field is not symmetric, and therefore requires a solution of the entire crossflow plane.

Given a symmetric configuration at a sideslip angle of $\beta = 0$, only the half-plane problem needs to be solved with the plane of symmetry boundary conditions imposed along $K = 2$ and $(KMAX - 1)$, as shown in Fig. 3a (see Ref. 4 for a complete description of the nomenclature). Imposing the flow conditions along $K = 1$ to be the same as the ones along $K = 3$ gives a tridiagonal system of equations for the L_ξ operator that can be easily solved. For a symmetric configuration, when yaw (or sideslip) angle is present, the entire crossflow plane needs to be solved, as shown in Fig. 3b. In this case, the flow conditions along $K = 1$ are set to be the same as the ones along $K = (KMAX - 2)$. This destroys the tridiagonal nature of the L_ξ operator. A special routine has been developed to invert a matrix of the following type:

$$L_\xi = \begin{bmatrix} X & X & \cdots & \cdots & X & 0 \\ X & X & X & \cdots & 0 & 0 \\ & X & X & X & & 0 \\ & & \ddots & \ddots & \ddots & \\ 0 & 0 & \cdots & X & X & X \\ 0 & X & \cdots & \cdots & X & X \end{bmatrix} \quad . \tag{8}$$

In the current formulation, positive angle of attack α represents a positive Cartesian velocity v in the freestream, and similarly positive yaw β produces a positive w in the freestream. When both angle of attack and yaw are present, first the freestream is turned by an angle β and then by α. Let (x, y, z) be the inertial Cartesian system. After an initial yaw turn β, let the wind axis system be (x', y', z'), and after a subsequent α turn let it become $(\tilde{x}, \tilde{y}, \tilde{z})$. Now, referring to Fig. 3c,

$$\begin{aligned} \begin{bmatrix} \tilde{x} \\ \tilde{y} \\ \tilde{z} \end{bmatrix} &= \begin{bmatrix} \cos\alpha & \sin\alpha & 0 \\ -\sin\alpha & \cos\alpha & 0 \\ 0 & 0 & 1 \end{bmatrix} \begin{bmatrix} \cos\beta & 0 & \sin\beta \\ 0 & 1 & 0 \\ -\sin\beta & 0 & \cos\beta \end{bmatrix} \begin{bmatrix} x \\ y \\ z \end{bmatrix} \\ &= \begin{bmatrix} \cos\alpha\cos\beta & \sin\alpha & \cos\alpha\sin\beta \\ -\sin\alpha\cos\beta & \cos\alpha & -\sin\alpha\sin\beta \\ -\sin\beta & 0 & \cos\beta \end{bmatrix} \begin{bmatrix} x \\ y \\ z \end{bmatrix} . \end{aligned} \tag{9}$$

The freestream is now along $\tilde{x}$. The normalized freestream velocity potential is given by

$$\phi'_\infty = \frac{\phi_\infty}{u_\infty} = x\cos\alpha\cos\beta + y\sin\alpha + z\cos\alpha\sin\beta. \tag{10}$$

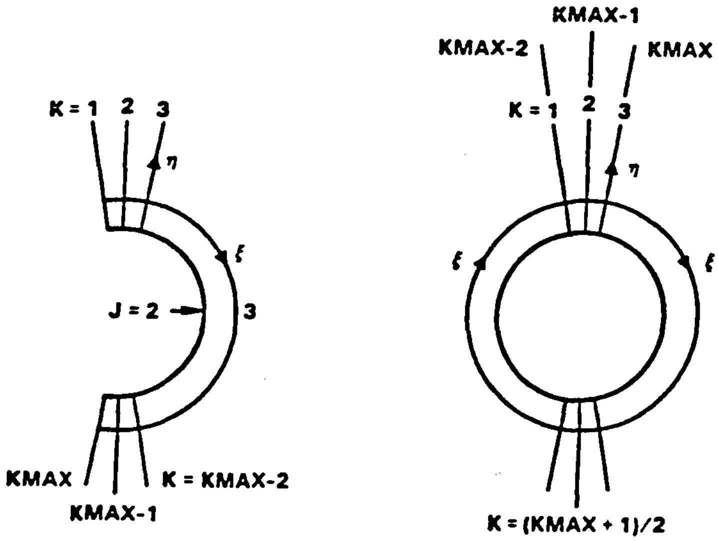

a) PLANE OF SYMMETRY
(YAW ANGLE = 0)
$\phi_{j,1} = \phi_{j,3}$
$\phi_{j,KMAX} = \phi_{j,KMAX-2}$

b) PERIODIC CONDITION FOR
YAW TREATMENT
$\phi_{j,1} = \phi_{j,KMAX-2}$
$\phi_{j,KMAX} = \phi_{j,3}$

Fig. 3a,b. Boundary conditions imposed for cases with and without yaw treatment.

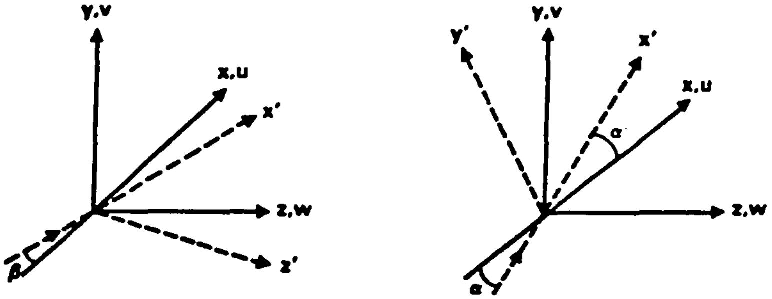

POSITIVE β → POSITIVE w

POSITIVE α → POSITIVE v

$$\begin{pmatrix} x' \\ y' \\ z' \end{pmatrix} = \begin{pmatrix} \cos\beta & 0 & \sin\beta \\ 0 & 1 & 0 \\ -\sin\beta & 0 & \cos\beta \end{pmatrix} \begin{pmatrix} x \\ y \\ z \end{pmatrix}, \qquad \begin{pmatrix} x' \\ y' \\ z' \end{pmatrix} = \begin{pmatrix} \cos\alpha & \sin\alpha & 0 \\ -\sin\alpha & \cos\alpha & 0 \\ 0 & 0 & 1 \end{pmatrix} \begin{pmatrix} x \\ y \\ z \end{pmatrix}$$

Fig. 3c. Coordinate transformation for yaw and angle-of-attack treatment.

Using Eq. (9), the drag, lift and side forces are easily calculated:

$$\begin{aligned}
\text{Drag} &= F_x \cos\alpha\cos\beta + F_y \sin\alpha + F_z \cos\alpha\sin\beta \\
\text{Lift} &= -F_x \sin\alpha\cos\beta + F_y \cos\alpha - F_z \sin\alpha\sin\beta\,. \\
\text{Side Force} &= -F_x \sin\beta + F_z \cos\beta
\end{aligned} \tag{11}$$

In Appendix B, the demonstration of the code for a combined yaw and angle of attack over a fighter–like configuration is presented to familiarize the user with the various input/output aspects of the code.

More results on the yaw capability of the code can be found in Ref. 13.

2.3 Nonisentropic Flows

The full potential equation is based on the assumption that the flow is isentropic. This is true only for very weak shocks (Mach number normal to the shock is less than 1.4). Some researchers have tried to modify the full potential formulation to correct the results for entropy effects[14]. No such attempt is made in the present work. Instead, an Euler capability is being developed[15] (included in Appendix C) to treat flows with strong shocks and rotational effects. A sample result from this Euler development is provided in the Results section of this report.

2.4 Salient Features of the Marching Code

The marching code developed under this NASA contract is named Supersonic Implicit Marching Program (SIMP) and is available from COSMIC under the designation LAR-13413[16]. The code structure is described in Appendix A. Some of the salient features of the code are:

- Equation in conservation form
- Flux linearized upwind differencing in the marching direction
- Conservative switch operators to treat embedded subsonic zones

- Treatment of wakes
- Yaw and angle of attack
- Complex geometry treatment (fuselage, canopy, wing, canard, nacelle, tail, multibody, etc.)
- Numerical grid generation with constraints
- Use of GEMPAK[17] or CDS[18] to generate geometry input files
- Vectorized code for supercomputers.

3.0 APPLICATIONS

To demonstrate the capability of this nonlinear full potential methodology, the application to several configurations is discussed:

1. Nonlinear aerodynamic wing design for an advanced fighter configuration.
2. Canard/wing/nacelle supersonic fighter analysis.
3. Shuttle, Transatmospheric Vehicle (TAV), and supersonic inlet cowl design.

Also, in Appendix B — User's Guide, a complete test case is presented for an advanced fighter configuration for a combined yaw and angle of attack flight condition.

3.1 Case 1 — Nonlinear Aerodynamic Wing Design

A cooperative effort between Rockwell International and the National Aeronautics and Space Administration–Langley Research Center was conducted to determine the effect on supersonic aerodynamic characteristics of increasing wing sweep on a North American Rockwell fighter design[19,20]. The effort was also to provide validation of the nonlinear full potential analysis code described in this report.

The configuration used in the study is a preliminary design version of a Rockwell fighter concept (see Fig. 4). This concept includes a slender forebody and prominent canopy blended smoothly into a highly swept wing center section. The outboard wing panel, selected for transonic performance requirements, extends outward from about 37 percent of the semispan and has a 48° swept leading edge. Leading- and trailing-edge devices for high lift and roll control extend along most of the span of the outer wing panel. The wing is twisted and cambered for transonic maneuvering. The propulsion system consists of two engines located beneath the center–wing section in nacelles which are blended into the lower surface inboard of the 37–percent semispan. The nozzles are vectorable in pitch. Twin vertical tails are located at the outboard edge of the center–wing section and are canted out 20°. Control surfaces located at the trailing edge of the wing center section, in conjunction with the canted vertical tails and vectorable nozzles, provide pitch control.

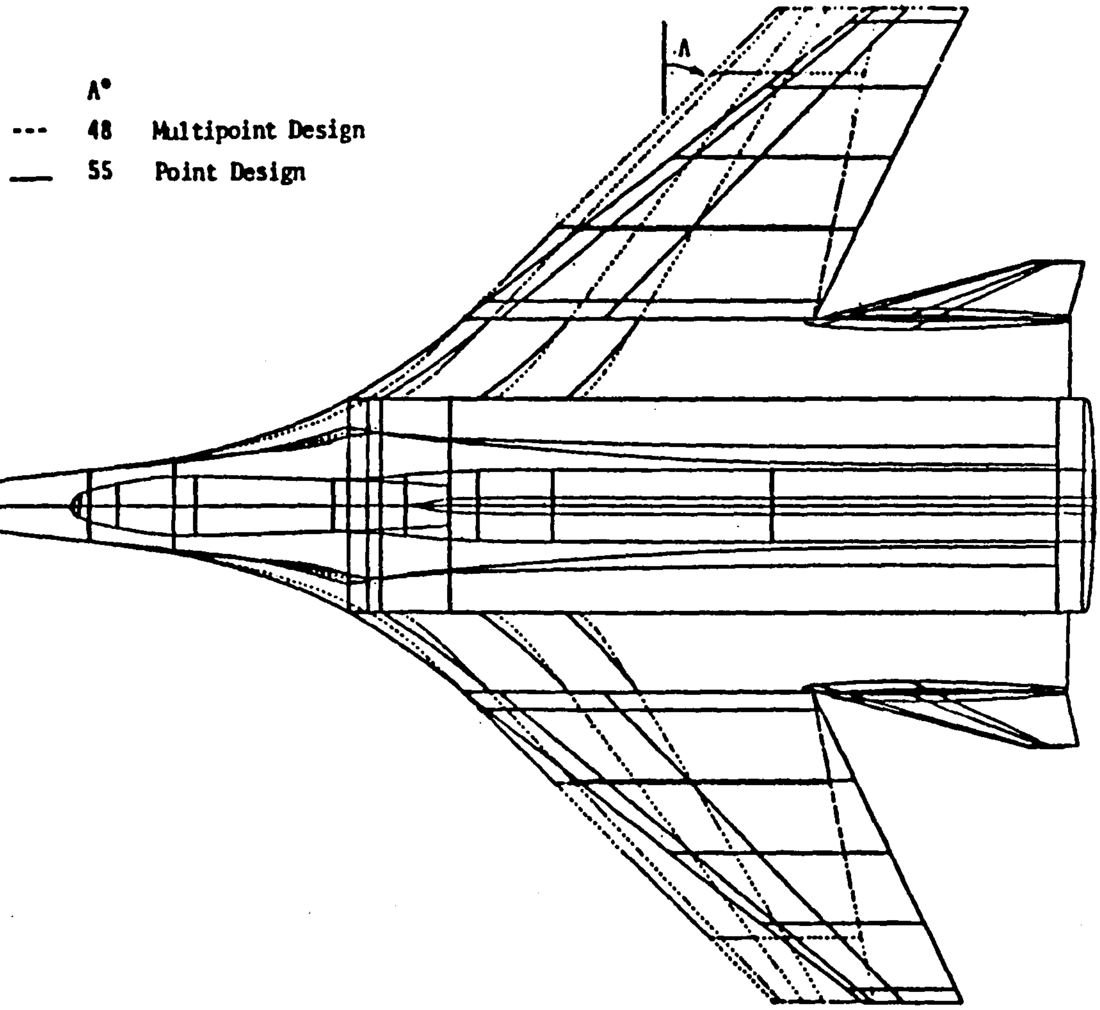

Fig. 4. General arrangement.

A model of the configuration was tested in the Langley Unitary Plan Wind Tunnel and Rockwell's Trisonic Test Facility. In addition to the 48° leading-edge outboard wing panel of the concept, two 55° leading-edge panels, and two new 48° leading-edge panels were designed and tested. One of the 55° panels was twisted and cambered for a Mach 1.6 maneuver design point. The two new 48° panels were designed with leading- and trailing-edge flap systems to best meet the subsonic/transonic/supersonic cruise and meneuver design points. For details of the wing panel design procedure, see Ref. 20. Aerodynamic force data for the 48° baseline panel and the 55° panels can be found in Ref. 19. Experimental data (aerodynamic force and surface pressure) for the new 48° panels and surface pressure data for the 55° panel will be reported in a forthcoming NASA report.

The computational model of the wing-body-tail-nacelle fighter under development is shown in terms of surface grid plots in Figs. 5 and 6. A typical marching plane contained a 75 × 20 mesh generated by the elliptic grid solver of Ref. 12. Figure 7 shows the cross-sectional grid and circumferential surface pressures at various axial stations in front of the nacelle face at the cruise flight conditions. Figures 8 and 9 show results at two different axial stations where the nacelles are present. The presence of a shock around the nacelles is clearly seen in Fig. 8. Details of the crossflow velocity vectors (projection of the total velocity vector on a unit sphere whose center is at the apex of the fighter configuration) around the wing-body-nacelle geometry is shown in Fig. 9. In Fig. 9, the freestream is aligned predominantly along the x-axis and away from the geometry and is seen as inflow crossflow velocity vectors. Crossflow velocity information provides insight into the behavior of vortical singularities and plays a key role in activating the density biasing switches in the code necessary to simulate crossflow shocks.

Linearized theory and full potential estimates of the 55° twisted and cambered wing panel configuration are presented in Fig. 10. Fully turbulent skin friction drag for a mean aerodynamic chord test Reynolds number of 1.56×10^6 is used for this assessment. Examination of the results indicates the design is an aerodynamically efficient one, taking into consideration nominal scale effects.

Figure 11 shows comparisons of chordwise pressures at two different span stations (60% and 80% span). The results show that the full potential predictions are in good

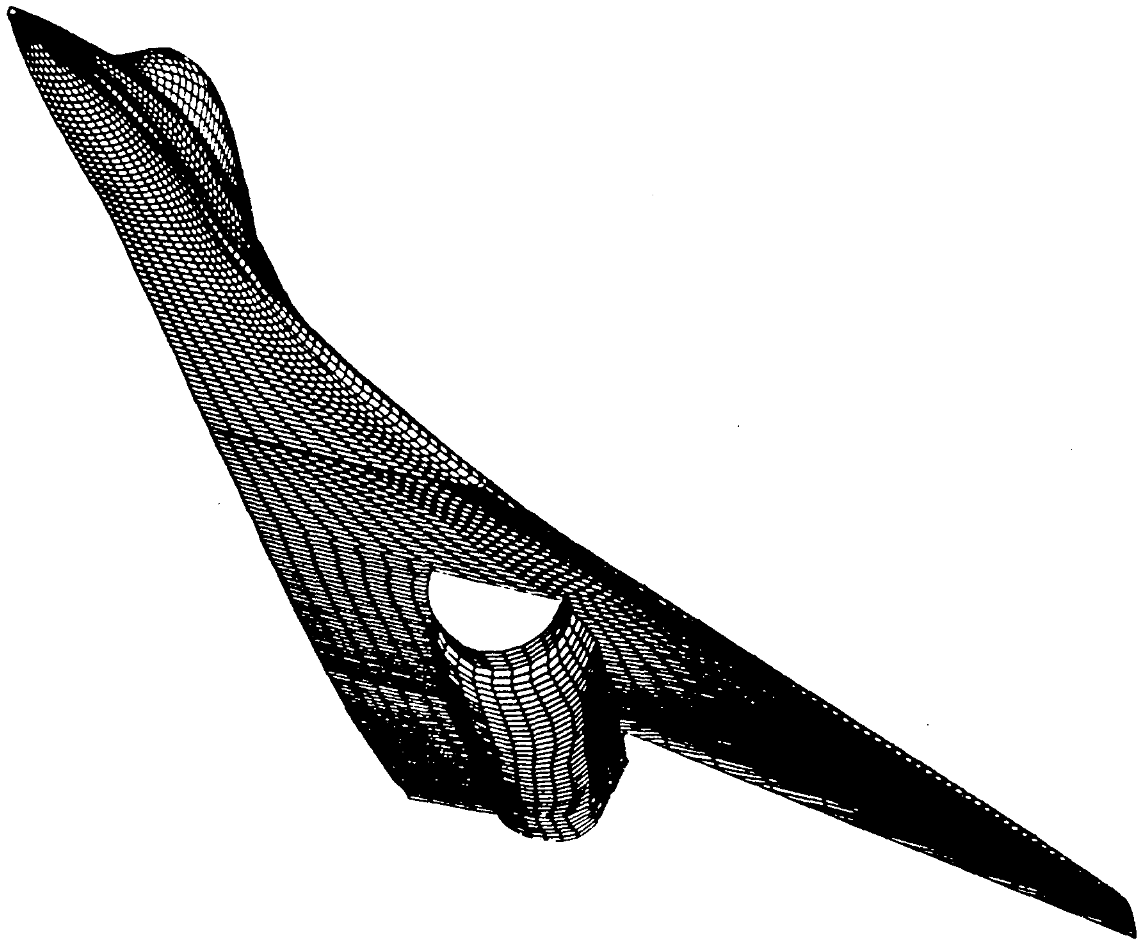

Fig. 5. Surface grid for ATF with nacelle.

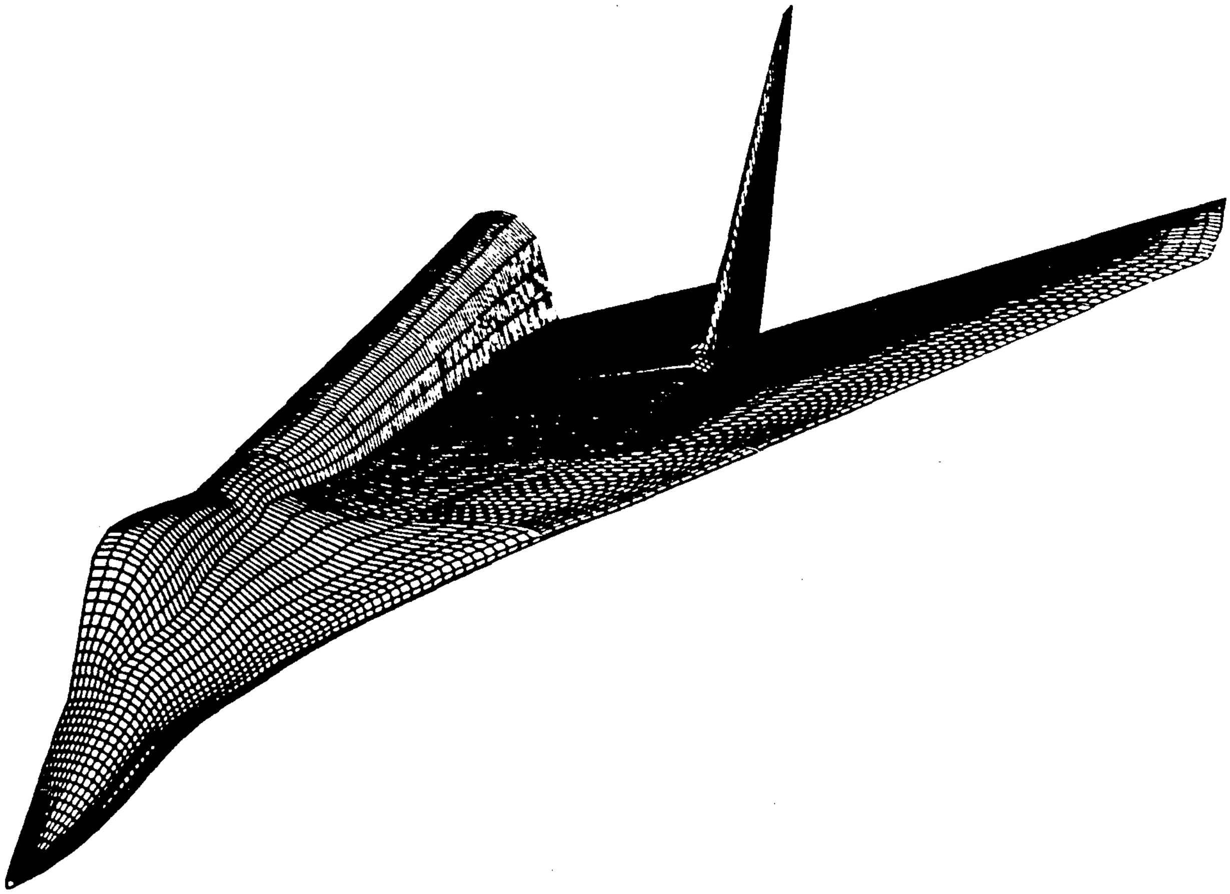

Fig. 6. Surface grid for ATF with tail.

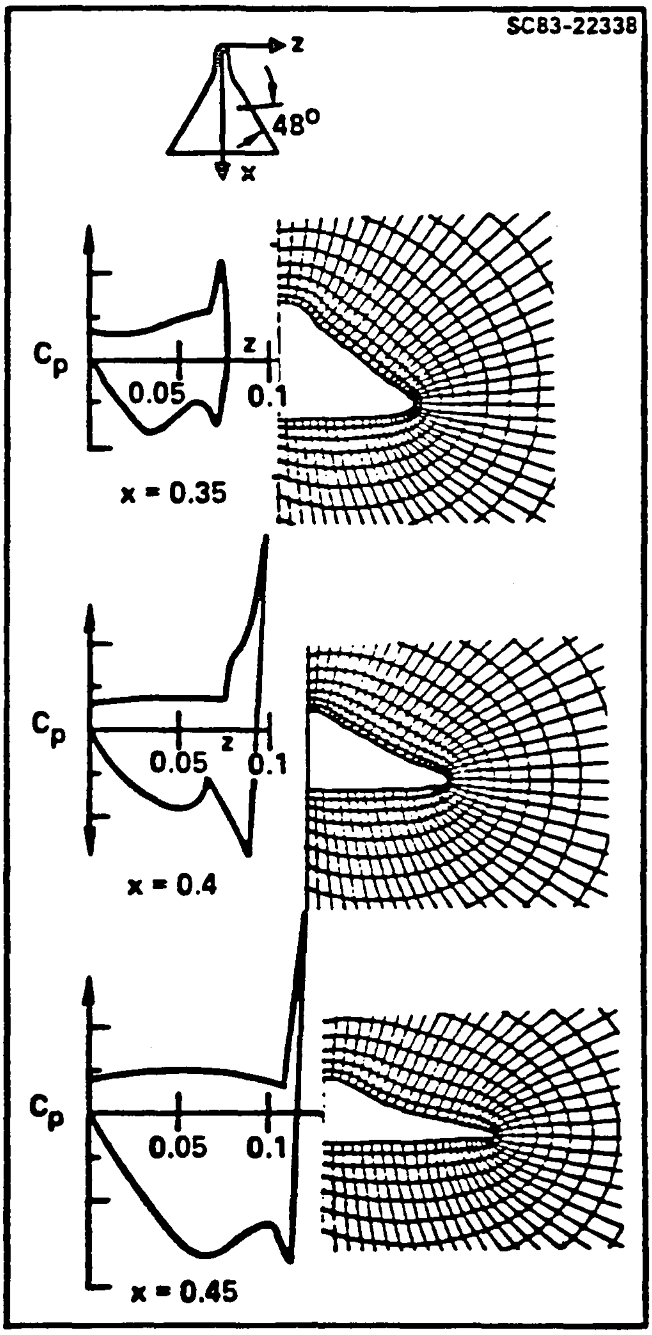

Fig. 7. Pressure distribution on a fighter-like (ATF) configuration; $M_\infty = 1.6$, $\alpha = 1.24$.

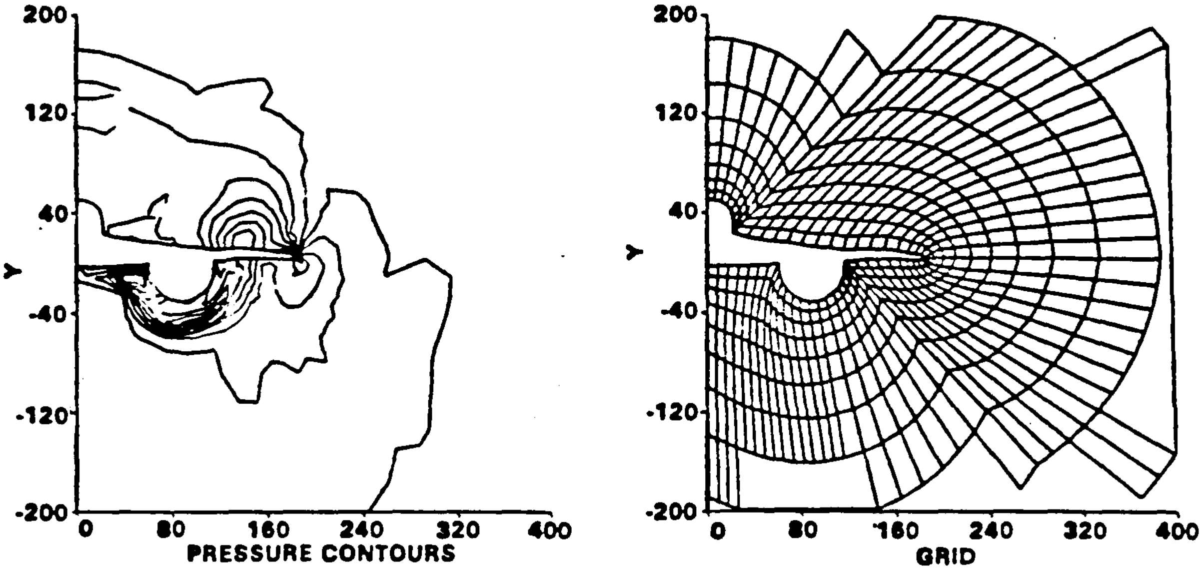

Fig. 8. Pressure contours and grid for ATF with nacelle; $M_\infty = 1.6$, $\alpha = 5°$, $\frac{x}{\ell} = 0.46$.

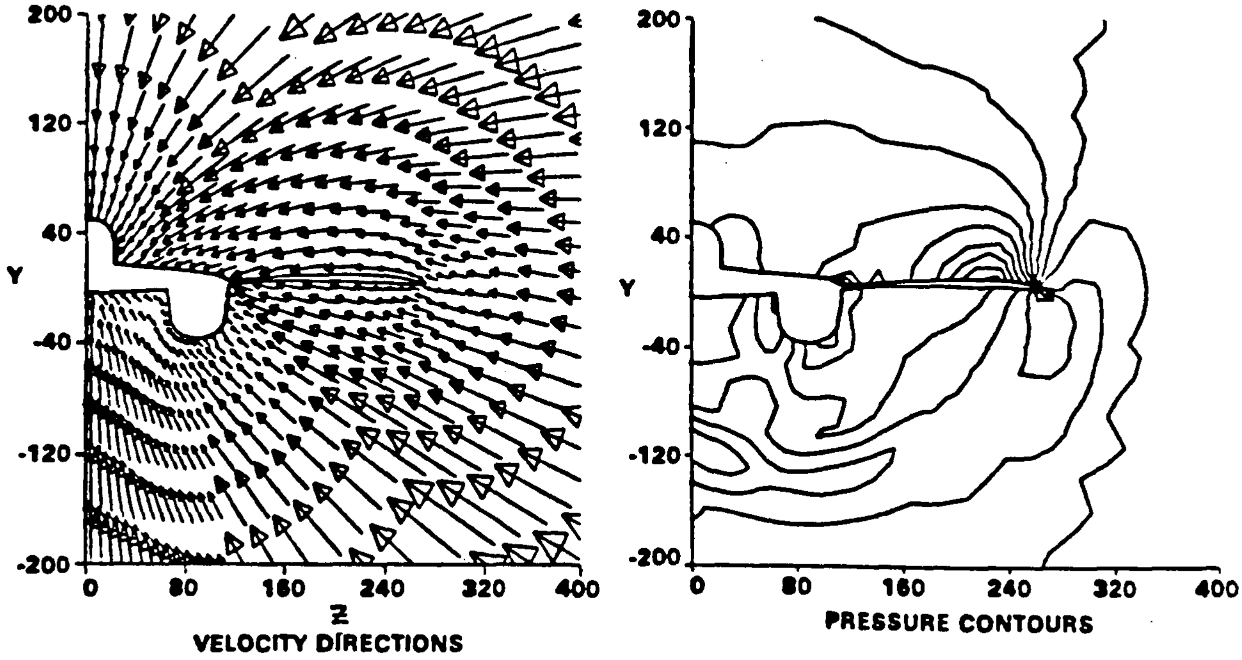

Fig. 9. Pressure contours and grid for ATF with nacelle; $M_\infty = 1.6$, $\alpha = 5°$, $\frac{x}{\ell} = 0.56$.

Turbulent Skin Friction

$$C_{D_F} = 0.0129 \text{ unitary }, \quad R_{N_c} = 1.56 \times 10^6$$

Linear Analysis

$$\alpha = 4.46 \text{ deg}$$

$$C_L = 0.32$$

$$C_{D_P} = C_{D_w} + C^*_{D_L} = 0.109 + 0.02185 = 0.03275$$

$$C_M = -0.061$$

$$L/D = 0.32/(0.0129 + 0.03275) = 7.0$$

Full Potential

$$\alpha = 4.46 \text{ deg}$$

$$C_L = 0.311$$

$$C_{D_P} = 0.0325$$

$$C_M = -0.0579$$

$$L/D = 0.311/(0.0129 + 0.0325) = 6.85$$

*Cambered plate fuselage

Fig. 10. Pretest $M = 1.6$ maneuver point design drag assessment.

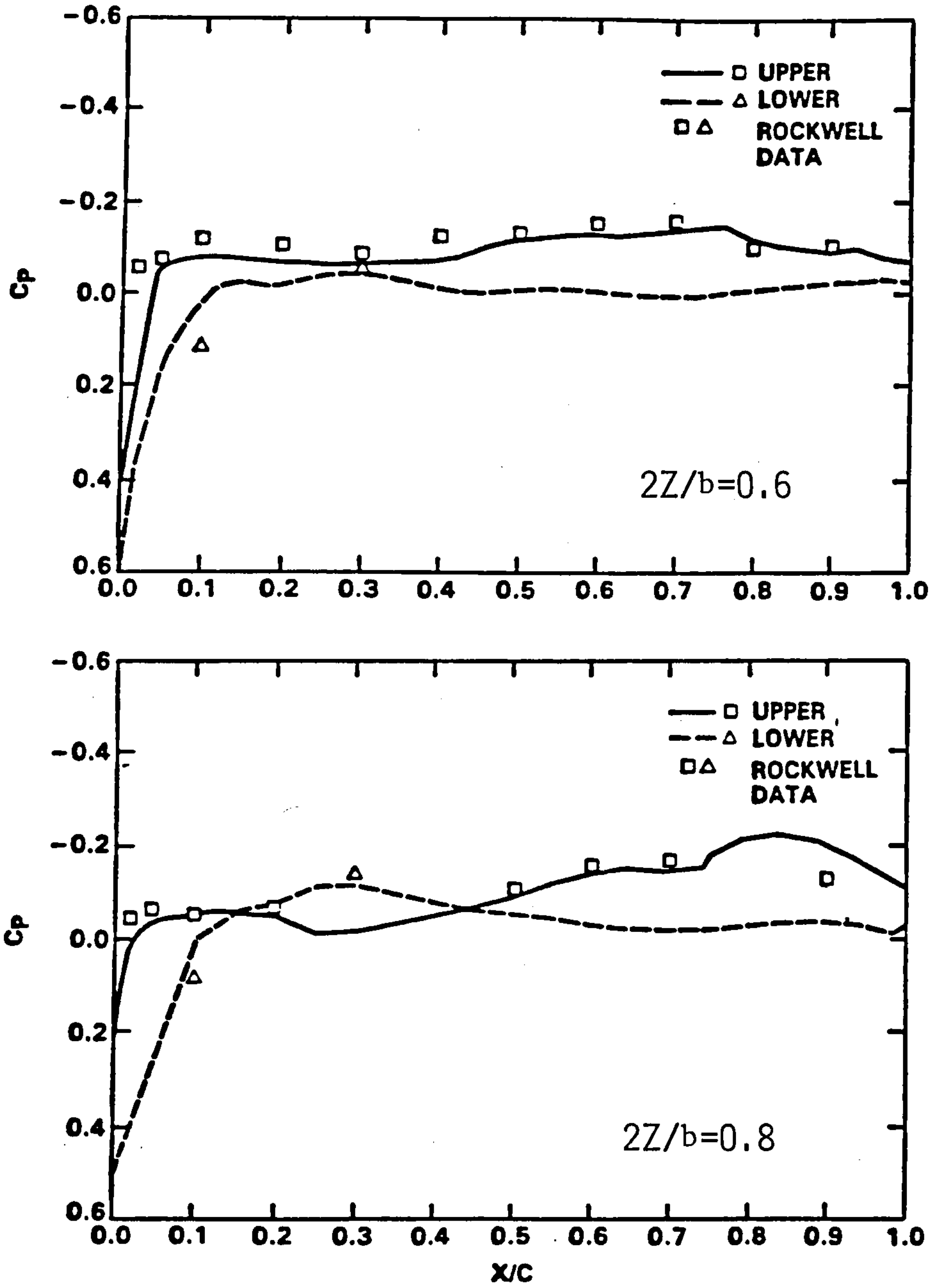

Fig. 11. ATF chordwise pressure distribution; $M_\infty = 1.6$, $\alpha = 1.24$.

agreement with Rockwell's experimental data. Figure 12 shows comparison of overall forces and moments in terms of C_L, C_{D_P} and C_M.

Supersonic cruise and maneuver pretest assessment of the new 48° leading-edge design is summarized in Fig. 13. Linear predictions indicate lift-drag ratio levels of 3.25 and 6.19, respectively, for the proposed Unitary Plan Wind Tunnel test condition. Comparison with the 55° point design result of Fig. 10 indicates a 13% reduction results from multipoint compromises associated with wing sweep and airfoil leading edge radius. Two-thirds of the penalty is associated with thickness considerations and one-third with drag due to lift. Figure 14 shows the lift, drag and pitching moment results for the 48° leading-edge sweep multipoint design. The full potential predictions are in good agreement.

The impact of multipoint considerations on the nacelle off untrimmed lift-drag ratio is presented in Fig. 15. For the 48° wing configuration, a 7.6% reduction at the nominal design point results from the decrease in planform sweep and increase in airfoil leading edge radius, twist and camber. This penalty is modest and overstated by full potential analysis which is slightly optimistic for the subsonic edge (55°) case and somewhat pessimistic for the supersonic edge (48°).

3.2 Case 2 — Canard-Wing-Nacelle Fighter Analysis

The full potential method of Refs. 2-6 can handle extremely complex geometries. This is demonstrated by applying the method to analyze the complex geometry[21] of Fig. 16, which has a canard, clipped wing tip, canopy and a flow-through nacelle mounted on the undersurface of the fuselage. Figure 17 shows the computational geometry and surface gridding. Note that the boundary layer diverter and swept nacelle were not modelled in the computations. Computations were performed for this configuration at $M_\infty = 2$ and $\alpha = 4°$. Figures 18 and 19 show the crossflow streamlines, surface pressures, pressure contours and crossflow velocity vectors at two different model axial stations. Figure 18 shows results at an axial station where the fuselage, wing, canard wake and canard are all present. The nodal singularity in pressure contour that is present at lower wing-body junction regions corresponds to a saddle singularity of crossflow streamlines, as shown in Fig. 18. Note the pressure match along the canard wake cut, Fig. 18. Figure 19 shows

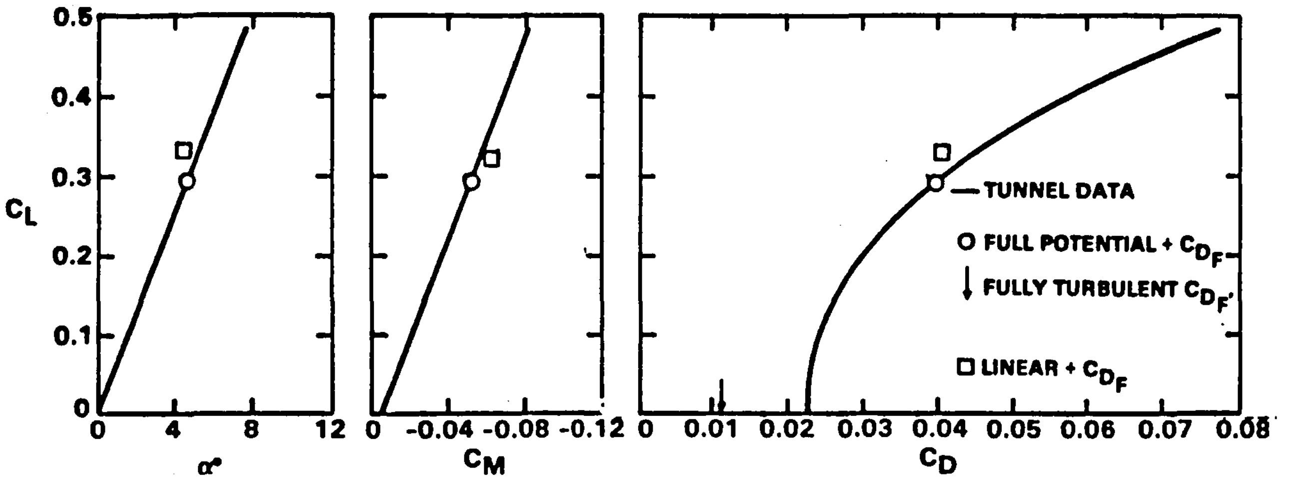

Fig. 12. Comparison of measurement with predictions at $M = 1.6$ for nonlinear point design, $\Lambda_{LE} = 55$ deg, nacelle off.

Turbulent Skin Friction

$$C_{D_F} = 0.0129 \text{ unitary}, \ R_{N_c} = 1.56 \times 10^6$$

Linear Analysis

$\alpha = 1.24$ deg

$C_L = 0.1$

$C_{D_P} = C_{D_w} + C^*_{D_L} = 0.0149 + 0.0031$

$= 0.180$

$C_M = -0.0136$

$L/D = 3.24$

$\alpha = 5.22$

$C_L = 0.32$

$C_{D_P} = C_{D_w} + C^*_{D_L} = 0.0149 + 0.0239$

$= 0.0388$

$C_M = -0.035$

$L/D = 6.19$

Full Potential

$\alpha = 1.24$ deg

$C_L = 0.119$

$C_{D_P} = 0.0164$

$C_M = -0.0284$

$L/D = 4.06$

$\alpha = 5.22$

$C_L = 0.336$

$C_{D_P} = 0.04075$

$C_M = -0.051$

$L/D = 6.26$

*Cambered plate fuselage

Fig. 13. Pretest $M = 1.6$ multipoint design drag assessment.

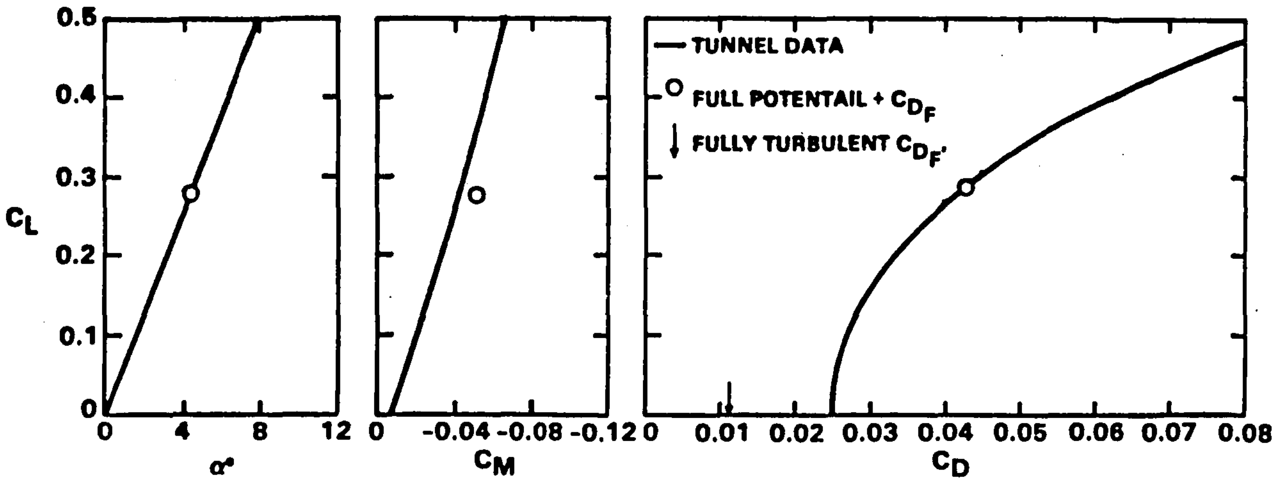

Fig. 14. Comparison of measurement prediction at $M = 1.6$ for first multipoint design, $\Lambda_{LE} = 48$ deg, nacelle off.

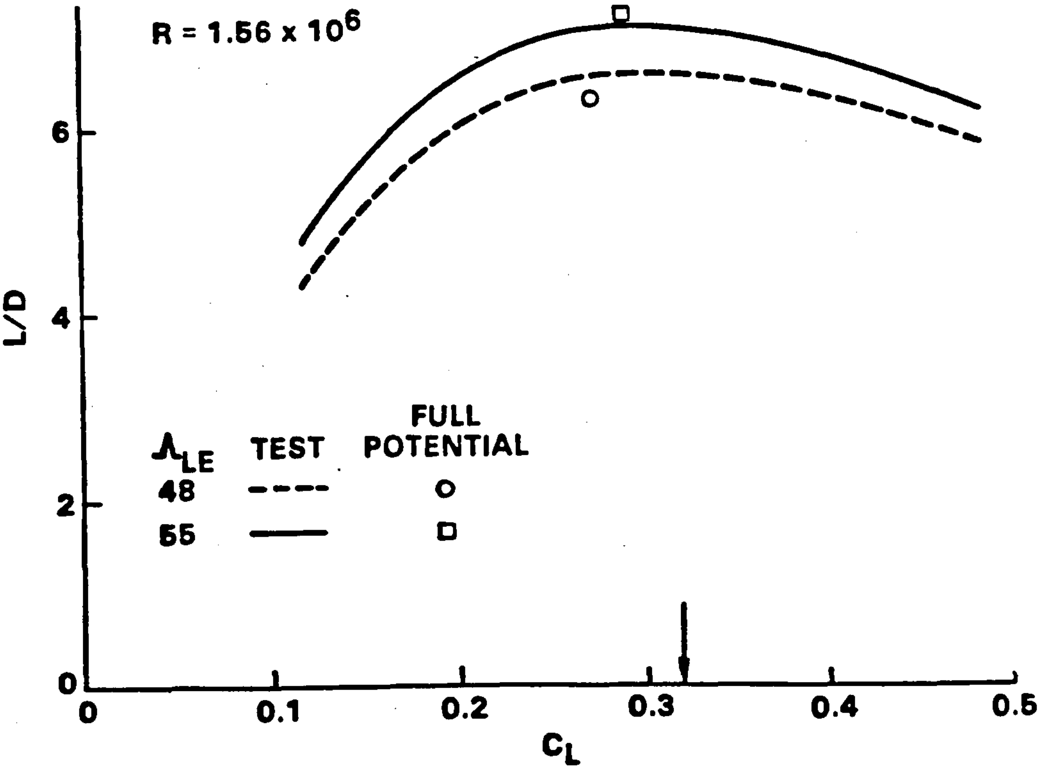

Fig. 15. Impact of sweep on lift–drag ratio at $M = 1.6$, nacelle off.

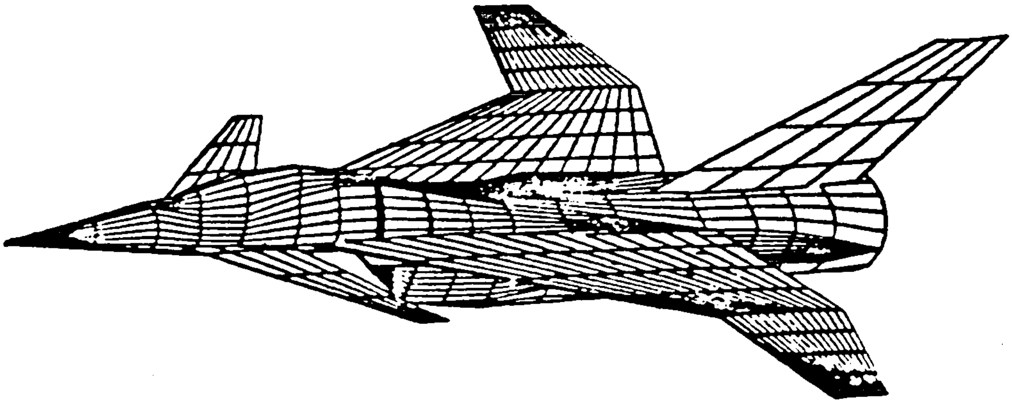

Fig. 16. Langley canard-wing fighter configuration.

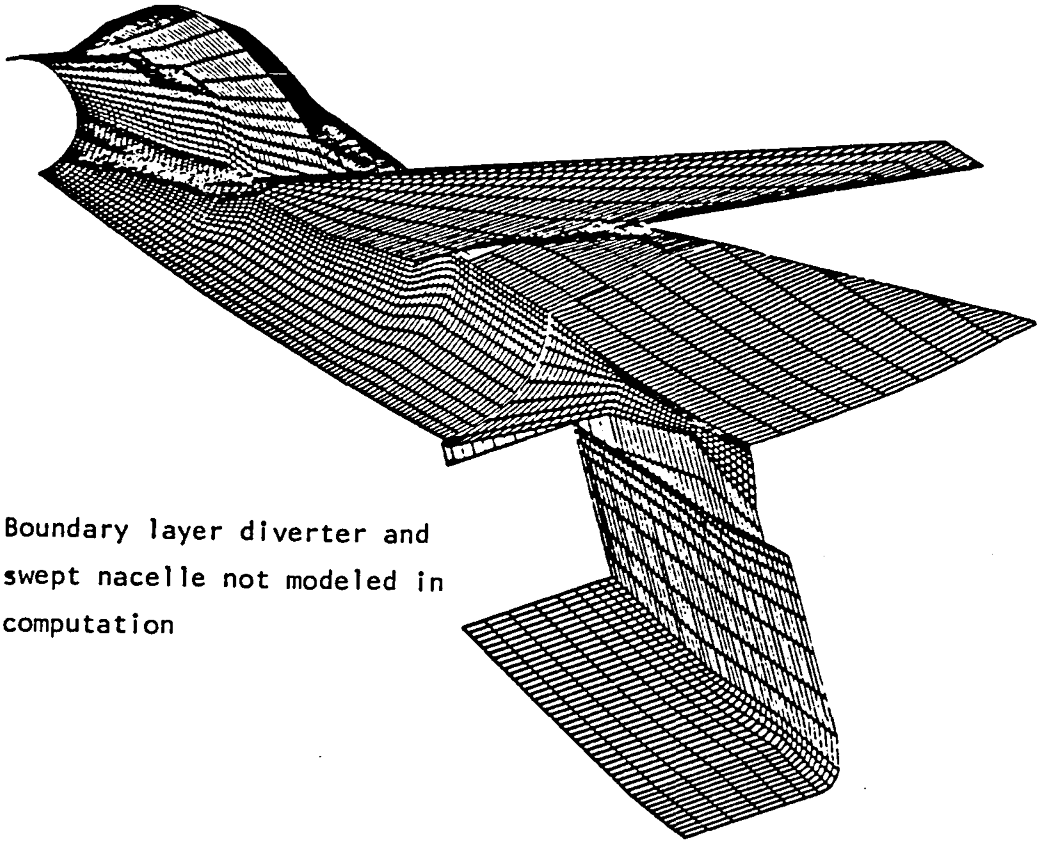

Note: Boundary layer diverter and swept nacelle not modeled in computation

Fig. 17. Computational geometry and surface gridding for Langley fighter configuration.

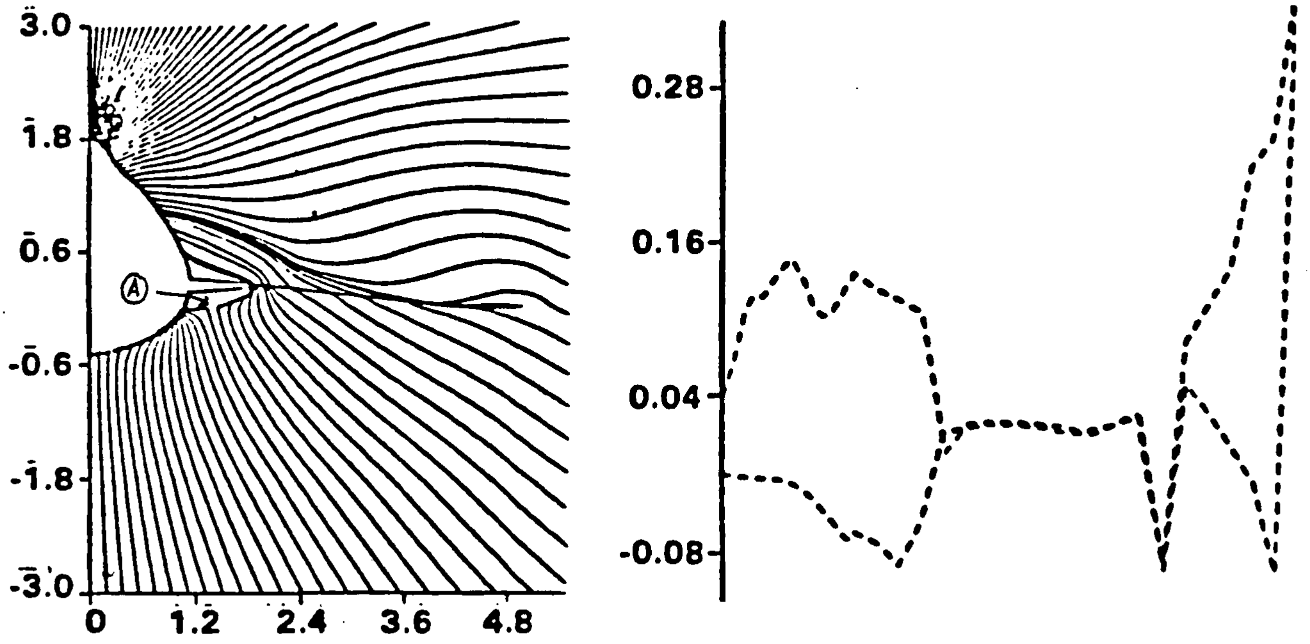

a)

Ⓐ - SADDLE SINGULARITY

b)

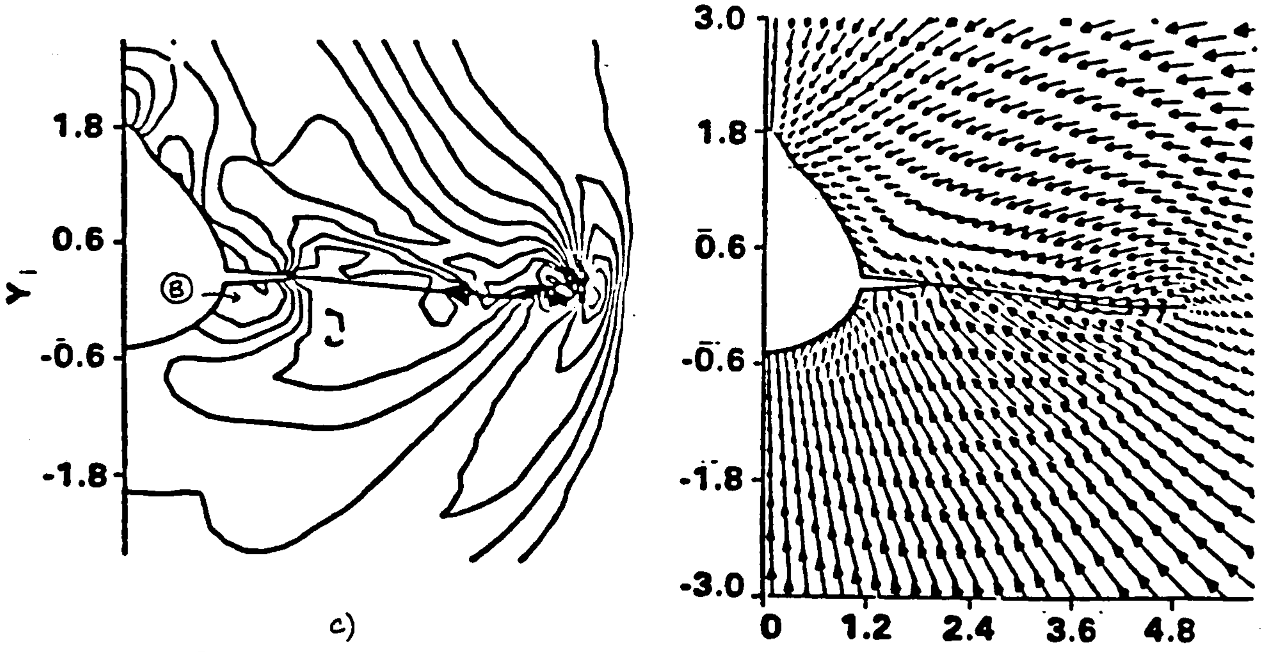

c)

Ⓑ - NODAL SINGULARITY

d)

Fig. 18. Solution for Langley fighter configuration; $M_\infty = 2.0$, $\alpha = 4.0$, $x = 11.0$; (a) streamline, (b) surface pressure coefficient, (c) pressure contour, (d) velocity contour.

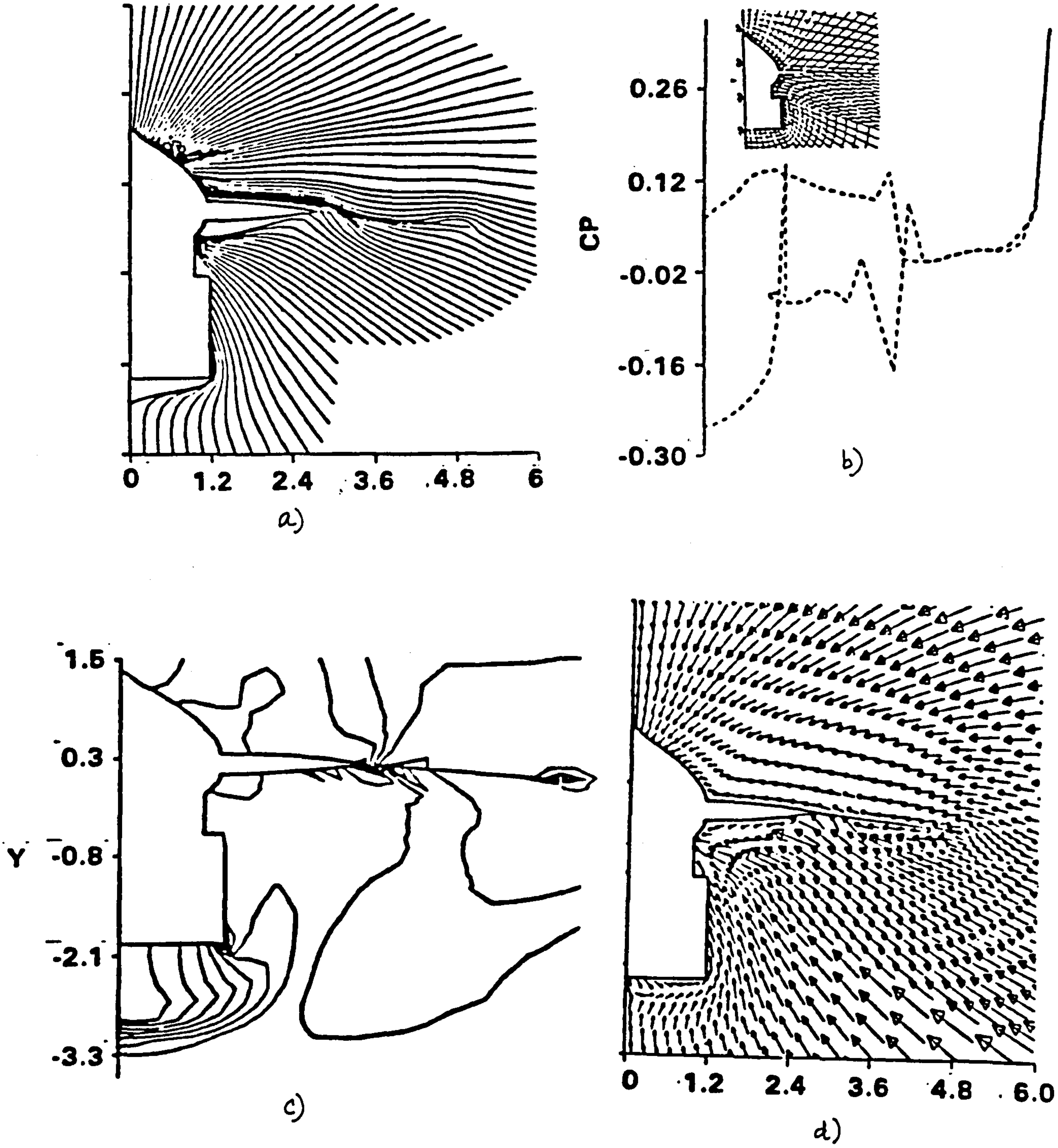

Fig. 19. Solution for Langley fighter configuration; $M_\infty = 2.0$, $\alpha = 4.0$, $x = 14.0$; (a) streamline, (b) surface pressure coefficient, (c) pressure contour, (d) velocity contour.

results at a station where the nacelle is present. The formation of a shock around the nacelle is clearly seen in Fig. 19. The upper and lower center plane pressure contours at $M_\infty = 2.0$ and $\alpha = 4°$ are shown in Fig. 20. The bow shock, canopy shock, nacelle shock and expansion wave are evident in this figure.

3.3 Case 3 — Miscellaneous Cases

3.3.1 Shuttle Aerodynamics

Appendix C contains the reprint of a paper[6] presented in January 1985 (AIAA-85-0272) that deals with applications of the full potential method to three dimensional geometries including multibody configurations. The paper presents the results of calculations for the isolated Shuttle Orbiter and the mated Shuttle configuration (Orbiter, External Tank, and Solid Rocket Boosters).

3.3.2 Transatmospheric Vehicle

The paper of Ref. 6 also presented some preliminary results for analysis of a proposed transatmospheric vehicle (TAV) concept. Figure 21 presents results of additional calculations on an alternate TAV configuration. Analysis of these TAV concepts indicates that the rapid execution times of the vectorized full potential code makes it a very useful design/analysis tool for preliminary design of TAV configurations.

Figures 22–24 show application of the full potential code to a TAV–like configuration with fuselage–mounted vertical tails.

3.3.3 Supersonic Inlet Cowl Design

Appendix C includes a paper[15] given in July 1985 (AIAA-85-1703) which illustrates the use of the SIMP program for the design of a twisted–cone inlet spike. The objective was to determine the proper location of the swept cowl lip such that the oblique shock emanating from the compression cone is attached at the cowl lip at the design supersonic Mach number. The SIMP calculations were compared with the results of an Euler solver[15] under development and, as expected, the SIMP code overpredicts the pressure on the upper surface where a nonisentropic shock is formed. This problem illustrates the limitations of the SIMP code and shows the need for an Euler method for supersonic flow computations which must capture strong shock waves.

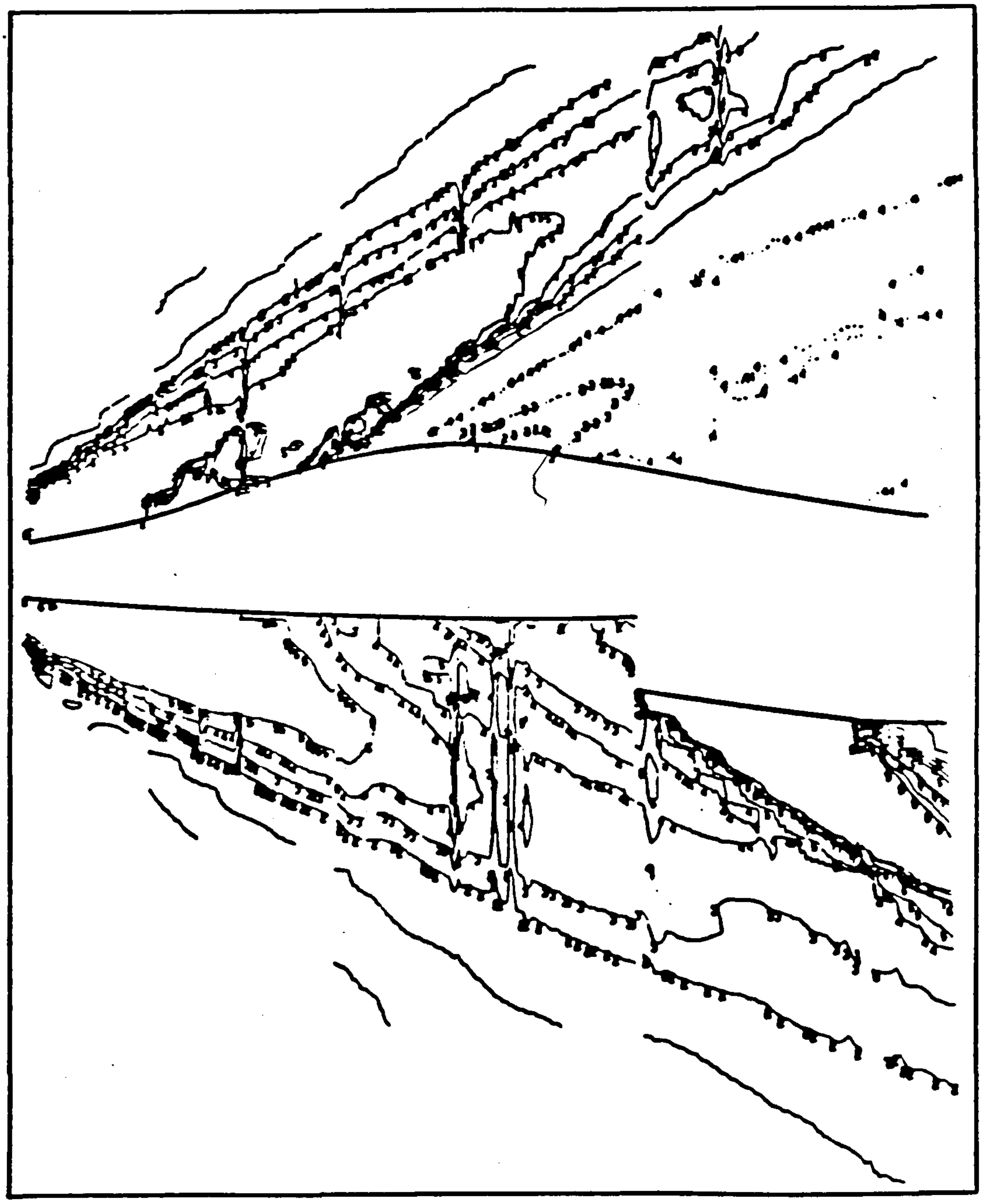

Fig. 20. Upper and lower centerplane pressure contour for Langley fighter configuration; $M_\infty = 2.0$, $\alpha = 4.0$.

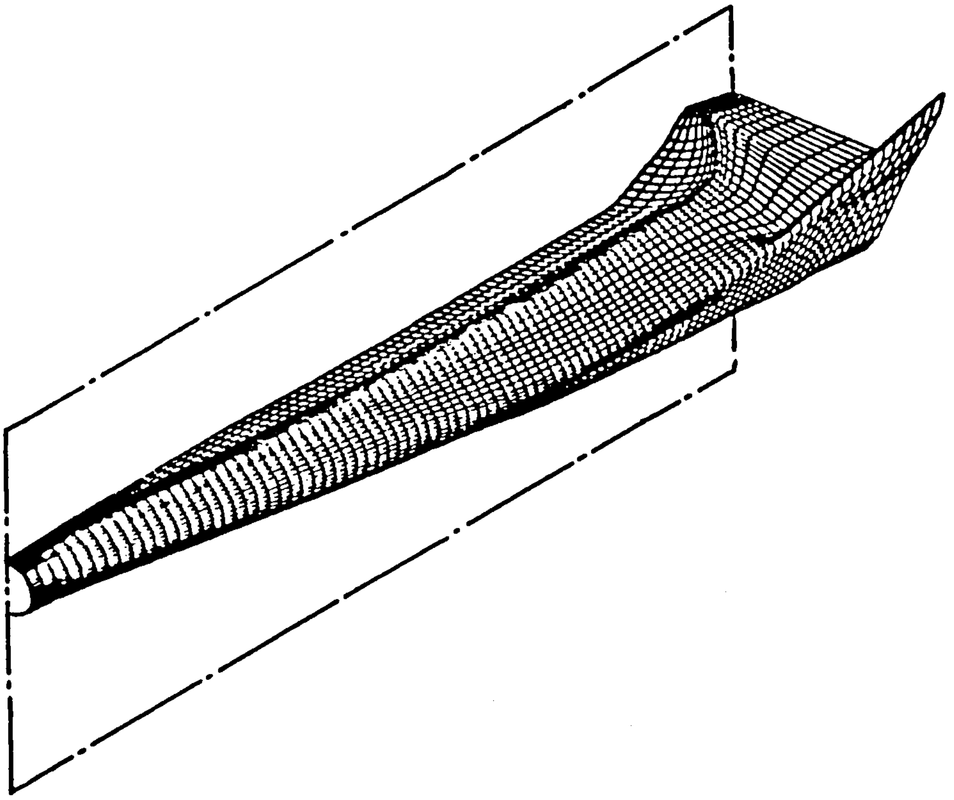

TAV CENTERLINE PRESSURE CONTOURS

$M_\infty = 1.4,\ \alpha = 0°$

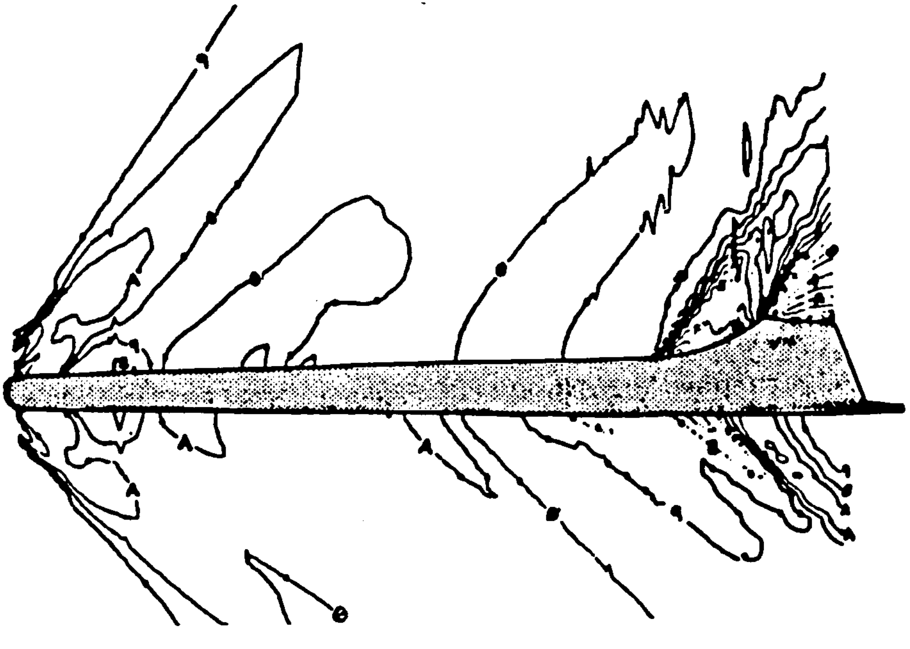

Fig. 21. TAV configuration and pressure contours.

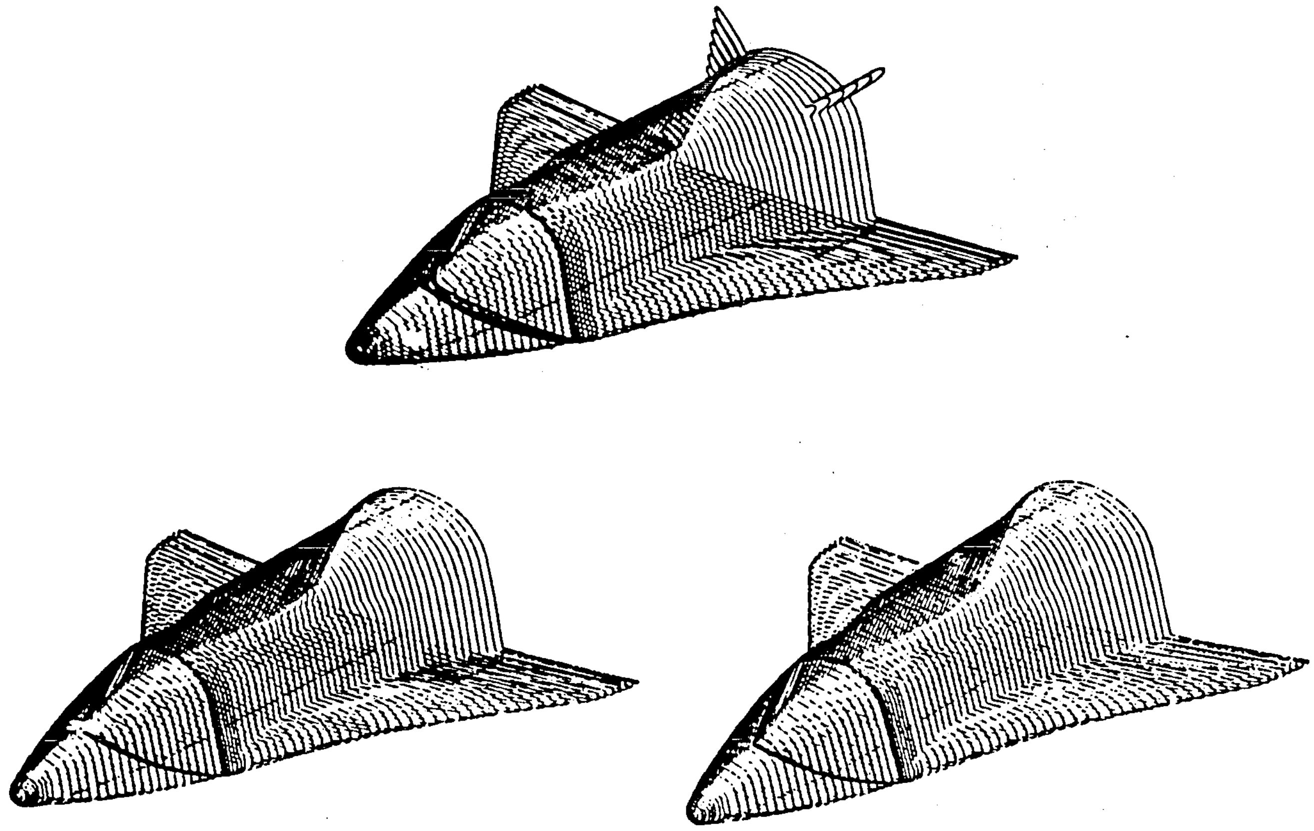

Fig. 22. TAV configurations.

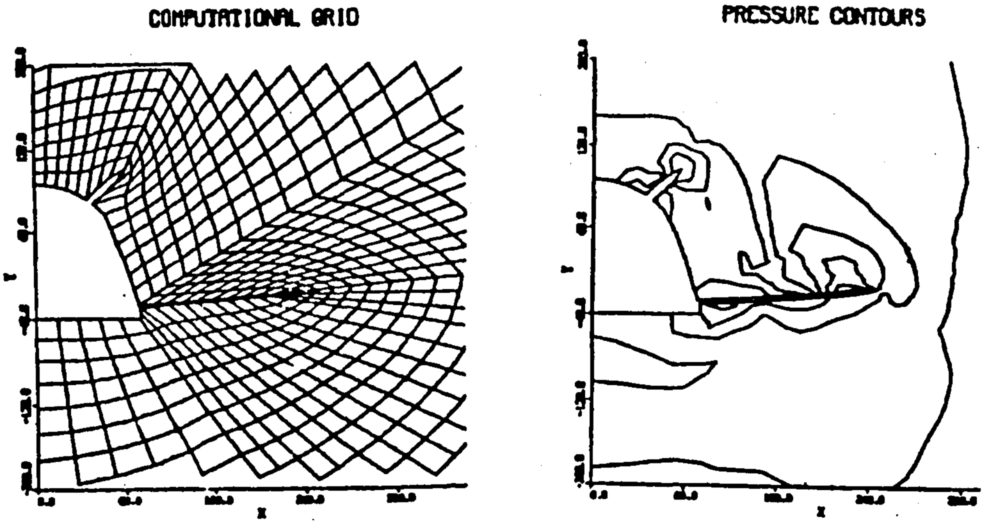

Fig. 23. Gridding and pressure contours.

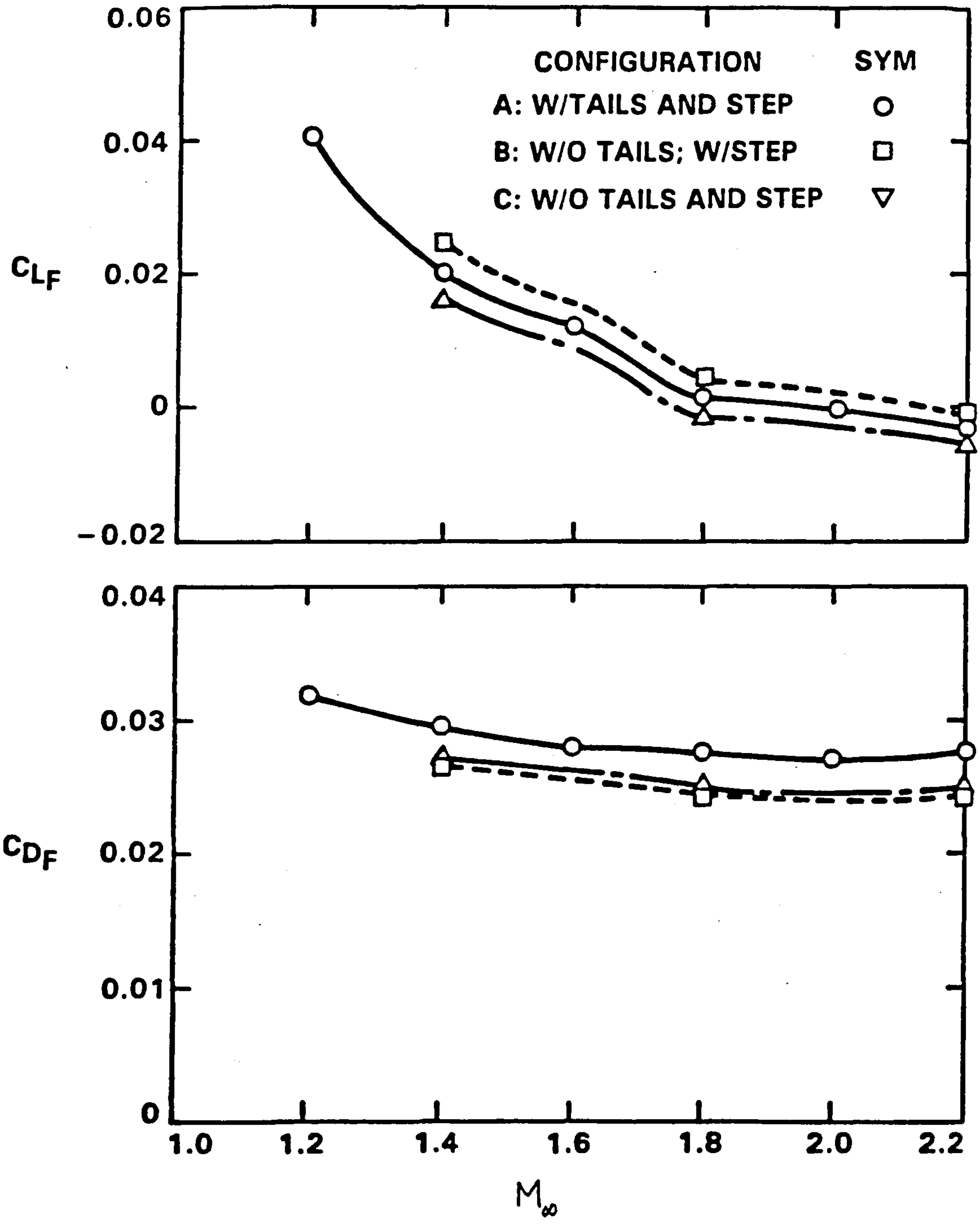

Fig. 24. Variation of TAV forebody lift and drag coefficients.

4.0 CONCLUSIONS

This report demonstrates the use of a nonlinear full potential aerodynamic prediction capability developed at Rockwell International under a contract from NASA–Langley Research Center. The method is now routinely employed to analyze and assist in the design of advanced fighter wings at supersonic flight conditions. Also, the nonlinear method is being used to analyze extremely complex geometries that include complete fighter geometries (canard, nacelle, vertical tail and wake effects). Use of supercomputers and vector coding make application of this powerful nonlinear method very attractive and cost–effective.

Appendices are included which give details of the code structure, input data, a sample test case and user's guide, and relevant publications.

5.0 REFERENCES

1. Shankar, V., "A Unified Full Potential Scheme for Subsonic, Transonic and Supersonic Flows," AIAA Paper No. 85-1643, AIAA 18th Fluid Dynamics and Plasmadynamics and Lasers Conference, Cincinnati, July 16–18, 1985.

2. Shankar, V., "A Conservative Full Potential, Implicit Marching Scheme for Supersonic Flows," AIAA J. 10 (11), 1508-1514 (1982).

3. Shankar, V. and Osher, S., "An Efficient Full Potential Implicit Method Based on Characteristics for Analysis of Supersonic Flows," AIAA J. 21 (9), 1262 (1983).

4. Shankar, V., Szema, K.–Y., and Osher, S., "A Conservative Type–Dependent Full Potential Method for the Treatment of Supersonic Flow with Embedded Subsonic Regions," AIAA Paper No. 83–1887, July 1983; AIAA J. 23 (1), 41 (1985).

5. Shankar, V. and Szema, K.–Y., "Conservative Full Potential Implicit Marching Scheme for Supersonic Flows," presented at the Univ. of Tenn. Space Inst. Workshop on Computational Fluid Dynamics, Article 6.1, UTSI Pub. No. E01–4005–023–84, March 1984.

6. Szema, K.–Y., Riba, W.L., Shankar, V., and Gorski, J.J., "Computation of Supersonic Flows over Three–Dimensional Configurations," AIAA Journal of Aircraft, Vol. 22, No. 12, 1079, 1985.

7. Bonner, E., Clever, W., and Dunn, K., "Aerodynamic Preliminary Analysis System," NASA CR–145284, April 1978.

8. Clever, W.C., "Supersonic Second Order Analysis and Optimization Program," NASA CR–172342, August 1984.

9. Shankar, V., Gorski, J., and Osher, S., "A Fast, Time–Accurate Unsteady Full Potential Scheme," AIAA Paper No. 85–1512, AIAA 7th Computational Fluid Dynamics Conf., Cincinnati, July 1985.

10. Caughey, D.A. and Jameson, A., "Recent Progress in Finite Volume Calculations for Wing–Fuselage Combinations," AIAA Paper No. 79–1513, July 1979.

11. Nash, J. and Scruggs, R., "An Implicit Method for the Calculation of Three-Dimensional Boundary Layers in Finite, Thick Wings," AFFDL TR–77–122, February 1977.

12. Shankar, V., Rudy, S., and Szema, K.–Y., "Application of a Two–Dimensional Grid Solver for Three–Dimensional Problems," ASME Applied Mechanics, Bioengineering and Fluids Engineering Conf., Vol. No. G00222, June 20–22, 1983; AIAA J. 23 (3), 326 (1985).

13. Jones, K.M., Talcott, N.A., and Shankar, V., "Full Potential Solutions of Three-Dimensional Supersonic Flows," J. of Aircraft 22 (10), 881 (1985).

14. Siclari, M.J. and Rubel, A., "Entropy Corrections to Supersonic Conical Nonlinear Potential Flows," AIAA Paper No. 84–1683, June 1984.

15. Chakravarthy, S.R. and Szema, K.–Y., "An Euler Solver for Three–Dimensional Supersonic Flows with Subsonic Pockets," AIAA Paper No. 85–1703, July 1985.

16. Shankar, V. and Szema, K.–Y., "Nonlinear Potential Analysis Techniques for Supersonic Aerodynamic Design," NASA CR–172507, March 1985.

17. Stack, S.H., Edwards, C.L.W., and Small, W.J., "GEMPAK: An Arbitrary Aircraft Geometry Generator," NASA TP–1022, December 1977.

18. Raymer, D.P., "Configuration Development System," Rockwell International Report TFD–78–755–4, April 1983.

19. Shrout, B.L. and Talcott, N.A., Jr., "Effect of Wing Sweep and Camber on Aerodynamic Characteristics of a Fighter Configuration at Supersonic Speeds," NASA TM–86427, October 1985.

20. Bonner, E., "Nonlinear Aerodynamic Wing Design," NASA CR–3950, Contract NAS1–15820, December 1985.

21. Hom, K.W. and Ticatch, L.A., "Aerodynamic Test and Analysis of an Advanced Supersonic Fighter Concept Including Effects of Horizontal Tail and Canard Control Surfaces over a Mach Number Range 1.6 to 2.5," NASA TP-2526, December 1985.

APPENDIX A — CODE STRUCTURE

CODE ORGANIZATION

The SIMP analysis code is applicable to arbitrary wing–body–nacelle–tail arrangements from moderate supersonic Mach numbers ($M_\infty \sim 1.2$) to values of the hypersonic similarity parameter $M\delta \leq 1$. The lower code limit is governed by the extent of the embedded subsonic flow while the upper limit results from a breakdown in the isentropic assumption for strong shock waves. Also, since the potential theory is irrotational, the modeling of any vortices is not attempted.

The program is written in FORTRAN V language. It can be executed on any CDC machine (CYBER 176, CDC 7600), as well as on the CRAY–XMP and CYBER 205. For a cross–plane (η, ξ) grid of 25 x 140, the program requires 660,000 words of memory. The program consists of a main routine and several subroutines. A brief description of the code along with input instructions needed to execute the code are given in this Appendix.

Program MAIN

Program MAIN coordinates the entire operation. A flowchart describing the various operations performed by the MAIN program is given in Fig. A1. The MAIN program sets up the initial (known) data plane and the body–fitted grid system and performs the L_ξ and L_η operators to advance the solution. The marching step size $\Delta\varsigma$ can either be prescribed or computed at each marching plane from a given Courant number and the maximum eigenvalue. The various read and write tapes used in the calculation are listed below.

Program MAIN (Tape 1, Tape 2, Tape 3, Tape 4, Tape 5, Tape 7, Tape 8, Output, Tape 6 = Output).

Tape 1: Output solutions for plot.

Tape 2: Output solutions for restart.

Tape 3: Read in starting solutions for restart.

Tape 4: Output solutions for restart.

Tape 5: Input data.

Tape 6: Solution output.

Tape 7: Read tape containing solutions for subsonic region.

Tape 8: Write tape for subsonic bubble calculation.

Subroutine INVSXI and Subroutine INVSETA

The factored implicit scheme for the governing full potential equation can be written as

$$L_\xi L_\eta(\Delta\phi) = R$$

and it is implemented as follows:

$$L_\xi(\Delta\phi)^* = R \quad , \quad L_\eta(\Delta\phi) = (\Delta\phi)^*$$

$$\phi_{i+1} = \phi_i + \Delta\phi.$$

The subroutine INVSXI performs the ξ inversion, and the η inversion is solved in subroutine INVSETA.

Subroutine EIGEN (EIGENY, EIGENZ)

This subroutine computes the maximum eigenvalue EIGENY in the (ς,η) plane and the maximum eigenvalue EIGENZ in the (ς,ξ) plane. The expression used for calculating the eigenvalue is given in Ref. 5. The maximum eigenvalue information is then used to compute a marching step-size $\Delta\varsigma$ for a specified Courant number.

Subroutine NFORCE (PX, PY, PM, AREA, KG)

At the end of each marching plane calculation, this subroutine computes the axial force, PX, vertical force, PY, and the side force, PZ, by integrating the pressure force acting on an elemental area, dA. The elemental area, dA, is computed from the transformation matrix using the formula (at a body point $j = 2$).

$$dA = \left\{ \left[y_\varsigma z_\xi - z_\varsigma y_\xi \right]^2 + \left[x_\xi z_\varsigma - x_\varsigma z_\xi \right]^2 + \left[y_\xi x_\varsigma - y_\varsigma x_\xi \right]^2 \right\}^{1/2} d\varsigma d\xi.$$

$KG = 0$, conical or blunt body nose force calculation

$= 1$, rest of the body force calculation.

The program also prints the force coefficients, C_L, C_D, and C_S (side force coefficient) information based on a prescribed reference area, and moment coefficients, C_M, C_Y, and C_R about a given reference point (X_0, Y_0, Z_0). C_Y is the yawing moment coefficient and C_R is the rolling moment coefficient. C_S, C_Y, and C_R are opposite in sign from the standard convention, since the W component of velocity is defined to be positive from the centerline out towards the left wing.

Subroutine GEOM (N9, NRP)

$N9 = 0$, geometry data at X_1 and X_2 are read in

> 0, geometry data at X_1 is updated and X_2 is read in

$NRP = 0$, constant x marching plane geometry calculation

$= 1$, spherical marching plane geometry calculation

Subroutine GEOM sets up the body grid points from a prescribed geometry shape. From the input geometry points, a key point system is established using cubic splines. These key points are then joined from one prescribed geometry station to the next to provide the geometry at any intermediate marching plane[12].

Subroutine GRID

Once the body points are obtained at a marching plane from GEOM, subroutine GRID sets up the entire crossflow plane grid using an elliptic grid solver that satisfies certain grid constraints.

Subroutine METRIC

This subroutine computes all the necessary transformation metrics and Jacobians at various node and half-node locations as required by the solution algorithm (L_ξ and L_η operators).

Subroutine UVW

This subroutine computes all the contravariant velocities, U, V, and W, and the density ρ.

Subroutine RHOBIAS

This subroutine performs the density biasing in the (η, ξ) plane based on characteristic signal propagation theory. This operation is essential to treat crossflow supersonic regions and to capture shock waves.

INPUT DATA

The input data can be divided into four parts: (1) header data describing mesh information, Mach number, angle of attack, aerodynamic coefficient reference quantities, center of gravity location, etc.; (2) detailed geometric coordinates defining configuration cross plane contours; (3) program update file directives defining code modifications; and (4) job control directives defining program and input/output file allocations (this depends on the particular computer).

Header Data

A typical analysis of a complete configuration requires several regions of marching calculations for a complete analysis. Each region calculation has a different set of header instructions for describing grid parameters, wake information if pertinent, restart directions, and number of mesh points for each patch of the region. A sample input is given in Appendix B for the configuration of Fig. A2, and a brief description of each variable is given in this section.

Card*	Symbol	Format	Description
100	NMAX	I5	Number of axial marching steps. If NMAX = 0, and ZTA1 = $\bar{\zeta}$ and TAPER = F the code generates geometry and grid data at $x = \bar{\zeta}$ for plotting. For NMAX$\neq$ 0, the code will march for NMAX steps unless XEND is encountered first. NMAX must include NCON iterations if applicable. (NMAX = 0 option for grid plot is provided to allow the user to review the quality of grid at various axial stations before the flow solver is turned on.)
110	JMAX	I5	Mesh points in the normal direction (η). Present maximum is 25. This can be increased by increasing the dimension. This number includes the $J = 1$ dummy line inside the geometry.
120	KMAX	I5	Mesh points in circumferential direction (ξ) (maximum value: 140). This number includes

---

* Card number (e.g., Card 100) is not part of the input file.

			the $K = 1$ and $K =$KMAX dummy lines. If this number is incorrectly specified, the code will reset KMAX properly using the KMAX $= 1 +$ (IPT1–1) $+$ (IPT2–1) $+$ (IPT3–1) $+ \cdots +$ (IPTn–1) $+ 1$ (definition of IPT follows in the next section). "n" is the number of patches.
130	NRM	I5	Number of grid regions (separated by dashed lines in Fig. A3). Maximum of 6 allowed.
140	NU0	I5	Not used.
150	NP	I5	Selected surface output for every NP steps.
160	KWKMIN	I5	K value of starting point of a patch containing wake (Fig. A3).
170	KWKMAX	I5	K value of ending point of a patch containing wake (Fig. A3).
180	NCON	I5	Number of iterations for conical starting solution (usually set to 30). To establish this starting solution, the geometry is initially assumed to be conical. The geometry at ZTA1 is projected forward conically to a point at (0,0,0). (The nose of the configuration is assumed to be at (0,0,0). If the geometry is not input this way,

			shift the geometry using PTNOSE and YSHIFT.) The solution is then obtained for this conical geometry based on NCON iterations. The conical solution is used as a starting solution for the nonconical case, beginning at ZTA1. The marching step size $\Delta\zeta$ for the conical calculation is based on a specified Courant number (CFLIN). The user should be aware that NCON is included in the NMAX total. Also, ZTA1 output values have no physical significance during conical calculation.
190	NITER	I5	Number of iterations to generate the marching grid using an elliptic grid solver. Usually set to 30. If grid routine fails, set this to 0 to analyze the geometry and the initial grid generated before grid relaxation (this is for debugging purposes). Set NITER back to 30 for flow field analysis. NMAX should be set to zero for analyzing the grid quality.
200	NSPTI	I5	Number of ζ locations for detailed flow field output (maximum of 10 locations).
210	ITERGE	I5	Number of global iterations for subsonic region calculations.

The marching calculation can encounter subsonic (MSR and TSR) regions, especially at low freestream supersonic Mach numbers ($M_\infty \sim 1.2$ to 1.8). For the first pass through subsonic regions, the relaxation routine in the code assumes sonic flux conditions (Ref. 4). If the extent of the subsonic region (usually confined near the body surface, especially near the leading edge) is very small, just the first pass with assumed sonic flux conditions will suffice for the marching calculation. However, if the subsonic zone is expected to be large, (around bumps on the geometry which might create detached shocks such as the canopy), several relaxation passes through the subsonic zone are essential for correct representation of the flow. ITERGE represents the number of relaxation passes for subsonic calculation. The user may not know ahead of time if a large subsonic zone is to be encountered during the marching calculation. The output prints the location of subsonic points encountered during the first pass. If too many subsonic points are predicted by the code during the first pass, then set ITERGE > 1 and TAPE8W = TRUE. Then, subsonic relaxation is carried out over the entire NMAX marching planes for ITERGE times. The relaxation solution from

			each pass is stored on tape (TAPE8W) to aid in the relaxation process (Ref. 4). If the initial prescription of ITERGE value is not enough for satisfactory subsonic convergence (RMS change in density between two relaxation cycles should be a small value, preferably 10^{-4}), then additional subsonic iterations can be performed through the restart option (TAPER = TRUE, TAPE8W = TRUE) by reading the previously stored solution on TAPE7. During subsonic calculations, the marching step size $\Delta\varsigma$ is to be kept constant.
220	CFLIN	F10.5	The CFL number. If DZTAIN (Card 230) is negative, the axial step size $\Delta\varsigma$ is generated based on CFL number. The relationship between $\Delta\varsigma$ and CFL number through the maximum eigenvalue is given in Ref. 3. When the geometry change in the axial direction is minimal (nearly conical shape), the marching step size $\Delta\varsigma$ is given by the CFL number (usually CFLIN set to 5). If the geometry changes are very abrupt (emergence of wing, canopy, tail, or any other component) or drastically nonconical, then $\Delta\varsigma$ is prescribed by the user (see Fig. A4).

230	DZTAIN	F10.5	Initial step size. For nonconical geometry calculations, DZTAIN is chosen to be either DZMIN or DZMAX. If DZTAIN is set to less than DZMAX, then during marching calculation, $\Delta\zeta$ will be slowly increased to DZMAX.
240	DZMAX	F10.5	Maximum step size.
250	DZMIN	F10.5	Minimum step size.
			(DZMAX and DZMIN depend on the complexity of the geometry. Suggested value: DZMAX = total length/400 and DZMIN = DZMAX/2.) If DZMIN is set equal to DZMAX, then constant step size is used.
260	FSM	F10.5	Freestream Mach number.
270	ALFA	F10.5	Angle of attack (degrees).
280	THTO	F10.5	Angle of outer boundary (degrees). This angle must be larger than the bow shock wave in order for the code to capture the bow shock. Often the best way to choose this value is to calculate the bow shock wave half angle and add 10°.

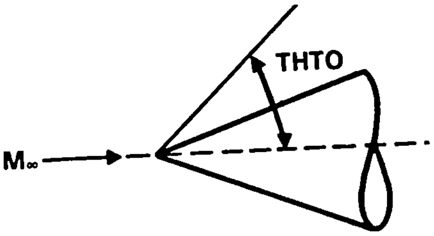

290	DZTA	F10.5	First step size for the marching calculation after conical starting solution. Usually, this value is set to DZMIN. 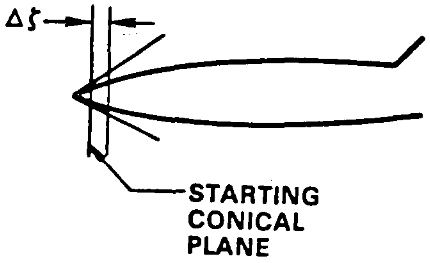
300	ZTA1	F10.5	Starting ζ location. If TAPER = TRUE, this value is overwritten by stored restart value.
310	XEND	F10.5	Final ζ location for this run.
320	AMU1	F10.5	1: first order accuracy in marching direction. 0: second-order accuracy in marching direction.
330	AMU2	F10.5	0: first-order accuracy in marching direction.

			1: second–order accuracy in marching direction.
			Usually, first–order accuracy is used for rapidly varying geometries. For nearly conical cases, second–order accuracy is recommended.
340	XWAKE	F10.5	Wake starting location in the axial direction (see Fig. A3).
350	BETANG	F10.5	Angle of yaw (degrees).
360	CHL	F10.5	Geometry scale factor. If set to total length, ζ will be scaled from 0 to 1. If set to 1, actual dimensions of the geometry are used. Use of dimensional (CHL = 1) or nondimensional (CHL = ℓ) option is left to user's choice.
370	PTNOSE	F10.5	Axial geometry shift. Equal to negative of apex of the forebody (i.e., shifts configuration nose to $\zeta = 0$).
380	YSHIFT	F10.5	Vertical geometry shift (i.e., shifts configuration nose to $\eta = 0$).

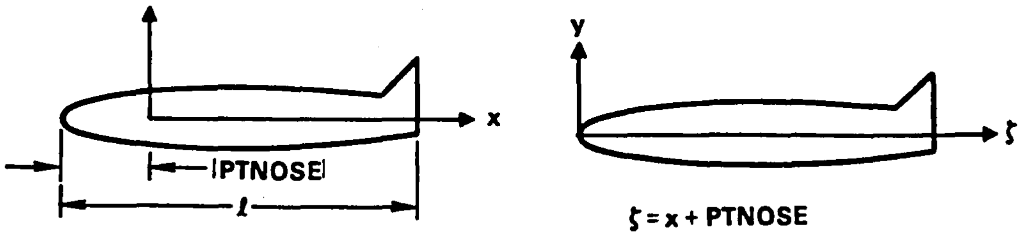

390	XO	F10.5	Moment reference x location (unit∼length).
400	YO	F10.5	Moment reference y location (unit∼length).
410	AAA	F10.5	Reference area to compute aerodynamic force coefficients (unit∼length^2).
420	ALL	F10.5	Reference length to compute aerodynamic moment coefficients (unit∼length).
			XO, YO, AAA, and ALL are to be chosen (dimensional or nondimensional) based on CHL.
430	OMEGA	F10.5	Overrelaxation parameter for grid generation. Suggested value: 1.0 (for vectorized code) 1.75 (for scalar code).
440	YAW	L5	T: Calculation with yaw (full cross-plane grid). F: Without yaw (half-plane grid).
450	NUGRID	L5	T: Numerical grid generation (normally used). F: User must adapt code for his particular need.
460	IREAD	L5	T: Read body geometry input which must be supplied in the format described in the next section titled "Geometry Data".

			F: Analytic geometry (which must be supplied by the user and inserted in subroutine GRID).
470	RPLANE	L5	T: Spherical plane marching (spherical plane marching is exercised only for conical flow calculations). F: Constant x plane marching.
480	TAPER	L5	T: Restart the calculation. F: Start the calculation from freestream ϕ values.
490	TAPEW	L5	T: Write restart data on Tapes 2 and 4. F: No data storage for restart.
500	TAPE8W	L5	T: Write entire flow field data for subsonic iterations on Tape 8. F: No flow field data saved.
			When a tape read or tape write is set TRUE, the user will have to provide the necessary job control cards.
510	FORCE	L5	T: Compute aerodynamic forces and moments. F: No force computation.
520	THTU(5)	5I5	Grid region terminal points (k) (see Fig. A3). These values are the K values of the points where the dashed lines intersect

			the body.
530	INU(5)	5F10.4	Polar angle (degrees) at respective terminal point.
540	ZTAPT(10)	10F8.4	x–locations of detailed flow field printouts.
550	ISC	I5	Number of patches (geometry) that define the cross–sectional shape of the configuration for this region of the configuration (see Figs. A3 and A5). (Maximum number of patches = 15.)
560	NPT(15)	15I5	Number of output points on each patch (maximum number of points per patch is 30).

Geometry Data

The cross–sectional geometry of a typical aircraft changes considerably in the axial direction due to emergence of various components such as canopy, wing, nacelle, and tail, etc. The marching computation, as it sweeps along the marching direction ζ, has to account for this geometry variation to set up the proper body–fitted coordinate system to aid in the application of body boundary conditions. To treat complex geometry cross sections, patches are introduced to define the geometry as indicated in Fig. A2. Using patches, a configuration is defined by several regions of cross sections. The number of patches defining a section is constant for a given region (Fig. A2).

A complete computation over a configuration such as the one in Fig. A2 is usually done in segments rather than in one shot. The calculation starts from the nose and proceeds along ζ. Even within a region (defined by the same number of patches), the calculation might be done in segments using the restart option in the code. Restart is used any time the calculation is halted and then continued with another run that picks up where the previous run left off. Pure restart is performed only when there is no alteration to the number of points along η (JMAX) and along ξ (KMAX), and no change in the number of grid points per patch between the previous run and the current restart run. If there is any alteration to the grid structure, the restart run will automatically perform a respace operation to interpolate the solution from the previous solution grid to the current grid. Respace is used whenever the following situations are encountered:

1) Number of patches defining the cross section is changed. This situation occurs when the cross-sectional geometry becomes more complex. This is illustrated in Fig. A2.

2) Number of JMAX and/or KMAX points is changed (even if the number of patches defining the cross section is kept the same as before). This situation often occurs for cases where a patch length is increasing with ς. For example, a swept wing is very small when it first appears in the cross section of the geometry and only requires a few grid points for accurate computation of the flow field. However, as the analysis is continued in the ς direction, the wing patches grow and will require more points for accurate flow field analysis.

3) Number of grid points per patch is changed (even if KMAX is kept the same as before).

Any time a respace is required, the code must be stopped. The code will automatically do a respace if KMAX or JMAX is different from the previous values of KMAX and JMAX.

One may be able to compute the entire configuration using the same number of patches and same KMAX and JMAX values throughout to avoid the respace requirement. This will mean even in the forebody region of a configuration, where the cross-sectional geometry is usually simple, more grid points and more patches are to be used than necessary to adequately resolve the flow field. Use of the same number of patches and grid points for throughout the length of the configuration is generally not recommended. This can substantially increase the total execution time.

Transitioning from one region to the next (number of patches is changed) requires an overlapped zone, as illustrated in Fig. A6, to allow for increased or decreased number of patches in the next region. The extent of this overlapped zone must be sufficient to include at least the final three marching data planes of the prior region. In the overlapped region, the data from the previous region is interpolated onto the grids of the new region. For the example of Fig. A6, the results from the 3–patch region are interpolated onto a 4–patch region grid at the same x location. This is required in order to continue marching along the body with the new patch definition.

Figure A6 illustrates how to transition from a fuselage computation to a wing–fuselage computation. First, the calculation is performed for the fuselage section denoted by REGION1 which ends just prior to the starting point of the wing. This calculation might involve, say, three patches. Then, to introduce the wing, a four patch representation is used in REGION2. In the overlapped zone, the fuselage which is defined using a three patch representation in REGION1 is represented by a four patch representation as part of REGION2. The second and third patch locations on the fuselage in REGION2 within the overlapped zone are chosen in the vicinity of where the leading edge of the wing is expected to emerge from the fuselage.

Wake Geometry

Behind the trailing edge of a lifting surface a cut is introduced (see Fig. A3), across which potential ϕ jumps are imposed (the ϕ jumps are computed at the trailing edge) to preserve density continuity across the flow through cut. Mathematical details of this so–called "wake model" are given in Ref. 4. The treatment of wake cut within the code requires the knowledge of starting and ending K index values of the upper wake cut and the lower one. Depending on the sweep of the trailing edge, the wake cut is appropriately modeled. This is illustrated in Fig. A3. The user has to define the shape of the trailing edge and also the starting x value where the wake begins to appear in the cross–sectional geometry (XWAKE). The wake cut is part of a patch which contains the wing also as illustrated in Fig. A3. As marching proceeds along the axial direction, the extent of the wake cut grows within that patch. The nomenclature for the starting and ending points of the wake cut are also indicated in Fig. A3. The number of points in the patch containing the wake cut is not allowed to change during the calculation. Thus, while exercising the respace option in the region containing the wake, the user has to ensure that the number of points in the wake patch (usually there are two wake patches; one corresponding to the upper cut and one for the lower cut) is not altered.

The shape of the trailing edge is provided by the user using the update option.

For the wing–body–vertical case of Fig. A2, a 3–patch initial region, a 6–patch center region, and an 8–patch final region was used. The patch definition for Region 1 is as indicated in Fig. A5. Zero length patches are not permissible. Since the analysis is marching in nature, a complete geometry data set is not required to begin and partially process a problem. Appropriate use of restart solutions allows continuation of the analysis as new or modified geometry becomes available.

The format for a typical station is shown below. The group of cards is repeated for each station of a region. The last point of each patch (except for the last patch of a station) should have the same coordinates as the first point of the next patch.

Card No.	Format	Field	Name	Description
A1	F15.6,I5	1	X1	The x value (longitudinal) of this station.
		2	ISC1	The number of patches for this section. $1 \leq \text{ISC1} \leq 15$.

The group of cards A2 through A3 are repeated ISC1 times.

Card No.	Format	Field	Name	Description
A2	3I5	1	ITH	Patch number ≤ 15.
		2	IPT	Number of points in this patch. $2 \leq \text{IPT} \leq 30$.

		3	ND	Mesh spacing parameters*. Typically the same for all stations of a region.

The A3 card is repeated IPT times

A3	2F15.6	1	YK	Vertical location of point (positive upwards). Points start at top centerline (see Fig. A5).
		2	ZK	Spanwise location of point.

Cubic spline interpolation is performed on input patch data to derive the geometry. Linear interpolation is performed to define the geometry at a marching plane between input stations.

Sample geometry data for the problem of Fig. A2 is presented in Table 1 and was developed using CDS[18].

Update File Directives

The SIMP code is not intended to compute all cases without the user having to interact with the code. There may be cases which will require the user to incorporate specific changes to the code to obtain a solution. The changes that are frequently encountered are listed here.

1) Shape of the trailing edge for wake calculation. In order to initiate the wake calculation, the code has to know the starting and ending K values of the wake region in the marching plane (see Fig. A3). Depending on whether the trailing edge has a positive slope or a negative slope, the K values in Fig. A3 are properly computed by the code. The user has to prescribe the shape of the trailing edge. This update change is done in Program MAIN by prescribing $Z_{TE} = f(\zeta) = a\zeta + b$ where "a" defines the trailing

---

* For segment AB: 0 equal space; 1 cluster near A; 2 cluster near B.

edge slope. The location where this change is made in MAIN is clearly marked in the code. If the trailing edge has no sweep, then KWKED1 = KWKST1 = K of leading edge (KLE).

2) Respecification of the relaxation parameter OP in the grid generation routine. For severe geometry cases, to impose orthogonality and required specific grid spacing in the η direction will require smaller values of OP (as low as 0.005). Generally, OP = 0.02. The parameter OP provides underrelaxation for the constraints P and Q which impose the orthogonality and grid spacing near the body surface. When OP = 0, the grid solver does not impose any constraints. For geometry sections with drastic variation in slopes in the cross section, imposition of P and Q constraints can lead to instability in the grid solver. Lowering the value of OP should relieve this problem.

   Usually, the grid in a marching plane is divided into several subregions (the NRM parameter defines the number of subregions, see Fig. A3). The value of OP can be set to different values for different grid regions depending on the severity of the geometry slope change in that particular region.

   The update change for OP is made in Subroutine GRID in loop "DO 100".

3) Averaging of ϕ. In regions of rapid flow expansion (flow around a sharp leading edge, clipped wing tip) the marching algorithm can run into instability problems. This will result in the density value at certain grid points becoming negative. Even though this might occur at only one or two points at a marching plane, the whole marching calculation comes to a halt. This problem, for most cases, can be alleviated by resetting the potential ϕ values, at grid points encountering negative density, by averaging the ϕ values surrounding those grid points. One such ϕ averaging technique usually specified through the update option is illustrated in Fig. A7 for a sharp leading edge point. If the problem persists, even after implementing the ϕ averaging procedure, one might consider a similar averaging procedure for density also. The user should carefully examine the grid to make sure that the negative density problem is not due to improper grid or improper geometry.

The update for ϕ averaging is made in Subroutine INVSETA. The location is after the statement "705 CONTINUE".

4) Restart for nacelle on. In order to introduce a flow through nacelle in the calculation, the respace/restart option is exercised just at the nacelle face location as illustrated in Fig. A8. The calculation is first performed just prior to the nacelle face location (Region N). Then, in the overlapped region, the nacelle face is extended forward (fictitious flow through nacelle surface) and a respace is performed to set up grid and ϕ values that correspond to the nacelle–on geometry. Such a respace calculation with a fictitious flow through nacelle is essential for a smooth transition into nacelle–on marching calculation. Through update, the user has to prescribe the K value of the starting and ending points of the nacelle to aid in the respace procedure. A sample update procedure for a nacelle–on calculation is given in Appendix B for the Zone 3 calculation.

TABLE I GEOMETRY DATA

```
 570=     -84.005810    3                       ─────────────────────
 580=    1    5    0                                      │
 590=       1.546702       0.000000  │                    │
 600=       1.546643       0.000323  │                    │
 610=       1.545103       0.018315  ├First Patch         │
 620=       1.540437       0.035744  │                    ▼
 630=       1.532035       0.051886  │
 640=    2    7    2                               First Station
 650=       1.532035       0.051886  │
 660=       1.522801       0.066404  │
 670=       1.510550       0.078012  │
 680=       1.496280       0.089136  ├ Second Patch
 690=       1.480402       0.096745  │
 700=       1.463290       0.101503  │
 710=       1.445334       0.103120  │
 720=    3   10    1
 730=       1.445334       0.103120  │
 740=       1.427338       0.101520  │
 750=       1.410231       0.096822  │
 760=       1.394302       0.089222  │
 770=       1.380160       0.078030  ├ Third Patch
 780=       1.367900       0.066460  │
 790=       1.357885       0.051917  │
 800=       1.350410       0.035707  │
 810=       1.345750       0.018258  │
 820=       1.344157       0.000000  │
 830=     -64.838013    3  ───────────────────────────────────
 840=    1    5    0                                      │
 850=       7.912823       0.000000                       │
 860=       7.907942       0.035226                       │
 870=       7.809140       1.704391                       │
 880=       7.543938       3.104908                       │
 890=       7.167405       4.202305                       ▼
 900=    2    7    2
 910=       7.167406       4.202305
 920=       6.712801       5.320372
 930=       6.104760       6.250120                Second Station
 940=       5.610!75       7.060505
 950=       4.937710       7.738470
 960=       4.138007       8.233154
 970=       3.153522       8.465744
 980=    3   10    1
 990=       3.153522       8.465744
1000=       1.927852       8.274061
1010=       1.140799       7.897685
1020=       0.640312       7.314930
1030=       0.265738       6.517867
1040=      -0.062191       5.512252
1050=      -0.386351       4.317586
1060=      -0.704225       2.967070
1070=      -0.967907       1.507670
1080=      -1.084095       0.000000
1090=     -44.675003    3
1100=    1    5    0
1110=      13.575716       0.000000
1120=      13.572840       0.035637
1130=      13.380405       2.761196
```

TABLE I Continued

```
8380:    289.670959     3
8390=   1   13    0
8400=     49.958420        0.000000
8410=     49.958382        1.937543
8420=     49.958420        4.388307
8430=     49.680511        7.428109
8440=     48.879784       10.266657
8450=     47.684164       12.876749
8460=     45.809948       15.224077
8470=     43.811752       17.267170
8480=     41.382515       18.957489
8490=     38.653479       20.230323
8500=     35.664185       21.049873
8510=     32.452553       21.319206
8520=     30.713291       21.295483
8530=   2   30    2
8540=     30.713291       21.295483
8550=     29.147690       23.898067
8560=     26.650154       28.498608
8570=     24.242348       33.629456
8580=     22.121189       38.922287
8590=     20.874866       42.500359
8600=     19.281048       47.515938
8610=     17.635311       53.495407
8620=     16.076260       61.088318
8630=     15.763639       65.987915
8640=     15.355867       68.569077
8650=     14.472219       73.730820
8660=     13.499191       78.891434
8670=     12.402630       84.404892
8680=     11.482655       88.847702
8690=     10.837719       91.789429
8700=     10.246025       94.368530
8710=      9.555044       97.232849
8720=      8.931576       99.526596
8730=      8.207584      102.105499
8740=      7.425758      104.684341
8750=      6.573520      107.263199
8760=      5.626501      109.842041
8770=      4.722771      112.048233
8780=      4.134672      113.304123
8790=      3.615775      114.227844
8800=      3.348063      114.597412
8810=      3.147297      114.798508
8820=      2.919736      114.946838
8830=      2.698931      114.993576
8840=   3   20    1
8850=      2.698931      114.993756
8860=      2.579846      114.980423
8870=      2.459620      114.933670
8880=      2.363239      114.838547
8890=      2.245280      114.634491
8900=      2.062772      113.952515
8910=      1.905408      112.702099
8920=      1.762813      111.130282
8930=      1.631411      109.008453
8940=      1.515947      106.502197
```

End of Region 1

```
8950=      1.424684      103.794922
8960=      1.356829      101.146477
8970=      1.204987       96.947678
8980=      1.095898       94.368591
8990=      0.917631       90.622636
9000=      0.640761       86.630768
9010=      0.257428       81.430713
9020=     -0.130081       76.311234
9030=     -0.450283       71.150040
9040=     -0.645550       65.987915
9050=     -0.994209       61.078348
9060=     -1.161518       57.469460
9070=     -1.294488       52.036896
9080=     -1.417318       45.258186
9090=     -1.456081       36.659615
9100=     -1.600638       27.491192
9110=     -1.781296       18.323032
9120=     -1.914585        9.163094
9130=     -1.960518        0.000000
9140=    257.762939     6
9150=   1    6    0
9160=     50.010979        0.000000
9170=     50.010979        0.611856
9180=     49.824493        3.408121
9190=     49.187645        6.642347
9200=     48.033119        9.893850
9210=     46.359802       12.845306
9220=   2    6    0
9230=     46.359802       12.845306
9240=     44.232117       15.282759
9250=     41.780586       17.095585
9260=     39.201439       18.276600
9270=     36.756943       18.921902
9280=     34.538315       19.328766
9290=   3   10    0
9300=     34.538315       19.328766
9310=     32.809967       21.765694
9320=     29.693047       26.516281
9330=     26.462524       31.830555
9340=     23.469040       37.253181
9350=     21.147877       42.008942
9360=     20.279148       43.921326
9370=     19.470787       46.044807
9380=     18.717278       48.341698
9390=     17.326115       53.398514
9400=   4   18    2
9410=     17.326115       53.398514
9420=     15.954689       59.162178
9430=     14.366322       65.990817
9440=     13.750040       68.714981
9450=     13.102150       71.150070
9460=     12.580235       73.730789
9470=     11.938618       76.311203
9480=     11.212303       78.891495
9490=     10.451151       81.471466
```

Beginning of Region 2

Note overlap in x

TABLE I Continued

End of Region 2

```
24360       520.031982    6
24370=    1    7    0
24380=       50.007111      0.000000
24390=       50.007019      2.742154
24400=       50.005111      4.956256
24410=       49.731850      7.991484
24420=       48.936188     10.893526
24430=       47.665405     13.590030
24440=       45.965707     16.014454
24450=    2    8    0
24460=       45.965707     16.014454
24470=       43.884506     18.106064
24480=       41.469543     19.809887
24490=       38.769760     21.076782
24500=       35.834953     21.863373
24510=       32.715767     22.132114
24520=       25.660957     22.127000
24530=       16.874676     22.126163
24540=    3   17    0
24550=       16.874676     22.126163
24560=       16.113289     30.020070
24570=       15.206806     39.139084
24580=       14.629675     48.051239
24590=       14.137501     56.337000
24600=       13.470024     65.900817
24610=       13.089690     71.150040
24620=       12.432905     78.891418
24630=       11.775507     86.630760
24640=       11.325478     91.789383
24650=       10.802713     96.947571
24660=       10.042408    104.684296
24670=        9.567081    109.842010
24680=        9.088606    113.689621
24690=        8.620009    114.515457
24700=        7.802448    114.869385
24710=        4.650239    114.999863
24720=    4   20    2
24730=        4.650239    114.999863
24740=        5.103719    123.433228
24750=        5.596378    130.728241
24760=        6.415631    141.596466
24770=        7.474397    155.155457
24780=        8.102022    164.925568
24790=        8.563284    174.694519
24800=        8.874420    184.462860
24810=        9.115957    194.230164
24820=        9.400442    208.878906
24830=        9.506882    223.523987
24840=        9.463659    233.285553
24850=        9.169333    243.043579
24860=        8.811359    248.582214
24870=        8.448650    252.798920
24880=        7.926655    257.676514
24890=        7.303553    262.513306
24900=        6.501266    267.634949
24910=        5.575104    272.557800
24920=        4.980721    275.272766
```

```
24930=        4.621628    276.748108
24940=        4.288194    278.013977
24950=        3.983303    279.084778
24960=        3.708123    279.972534
24970=        3.461858    280.685852
24980=        3.242233    281.231323
24990=        3.045600    281.613525
25000=        2.866371    281.836182
25010=        2.697909    281.901428
25020=    5   30    1
25030=        2.697909    281.901428
25040=        2.555275    281.812378
25050=        2.455352    281.571533
25060=        2.390940    281.174377
25070=        2.356308    280.615479
25080=        2.347210    279.888855
25090=        2.360858    278.988037
25100=        2.395871    277.904068
25110=        2.451631    276.630676
25120=        2.360858    278.988037
25130=        2.451631    276.630676
25140=        2.687582    272.557922
25150=        2.998391    267.635010
25160=        3.301361    262.630127
25170=        3.633046    256.589478
25180=        4.020399    248.358643
25190=        4.345508    240.274780
25200=        4.592886    232.249451
25210=        4.820795    223.524078
25220=        5.055776    213.761658
25230=        5.270200    201.888916
25240=        5.509740    189.346741
25250=        5.704358    179.578674
25260=        5.801357    169.810730
25270=        5.711005    160.040466
25280=        5.460247    150.270203
25290=        5.115679    140.499298
25300=        4.824990    130.728210
25310=        4.676692    123.433243
25320=        2.500000    115.000000
25330=    6   16    0
25340=        2.500000    115.000000
25350=        0.234524    112.990997
25360=        0.205185    109.842010
25370=        0.049130    104.684326
25380=       -0.214951     96.947586
25390=       -0.615489     86.630768
25400=       -0.909250     78.891403
25410=       -1.228700     71.160055
25420=       -1.472083     65.987000
25430=       -1.546140     59.730128
25440=       -1.985137     50.456306
25450=       -2.540106     40.541016
25460=       -3.078060     28.682934
25470=       -3.383093     16.570712
25480=       -3.529747      8.120135
25490=       -3.599054      0.000000
25500=      400.712952    8
```

Beginning of Region 3

TABLE I Continued

```
25510=   1   7   0
25520=      50.007126      0.000000
25530=      50.007095      2.742039
25540=      50.005126      4.956260
25550=      49.737724      7.991527
25560=      48.950752     10.893637
25570=      47.682236     13.590189
25580=      45.974167     16.014576
25590=   2   8   0
25600=      45.974167     16.014576
25610=      43.874229     18.105961
25620=      41.436036     19.809288
25630=      38.718979     21.075272
25640=      35.788315     21.860439
25650=      32.715111     22.127048
25660=      26.359161     22.127010
25670=      18.414383     22.127018
25680=   3  10   0
25690=      18.414383     22.127018
25700=      17.814926     26.774406
25710=      16.923122     34.597984
25720=      16.013092     43.651665
25730=      15.325804     52.031616
25740=      14.666439     60.607819
25750=      13.918823     68.569077
25760=      13.272402     76.311203
25770=      12.510948     84.051117
25780=      11.722996     91.789398
25790=   4   4   2
25800=      11.722996     91.789398
25810=      10.950851     99.526520
25820=      10.160648    107.263123
25830=       9.658892    112.420868
25840=   5   3   1
25850=       9.658892    112.420868
25860=       7.128384    115.000000
25870=       5.126293    117.956802
25880=   6  29   2
25890=       5.126293    117.956802
25900=       5.863479    125.842819
25910=       6.825004    133.837067
25920=       8.132015    145.828949
25930=       8.709452    153.823059
25940=       9.262857    161.816895
25950=       9.645987    173.806427
25960=       9.769035    181.798798
25970=       9.833309    193.786194
25980=       9.785547    201.776581
25990=       9.639191    209.766571
26000=       9.369663    217.755157
26010=       8.956194    226.046539
26020=       8.400652    233.096222
26030=       7.640726    239.993317
26040=       6.849148    245.704193
26050=       5.749837    251.973328
26060=       5.238540    254.410126
26070=       4.662115    256.886719
```

```
26080=       4.369453    258.021057
6090=        4.097445    259.004211
26100=       3.846460    259.842205
26110=       3.616040    260.540894
26120=       3.404875    261.104858
26130=       3.210836    261.537354
26140=       3.102296    261.720947
26150=       3.030986    261.841614
26160=       2.861572    262.018860
26170=       2.697999    262.070618
26180=   7  30   1
26190=       2.697999    262.070618
26200=       2.627872    262.051697
26210=       2.569114    262.012207
26220=       2.513620    261.944702
26230=       2.458793    261.845093
26240=       2.418955    261.742126
26250=       2.378328    261.578125
26260=       2.319113    261.204773
26270=       2.278214    260.722534
26280=       2.253218    260.128967
26290=       2.242231    259.419250
26300=       2.243885    258.591797
26310=       2.257326    257.642151
26320=       2.282346    256.567322
26330=       2.368329    254.016083
26340=       2.521813    250.454346
26350=       2.709336    246.293915
26360=       3.116043    235.725586
26370=       3.460886    221.933502
26380=       3.839483    206.437592
26390=       4.086307    195.451019
26400=       4.351102    184.462891
26410=       4.609918    173.473694
26420=       4.703060    166.146942
26430=       4.687814    158.819366
26440=       4.501820    151.102020
26450=       3.955367    140.409268
26460=       3.023705    127.743134
26470=       2.482436    116.711746
26480=       1.313319    114.990817
26490=   8  13   0
26500=       1.313319    114.990817
26510=       0.154916    112.420914
26520=       0.021698    107.263168
26530=      -0.209001     99.526550
26540=      -0.567024     89.210129
26550=      -0.849183     81.471390
26560=      -1.263398     71.150055
26570=      -1.696522     59.699020
26580=      -2.194694     50.229889
26590=      -2.726831     40.469147
26600=      -3.224504     28.843315
26610=      -3.657449     16.538712
26620=      -3.791033      0.000000
26630=     519.784912    0
26640=   1   7   0
26650=      50.007103      0.000000
```

TABLE I Concluded

```
41690=     721.499878   8
41700=   1   7   0
41710=      50.007126        0.000000
41720=      50.007111        2.190036
41730=      50.007128        4.956260
41740=      49.737625        7.991241
41750=      48.950493       10.892822
41760=      47.681923       13.589085
41770=      45.074007       16.013924
41780=   2  15   0
41790=      45.074007       16.013924
41800=      43.874474       18.106983
41810=      41.436968       19.813690
41820=      38.720818       21.085270
41830=      35.791206       21.878693
41840=      32.719025       22.156746
41850=      29.372906       22.153080
41860=      26.042725       22.151500
41870=      22.696865       22.149920
41880=      19.303780       22.149937
41890=      15.831873       22.152149
41900=      12.249571       22.157227
41910=       8.525335       22.165813
41920=       4.627608       22.178566
41930=       0.524876       22.196121
41940=   3   2   0
41950=       0.524876       22.196121
41960=       1.755000      112.214996
41970=   4   2   2
41980=       1.755000      112.214996
41990=     103.760988      148.779999
42000=   5   2   1
42010=     103.760986      148.779999
42020=       1.755000      112.214996
42030=   6   2   2
42040=       1.755000      112.214996
42050=       5.874999      306.528992
42060=   7   2   1
42070=       5.874999      306.528992
42080=       1.755000      112.214996
42090=   8   3   0
42100=       1.755000      112.214996
42110=       0.524876       22.196121
42120=       0.525000        0.000000
42130=*EOF
--
```

← End of
Region 3

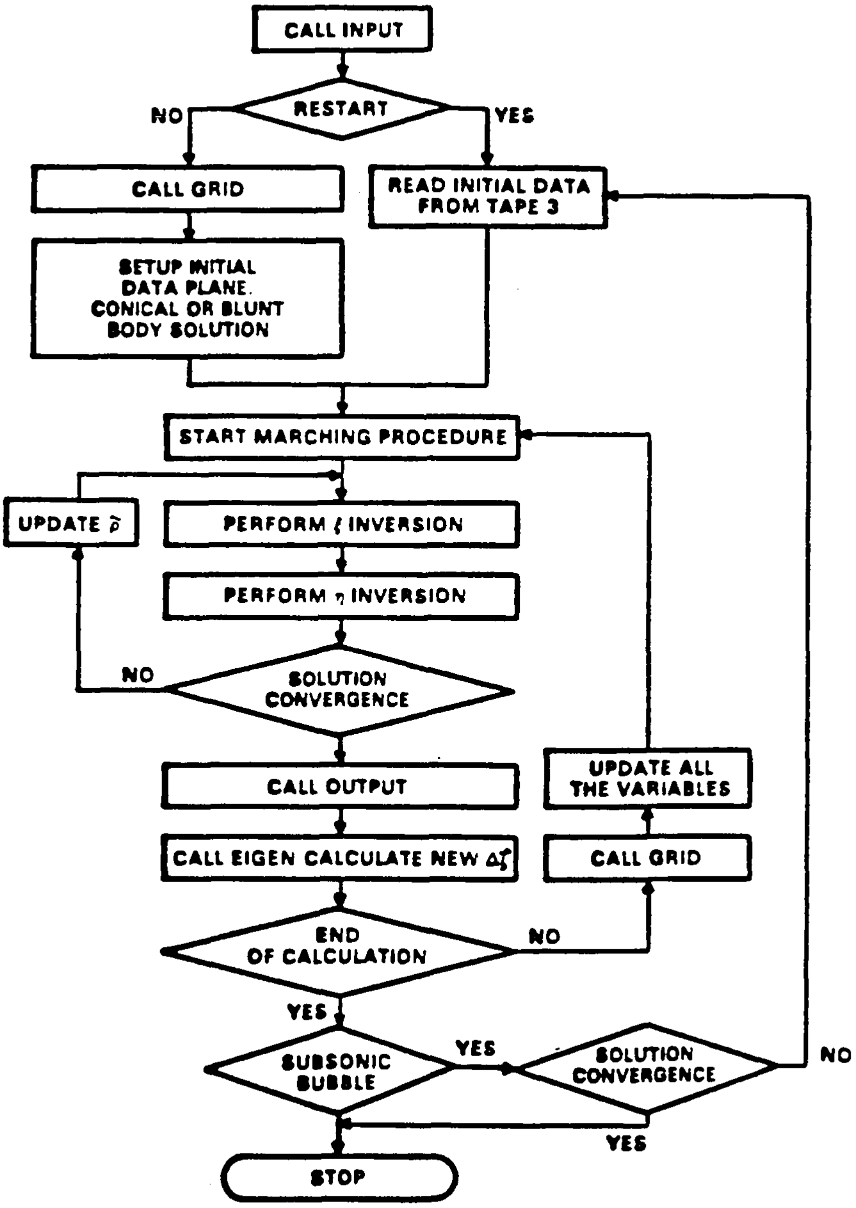

Fig. A1. Flow chart for the full potential code.

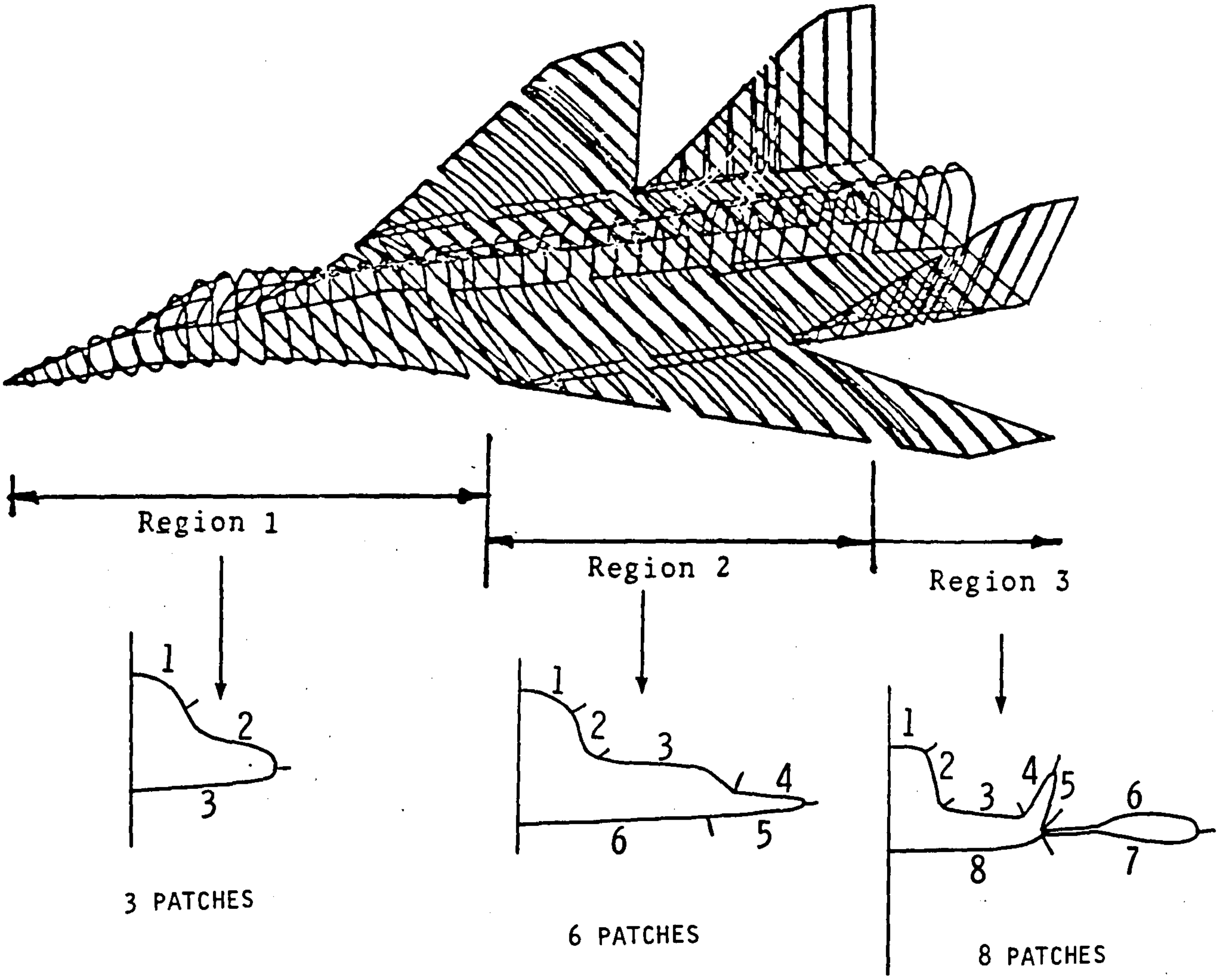

Fig. A2. Sample problem.

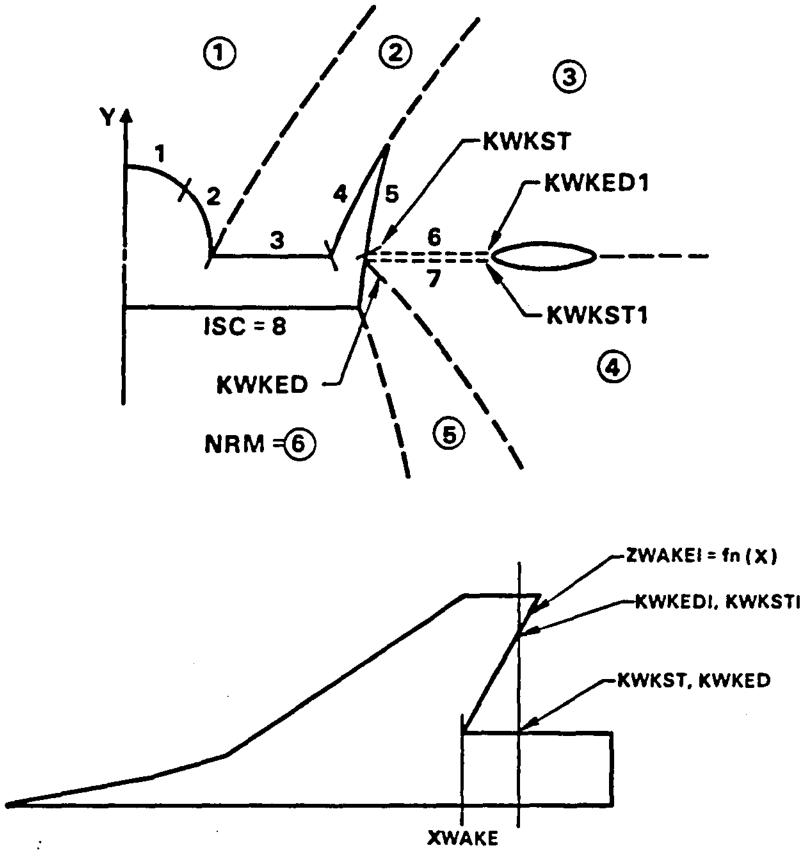

a) AFT-SWEPT TRAILING EDGE
KWKST = KWKMIN; KWKED = KWKMAX
K VALUES OF KWKEDI AND KWKSTI ARE COMPUTED FROM ZWAKEI

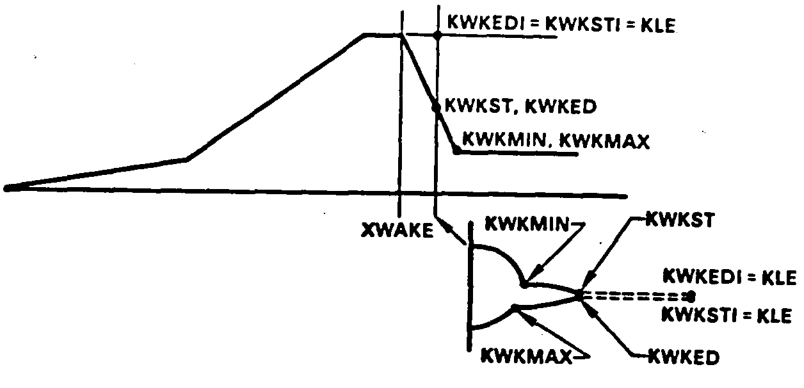

b) FORWARD-SWEPT TRAILING EDGE

Fig. A3. Cross–section patches and nomenclature.

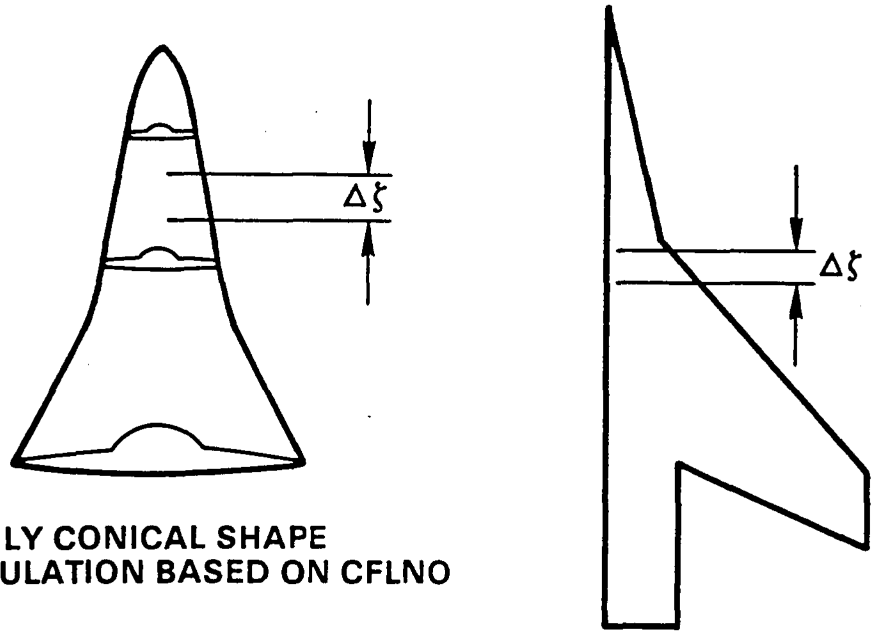

NEARLY CONICAL SHAPE
CALCULATION BASED ON CFLNO

NONCONICAL SHAPE
Δζ BASED ON DZMIN AND DZMAX

Fig. A4. Marching step size selection.

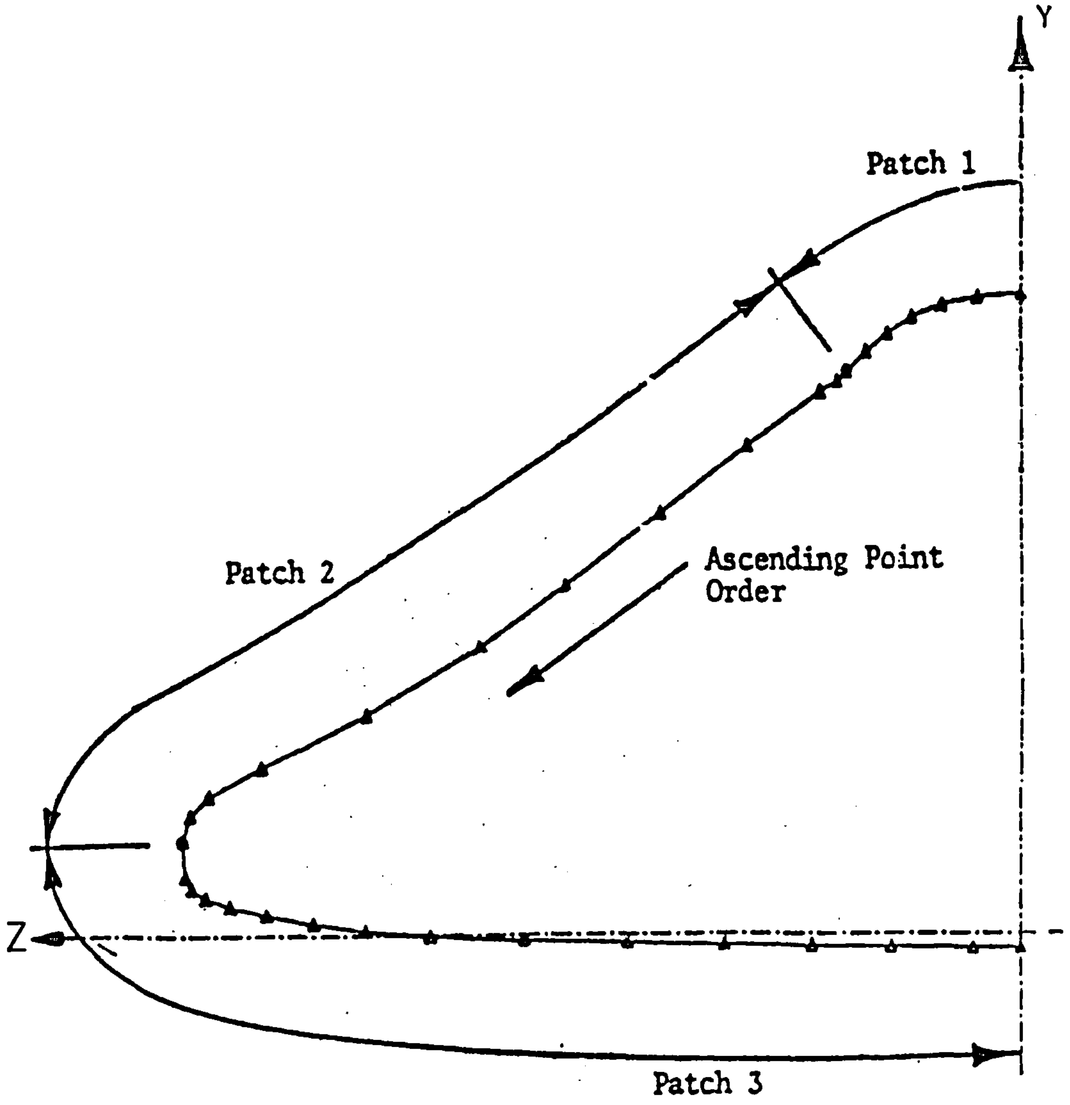

Fig. A5. REGION1 patching.

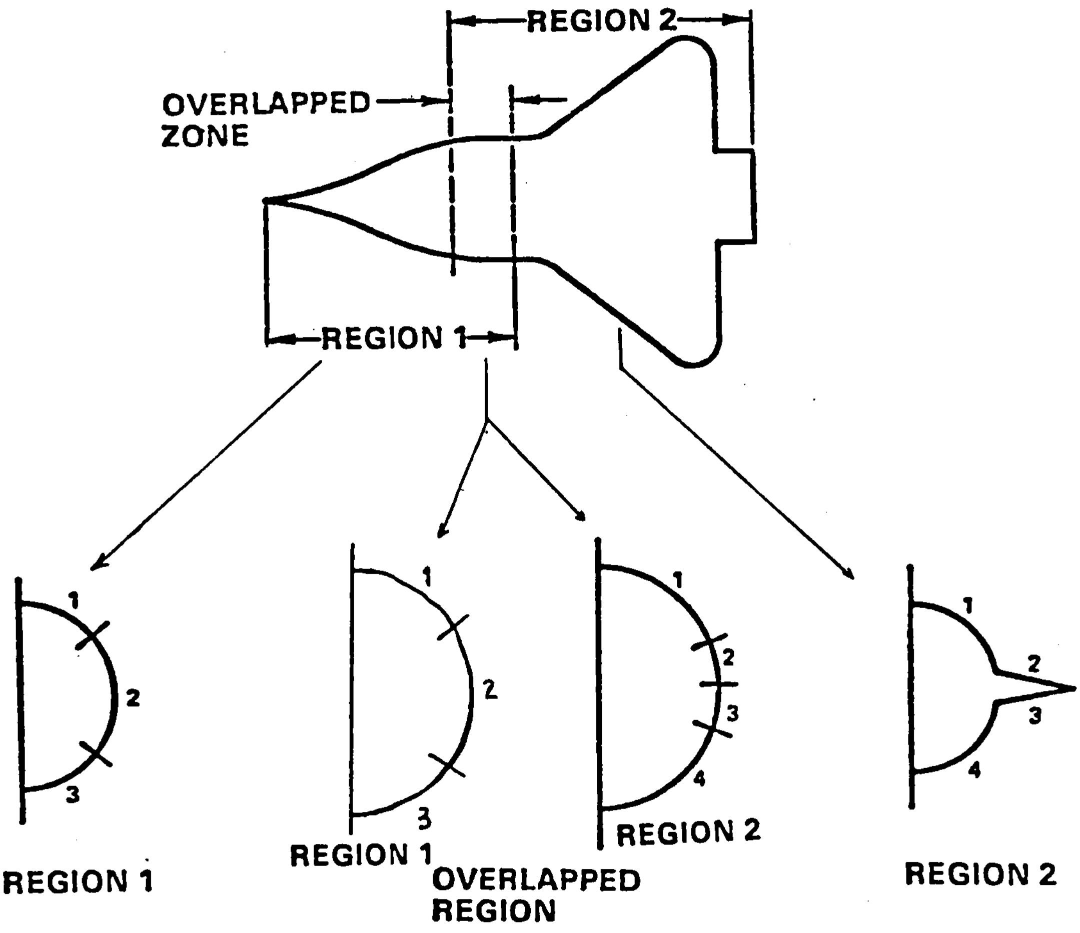

Fig. A6. Cross section patches in overlap region.

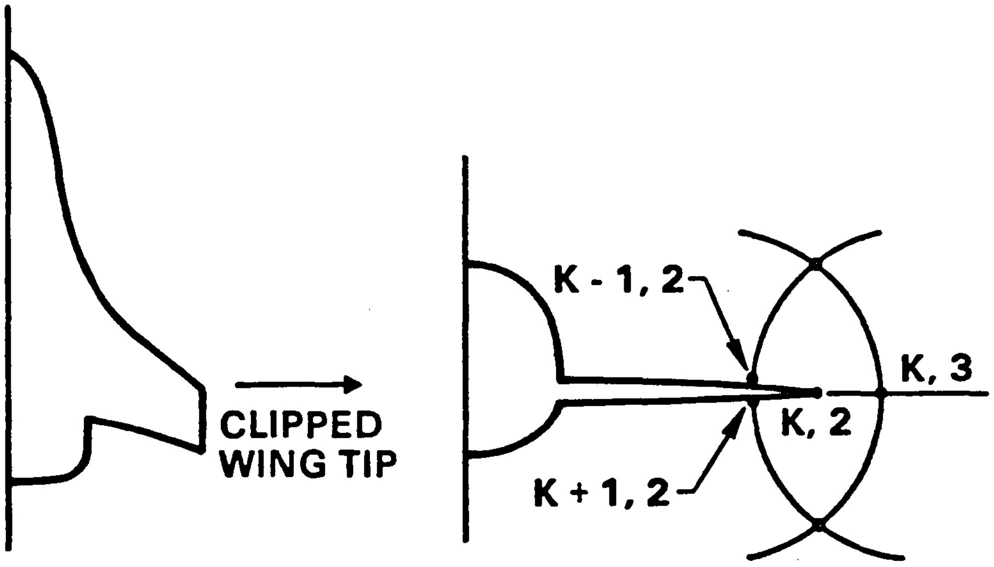

$$\phi(K, 2) = [\phi(K - 1, 2) + \phi(K + 1, 2) + \phi(K, 3)]/3.$$

Fig. A7. Potential averaging at wing tip clip region.

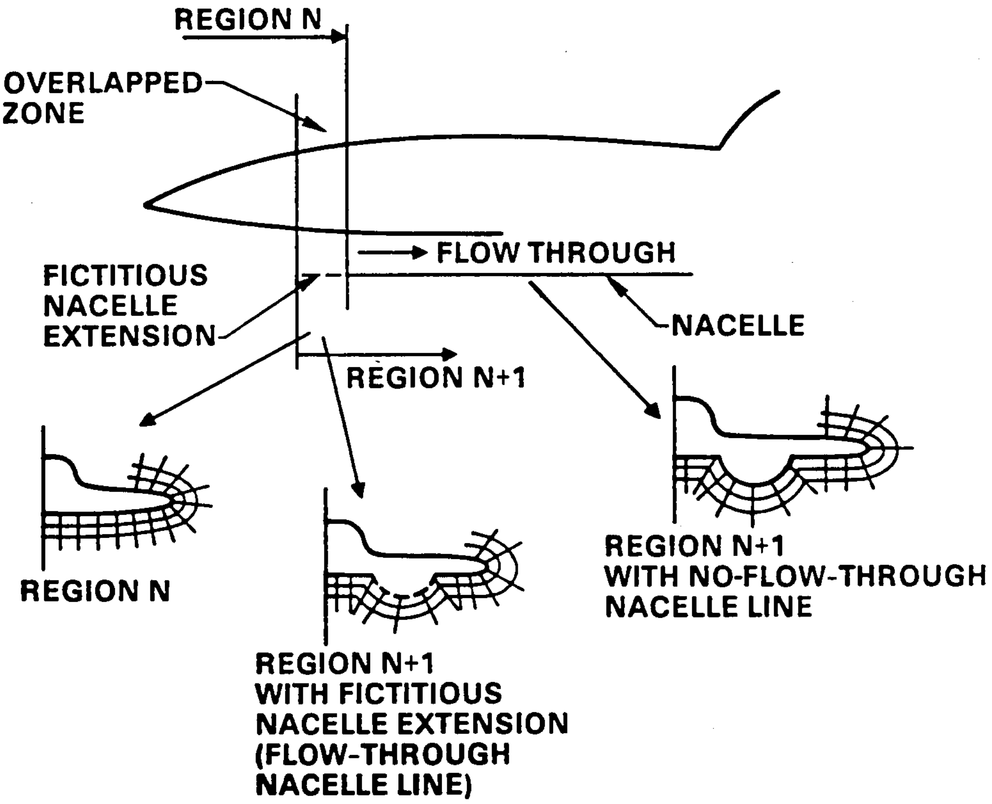

Fig. A8. Nacelle–on calculation.

APPENDIX B — DEMONSTRATION OF A TEST CASE

A sample test case is presented here to familiarize the user with the operation of the code.

Figure B1 shows the surface grid for the fighter configuration discussed in Appendix A. The configuration is an advanced fighter concept consisting of a blended wing/body with underslung nacelles and twin vertical tails. As mentioned in Appendix A, the solution for a complex configuration is accomplished by breaking the configuration up into regions or zones. These separate calculations are necessary because the configuration becomes increasingly complex in cross-sectional shape as marching is done in the axial direction. To accommodate the emergence of the wing, nacelle, tail, and wake region requires that the number of points in the circumferential direction be increased from zone to zone through use of a respace option.

A brief description of the appropriate header information for each analysis zone is given below. The test case is for a combined yaw and angle of attack flight condition, $M = 1.6$, $\beta = 4°$, and $\alpha = 6°$.

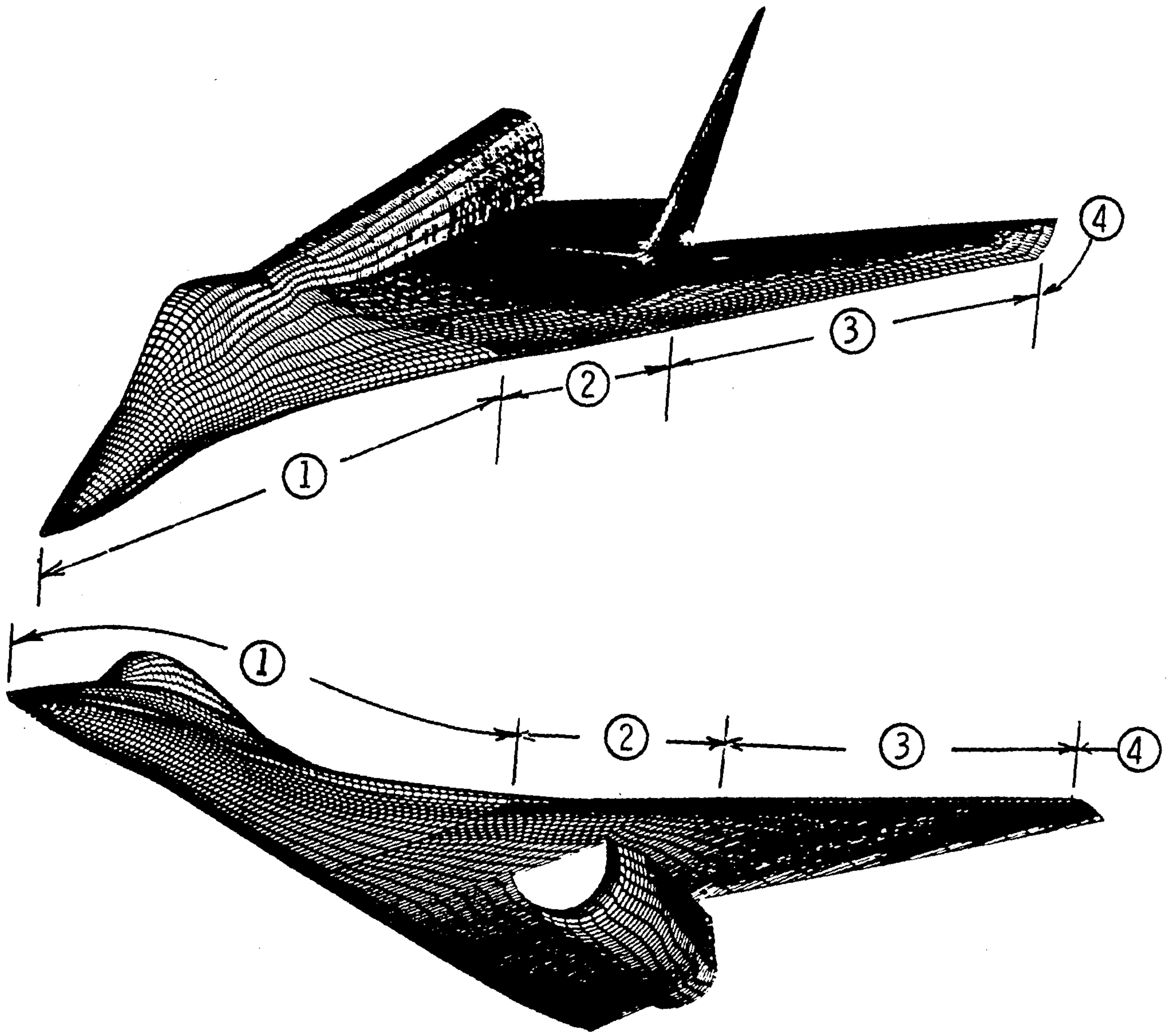

Fig. B1. Different zone calculation.

Zone 1 — Input Description

This zone initially performs the conical calculation necessary to set up the starting plane solution needed to initiate the marching calculation. The parameter NCON specifies the number of conical iterations to be performed for the crossflow geometry at ZTA1.

The header data for this region is given and a display of the flow field pressure contours and grid at the end of Zone 1 is shown. A sample of the printed output data and a discussion of the display postprocessor will be given at the end of Appendix B.

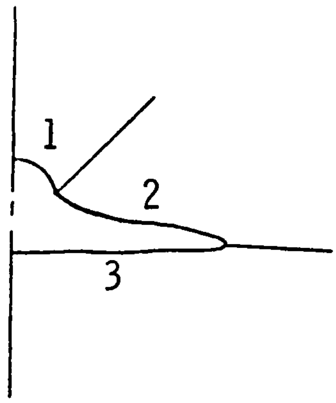

Cross-section patch definition for Zone 1.

```
100=  300       NMAX   I5     NO. OF AXIAL STEPS.
110=   15       JMAX          MESH PTS IN NORMAL DIR.<26
120=   33       KMAX          MESH PTS IN CIRCUM DIR;ISC1+ISC2-1+..+ISC6+1<81

130=    2       NRM           NO. GRID REGIONS<7;B&WB-2,WBV-3,WBNV-5
140=   13       NU0           SECOND SHARP EDGE K.
150=   10       NP            OUTPUT FOR EVERY NP STEPS
160=   18       KWKST         WAKE START K;ISC1+ISC2-1...+ISC5
170=   36       KWKED         WAKE END K;ISC1+ISC2-1+...+ISC7
180=   30       NCON          NO. CONE STARTING SOL. STEPS
190=   50       NITER         NO. OF GRID ITERATIONS.
200=    6       NSPTI         NO. OF ZTA FOR FLOW FIELD OUTPUT.
210=    1       ITERGE        NO. OF GLOB ITERATION.
220=  5.0       CFLIN  F10.5  CFL NUMBER.
230=  1.5       DZTAIN        IF>0.;FIXED STEP SIZE. IF<0.; CFL NO.
240=  2.5       DZMAX         MAX. AXIAL STEP SIZE
250=  1.0       DZMIN         MIN. AXIAL STEP SIZE
260=  1.6       FSM           FREE STREAM MACH NO.
270=  6.00      ALFA          ANGLE OF ATTACK-DEG.
280=   60.      THTO          OUTER BOUNDARY-DEG.
290=  0.1       DETA          STEP SIZE IN ETA DIR.
300=  0.1       DXI           STEP SIZE IN XI DIR.
310=   1.5      DZTA          FIRST STEP AFTER CONE START. SOL.
320=  15.0      ZTA1          STARTING ZTA >3*DZTAIN
330= 372.0      XEND          END ZTA<MAX INPUT ZTA-DZTAIN.
340=  1.        AMU1          1:FIRST ORDER,2:2ND ORDER.
350=   0.       AMU2          0:FIRST ORDER,1:2ND ORDER.
360=  613.      XWAKE         WAKE MINIMUM ZTA.
370=  4.00      BETANG        ANGLE OF YAW.
380=    1.0     CHL           GEOMETRY SCALE FACTOR
390=   85.0     PTNOSE        AXIAL GEOMETRY SHIFT FOR ZTA>0.
400=   0.0      YSHIFT        VERTICAL GEOMETRY SHIFT.
```

```
410=  500.    XO            AXIAL C.G. ZTA.
420=    0.    YO            VERTICAL C.G.
430=125280.   AAA           REFERENCE AREA.
440=234.627   ALL           REFERENCE LENGTH.
450=   1.0    OMEGA         RELAXATION.
460=    T     YAW           YAW
470=    T     NUGRID        GENERATE GRID?
480=    T     IREAD         INPUT GEOMETRY?
490=    F     RPLANE        R-MARCHING?
500=    F     TAPER         RESTART DATA FROM TAPE?
510=    T     TAPEW         WRITE RESTART DATA ON UNIT 2 & 4?
520=    F     TAPE8W        WRITE SUBSONIC RESTART DATA ON UNIT 8?
530=    T     FORCE         CALCULATE FORCES?
540=   18   00   00   00    GRID REGION TERMINAL K,5I5;ISC1+ISC2-1+..+ISCN
550=    0.0     00.0       00.0      00.0   =      POLAR ANGLE-DEG;5F10.4
560=900.    950.    900.    950.    900.    350.    FLOW FIELD OUTPUT ZTA
570=    3     ISC                                   NO. GEOM. SEGMENTS
580=   08   10   15                                 NO. MESH PTS/SEGMENT
```

Zone 1 Input Concluded

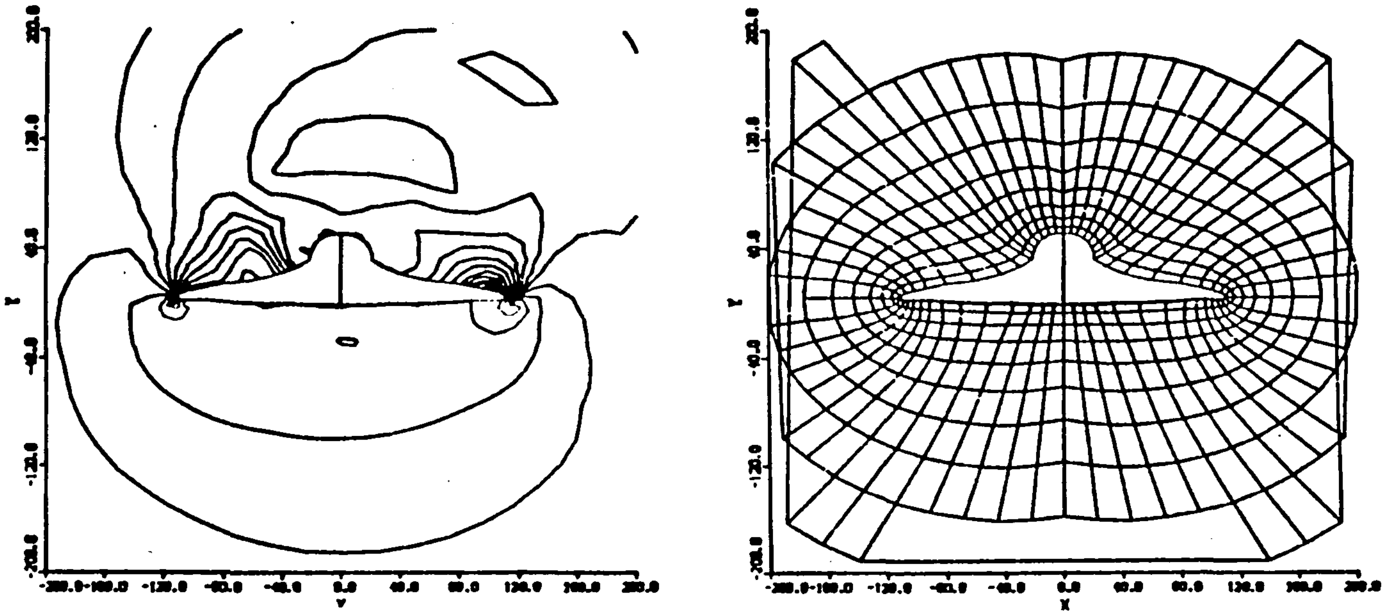

Zone 1 — Flow field pressure contours and gridding at $x = 370$.

Zone 2 — Input Description

This zone is required to increase the number of circumferential points to accommodate definition of the wing. The number of cross-sectional patches increases from three to six and there is a slight overlap region to adjust the Zone 1 flow field solution to the new grid.

The header data is given along with a flow field display at the end of Zone 2.

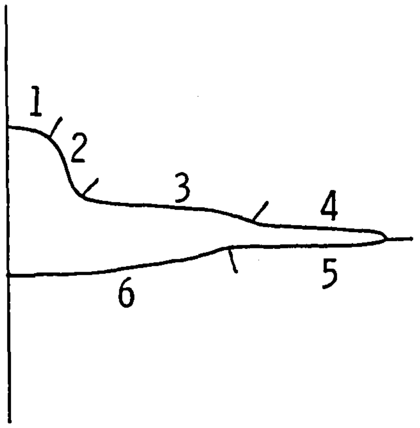

Cross-section patch definition for Zone 2.

```
100-   50      NMAX   I5     NO. OF AXIAL STEPS.
110-   15      JMAX          MESH PTS IN NORMAL DIR.<26
120-   57      KMAX          MESH PTS IN CIRCUM DIR;ISC1+ISC2-1+..+ISC6+1<81

130-    2      NRM           NO. GRID REGIONS<7;B&WB-2,WBV-3,WBNV-5
140-   13      NU0           SECOND SHARP EDGE K.
150-   10      NP            OUTPUT FOR EVERY NP STEPS
160-   28      KWKST         WAKE START K;ISC1+ISC2-1...+ISC5
170-   47      KWKED         WAKE END K;ISC1+ISC2-1+...+ISC7
180-   30      NCON          NO. CONE STARTING SOL. STEPS
190-   50      NITER         NO. OF GRID ITERATIONS.
200-    6      NSPTI         NO. OF ZTA FOR FLOW FIELD OUTPUT.
210-    1      ITERGE        NO. OF GLOB ITERATION.
220-  5.0      CFLIN  F10.5  CFL NUMBER.
230-  1.5      DZTAIN        IF>0.;FIXED STEP SIZE. IF<0.; CFL NO.
240-  2.0      DZMAX         MAX. AXIAL STEP SIZE
250-  1.0      DZMIN         MIN. AXIAL STEP SIZE
260-  1.6      FSM           FREE STREAM MACH NO.
270-  6.00     ALFA          ANGLE OF ATTACK-DEG.
280-   60.     THTO          OUTER BOUNDARY-DEG.
290-  0.1      DETA          STEP SIZE IN ETA DIR.
300-  0.1      DXI           STEP SIZE IN XI DIR.
310-   1.5     DZTA          FIRST STEP AFTER CONE START. SOL.
320- 371.0     ZTA1          START ZTA.
330- 455.0     XEND          END ZTA<MAX INPUT ZTA-DZTAIN
340-   1.      AMU1          1:FIRST ORDER,2:2ND ORDER.
350-   0.      AMU2          0:FIRST ORDER,1:2ND ORDER.
360-  613.     XWAKE         WAKE MINIMUM ZTA.
370-  004.     BETANG        ANGLE OF YAW
380-    1.0    CHL           GEOMETRY SCALE FACTOR.
390-   85.0    PTNOSE        AXIAL GEOMETRY SHIFT FOR ZTA>0.
400-   0.0     YSHIFT        VERTICAL GEOMETRY SHIFT.
```

Zone 2 Input

```
410=  500.      XO              AXIAL C.G. ZTA.
420=    0.      YO              VERTICAL C.G.
430=125280.     AAA             REFERENCE AREA.
440=234.627     ALL             REFERENCE LENGTH.
450=   1.0      OMEGA           RELAXATION.
460=    T       YAW             YAW
470=    T       NUGRID          GENERATE GRID?
480=    T       IREAD           INPUT GEOMETRY?
490=    F       RPLANE          R-MARCHING?
500=    T       TAPER           RESTART DATA FROM TAPE?
510=    T       TAPEW           WRITE RESTART DATA ON UNIT 2 & 4?
520=    F       TAPE8W          WRITE SUBSONIC RESTART DATA ON UNIT 8?
530=    T       FORCE           CALCULATE FORCES?
540=   32   00   00   00        GRID REGION TERMINAL K,5I5;ISC1+ISC2-1+..+ISCN
550=    0.0     00.0        00.0      00.0              POLAR ANGLE-DEG;5F10.4
560=900.     950.     900.    950.     975.     600.    FLOW FIELD OUTPUT ZTA
570=    6       ISC                                     NO. GEOM. SEGMENTS
580=   04   05   10   15   15   11                      NO. MESH PTS/SEGMENT
        0
```

Zone 2 Input Concluded

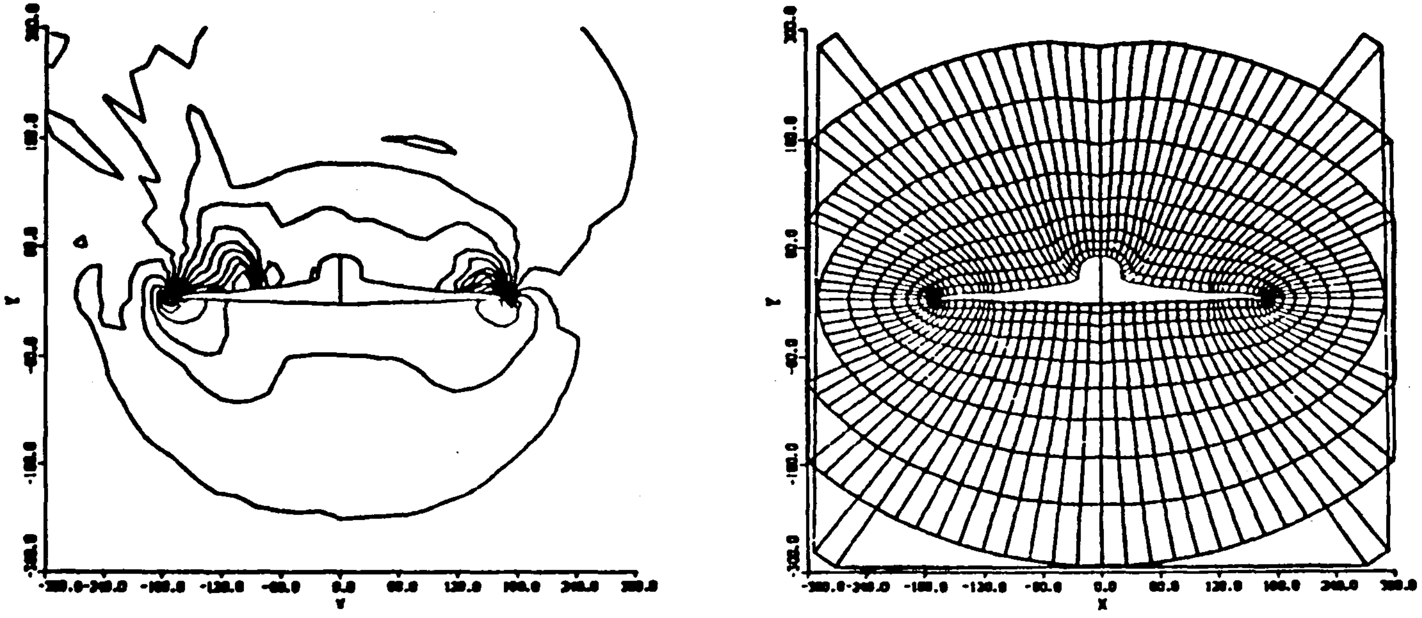

Zone 2 — Flow field pressure contours and gridding at $x = 450$.

Zone 3 — Input Description

Zone 3 is required because the underslung nacelles on the configuration will be modeled as flow-through ducts. The primary changes required other than the obvious one of modifying the contour geometry is to overlap Zone 2 and Zone 3 both upstream and downstream of the inlet face. This permits both transition between six and nine patch definition required to add the two sides and the bottom of the rectangular-like nacelle, and allows associated grid index information and temporary code corrections to be supplied via the update file.

Again, the header data is given as well as the necessary update statements and a flow field display at the face of the nacelle.

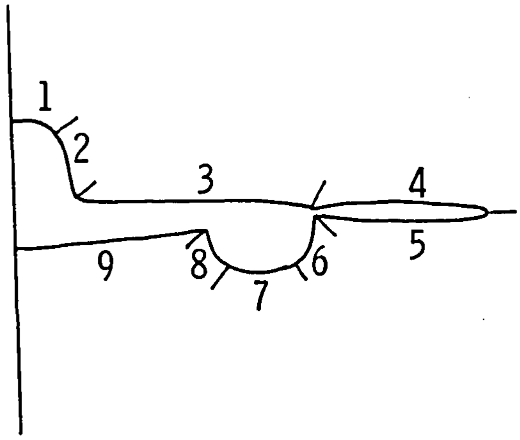

Cross-section patch definition for Zone 3.

Update for Nacelle

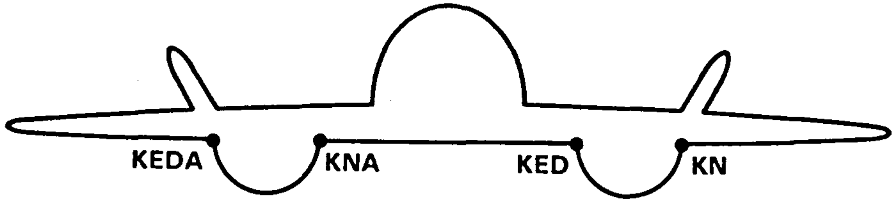

```
100=*IDENT YUP1
110=*I RESPACE.24
120=C    RESPACE NACELLE STARTING DIRECTIVES;DELETE FOR NEXT RUN
130=C    KN-BEGINNING K;KED-END K
140=      KN=41
150=      KED=55
160=      KM=KN-1
170=      KP=KN+1
180=      KNA=69
190=      KEDA=83
200=      KMA=KNA-1
210=      KPA=KNA+1
220=*I RESPACE.77
230=      IF (K.GT.KN             ) GO TO 130
240=C     IF (K.GT.KNA.AND.K.LT.KEDA) GO TO 130
250=*D RESPACE.97
260=      JST=2
270=      IF (K.GT.KN.AND.K.LT.KED) JST=1
280=      IF (K.GT.KNA.AND.K.LT.KEDA) JST=1
290=      DO 100 J=JST,JMAXC
300=*I RESPACE.105
310=      IF (J.EQ.2.AND.K.GT.KN             ) GO TO 113
320=C     IF (J.EQ.2.AND.K.GT.KNA.AND.K.LT.KEDA) GO TO 113
330=*I RESPACE.119
340=      IF (J.EQ.2.AND.K.GT.KN             ) GO TO 117
350=C     IF (J.EQ.2.AND.K.GT.KNA.AND.K.LT.KEDA) GO TO 117
360=*I RESPACE.120
370=  117 CONTINUE
380=*I RESPACE.121
390=      IF (J.LE.2.AND.K.GT.KN             ) JJ=JJS
400=      IF (J.LE.2.AND.K.GT.KN             ) KB=KBS
```

```
400=      IF (J.LE.2.AND.K.GT.KN                   ) KB=KBS
410=*I RESPACE.169
420=      IF (JJ.EQ.0) KB=KB-1
430=      IF (JJ.EQ.0) JJ=3
440=*I RESPACE.173
450=      IF (J.EQ.3.AND.K.GT.KM                   ) JJS=JJ
460=      IF (J.EQ.3.AND.K.GT.KM                   ) KBS=KB
470=*I RESPACE.181
480=      IF (DZZ .LT. 1.E-10. AND.  ABS(ZN).GT.2) GOTO 177
490=*I RESPACE.255
500=      IF (K2.GT.KN.AND.K2.LT.KED) GO TO 341
510=      IF (K2.GT.KNA.AND.K2.LT.KEDA) GO TO 341
520=*I UVW.17
530=C    UVW NACELLE STARTING DIRECTIVES;DELETE FOR NEXT RUN
540=C    KN-BEGINNING K;KED-END K
550=      KN=41
560=      KED=55
570=      KNA=69
580=      KEDA=83
590=*I UVW.71
600=      IF (K.GT.KN.AND.K.LT.KED) GO TO 312
610=      IF (K.GT.KNA.AND.K.LT.KEDA) GO TO 312
```

```
100=   85       NMAX    I5      NO. OF AXIAL STEPS.
110=   15       JMAX            MESH PTS IN NORMAL DIR.<26
120=   63       KMAX            MESH PTS IN CIRCUM DIR;ISC1+ISC2-1+..+ISC9+1<81

130=    4       NRM             NO. GRID REGIONS<7;B&WB-2,WBV-3,WBNV-5
140=   13       NU0             SECOND SHARP EDGE K.
150=   10       NP              OUTPUT FOR EVERY NP STEPS
160=   28       KWKST           WAKE START K;ISC1+ISC2-1...+ISC5
170=   47       KWKED           WAKE END K;ISC1+ISC2-1+...+ISC7
180=   30       NCON            NO. CONE STARTING SOL. STEPS
190=   50       NITER           NO. OF GRID ITERATIONS.
200=    6       NSPTI           NO. OF ZTA FOR  FLOW FIELD OUTPUT.
210=    1       ITERGE          NO. OF GLOB ITERATION.
220=  5.0       CFLIN   F10.5   CFL NUMBER.
230=  1.5       DZTAIN          IF>0.;FIXED STEP SIZE.IF<0.;CFL NO.
240=  2.0       DZMAX           MAX. AXIAL STEP SIZE
250=  1.0       DZMIN           MIN. AXIAL STEP SIZE
260=  1.6       FSM             FREE STREAM MACH NO.
270=  6.00      ALFA            ANGLE OF ATTACK-DEG.
280=   60.      THTO            OUTER BOUNDARY-DEG.
290=  0.1       DETA            STEP SIZE IN ETA DIR.
300=  0.1       DXI             STEP SIZE IN XI DIR.
310=   1.5      DZTA            FIRST STEP AFTER CONE START. SOL.
320= 455.0      ZTA1            START ZTA.
330= 609.0      XEND            END ZTA>MAX INPUT ZTA-DZTAIN.
340=   1.       AMU1            1:FIRST ORDER,2:2ND ORDER.
350=   0.       AMU2            0:FIRST ORDER,1:2ND ORDER.
360=  614.      XWAKE           WAKE MINIMUM ZTA.
370=  004.      BETANG          ANGLE OF YAW
380=    1.0     CHL             GEOMETRY SCALE FACTOR
390=   85.0     PTNOSE          AXIAL GEOMETRY SHIFT FOR ZTA>0.
400=   0.0      YSHIFT          VERTICAL GEOMETRY SHIFT
```

Zone 3 Input

```
410=  500.      XO              AXIAL C.G. ZTA.
420=    0.      YO              VERTICAL C.G.
430=125280.     AAA             REFERENCE AREA.
440=234.627     ALL             REFERENCE LENGTH.
450=   1.0      OMEGA           RELAXATION.
460=    T       YAW             YAW
470=    T       NUGRID          GENERATE GRID?
480=    T       IREAD           INPUT GEOMETRY?
490=    F       RPLANE          R-MARCHING?
500=    T       TAPER           RESTART DATA FROM TAPE?
510=    T       TAPEW           WRITE RESTART DATA ON UNIT 2 & 4?
520=    F       TAPE8W          WRITE SUBSONIC RESTART DATA ON UNIT 8?
530=    T       FORCE           CALCULATE FORCES?
540=   32   41   48   00        GRID REGION TERMINAL K,5I5;ISC1+ISC2-1+..+ISCN
550=    0.      -45.0       -80.0      00.0           POLAR ANGLE-DEG;5F10.4
560=975.     900.     925.     950.     975.     600.    FLOW FIELD OUTPUT ZTA
570=    9      ISC                                     NO. GEOM. SEGMENTS
580=   04   05   10   15   10   05   07   05   08    NO. MESH PTS/SEGMENT
```

Zone 3 Input Concluded

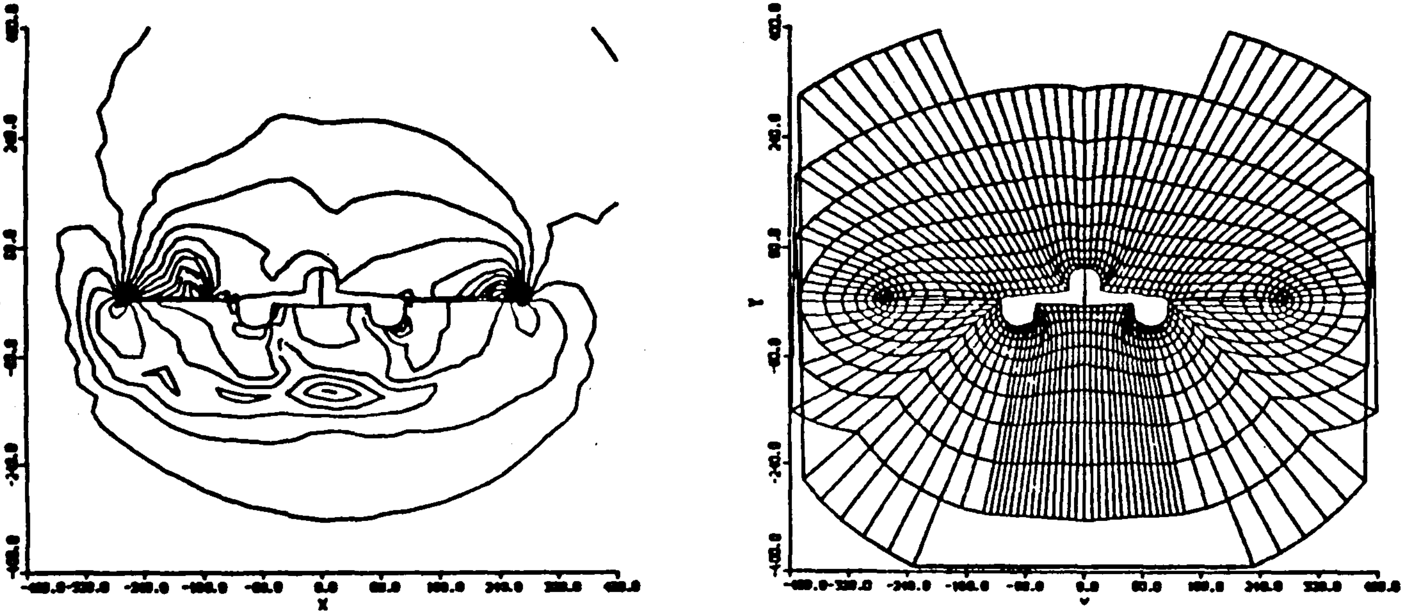

Zone 3 — Flow field pressure contours and gridding at $x = 455$.

Zone 4 — Input Description

Zone 4 is required to incorporate the vertical tail and the wing wake. This region corresponds to the region 3 solution 2 discussion of Appendix A. The number of patches is increased to 11 and the solution of Zone 3 is interpolated on to the new respaced grid through an overlap region between Zone 3 and Zone 4.

The total solution is now composed of four sequential regional solutions for Zones 1 through 4. The header data for Zone 4 is given with a flow field display approximately midway in the region.

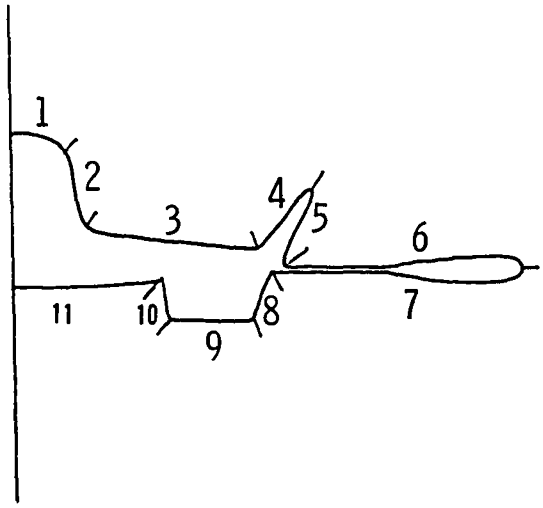

Cross–sectional patch definition for Zone 4.

```
100■   90       NMAX   I5     NO. OF AXIAL STEPS.
110■   15       JMAX          MESH PTS IN NORMAL DIR.<26
120■   64       KMAX          MESH PTS IN CIRCUM DIR;ISC1+ISC2-1+.+ISC11+1<
130■    5       NRM           NO. GRID REGIONS<7;B&WB-2,WBV-3,WBNV-5
140■   21       NU0           TAIL EDGE K;ISC1+ISC2-1+...+ISC4
150■   11       NP            OUTPUT FOR EVERY NP STEPS
160■   24       KWKST         WAKE START K;ISC1+ISC2-1...+ISC5
170■   42       KWKED         WAKE END K;ISC1+ISC2-1+...+ISC7
180■   30       NCON          NO. CONE STARTING SOL. STEPS.
190■   50       NITER         NO. OF GRID ITERATIONS.
200■    3       NSPTI         NO. OF ZTA FOR FLOW FIELD OUTPUT.
210■    1       ITERGE        NO. OF GLOB ITERATION.
220■  5.0       CFLIN  F10.5  CFL NUMBER.
230■  2.0       DZTAIN        IF>0.;FIXED STEP SIZE.IF<0.;CFL NO.
240■  3.0       DZMAX         MAX. AXIAL STEP SIZE
250■  1.0       DZMIN         MIN. AXIAL STEP SIZE
260■  1.6       FSM           FREE STREAM MACH NO.
270■  6.00      ALFA          ANGLE OF ATTACK-DEG.
280■   60.      THTO          OUTER BOUNDARY-DEG.
290■  0.1       DETA          STEP SIZE IN ETA DIR.
300■  0.1       DXI           STEP SIZE IN XI DIR.
310■   1.5      DZTA          FIRST STEP AFTER CONE START. SOL.
320■ 600.       ZTA1          START ZTA.
330■ 801.       XEND          END ZTA<MAX INPUT ZTA-DZTAIN.
340■  1.        AMU1          1:FIRST ORDER,2:2ND ORDER.
350■  0.        AMU2          0:FIRST ORDER,1:2ND ORDER.
360■  614.      XWAKE         WAKE MINIMUM ZTA.
370■  004.      BETANG        ANGLE OF YAW.
380■    1.0     CHL           GEOMETRY SCALE FACTOR
390■   85.0     PTNOSE        AXIAL GEOMETRY SHIFT FOR ZTA>0.
400■   0.0      YSHIFT        VERTICAL GEOMETRY SHIFT
```

Zone 4 Input

```
410=  500.      XO              AXIAL C.G. ZTA.
420=    0.      YO              VERTICAL C.G.
430=125280.     AAA             REFERENCE AREA.
440=234.627     ALL             REFERENCE LENGTH.
450=   1.0      OMEGA           RELAXATION.
460=    T       YAW             YAW
470=    T       NUGRID          GENERATE GRID?
480=    T       IREAD           INPUT GEOMETRY?
490=    F       RPLANE          R-MARCHING?
500=    T       TAPER           RESTART DATA FROM TAPE?
510=    T       TAPEW           WRITE RESTART DATA ON UNIT 2 & 4?
520=    F       TAPE8W          WRITE SUBSONIC RESTART DATA ON UNIT 8?
530=    T       FORCE           CALCULATE FORCES?
540=   21   33   42   49        GRID REGION TERMINAL K,5I5;ISC1+ISC2-1+..+ISC
550=   70.0      0.0       -45.0     -80.0             POLAR ANGLE-DEG;5F10.4
560=855.    850.    875.                               FLOW FIELD OUTPUT ZTA
570=   11       ISC                                    NO. GEOM. SEGMENTS
580=   04   05   10   04   04   10   10   05   07   05   08
```

Zone 4 Input Concluded

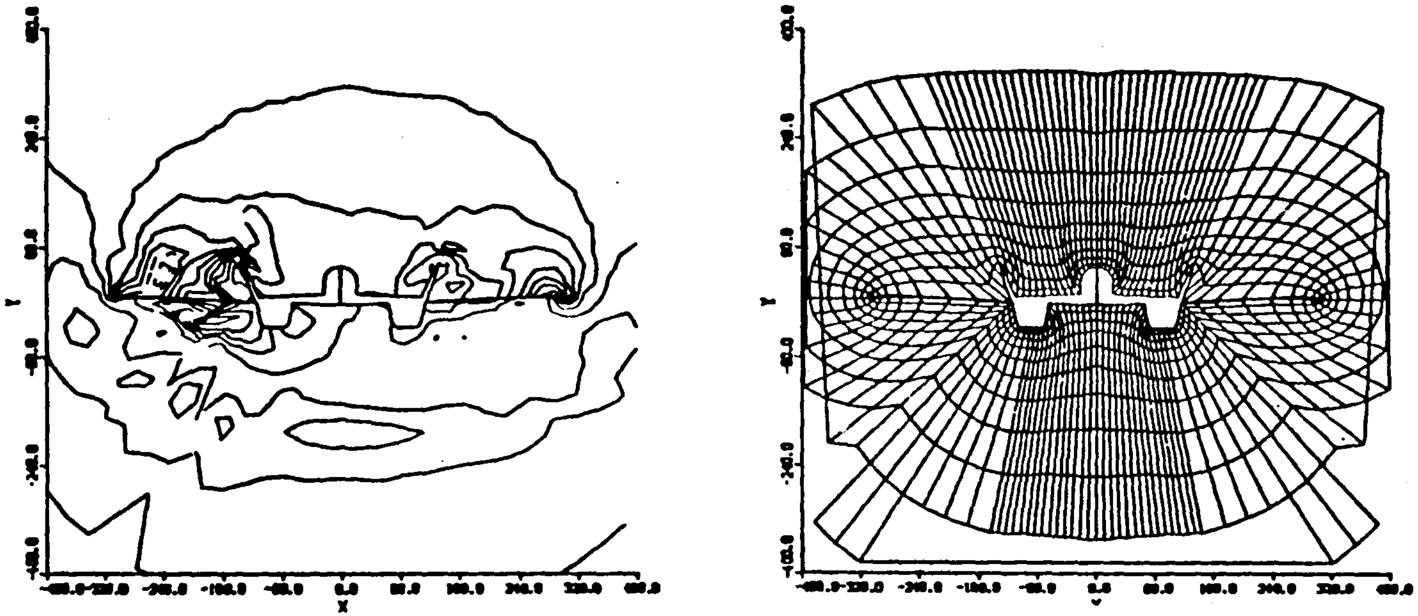

Zone 4 — Flow field pressure contours and gridding at $x = 680$.

Output Data Description

Sample printed output data is presented on Table B1. Standard tabulated data is produced every NP marching steps as defined in the header data. More detailed physical plane data can be output at specified stations using the parameter NSPTI and the tabulated stations following the true/false header data input. Cartesian coordinates, velocities, and mesh indices are indicated in the following sketch. The axial velocity component, U, is positive out of the plane of the paper.

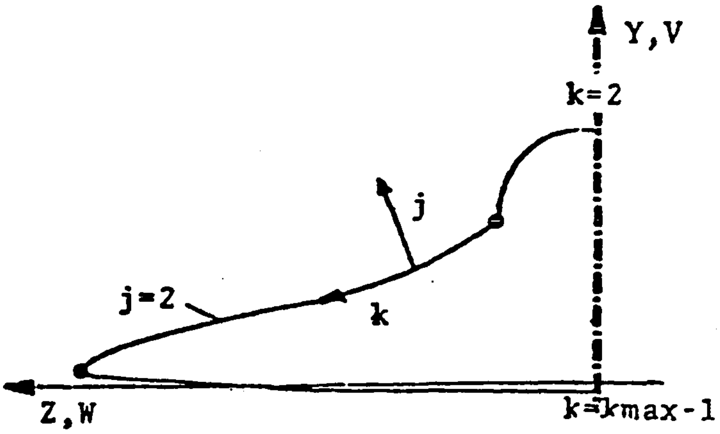

Crossplane data and tabulated surface pressure coefficient data at constant span stations (i.e., z) are output via Tape 1. These files are displayed using the postprocessor described in the next section.

TABLE B1 SAMPLE OUTPUT DATA

```
       ITER=      5     DZTA=    2.50000        ZTA1= 696.58878      Contravariant Velocities
      (STEP)                       Cp                                ________________________________
  J   K      RHO ρ/ρ∞            CP           PHI            U            V            W            X            Y            Z
  2   1     .872618       -.096915    714.215315            I            I            I    696.588384    49.946005    -5.649278
  2   2     .872623       -.096910    714.204522     1.050523     0.000000     0.000000    696.588384    50.007111     0.000000
  2   3     .872616       -.096915    714.215316     1.050518     0.000000      .000071    696.588384    49.946008     5.649278
  2   4     .873174       -.096503    714.248745     1.050269     0.000000      .000147    696.588384    48.830048    11.157859
  2   5     .874368       -.095620    714.305288     1.049568     0.000000      .000251    696.588384    45.876709    16.013771
  2   6     .872136       -.097271    714.504890     1.050287     0.000000      .000103    696.588384    38.523018    21.151141
  2   7     .862499       -.104383    714.836467     1.053838     0.000000     -.000019    696.588384    29.496730    22.217937
  2   8     .850378       -.113283    715.239224     1.058207     0.000000     -.000116    696.588384    20.360161    22.099892
  2   9     .841292       -.119921    715.803286     1.060812     0.000000     -.000339    696.588384    11.222849    22.130118
  2  10     .840717       -.114499    715.640202     1.057427     0.000000     -.000110    696.588384    10.836039    34.670301
  2  11     .856343       -.108909    715.540134     1.054610     0.000000     -.000183    696.588384    10.187208    47.231018
  2  12     .862010       -.104742    715.215639     1.051803     0.000000     -.000364    696.588384     9.900013    59.701822
  2  13     .896789       -.078948    714.493998     1.036773     0.000000     -.000590    696.588384     9.546000    72.346230
  2  14     .870214       -.092769    713.454512     1.044120     0.000000     -.000634    696.588384     9.033332    84.097088
  2  15     .855106       -.109817    712.630572     1.055693     0.000000     -.000403    696.588384     8.453547    97.446525
  2  16     .796150       -.152476    712.365240     1.079943     0.000000     -.000323    696.588384     7.656034   100.983178
  2  17     .750268       -.184816    711.603647     1.098479     0.000000     -.001455    696.588384    19.543347   114.612843
  2  18     .571523       -.303054    710.240665     1.178196     0.000000     -.002982    696.588384    34.426818   120.830436
  2  19     .988566       -.024403    709.952537     1.011578     0.000000     -.004748    696.588384    40.662360   125.805400
  2  20    1.384285        .321761    710.088083      .851226     0.000000     -.008018    696.588384    53.717097   129.108570
  2  21    1.687214        .502611    709.537858      .731483     0.000000     -.009591    696.588384    58.456765   131.626700
  2  22    1.203788        .165454    710.328615      .688019     0.000000     -.023466    696.588384    61.440687   133.958279
  2  23    1.187687        .151942    708.419447      .856460     0.000000      .004271    696.588384    57.404303   133.773184
  2  24    1.211263        .171750    707.036204      .905288     0.000000      .005404    696.588384    51.839495   132.488912
  2  25     .938402       -.047523    706.321779     1.021979     0.000000      .003958    696.588384    43.679468   130.254218
  2  26     .814356       -.139434    705.713319     1.074143     0.000000      .002269    696.588384    30.141000   126.154023
  2  27     .747032       -.187087    706.033838     1.102131     0.000000      .001185    696.588384    13.793620   120.801278
  2  28     .778193       -.165224    706.225323     1.088395     0.000000      .000573    696.588384      .867854   116.363281
  2  29    1.040903        .032214    707.005377      .983751      .000066      .000109    696.588384     2.142344   140.624250
  2  30    1.047007        .037087    707.509698      .981139      .000330     -.000188    696.588384     3.497559   166.660347
  2  31    1.020956        .016441    706.811346      .989676      .000578     -.000335    696.588384     4.974130   195.631617
  2  32     .997484       -.001964    705.783749      .998770      .000690     -.000321    696.588384     6.431195   224.529098
  2  33     .905790       -.072188    705.017271     1.033382      .000656     -.000571    696.588384     7.684317   247.718921
  2  34     .861733       -.112290    702.271370     1.052011      .000490     -.000891    696.588384     8.282303   264.931800
  2  35     .358600       -.425312    701.301114     1.275561     0.000000     -.001226    696.588384     8.611510   278.402489
  2  36     .387657       -.409959    698.161108     1.230990     0.000000     -.002962    696.588384     8.820093   289.487817
  2  37     .549374       -.316780    694.830764     1.097884     0.000000     -.005217    696.588384     8.753903   290.793426
  2  38     .457297       -.371424    690.329619     1.008294     0.000000     -.014518    696.588384     7.796446   306.528992
  2  39    1.008353        .006537    688.484540      .978897     0.000000     -.002028    696.588384     7.459420   298.747500
  2  40    1.072089        .057120    687.482653      .962986     0.000000     -.001175    696.588384     7.958001   289.456406
  2  41    1.272637        .224039    686.206321      .885956     0.000000     -.001111    696.588384     8.007802   278.373004
  2  42     .864753       -.102722    684.305635     1.051430      .000004     -.000468    696.588384     7.946608   264.900973
  2  43     .908679       -.070017    684.290840     1.035219     -.000700     -.000280    696.588384     7.716527   247.884788
  2  44     .998102       -.001482    683.209029      .998065     -.000577     -.000280    696.588384     6.419563   224.503204
  2  45    1.020192        .015938    681.803950      .990154     -.000501     -.000267    696.588384     5.010471   195.610113
  2  46    1.042044        .033121    680.575873      .982155     -.000397     -.000253    696.588384     3.548817   166.645427
  2  47    1.031691        .024915    679.795940      .984745     -.000376     -.000346    696.588384     2.174109   140.616672
  2  48    1.032494        .025550    677.918751      .985072     0.000000     -.000445    696.588384      .867854   116.363281
  2  49    1.029608        .023267    677.213594      .987619     0.000000     -.000394    696.588384      .522167   101.820516
  2  50    1.028351        .022274    676.768143      .988660     0.000000     -.000264    696.588384      .069302    87.274129
  2  51    1.044217        .034847    676.523870      .982598     0.000000     -.000167    696.588384     -.411648    72.728832
  2  52    1.047296        .037297    676.410182      .981438     0.000000     -.000116    696.588384     -.962048    58.179577
  2  53    1.038723        .030486    676.318889      .984731     0.000000     -.000096    696.588384    -1.203779    43.640848
  2  54    1.029345        .023060    676.204160      .988351     0.000000     -.000077    696.588384    -1.889275    29.104001
  2  55    1.026936        .021157    676.126533      .989269     0.000000     -.000042    696.588384    -2.116542    14.552648
  2  56    1.027394        .021518    676.006079      .989098     0.000000     0.000000    696.588384    -2.257743     0.000000
  2  57    1.026936        .021157    676.126533            I            I            I    696.588384    -2.116542   -14.552648
```

TABLE B1 CONTINUED

```
 15 56     1.006286      .004917   652.950876     .994820    -.000576    0.000000   696.588384  -530.992758     0.000000
 16 56     1.000046      .000036   645.388007     .996996    -.000649    0.000000   696.588384  -629.183474     0.000000
 17 56     1.001168      .000913   636.587362     .996560    -.000719    0.000000   696.588384  -742.906384     0.000000
 18 56     1.000015      .000011   626.447526     .997006    -.000793    0.000000   696.588384  -874.618431     0.000000
 19 56      .998626     -.001073   614.629798     .997515    -.000871    0.000000   696.588384 -1027.166207     0.000000
 20 56     1.000000     0.000000   600.864605           1    -.000983           1   696.588384 -1203.842432     0.000000

     RMS DENSITY=        .09867186


+++UPER SURFACE+++
                                            Cp                P/P∞
  X=   .69659E+03    Z= 0.               CP= -.98910E-01   RHO=  .87262E+00   IU=  1
  X=   .69659E+03    Z=  .30600E+02      CP= -.11826E+00   RHO=  .84630E+00   IU=  2
  X=   .69659E+03    Z=  .61200E+02      CP= -.10188E+00   RHO=  .86591E+00   IU=  3
  X=   .69659E+03    Z=  .91800E+02      CP= -.10216E+00   RHO=  .86550E+00   IU=  4
  X=   .69659E+03    Z=  .12240E+03      CP= -.20914E+00   RHO=  .70533E+00   IU=  5
  X=   .69659E+03    Z=  .15300E+03      CP=  .34521E-01   RHO=  .10438E+01   IU=  6
  X=   .69659E+03    Z=  .18360E+03      CP=  .25006E-01   RHO=  .10318E+01   IU=  7
  X=   .69659E+03    Z=  .21420E+03      CP=  .46142E-02   RHO=  .10059E+01   IU=  8
  X=   .69659E+03    Z=  .24480E+03      CP= -.63349E-01   RHO=  .91733E+00   IU=  9
  X=   .69659E+03    Z=  .27540E+03      CP= -.35884E+00   RHO=  .46844E+00   IU= 10
  X=   .69659E+03    Z=  .30600E+03      CP= -.37142E+00   RHO=  .90433E+00   IU=
                                    /LEADING EDGE                                       SPECIFIED  Z SURFACE
+++LOWER SURFACE+++                                                                     PRESSURE COEFFICIENT

  X=   .69659E+03    Z= 0.               CP=  .21518E-01   RHO=  .10274E+01   IU=  1
  X=   .69659E+03    Z=  .30600E+02      CP=  .23824E-01   RHO=  .10303E+01   IU=  2
  X=   .69659E+03    Z=  .61200E+02      CP=  .36788E-01   RHO=  .10407E+01   IU=  3
  X=   .69659E+03    Z=  .91800E+02      CP=  .22583E-01   RHO=  .10287E+01   IU=  4
  X=   .69659E+03    Z=  .12240E+03      CP=  .25391E-01   RHO=  .10323E+01   IU=  5
  X=   .69659E+03    Z=  .15300E+03      CP=  .28819E-01   RHO=  .10366E+01   IU=  6
  X=   .69659E+03    Z=  .18360E+03      CP=  .23005E-01   RHO=  .10293E+01   IU=  7
  X=   .69659E+03    Z=  .21420E+03      CP=  .46942E-02   RHO=  .10060E+01   IU=  8
  X=   .69659E+03    Z=  .24480E+03      CP= -.61488E-01   RHO=  .91981E+00   IU=  9
  X=   .69659E+03    Z=  .27540E+03      CP=  .15193E+00   RHO=  .11826E+01   IU= 10
RMSR3=    .17218128E-01     NN=  312     NR3ITER=    2
RMSR3=    .16091918E-01     NN=  312     NR3ITER=    3
RMSR3=    .11200070E-04     NN=  312     NR3ITER=    4
 EIGENY=    .92064673E-01   CFLE=    .23016160E+01   EIGENZ=    .78797052E-01   CFLX=       .1970E+01   DZTA=       .2500E+01
 KST,KED1,KST1,KED,KS,KE,KIA,KAWK    28    35    41    48    35    35     1     2
 VORT,PHM,K      .16133E+02      .68830E+03    35
 KST,KED1,KST1,KED,KS,KE,KIA,KAWK    28    35    41    48    41    41     2     2
 VORT,PHM,K     -.16138E+02      .70444E+03    41
 L= .31948E+06   D= .28019E+04   CL= .25501E+00   CD= .22388E-01   SURFACE A= .36079E+06   REF. A= .12828E+06
 PITCH MOMENT=   -.4698E+06   CP=  -.1098E-01   XO=   .5000E+03   YO=  0.          .1948E+03    .1003E+05    .2346E+03
         FLOW FIELD AT ZTA=  699.0884
  J  K        RHO P/P∞     P P/P∞     U-VEL u/V∞     V-VEL v/V∞      W-VEL w/V∞      A T∞/Tt      M             X              Y              Z
  2  2    .8731E+00    .8270E+00    .1050E+01    .7814E-08   0.                .6083E+00    .1727E+01    .6991E+03    .5001E+02   0.
  3  2    .8758E+00    .8306E+00    .1049E+01   -.1508E-01   0.                .6086E+00    .1724E+01    .6991E+03    .6383E+02   0.
  4  2    .8764E+00    .8314E+00    .1049E+01   -.1420E-01   0.                .6087E+00    .1723E+01    .6991E+03    .7985E+02   0.
  5  2    .8801E+00    .8362E+00    .1047E+01   -.9394E-02   0.                .6092E+00    .1719E+01    .6991E+03    .9845E+02   0.
  6  2    .8890E+00    .8481E+00    .1044E+01   -.7727E-03   0.                .6108E+00    .1710E+01    .6991E+03    .1200E+03   0.
  7  2    .8963E+00    .8579E+00    .1041E+01    .9083E-02   0.                .6115E+00    .1702E+01    .6991E+03    .1450E+03   0.
  8  2    .9038E+00    .8679E+00    .1038E+01    .1903E-01   0.                .6125E+00    .1695E+01    .6991E+03    .1740E+03   0.
  9  2    .9099E+00    .8762E+00    .1035E+01    .2816E-01   0.                .6133E+00    .1688E+01    .6991E+03    .2077E+03   0.
 10  2    .9238E+00    .8950E+00    .1029E+01    .3802E-01   0.                .6152E+00    .1674E+01    .6991E+03    .2467E+03   0.
 11  2    .9404E+00    .9175E+00    .1022E+01    .4930E-01   0.                .6174E+00    .1658E+01    .6991E+03    .2919E+03   0.
 12  2    .9633E+00    .9490E+00    .1012E+01    .6413E-01   0.                .6203E+00    .1635E+01    .6991E+03    .3444E+03   0.
```

```
  7 56   .1068E+01   .1092E+01   .9745E+00   .2535E-01  0.          .6329E+00   .1540E+01   .6991E+03  -.1020E+03  0.
  8 56   .1071E+01   .1101E+01   .9721E+00   .2646E-01  0.          .6336E+00   .1535E+01   .6991E+03  -.1323E+03  0.
  9 56   .1071E+01   .1101E+01   .9718E+00   .3007E-01  0.          .6337E+00   .1534E+01   .6991E+03  -.1675E+03  0.
 10 56   .1061E+01   .1086E+01   .9756E+00   .3697E-01  0.          .6324E+00   .1544E+01   .6991E+03  -.2083E+03  0.
 11 56   .1052E+01   .1074E+01   .9787E+00   .4351E-01  0.          .6314E+00   .1561E+01   .6991E+03  -.2555E+03  0.
 12 56   .1051E+01   .1072E+01   .9790E+00   .4808E-01  0.          .6312E+00   .1563E+01   .6991E+03  -.3102E+03  0.
 13 56   .1046E+01   .1065E+01   .9806E+00   .5437E-01  0.          .6307E+00   .1557E+01   .6991E+03  -.3736E+03  0.
 14 56   .1028E+01   .1039E+01   .9872E+00   .5436E-01  0.          .6284E+00   .1574E+01   .6991E+03  -.4470E+03  0.
 15 56   .1006E+01   .1009E+01   .9948E+00   .7363E-01  0.          .6258E+00   .1594E+01   .6991E+03  -.5321E+03  0.
 16 56   .1000E+01   .1000E+01   .9970E+00   .7722E-01  0.          .6250E+00   .1600E+01   .6991E+03  -.6307E+03  0.
 17 56   .1001E+01   .1002E+01   .9966E+00   .7717E-01  0.          .6251E+00   .1599E+01   .6991E+03  -.7449E+03  0.
 18 56   .1000E+01   .1000E+01   .9970E+00   .7724E-01  0.          .6250E+00   .1600E+01   .6991E+03  -.8773E+03  0.
 19 56   .9986E+00   .9980E+00   .9975E+00   .7771E-01  0.          .6248E+00   .1601E+01   .6991E+03  -.1031E+04  0.

     ITER=     6 ZTA1= 699.08838 DZTA1=    2.50000
RMSR3=    .23415121E-01       NN=  313       NR3ITER=    2
RMSR3=    .16881968E-01       NN=  313       NR3ITER=    3
RMSR3=    .92558456E-05       NN=  313       NR3ITER=    4
  EIGENY=    .21338727E+00  CFLE= cL .53346819E+01  EIGENZ=    .63246441E-01  CFLX=        .1581E+01  DZTA=        .2500E+01
 L= .32070E+05   D= .28180E+04   CL= .25599E+00   CD= .22494E-01   SURFACE A= .37196E+06   REF. A= .12528E+06   SREF
 PITCH MOMENT=  -.4946E+06   CP=  -.1683E-01   XO= CD .5000E+03   YO=  0.             .1578E+03   .1610E+05   .2346E+03
                                    CM
     ITER=     7 ZTA1= 701.58838 DZTA1=    2.50000
RMSR3=    .16894983E-01       NN=  314       NR3ITER=    2
RMSR3=    .19344000E-01       NN=  314       NR3ITER=    3
RMSR3=    .17461672E-04       NN=  314       NR3ITER=    4
     COMPLEX EIGEN VALUE  J=    2  K=   22  NN=  314  Q2ETA=    .20812154E-04  Q2XI=   .32109857E-04
  EIGENY=    .24856313E-01  CFLE=    .62140783E+00  EIGENZ=    .42286298E-01  CFLX=        .1057E+01  DZTA=        .2500E+01
 L= .32201E+05   D= .28350E+04   CL= .25703E+00   CD= .22629E-01   SURFACE A= .37414E+06   REF. A= .12528E+06
 PITCH MOMENT=  -.5214E+06   CP=  -.1774E-01   XO=    .5000E+03   YO=  0.             .1612E+03   .1618E+05   .2346E+03

     ITER=     8 ZTA1= 704.08838 DZTA1=    2.50000
RMSR3=    .19873105E-01       NN=  315       NR3ITER=    2
RMSR3=    .19259946E-01       NN=  315       NR3ITER=    3
RMSR3=    .16920610E-04       NN=  315       NR3ITER=    4
     COMPLEX EIGEN VALUE  J=    2  K=   22  NN=  315  Q2ETA=    .10370612E-04  Q2XI=  -.74477587E-03
  EIGENY=    .18347013E-01  CFLE=    .48887532E+00  EIGENZ=    .29677634E-01  CFLX=        .7419E+00  DZTA=        .2500E+01
 KST,KED1,KST1,KED,KS,KE,KIA,KAWK    28    38    40    48    36    36     1     2
 VORT,PHM,K    -.14187E+02      .69610E+03    36
 KST,KED1,KST1,KED,KS,KE,KIA,KAWK    28    38    40    48    40    40     2     2
 VORT,PHM,K    -.14187E+02      .71029E+03    40
 L= .32302E+05   D= .28506E+04   CL= .25784E+00   CD= .22754E-01   SURFACE A= .37624E+06   REF. A= .12528E+06
 PITCH MOMENT=  -.5426E+06   CP=  -.1846E-01   XO=    .5000E+03   YO=  0.             .1650E+03   .1621E+05   .2346E+03

     ITER=     9 ZTA1= 706.58838 DZTA1=    2.50000
RMSR3=    .24927362E-01       NN=  316       NR3ITER=    2
RMSR3=    .18872039E-01       NN=  316       NR3ITER=    3
RMSR3=    .20722912E-04       NN=  316       NR3ITER=    4
     COMPLEX EIGEN VALUE  J=    2  K=   22  NN=  316  Q2ETA=    .10124578E-04  Q2XI=  -.78430692E-03
  EIGENY=    .15843887E-01  CFLE=    .39609718E+00  EIGENZ=    .23966680E-01  CFLX=        .5992E+00  DZTA=        .2500E+01
 L= .32412E+05   D= .28674E+04   CL= .25872E+00   CD= .22888E-01   SURFACE A= .37835E+06   REF. A= .12528E+06
 PITCH MOMENT=  -.5658E+06   CP=  -.1925E-01   XO=    .5000E+03   YO=  0.             .1691E+03   .1627E+05   .2346E+03
          +++++RESTART DATA WRITE ON UNIT  4+++++
```

Postprocessor Description

A Tektronix based graphics display capability is available for displaying results. The file containing the cross-sectional data is generated for ZTA1 by the supersonic full potential analysis as Tape 1.

Typical program prompt response is

```
     X-STATION =  54.95

IPLOT...IS
      =   2 FOR MACH NO. CONTOURS
      =   3 FOR PRESSURE CONTOURS
      =  10 FOR COMPUTATIONAL GRID
      =  12 FOR MACH NO. PROFILES
      =  13 FOR PRESSURE PROFILES
 0----+----0----+----0----+----0----+----0
?   10
XMIN,XMAX,YMIN,YMAX...4F10.4
X  IS THE PLOT'S X COORDINATE
Y  IS THE PLOT'S Y COORDINATE
Y  IS THUS  MACH NO. FOR IPLOT=12
Y  IS THUS  PRESSURE FOR IPLOT=13
Y  IS OTHERWISE THE PHYSICAL Y COORDINATE
X IS ALWAYS THE PHYSICAL X COORDINATE
XMIN=  0.              XMAX=   .22787093E+03
YMIN=  -.22351750E+03YMAX=   .22938620E+03
 0----+----0----+----0----+----0----+----0
? 0.0          25.        -10.      10.
```

Typical output is shown below. The results are truncated at $Z = 25$ and $Y = \pm 10$ as specified in the input above.

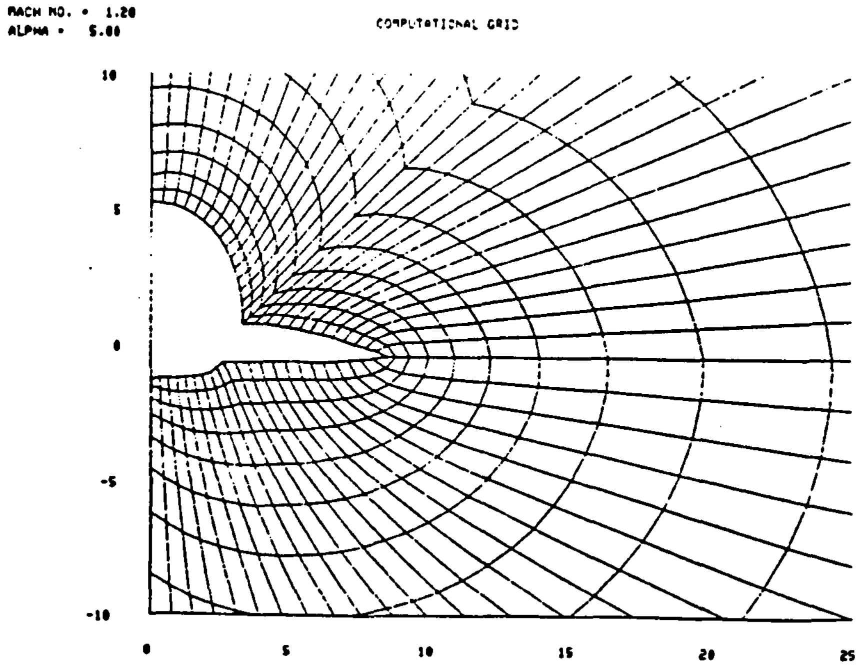

```
     X-STATION =  54.95

IPLOT...I5
     =   2 FOR MACH NO. CONTOURS
     =   3 FOR PRESSURE CONTOURS
     =  10 FOR COMPUTATIONAL GRID
     =  12 FOR MACH NO. PROFILES
     =  13 FOR PRESSURE PROFILES
 0----+----0----+----0----+----0----+----0
?     3
XMIN,XMAX,YMIN,YMAX...4F10.4
X  IS THE PLOTES X COORDINATE
Y  IS THE PLOTES Y COORDINATE
Y  IS THUS  MACH NO. FOR IPLOT=12
Y  IS THUS  PRESSURE FOR IPLOT=13
Y  IS OTHERWISE THE PHYSICAL Y COORDINATE
X IS ALWAYS THE PHYSICAL X COORDINATE
XMIN=  0.                XMAX=   .22787093E+03
YMIN=  -.22351750E+03YMAX=   .22938620E+03
 0----+----0----+----0----+----0----+----0
? 0.0           25.        -10.      10.
FMIN=  -.7403621E+00      FMAX=   .2501863E+00
CMIN,CMAX,DCL...3F10.4
CMIN=  LOWEST CONTOUR LEVEL
CMAX=  HIGHEST CONTOUR LEVEL
DCL =  INCREMENT BETWEEN CONTOUR LEVELS
 0----+----0----+----0----+----0----+----0
? -.64          .25        .05
SYMBOLS ARE TO BE PLOTTED ON EVERY (I2) CONTOUR LINE.
? 02
SYMBOLS ARE TO BE PLOTTED EVERY (I2) POINT(S).
? 02
```

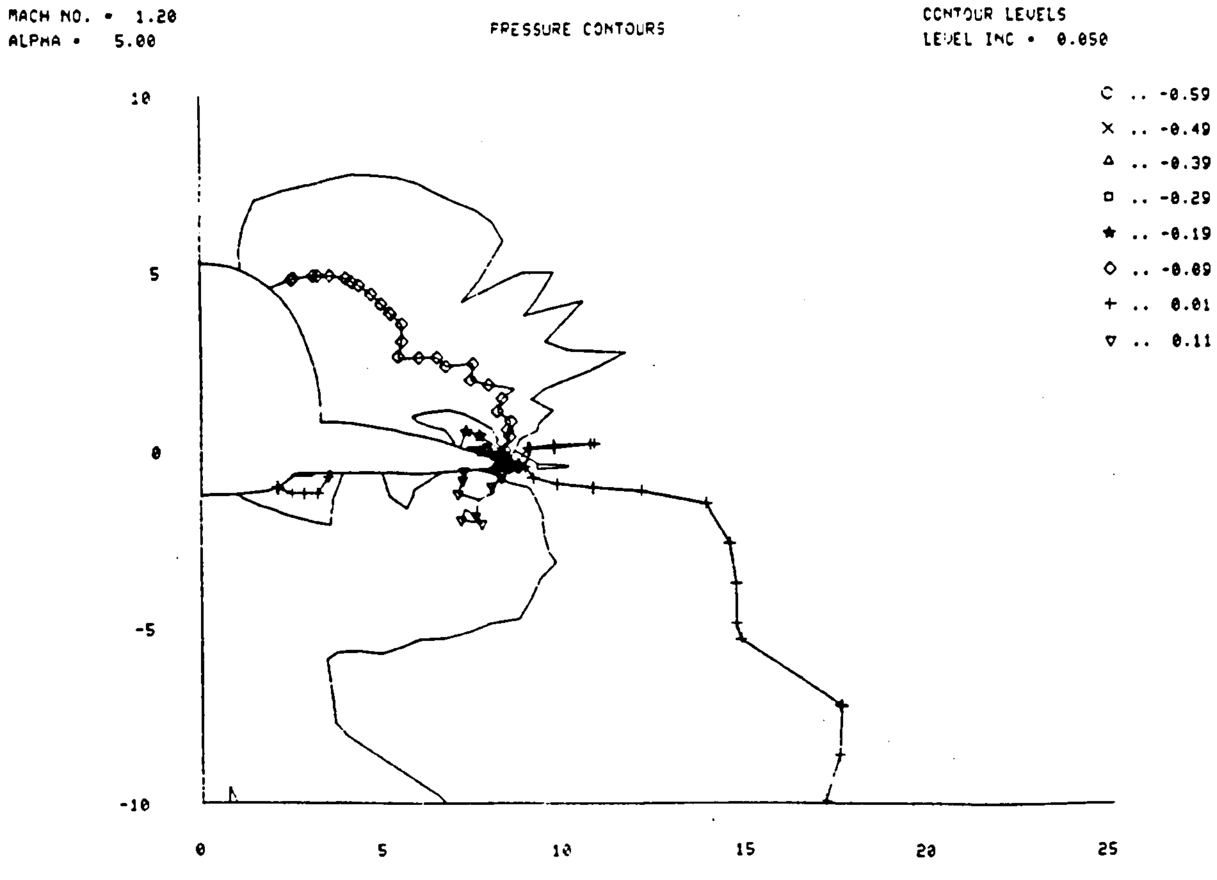

```
     X-STATION •  54.95

IPLOT...IS
      •   2 FOR MACH NO. CONTOURS
      •   3 FOR PRESSURE CONTOURS
      •  10 FOR COMPUTATIONAL GRID
      •  12 FOR MACH NO. PROFILES
      •  13 FOR PRESSURE PROFILES
 0----+----0----+----0----+----0----+----0
?    13
FMIN•  -.7403621E+00     FMAX•   .2501863E+00
XMIN,XMAX,YMIN,YMAX...4F10.4
X  IS THE PLOTES X COORDINATE
Y  IS THE PLOTES Y COORDINATE
Y  IS THUS  MACH NO. FOR IPLOT•12
Y  IS THUS  PRESSURE FOR IPLOT•13
Y  IS OTHERWISE THE PHYSICAL Y COORDINATE
X IS ALWAYS THE PHYSICAL X COORDINATE
XMIN•  0.               XMAX•   .22787093E+03
YMIN•  -.22351750E+03YMAX•   .22938620E+03
 0----+----0----+----0----+----0----+----0
? 0.0        25.
```

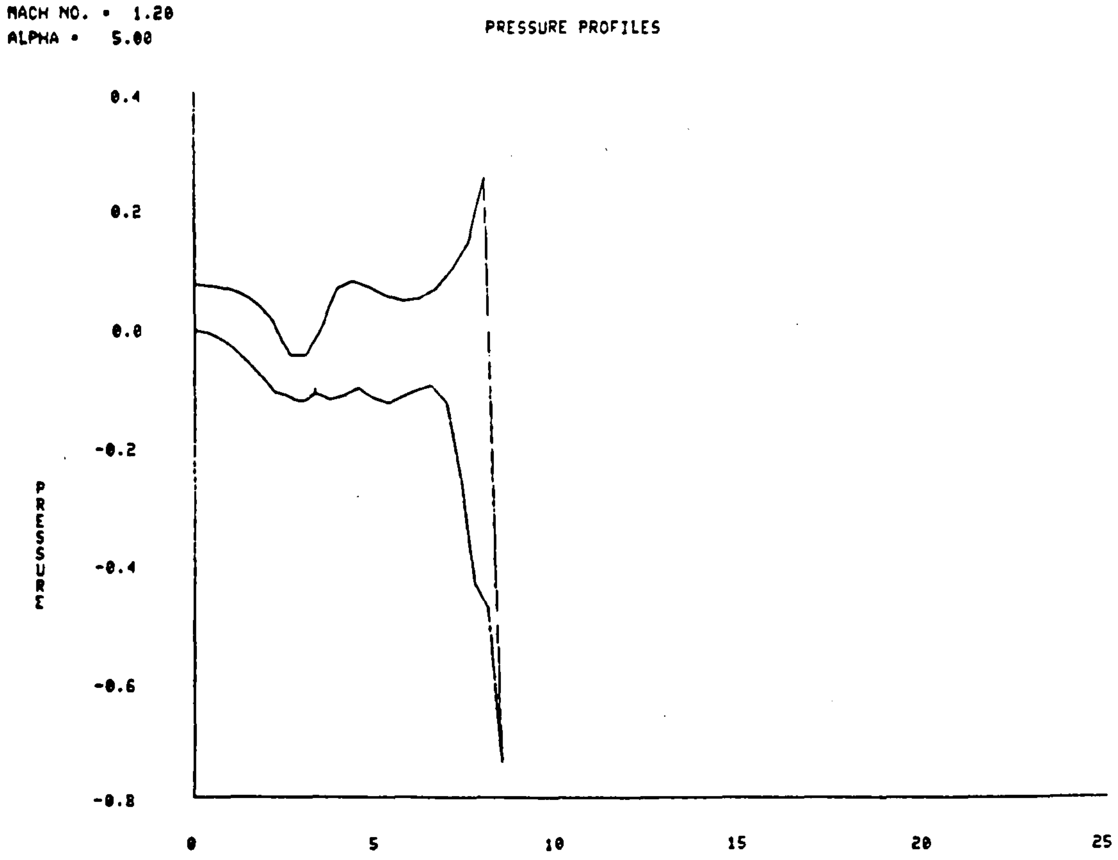

APPENDIX C — RELEVANT PUBLICATIONS*

1. AIAA J. 20 (11), 1508 (1982).
2. AIAA J. 21 (9), 1262 (1983).
3. AIAA J. 23 (1), 41 (1985).
4. AIAA Paper No. 85-0272.
5. AIAA Paper No. 85-1703.

---

*Permission to reprint the papers appearing in this Appendix was granted by the AIAA.

AIAA 81-1004R

Conservative Full Potential, Implicit Marching Scheme for Supersonic Flows

V. Shankar

Reprinted from

AIAA Journal Volume 20, Number 11, November 1982, Page 1508

AMERICAN INSTITUTE OF AERONAUTICS AND ASTRONAUTICS • 1290 AVENUE OF THE AMERICAS • NEW YORK, NEW YORK, N.Y. 10104

AIAA 81-1004R

Conservative Full Potential, Implicit Marching Scheme for Supersonic Flows

Vijaya Shankar*
Rockwell International Science Center, Thousand Oaks, California

An aerodynamic prediction technique based on the full potential equation in conservation form is developed for the treatment of supersonic flows. This technique bridges the gap between simplistic linear theory methods and complex Euler solvers. A local density linearization concept and a second-order-accurate retarded density scheme, both producing the correct artificial viscosity, are introduced in developing an implicit marching scheme for solving the scalar potential ϕ. Results for conical flows over delta wings, cones, and wing-body combinations, and for nonconical flows over bodies of revolution at angles of attack are compared with Euler and nonconservative full potential calculations and experimental data. The present formulation requires an order of magnitude less computer time and significantly less computer memory over Euler methods.

I. Introduction

AERODYNAMIC prediction techniques that can handle significant geometric complexity for use in supersonic or hypersonic configuration design are based on either hypersonic impact methods[1] or linear theory analysis,[2] both of which require minimum response time and cost. However, shortcomings are present in both the impact and linearized methods. Aside from these simplified techniques, limited capabilities also exist for calculating supersonic flowfields using very complex Euler codes,[3-6] using either shock capturing[3] or shock fitting[4-6] methods. The use of these codes as viable aerodynamic prediction techniques for configuration design is, however, not practical due to their slow response time (requirement of large computer memory) and excessive computer cost per run due to strict stability requirements. Thus, we have on one end of the spectrum, very simplified codes that require minimum computer time to provide less accurate results and, on the other end, very complex Euler codes that require excessive computer time to provide quality results.

In an attempt to bridge this gap between simplistic linear theory methods and complex Euler solvers, several methodologies such as the second-order potential analysis,[7] hypersonic small disturbance theory,[8] and, more recently, nonconservative full potential methods[9,10] have been considered by various investigators. The second-order theory,[7] in spite of the significant improvements reported, suffers from the lack of nonlinearity in resolving proper cross flow shocks and sonic lines. Also, the singularities inherent in the formulation create difficulties in the numerical treatment of subsonic leading edges. The finite difference analysis of the hypersonic small disturbance theory[8] indicates that the solution procedure is as complex as that for the Euler equation and not particularly responsive to preliminary design level of effort.

Recently, Grossman[9] and Grossman and Siclari[10] have computed supersonic flowfields over conical and nonconical cambered and twisted delta wings with remarkable success using the nonconservative full potential equation and a transonic relaxation method. However, their approach is made complicated by the use of global conformal mappings which apply only to certain classes of configurations. Also, the nonconservative form of the full potential equation is in terms of second derivatives of the potential ϕ, which, when a transformation is applied, generates a large number of first and second derivative transformation terms.

The full potential method proposed in this paper is significantly different from that of Refs. 9 and 10. First of all, the method is based on the conservative form of the full potential equation, since for a shock capturing procedure to conserve mass across the shock wave,[11] it is essential that the equation be cast in conservation form.[12] Second, the method can accommodate a numerical or analytical mapping procedure that is either orthogonal or nonorthogonal without complicating the form of the equation, in contrast to Refs. 9 and 10. Third, the method is based on an approximate factorization implicit algorithm that can yield convergence much faster than the conventional successive line over-relaxation method.[10] Finally, the method is not an adaptation of a transonic code using type dependent operators, but a scheme specifically developed and tailored for supersonic marching problems using a density linearization concept and has no step size restrictions.

To validate the present methodology, results are shown for a variety of conical and nonconical geometries and are compared with Euler solutions and full potential results of Refs. 9 and 10. Results indicate that the method works just as fast and efficient for nonconical flows as in the case of conical geometry treatment. Results also indicate that the method is very useful in computing very high-speed flows ($M_\infty \sim 2$-6) for the moderate flow deflection angles ($\alpha \sim 4$-10 deg) where the neglect of entropy generation does not seriously distort the main features of the flowfield.

The present method can also handle more complicated geometries (realistic wing-body combinations) than the ones reported in the paper, but requires a suitable grid generation routine, especially near wing-body junction regions. In a subsequent paper,[13] results for nonconical wing-body flows will be presented along with a formal method of characteristics treatment for cross flow signal propagation.

II. Formulation

The conservative form of the full potential equation in Cartesian coordinates x, y, z can be written as

$$\frac{\partial(\rho u)}{\partial x} + \frac{\partial(\rho v)}{\partial y} + \frac{\partial(\rho w)}{\partial z} = 0 \tag{1}$$

where ρ is the density and u, v, w are the velocity components. They are calculated as the gradient of the potential ϕ,

$$u = \phi_x; \quad v = \phi_y; \quad w = \phi_z \tag{2}$$

Presented as Paper 81-1004 at the AIAA Fifth Computational Fluid Dynamics Conference, Palo Alto, Calif., June 22-23, 1981; submitted June 24, 1981; revision received March 22, 1982.

*CFD Project Leader. Associate Fellow AIAA.

The density ρ is computed from the isentropic formula

$$\rho=\left[1-\frac{\gamma-1}{2}M_\infty^2(u^2+v^2+w^2-1)\right]^{1/\gamma-1} \tag{3}$$

If the density is normalized with respect to the freestream value, then the speed of sound a is given by

$$a^2=\rho^{\gamma-1}/M_\infty^2 \tag{4}$$

where M_∞ is the freestream Mach number.

The objective of the paper is to solve for the scalar potential ϕ from Eq. (1) subject to the surface tangency condition $\phi_n=0$ (n is normal to the body surface). Examining Eq. (1), it is very clear that ϕ appears in a nonlinear form due to the presence of the density term inside the derivative. The approach to be described here is a method that treats the density term in such a way that it produces the correct artificial viscosity needed for shock capturing and that enables one to solve for ϕ with relative ease.

In order to apply the surface tangency condition at the actual body location, a body-fitted coordinate transformation is essential. Introducing a body-fitted coordinate transformation, $\zeta=\zeta(x,y,z)$, $\eta=\eta(x,y,z)$, and $\xi=\xi(x,y,z)$, Eq. (1) transforms to

$$\left(\rho\frac{U}{J}\right)_\zeta+\left(\rho\frac{V}{J}\right)_\eta+\left(\rho\frac{W}{J}\right)_\xi=0 \tag{5}$$

where U, V, and W are the contravariant velocity components. Introducing the following notation for convenience:

$$U=U_1,\quad V=U_2,\quad W=U_3$$

$$x=x_1,\quad y=x_2,\quad z=x_3$$

$$\zeta=X_1,\quad \eta=X_2,\quad \xi=X_3$$

the contravariant velocities and density are given by

$$U_i=\sum_{j=1}^{3}a_{ij}\phi_{X_j}\qquad i=1,2,3$$

$$a_{ij}=\sum_{k=1}^{3}\frac{\partial X_i}{\partial x_k}\frac{\partial X_j}{\partial x_k}\qquad i=1,2,3,\quad j=1,2,3$$

$$\rho=\left[1-\left(\frac{\gamma-1}{2}\right)M_\infty^2\{U\phi_\zeta+V\phi_\eta+W\phi_\xi-1\}\right]^{1/(\gamma-1)} \tag{6}$$

The Jacobian of the transformation J is represented by

$$J=\frac{\partial(\zeta,\eta,\xi)}{\partial(x,y,z)}=\begin{bmatrix}\zeta_x & \zeta_y & \zeta_z\\ \eta_x & \eta_y & \eta_z\\ \xi_x & \xi_y & \xi_z\end{bmatrix} \tag{7}$$

Equation (5) is in terms of a general coordinate system (ζ,η,ξ) and can accommodate any kind of mapping procedure, either analytical (conformal mapping) or numerical type. Any numerical marching procedure applied to Eq. (5) to simulate a supersonic flow should have a truncation error whose leading terms represent a correct artificial viscosity. This is essential to ensure marching numerical stability and to exclude the formation of expansion shocks which are unphysical and correspond to a decrease in entropy. The nature of the required artificial viscosity can be studied by an analysis[14] of the canonical form of Eq. (5), which indicates that for stability, the form of artificial viscosity be

$$\begin{aligned}\frac{\rho}{Ja^2}\left\{1-\frac{a^2}{q^2}\right\}[&\Delta\zeta U\{U\phi_{\zeta\zeta\zeta}+V\phi_{\eta\zeta\zeta}+W\phi_{\xi\zeta\zeta}\}\\ &+\Delta\eta V\{U\phi_{\zeta\eta\eta}+V\phi_{\eta\eta\eta}+W\phi_{\xi\eta\eta}\}\\ &+\Delta\xi W\{U\phi_{\zeta\xi\xi}+V\phi_{\eta\xi\xi}+W\phi_{\xi\xi\xi}\}]\end{aligned} \tag{8}$$

assuming that U, V, W are positive. What this implies is that if the flowfield is hyperbolic ($q>a$), then solution can be obtained by marching along the hyperbolic flow direction s. Once the total velocity q becomes less than a, then marching along s is not possible. This is reflected in the fact that the effective artificial viscosity given by Eq. (8) is now negative.

Now we will proceed with the numerical procedure for solving Eq. (5), and show the resemblance of the resulting artificial viscosity to that of Eq. (8).

A. Treatment of $\dfrac{\partial(\rho U/J)}{\partial\zeta}$ in Eq. (5)

Consider the direction ζ to be the marching direction. The condition to be satisfied for this to be true will become evident at the end of this analysis. Both the density ρ and the contravariant velocity U are functions of the potential ϕ and the transformation metrics, as represented in Eq. (6). In order to finite difference this ζ derivative quantity in terms of ϕ only will require some linearization treatment of the density. This will be termed the "local density linearization" procedure. In the transonic formulation described by Holst,[15] the density is upwind biased and computed at the old level, while retaining central differencing for the (U/J) term at the current level. Such an upwind density bias is shown to produce the right artificial viscosity in Ref. 14. Referring to Fig. 1, for a pure supersonic marching problem (say we want to march from the ith plane to the $i+1$th plane), a transonic relaxation procedure[15] in the marching direction ζ is not appropriate because the solution ϕ at the $i+1$th plane is not influenced by the $i+2$th plane. Hence, the following marching procedure is developed.

Given the ϕ information at all the previous planes i, $i-1$, $i-2$,..., the problem is to compute ϕ at the $i+1$th plane. Now, expand the unknown $\rho=\rho(\phi)$ in terms of a neighboring known state denoted here by a subscript 0 (ith plane information would represent the neighboring known state for the $i+1$th plane).

$$\rho=\rho_0+\left(\frac{\partial\rho}{\partial\phi}\right)_0\Delta\phi+\ldots \tag{9}$$

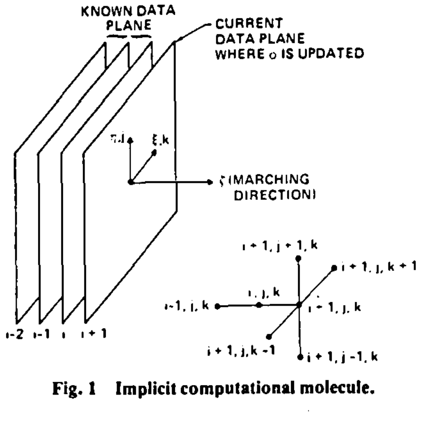

Fig. 1 Implicit computational molecule.

where $\Delta\phi = \phi - \phi_0$ and $\partial\rho/\partial\phi$ can be shown to be a differential operator[16]

$$\left(\frac{\partial\rho}{\partial\phi}\right)_0 \Delta\phi = -\frac{\rho_0}{a_0^2}\left\{U_0\frac{\partial}{\partial\zeta} + V_0\frac{\partial}{\partial\eta} + W_0\frac{\partial}{\partial\xi}\right\}(\phi-\phi_0) \quad (10)$$

Substituting Eqs. (9) and (10) into the first term in Eq. (5), we get

$$\frac{\partial(\rho U/J)}{\partial\zeta} \doteq \frac{\partial}{\partial\zeta}\left(\left[\rho_0 - \frac{\rho_0}{a_0^2}\left\{U_0\frac{\partial}{\partial\zeta} + V_0\frac{\partial}{\partial\eta} + W_0\frac{\partial}{\partial\xi}\right\}(\phi-\phi_0)\right]\frac{U}{J}\right) \quad (11)$$

Substituting for U in terms of ϕ from Eq. 6 and rearranging Eq. (11) in terms of the potential difference $\Delta\phi$, we get

$$\frac{\partial(\rho U/J)}{\partial\zeta} \doteq \frac{\partial}{\partial\zeta}\left\{\frac{\rho_0}{J}\left[\left(a_{11} - \frac{U^2}{a^2}\right)_0\frac{\partial}{\partial\zeta}\Delta\phi + \left(a_{12} - \frac{UV}{a^2}\right)_0 \times \frac{\partial}{\partial\eta}\Delta\phi + \left(a_{13} - \frac{UW}{a^2}\right)_0\frac{\partial}{\partial\xi}\Delta\phi + U_0\right]\right\} \quad (12)$$

where the speed of sound a_0, the density ρ_0, and the contravariant velocities U_0, V_0, W_0, represent information at the neighboring known plane. The ζ derivative term of Eq. (12) will now be one-sided differenced. Assuming U is positive,

$$\frac{\partial(\ )}{\partial\zeta} = \frac{1}{\Delta\zeta}\{(\ )_{i+1,j,k} - (\ )_{i,j,k}\} \quad (13)$$

An upwind differencing of the form Eq. (13) applied to Eq. (12) can be shown to produce a truncation term whose leading term is

$$\frac{\rho}{Ja^2}\left\{1 - \frac{a^2 a_{11}}{U^2}\right\}U^2\phi_{\zeta\zeta\zeta}\Delta\zeta \quad (14)$$

which will always represent a positive artificial viscosity as long as

$$\frac{U^2}{a_{11}} > a^2 \quad (15)$$

The preceding relation sets the condition for ζ to be the marching direction, for if U^2/a_{11} is less than the square of the local speed of sound, then the artificial viscosity becomes negative and a marching instability will occur. This also implies that the projection of the total velocity vector q in the direction normal to the ζ=const plane (η,ξ plane) is supersonic. For example, in a spherical system, for the radial direction r to be the marching direction, the radial velocity q_r must be supersonic. The similarity between the artificial viscosity term given by Eq. (14) and the first term appearing in Eq. (8) can be noted. When backward differenced, the terms in Eq. (12) will lead to a diagonally dominant tridiagonal set of equations for the unknown $\Delta\phi$ when coupled with the other two terms in Eq. (5). The mixed derivative terms like $\phi_{\zeta\eta}$ and $\phi_{\zeta\xi}$ appearing in Eq. (12) will be upwind biased, depending on the sign of the coefficient multiplying them to preserve diagonal dominance and to provide the right artificial viscosity.

B. Treatment of $\frac{\partial(\rho V/J)}{\partial\eta}$ in Eq. (5)

This term will be written at the $i+1$th plane to make the resulting scheme fully implicit.

$$\frac{\partial(\rho V/J)}{\partial\eta} = \frac{\partial}{\partial\eta}\left\{\frac{\rho}{J}(a_{21}\phi_\zeta + a_{22}\phi_\eta + a_{23}\phi_\xi)\right\} \quad (16)$$

The density term ρ in Eq. (16) cannot be represented at the $i+1$th plane since that would result in a very complicated nonlinear form for ϕ. Hence, a density approximation is introduced by setting $\rho = \rho^*$ where $\rho^* = \rho_0$ for conical flow treatment. In the case of nonconical flows, while advancing from i to the $i+1$th plane, several iterations are performed within each cross flow plane (η,ξ) to refine the density ρ^* to properly account for the axial geometry variation. This is done by initially setting ρ^* to ρ_0 and then subsequently refining it by setting ρ^* to the previous iterate value of ρ at the current plane. In many cases where the axial variation of the geometry is gradual (especially for smaller step size calculations) it was found that setting $\rho^* = \rho_0$ even for nonconical flows produced very good results without having to refine the density subsequently.

Writing Eq. (16) in terms of the potential difference $\Delta\phi$

$$\frac{\partial(\rho V/J)}{\partial\eta} \doteq \left(\frac{\rho^* a_{21}}{J}\frac{\Delta\phi}{\Delta\zeta}\right)_\eta + \left(\frac{\rho^* a_{22}}{J}\frac{\partial}{\partial\eta}\Delta\phi\right)_\eta + \left(\frac{\rho^* a_{23}}{J}\frac{\partial}{\partial\xi}\Delta\phi\right)_\eta + \left(\frac{\rho^* a_{22}}{J}\frac{\partial}{\partial\eta}\phi_0\right)_\eta + \left(\frac{\rho^* a_{23}}{J}\frac{\partial}{\partial\xi}\phi_0\right)_\eta \quad (17)$$

A simple central differencing for the various terms in Eq. (17) will not be sufficient as that would not provide the desired artificial viscosity given by Eq. (8), required for shock capturing. To simulate an artificial viscosity of the form given by Eq. (8), the density will be upwind biased based on the previous work reported in Refs. 14-16. The density ρ^* will be replaced by a modified density $\bar\rho^*$ given by

$$(\bar\rho^*)_{j+1/2,k} = (1 - \nu_{j+1/2,k})(\rho^*)_{j+1/2,k} + \tfrac{1}{2}\nu_{j+1/2,k}\{(1+\theta)(\rho^*)_{j+2m,k} + (1-\theta)(\rho^*)_{j-1+2m,k}\} \quad (18)$$

where $m=0$ when $(V_0)_{j+1/2,k}>0$ and $m=+1$ when $(V_0)_{j+1/2,k}<0$. When θ is set to zero, first-order accurate density biasing is achieved while $\theta=2$ gives second-order accuracy. The artificial viscosity coefficient $\nu_{j+1/2,k}$ is computed as follows:

$$\nu_{j+1/2,k} = [1 - (a_0^2/q_0^2)]_{j+s,k} \quad (19)$$

where $s=0$ for $V_{j+1/2,k}>0$ and $s=1$ for $V_{j+1/2,k}<0$.

Treatment of density as represented by Eqs. (18) and (19) would always produce a positive artificial viscosity as long as the local total velocity q_0 is supersonic. If that becomes subsonic, then the marching procedure would fail and the problem have to be treated as a transonic problem.

The treatment of the $(\partial/\partial\xi)[\rho W/J]$ term in Eq. (5) is very similar to the just described $(\partial/\partial\eta)[\rho V/J]$ term, except that the density biasing will be in the ξ direction and will be based on the sign of W.

C. Implicit Factorization Algorithm

Combining the various terms in Eqs. (12) and (17), and the terms arising from $(\partial/\partial\xi)[\rho W/J]$ will result in a fully implicit representation of Eq. (5) which cannot be solved without introducing an approximate factorization procedure. After some rearrangement of the terms, the factored implicit scheme becomes

$$\left[1 + \frac{A_3}{\beta\Delta\zeta}\frac{\partial}{\partial\xi} + \frac{1}{\beta}\frac{\partial}{\partial\xi}\left(\frac{\bar\rho^*}{J}\frac{a_{31}}{\Delta\zeta}\right) + \frac{1}{\beta}\frac{\partial}{\partial\xi}\frac{\bar\rho^* a_{33}}{J}\frac{\partial}{\partial\xi}\right] \times \left[1 + \frac{A_2}{\beta\Delta\zeta}\frac{\partial}{\partial\eta} + \frac{1}{\beta}\frac{\partial}{\partial\eta}\left(\frac{\bar\rho^* a_{21}}{J\Delta\zeta}\right) + \frac{1}{\beta}\frac{\partial}{\partial\eta}\frac{\bar\rho^* a_{22}}{J}\frac{\partial}{\partial\eta}\right]\Delta\phi = R \quad (20)$$

This equation has the form

$$L_\xi L_\eta(\Delta\phi)=R \tag{21}$$

and it is implemented as follows:

$$L_\xi(\Delta\phi)^*=R \qquad L_\eta(\Delta\phi)=(\Delta\phi)^* \qquad \phi=\phi_0+\Delta\phi \tag{22}$$

The various quantities appearing in Eq. (20) are given by

$$\beta=\frac{A_1}{(\Delta\zeta)^2} \qquad A_1=\frac{\rho_0}{J}\left(a_{11}-\frac{U^2}{a^2}\right)_0$$

$$A_2=\frac{\rho_0}{J}\left(a_{12}-\frac{UV}{a^2}\right)_0 \qquad A_3=\frac{\rho_0}{J}\left(a_{13}-\frac{UW}{a^2}\right)_0 \tag{23}$$

and the right-hand side term R consists of various known quantities.

The algorithm Eq. (22) requires only scalar tridiagonal inversions. Also, the scheme does not pose any restrictions on the direction of sweep that are present in the successive line over-relaxation method.[9,10]

D. Freestream Truncation Errors

To subtract out any numerical truncation error due to incomplete metric cancellation,[16] it is essential to add the terms (especially for a highly stretched nonorthogonal grid)

$$\frac{\partial}{\partial\zeta}\left(\frac{\rho_\infty U_\infty}{J}\right)+\frac{\partial}{\partial\eta}\left(\frac{\rho_\infty V_\infty}{J}\right)+\frac{\partial}{\partial\xi}\left(\frac{\rho_\infty W_\infty}{J}\right) \tag{24}$$

to the right-hand side of Eq. (20).

E. Boundary Conditions

In order to solve for $\Delta\phi$ from Eq. (20), boundary conditions will have to be prescribed at all four boundaries as shown in Fig. 2 at the current $i+1$th plane. While performing the L_ξ operator in Eq. (21), boundary conditions in terms of $\Delta\phi^*$ will be required along the $k=2$ and $k=K\mathrm{MAX}-1$ boundaries. For a pure angle-of-attack problem, $k=2$ and $k=K\mathrm{MAX}-1$ can be considered as planes of symmetry across which all flow variables reflect. The quantity $\Delta\phi^*$, even though it has no physical significance, can be safely set

$$(\Delta\phi)^*_{i+1,j,K\mathrm{MAX}}=(\Delta\phi)^*_{i+1,j,K\mathrm{MAX}-2}$$

$$(\Delta\phi)^*_{i+1,j,1}=(\Delta\phi)^*_{i+1,j,3} \tag{25}$$

The L_η operator would require boundary conditions along $j=2$ and $j=J\mathrm{MAX}$ in terms of $\Delta\phi$. Since $j=2$ is the body, the surface tangency condition

$$V=a_{21}\phi_\zeta+a_{22}\phi_\eta+a_{23}\phi_\xi=0 \tag{26}$$

will be set at all points $(i+1,2,k)$. Along $j=J\mathrm{MAX}$, freestream $\Delta\phi$ will be imposed.

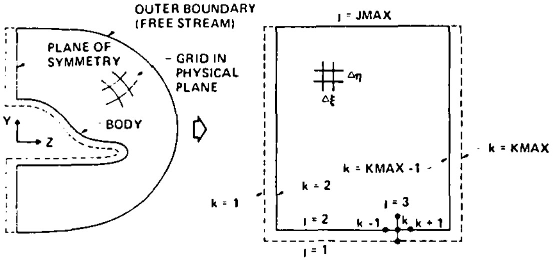

j = 2 IS BODY
j = 1, k = 1, k = KMAX ARE DUMMY ARRAYS
j = JMAX IS FREE STREAM

Fig. 2 Physical and computational plane.

F. Grid System

As shown in Fig. 2, the physical space (x,y,z) is transformed into a body-fitted (ζ,η,ξ) computational space. The transformation is performed numerically by using the elliptic grid generation techniques originally developed by Thompson et al.,[17] and later modified by Steger and Sorenson,[18] and Middlecoff and Thomas.[19] The present full potential method does not require an orthogonal grid; however, the error introduced by the approximate factorization, Eq. (20), can be minimized if the grid is orthogonal in the cross flow plane (η,ξ). For conical flow calculations, the grid is generated only once, and, as the marching procedure continues, the grid is allowed to grow conically. For a general nonconical body, it would be necessary to construct the grid in every marching plane.

III. Results

Results are presented for both conical and nonconical supersonic flows. Comparisons are made with Euler[3,5] and full potential[9,10] results and experimental data. All the calculations were performed using a CDC 7600 machine.

A. Conical Flows

Besides validating the methodology, computation of conical flows is of interest for generating the initial data plane for nonconical calculations. For a conical geometry (radially invariant), the initial data plane with freestream conditions is chosen at some location $\zeta=\zeta_0$ (usually set at $\zeta=1$). The solution is then marched along ζ using Eq. (20) and boundary conditions. The conical flow calculation is assumed to have converged when the change in the root mean square density is less than 10^{-4}.

Supersonic Leading-Edge Delta Wing

Figure 3 shows the compression surface pressures for a supersonic leading-edge delta wing at $M_\infty=6$, angle of attack $\alpha=-8$ deg, and leading-edge sweep $\Lambda=70$ deg. The present full potential solution compares well with the Euler solution[19] and experimental data. Also shown are the results from the first- and second-order linear theory.[7] Using a 30×40 grid in the (η,ξ) plane, the present approach required 40 iterations to achieve convergence, and 12-15 s of computer time to produce the results shown in Fig. 3.

It is interesting to note that in spite of the limitations of the full potential theory, even at a very high Mach number of 6, the comparison is in reasonable agreement with the Euler

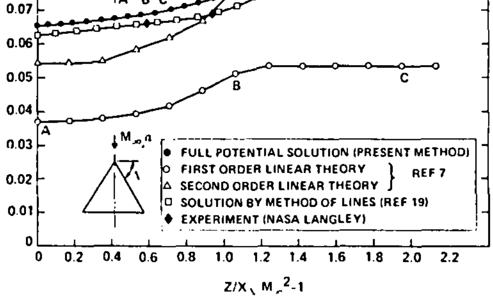

Fig. 3 Predicted compression surface pressure for a 70-deg sweep delta wing at $M_\infty=6$, $\alpha=-8$ deg.

solution and is significantly better than the second-order theory. The discrepancy between the full potential and Euler results is mainly due to neglect of entropy generation in the present approach.

Circular Cone and Ellipse

Figure 4 shows the surface pressure distribution for a circular cone, half angle 7.5 deg, $M_\infty = 3$ at 15 deg angle of attack. At this angle of attack the cross flow Mach number becomes supersonic as the flow turns around the cone from the windward symmetry to the leeward symmetry. This cross flow supersonic region is terminated by the formation of an embedded shock on the cone surface. This is evident from the results of Fig. 4. Grid clustering near the cross flow shock was used both in the Euler calculation of Kutler,[3] and in the present method, to finely resolve the pressure jump. The present calculation required 25 s of computer time, using a 30×60 grid in the (η, ξ) plane.

The liftoff of the vortical singularity on the leeward symmetry plane associated with the formation of the embedded shock is shown in Fig. 5. The location where the contravariant velocity V goes through zero on the leeward symmetry plane ($W=0$) denotes the location of the vortical singularity. The behavior of the cross flow streamlines converging to the vortical singularity is also shown in Fig. 5.

Figure 6 shows the full potential and Euler cross flow Mach number contours for the circular cone case. The presence of the embedded shock wave in both the results is very clear. The location of the vortical singularity liftoff is also shown in the figure. The Euler result is very oscillatory near the vortical singularity location while the present method predicts a smoother flowfield in the vicinity of the vortical singularity.

The surface pressure distribution on an elliptic cone $\theta_c = 18.39$ deg, $\delta_c = 3.17$ deg at $M_\infty = 1.97$ and $\alpha = 10$ deg is shown in Fig. 7. The results of the present study are compared with Euler calculations of Siclari,[5] full potential results of Grossman,[9] and the linearized thin wing solution of Jones and Cohen.[20] The agreement between the various nonlinear methods is very good, including the position and strength of the embedded shock wave.

Wing-Body Combination

Figure 8 shows the numerically generated grid distribution in the cross flow plane (η, ξ) of a conical wing-body combination. The design of this conically cambered delta wing to achieve shockless recompression is reported in Ref. 21. Figure 9 shows the pressure distribution around this wing-body combination at $M_\infty = 2$, and $\alpha = 7.81$ deg. The leading-edge sweep Λ is 57 deg. The comparison of the results from the present method with the experimental data[21] is excellent. The calculation used a 15×49 grid in the (η, ξ) plane and required less than a minute of computer time.

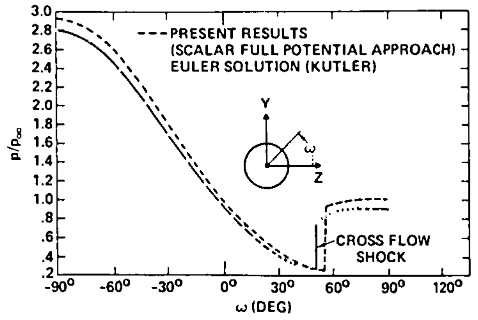

Fig. 4 Surface-pressure distribution for cone at angle of attack; $M_\infty = 3$, $\alpha = 15$ deg, $\theta_c = 7.5$ deg.

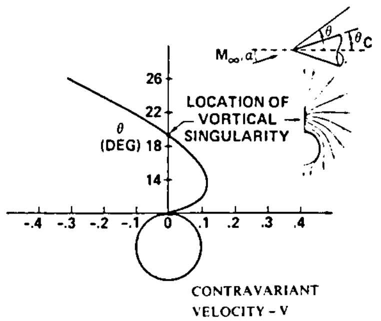

Fig. 5 Vortical singularity liftoff for a circular cone at $M_\infty = 3$, $\alpha = 15$ deg, $\theta_c = 7.5$ deg.

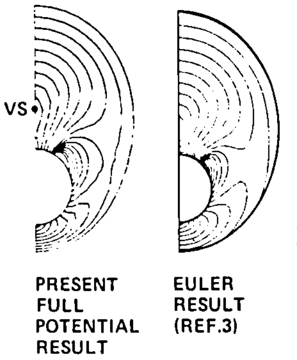

Fig. 6 Comparison of cross flow Mach number contours for cone at angle of attack; $M_\infty = 3$, $\alpha = 15$ deg, $\theta_c = 7.5$ deg (VS = vortical singularity).

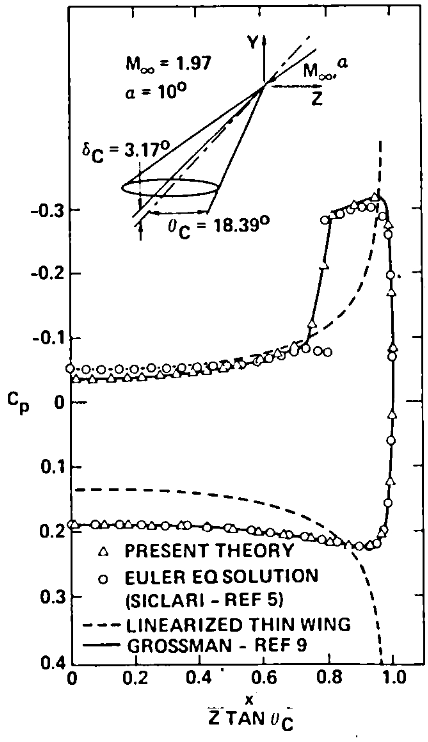

Fig. 7 Surface-pressure distribution on an elliptic cone; $M_\infty = 1.97$, $\theta_c = 18.39$ deg, $\delta_c = 3.17$ deg, $\alpha = 10$ deg.

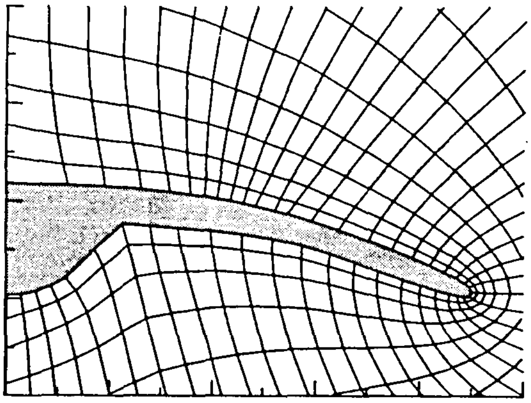

Fig. 8 Computational grid around a wing-body combination.

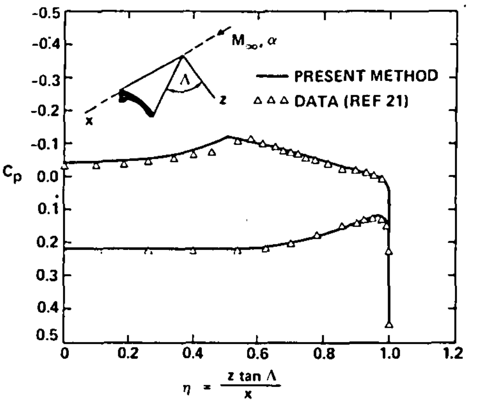

Fig. 9 Surface-pressure distribution for a conically cambered wing-body combination; $M_\infty = 2$, $\alpha = 7.81$ deg, $\Lambda = 57$ deg.

B. Nonconical Flows

Results are also presented for nonconical bodies of revolution and compared with experimental data. The initial data plane for the nonconical marching calculation is first obtained by performing a conical calculation over an assumed very small conical nose. This conical calculation usually takes 20-30 iterations on a typical 30×30 grid in the (η,ξ) plane. The nonconical calculations did not exhibit any increase in computational time over the conical procedure. As mentioned earlier, for the applications considered here where the cross flow station does not vary substantially from the previous one, it was found that there was no need to iterate the solution at each cross flow plane (η,ξ) to converge the density, and plottable accuracy was achieved by simply marching right along the body. However, if the body changes shape appreciably, the current implicit procedure might take 3-5 iterations per cross flow plane to refine the solution.

Reference 22 contains experimental data for several bodies of revolution at various Mach numbers and angles of attack. The shape chosen for comparison here is a circular arc-cylinder body. After the initial data plane was computed using a conical nose assumption, the current method typically used 60 marching steps to reach the end of the body but the calculations are not subject to any step size restriction. A typical calculation required 40-45 s of computer time. Figure 10 shows the circumferential surface pressure distribution at two different axial stations ($x/\ell = 0.225$ and 0.425) for 4 and 8 deg angles of attack at $M_\infty = 2.3$. The results from the present method are compared with experimental data,[22] showing very good agreement for the windward region with some discrepancy on the leeward side, possibly due to boundary-layer buildup.

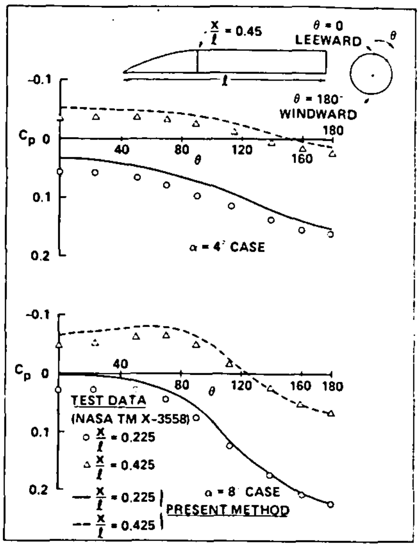

Fig. 10 Circumferential pressure distribution for a circular-arc-cylinder body at $M_\infty = 2.3$.

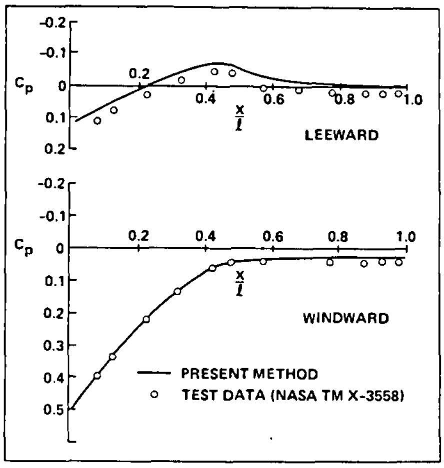

Fig. 11 Surface-pressure distribution for a circular-arc-cylinder body at $\alpha = 8$ deg, $M_\infty = 2.3$.

Figure 11 shows the surface pressure distribution in the axial direction along the windward and leeward plane of symmetry, at $M_\infty = 2.3$ and $\alpha = 8$ deg. Again, results from the present method compare very well with the experimental data.[22]

IV. Conclusions

An aerodynamic prediction technique based on the full potential equation in conservation form is developed for the treatment of supersonic flowfields. A local density linearization concept and a second-order accurate density biasing scheme are introduced in developing an implicit marching procedure. The method produces results that compare well with Euler solvers, and requires an order of magnitude less computer time and significantly less computer memory over existing Euler codes for the cases presented in the paper. In a subsequent paper,[13] results for more complicated nonconical wing-body flows are presented, along with a formal theory for the characteristic signal propagation in the cross flow plane.

Acknowledgment

This work was supported in full by NASA Langley Research Center under Contract NAS1-15820.

References

[1] Brooke, D. and Vondrasek, D. V., "Feasibility of Combining Linear Theory and Impact Theory Methods for the Analysis and Design of High Speed Configurations," NASA CR 3069, Dec. 1978.

[2] Woodward, F. A., Tinoco, E. N., and Larsen, J. W., "Analysis and Design of Supersonic Wing-Body Combinations, Including Flow Properties in the Near Field. Part I—Theory and Application," NASA CR 73106, 1967.

[3] Kutler, P., "Computation of Three-Dimensional, Inviscid Supersonic Flows," *Lecture Notes in Physics*, Vol. 41, Springer-Verlag, New York, 1975, pp. 293-374.

[4] Marconi, F., Salas, M., and Yeager, L., "Development of a Computer Code for Calculating the Steady Super/Hypersonic Inviscid Flow Around Real Configurations, Vol. I—Computational Techniques," NASA CR 2675, April 1976.

[5] Siclari, M. J., "Investigation of Cross Flow Shocks on Delta Wings in Supersonic Flow," *AIAA Journal*, Vol. 18, Jan. 1980, p. 85.

[6] Moretti, G., "Conformal Mappings for the Computation of Steady Three-Dimensional Supersonic Flows," *Numerical/Laboratory Computer Methods in Fluids Mechanics*, edited by A. A. Pouring and V. I. Shah, ASME, New York, 1979, pp. 13-28.

[7] "Formulation of Aerodynamic Prediction Techniques for Hypersonic Configuration Design," NASA CR 158994, Feb. 1979.

[8] Gunness, R. C. Jr., Knight, C. J., and Sylvia, E. D., "Flow Field Analysis of Aircraft Configurations using a Numerical Solution to the Three-Dimensional Unified Supersonic/Hypersonic Small-Disturbance Equations," NASA CR 1926, Feb. 1972.

[9] Grossman, B., "Numerical Procedure for the Computation of Irrotational Conical Flows," *AIAA Journal*, Vol. 17, Aug. 1979, pp. 828-837.

[10] Grossman, B. and Siclari, M. J., "The Nonlinear Supersonic Potential Flow over Delta Wings," AIAA Paper 80-0269, Jan. 1980.

[11] Jameson, A., "Transonic Potential Flow Calculations using Conservation Form," *AIAA Second Computational Fluid Dynamics Conference Proceedings*, 1975, pp. 148-155.

[12] Lax, P. D., "Weak Solutions of Nonlinear Hyperbolic Equations and Their Numerical Computation," *Communications on Pure and Applied Mathematics*, Vol. 7, No. 1, 1954, pp. 159-193.

[13] Shankar, V. and Osher, S., "An Efficient Full Potential Implicit Method Based on Characteristics for Analysis of Supersonic Flow," AIAA Paper 82-0974, June 1982.

[14] Jameson, A. and Caughey, D. A., "A Finite Volume Method for Transonic Potential Flow Calculations," AIAA Paper 77-635, June 1977.

[15] Holst, T. L., "A Fast, Conservative Algorithm for Solving the Transonic-Potential Equation," AIAA Paper 79-1456, July 1979.

[16] Steger, J. L. and Caradona, F. X., "A Conservative Implicit Finite Difference Algorithm for the Unsteady Transonic Full Potential Equation," Flow Simulations, Inc. Rept. 79-04, Dec. 1979.

[17] Thompson, J. F., Thames, F. C., and Mastin, C. W., "TOMCAT—A Code for Numerical Generation of Boundary-Fitted Curvilinear Coordinate Systems on Fields Containing Any Number of Arbitrary Two-Dimensional Bodies," *Journal of Computational Physics*, Vol. 24, 1977, p. 274.

[18] Steger, J. L. and Sorenson, R. L., "Automatic Mesh-Point Clustering Near a Boundary in Grid Generation with Elliptic Partial Differential Equations," *Journal of Computational Physics*, Vol. 33, Dec. 1979, p. 405.

[19] South, J. C. and Klunker, E. B., "Method for Calculating Nonlinear Conical Flows," NASA SP-228, 1969, pp. 131-158.

[20] Jones, R. T. and Cohen, D., *High Speed Wing Theory*, Princeton University Press, Princeton, N.J., 1960, pp. 157, 160.

[21] Miller, D. S., Landrum, E. J., Townsend, J. C., and Mason, W. H., "Pressure and Force Data for a Flat Wing and a Warped Conical Wing Having a Shockless Recompression at Mach 1.62," NASA TP 1759, April 1981.

[22] Landrum, E. J., "Wind Tunnel Pressure Data at Mach Numbers from 1.6 to 4.63 for a Series of Bodies of Revolution at Angles of Attack from −4 to 60°," NASA TM X-3558, Oct. 1977.

An Efficient, Full-Potential Implicit Method Based on Characteristics for Supersonic Flows

V. Shankar and S. Osher

Reprinted from
AIAA Journal Volume 21, Number 9, September 1983, Page 1262
AMERICAN INSTITUTE OF AERONAUTICS AND ASTRONAUTICS • 1633 BROADWAY • NEW YORK, N.Y. 10019

An Efficient, Full-Potential Implicit Method Based on Characteristics for Supersonic Flows

Vijaya Shankar*
Rockwell International Science Center, Thousand Oaks, California
and
Stanley Osher†
University of California, Los Angeles, California

A nonlinear aerodynamic prediction technique based on the full-potential equation in conservation form has been developed for the treatment of supersonic flows. The method uses the theory of characteristic signal propagation to accurately simulate the flow structure, which includes shock waves and mixed elliptic-hyperbolic crossflow. An implicit approximate factorization scheme is employed to solve the finite-differenced equation. The necessary body-fitted grid system in every marching plane is generated numerically, using an elliptic grid solver. Results are shown for conical and nonconical wing-body combinations and compared with experimental data and Euler calculations. The method demonstrates an enormous savings in execution time and memory requirements over Euler methods.

I. Introduction

NONLINEAR aerodynamic prediction techniques based on the Euler equations[1-3] and the full-potential equation[4-7] are steadily maturing into complex aerodynamic tools and becoming an attractive alternate approach to using the linearized panel methods.[8] Panel methods can handle very complicated geometries requiring minimal computer time to provide less accurate results, while the Euler solvers need expensive computer runs even for simple wing-body configurations. The full-potential methods[6,7] are a substitute for the Euler methods[1,3] to avoid the requirement of excessive computer time and memory allocation. While using a full-potential method for supersonic flows, one should be aware of the isentropic limitations of the theory. As a general rule, the full-potential theory is expected to perform well when the product of the Mach number and the characteristic flow deflection angle is less than 1 ($M\delta \leq 1$).

The full-potential method of Refs. 4-6 is based on the nonconservative form of the equation, while Ref. 7 and the present paper deal with the conservative form, to conserve mass across the shock.[9,10] In order to properly treat the supersonic flow structure, which includes shock waves and mixed elliptic-hyperbolic crossflow, the present method uses the theory of characteristic signal propagation based on the eigenvalue system of the full-potential equation. An approximate factorization implicit scheme, which includes a density biasing procedure in the crossflow plane, is incorporated to accelerate the computational efficiency. The density biasing procedure is activated by the eigenvalue system and properly takes into account the direction of the crossflow. The implicit approximate factorization scheme does not pose any restrictions on the direction of sweep that are present in the successive line overrelaxation method (SLOR).[4-6]

The full-potential as well as Euler methods require the application of boundary conditions at the actual body surface location. This, in general, necessitates the use of a body-fitted coordinate system. In the present method, the equation is cast in a more general arbitrary coordinate system and the appropriate body-fitted grid is generated numerically, employing an elliptic grid solver.[11]

The paper presents various results for conical and nonconical wing-body configurations and comparison is made with experimental data and Euler solution. The effect of the density biasing based on the characteristic signal propagation is demonstrated in terms of a sharper pressure profile across the shock wave. References 5 and 6 present excellent results at low supersonic Mach numbers, while Ref. 7 and the present paper demonstrate the capability of the conservative full-potential approach in handling even very high Mach number flows ($M_\infty \sim 4$-6, $\alpha \sim 0$-8 deg). All of the calculations reported in this paper were performed using the CDC 7600 computer and clearly demonstrated an order-of-magnitude or more reduction in computer time over Euler methods. A typical nonconical wing-body calculation takes less than 2 min of execution time to produce results comparable with experimental data.

II. Formulation

The conservative full-potential equation cast in an arbitrary coordinate system defined by $\zeta = \zeta(x,y,z)$, $\eta = \eta(x,y,z)$, and $\xi = \xi(x,y,z)$ takes the form

$$\left(\rho \frac{U}{J}\right)_\zeta + \left(\rho \frac{V}{J}\right)_\eta + \left(\rho \frac{W}{J}\right)_\xi = 0 \qquad (1)$$

where U, V, and W are the contravariant velocity components. Introducing the following notation for convenience

$$U = U_1, \quad V = U_2, \quad W = U_3$$

$$x = x_1, \quad y = x_2, \quad z = x_3$$

$$\zeta = X_1, \quad \eta = X_2, \quad \xi = X_3$$

the contravariant velocities and density are given by

$$U_i = \sum_{j=1}^{3} a_{ij} \phi_{x_j} \qquad i = 1,2,3 \qquad \ldots$$

Presented as Paper 82-0974 at the AIAA/ASME Third Joint Thermophysics, Fluids, Plasma and Heat Transfer Conference, St. Louis, Mo., June 7-11, 1982; submitted July 7, 1982; revision received Dec. 23, 1982.

*Manager, CFD Group. Associate Fellow AIAA.

†Professor, Department of Mathematics.

$$a_{ij}=\sum_{k=1}^{3}\frac{\partial X_i}{\partial x_k}\frac{\partial X_j}{\partial x_k}\qquad \begin{matrix} i=1,2,3\\ j=1,2,3\end{matrix}$$

$$\rho=\left[1-\left(\frac{\gamma-1}{2}\right)M_\infty^2\{U\phi_\zeta+V\phi_\eta+W\phi_\xi-1\}\right]^{1/(\gamma-1)}\qquad(2)$$

The Jacobian of the transformation J is represented by

$$J=\frac{\partial(\zeta,\eta,\xi)}{\partial(x,y,z)}=\begin{bmatrix}\zeta_x & \zeta_y & \zeta_z\\ \eta_x & \eta_y & \eta_z\\ \xi_x & \xi_y & \xi_z\end{bmatrix}\qquad(3)$$

Equation (1) is in terms of a general coordinate system (ζ,η,ξ) and can accommodate any kind of mapping procedure, either analytical (conformal mapping) or numerical. Use of Eq. (1) to simulate the supersonic flow by marching in the ζ direction first requires the establishment that the equation is indeed hyperbolic with respect to the marching direction. The nature of Eq. (1) can be analyzed by studying its eigenvalue system. Combining the irrotationality condition in the (ζ,η) and (ζ,ξ) plane and Eq. (1), one can write the following matrix equation:

$$Aq_\zeta+Bq_\eta+Cq_\xi=0\qquad(4)$$

where

$$A=\begin{bmatrix}(1/J)(\rho U)_{\phi_\zeta} & (1/J)(\rho U)_{\phi_\eta} & (1/J)(\rho U)_{\phi_\xi}\\ 0 & 1 & 0\\ 0 & 0 & 1\end{bmatrix}$$

$$B=\begin{bmatrix}(1/J)(\rho V)_{\phi_\zeta} & (1/J)(\rho V)_{\phi_\eta} & (1/J)(\rho V)_{\phi_\xi}\\ -1 & 0 & 0\\ 0 & 0 & 0\end{bmatrix}$$

$$C=\begin{bmatrix}(1/J)(\rho W)_{\phi_\zeta} & (1/J)(\rho W)_{\phi_\eta} & (1/J)(\rho W)_{\phi_\xi}\\ 0 & 0 & 0\\ -1 & 0 & 0\end{bmatrix}$$

$$q=\begin{bmatrix}\phi_\zeta\\ \phi_\eta\\ \phi_\xi\end{bmatrix}$$

The subscripts in Eq. (4) denote differentiation with respect to that variable.

In order for Eq. (4) or Eq. (1) to be hyperbolic in the ζ direction, the following two conditions must be satisfied:

1) A^{-1} must exist.

2) All real linear combinations of $A^{-1}B$ and $A^{-1}C$ must have real eigenvalues (characteristics). This implies $A^{-1}(\alpha B+\beta C)$ must have real eigenvalues for all combinations of α and β satisfying $\alpha^2+\beta^2=1$.

When the two conditions are applied to Eq. (4), the following criterion is obtained for ζ to be the marching direction.

$$(\rho U)_{\phi_\zeta}=\rho\left(a_{11}-\frac{U^2}{a^2}\right)<0\qquad(5)$$

where the transformation metric a_{11} is defined in Eq. (2) and a is the local speed of sound. Equation (5) is the most general form. For example, in a spherical system (r,θ,ϕ), for the radial direction r to be the marching direction, according to Eq. (5), the radial velocity q_r must be supersonic. In a Cartesian system (x,y,z), for x to be the marching direction, the velocity u must be supersonic. For convenience, the derivation of Eq. (5) for a Cartesian system is described in Appendix A, and the derivation for an arbitrary coordinate system (ζ,η,ξ) has been derived in a similar manner.

Thus far, the condition for ζ to be a marching direction has been identified from the characteristic theory. This means the (η,ξ) plane will be treated as a marching plane, which will be defined from here on in this paper as the crossflow plane (the real crossflow is the projection of the velocity vector on a unit sphere with center at the origin). Even though the flow is supersonic in the marching direction (i.e., hyperbolic type), the behavior of the flow structure in the crossflow plane (η,ξ) can be a mixed elliptic-hyperbolic type. Depending on the nature of the flow at a crossflow plane grid point (whether elliptic, parabolic, or hyperbolic), the η and ξ derivative terms in Eq. (1) will be appropriately modeled. Again, the theory of characteristics will dictate how the signals are propagated in the crossflow plane.

A. Crossflow Signal Propagation

The nature of the flow in the (η,ξ) plane can be analyzed by separately studying the eigenvalues of $A^{-1}B$ and $A^{-1}C$. The eigenvalue character of $A^{-1}B$ will determine the η-derivative treatment and similarly $A^{-1}C$ for the ξ derivative. For illustration, only the study of $A^{-1}B$ is shown here, and $A^{-1}C$ follows the same procedure.

The eigenvalues λ of $A^{-1}B$ are obtained by setting the determinant $|A^{-1}B-\lambda I|=0$. Since A^{-1} is assumed to exist [condition 1 preceding Eq. (5)], the following is true.

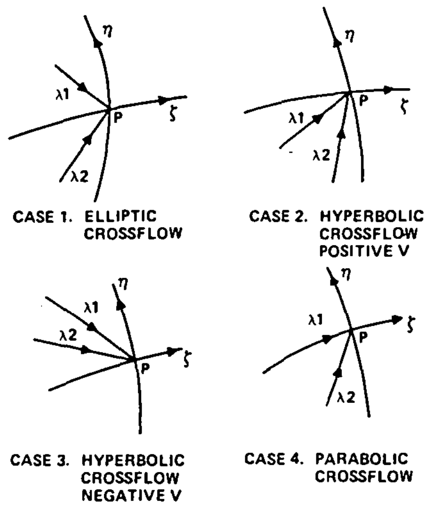

Fig. 1 Eigenvalue structure in (ζ,η) plane.

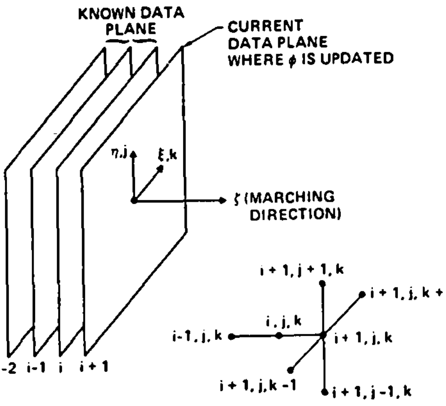

Fig. 2 Implicit computational molecule.

$$|B-\lambda A|=\begin{bmatrix} \frac{1}{J}(\rho V)_{\phi_\zeta}-\frac{\lambda}{J}(\rho U)_{\phi_\zeta} & \frac{1}{J}(\rho V)_{\phi_\eta}-\frac{\lambda}{J}(\rho U)_{\phi_\eta} & \frac{1}{J}(\rho V)_{\phi_\xi}-\frac{\lambda}{J}(\rho U)_{\phi_\xi} \\ -1 & -\lambda & 0 \\ 0 & 0 & -\lambda \end{bmatrix}=0 \tag{6}$$

Solving for λ from Eq. (6), one gets

$$\lambda_{1,2}=\frac{\{(\rho U)_{\phi_\eta}+(\rho V)_{\phi_\zeta}\}\pm\sqrt{\{(\rho U)_{\phi_\eta}+(\rho V)_{\phi_\zeta}\}^2-4(\rho U)_{\phi_\zeta}(\rho V)_{\phi_\eta}}}{2(\rho U)_{\phi_\zeta}} \tag{7}$$

When Eq. (5) is satisfied, the discriminant in Eq. (7) is always positive.

Now, analyzing λ_1 and λ_2, the following combinations are possible.

1) λ_1 is positive and λ_2 is negative, or λ_1 is negative and λ_2 is positive.

2) λ_1 and λ_2 are both positive.

3) λ_1 and λ_2 are both negative.

4) λ_1 or λ_2 is zero.

These possible combinations are schematically shown in Fig. 1. Each one of these combinations describes a different feature of the flow in the crossflow direction η. Referring to the diagrams of Fig. 1, the following descriptions are made.

Case 1

Here, one eigenvalue is positive and one negative. This implies an *elliptic-type* crossflow because the characteristic signals are brought into point *P* from both the positive and negative direction of η.

Case 2

Here, both the characteristics are positive, which means the characteristic signals propagate into point *P* only from below and anything happening above point *P* does not influence that point. This describes a *hyperbolic-type* crossflow point with a positive contravariant velocity *V*.

Case 3

Here, the characteristic signals propagate from above into point *P* and, similar to case 2, this describes a *hyperbolic-type* crossflow with a negative contravariant velocity *V*.

Case 4

Here, one of the eigenvalues is zero and describes a *parabolic-type* crossflow. This will represent the crossflow sonic line.

The transition from an elliptic to a hyperbolic crossflow type takes place through a parabolic point, which is indicated by one of the eigenvalues going to zero. Thus, by monitoring the eigenvalues λ_1 and λ_2, one can precisely model the crossflow plane terms. Depending on whether it is elliptic or hyperbolic, appropriate finite-difference models for the η-derivative term in Eq. (1) are chosen. This will be described later in this paper.

One can readily see from Eq. (7) that one of the eigenvalues goes to zero when $(\rho V)_{\phi_\eta}=0$. From the definition of ρ and *V* from Eq. (2), one can write

$$(\rho V)_{\phi_\eta}=\rho\left\{a_{22}-\frac{V^2}{a^2}\right\} \tag{8}$$

Thus, when $a_{22}=V^2/a^2$ occurs, the method will anticipate a switch in the character of the crossflow and realize the onset of the formation of a supercritical crossflow.

Besides providing valuable information regarding the type of crossflow, the eigenvalues λ_1 and λ_2 of $A^{-1}B$ and, similarly, λ_3 and λ_4 of $A^{-1}C$ can also be used to determine the marching step size Δζ from a given Courant number.

$$\Delta\zeta=\min\left\{\frac{\text{CFL}*\Delta\eta}{(\lambda_{\max})_\eta},\ \frac{\text{CFL}*\Delta\xi}{(\lambda_{\max})_\xi}\right\} \tag{9}$$

The quantities $(\lambda_{\max})_\eta$ and $(\lambda_{\max})_\xi$ define the maximum of (λ_1,λ_2) and (λ_3,λ_4), respectively, and CFL is the user-prescribed Courant number, usually set to values much greater than one for implicit schemes (CFL ~ 5-20).

B. Treatment of $(\rho U/J)_\zeta$ in Eq. (1)

The direction ζ has been identified to be the hyperbolic marching direction satisfying the condition given by Eq. (5). Referring to Fig. 2, this derivative term will be backward differenced as

$$\left(\rho\frac{U}{J}\right)_\zeta=\frac{(a_1-\theta b_1)\left\{\left(\rho\frac{U}{J}\right)_{i+1}-\left(\rho\frac{U}{J}\right)_i\right\}-\theta b_1\left\{\left(\rho\frac{U}{J}\right)_i-\left(\rho\frac{U}{J}\right)_{i-1}\right\}}{a_1\Delta\zeta_1-\theta b_1(\Delta\zeta_1+\Delta\zeta_2)} \tag{10}$$

where

$a_1=(\Delta\zeta_1+\Delta\zeta_2)^2$
$b_1=(\Delta\zeta_1)^2$
$\theta=0$ first-order accurate
$=1$ second-order accurate

Given the velocity potential ϕ information at all previous planes *i*, *i*−1, *i*−2,..., the problem is to compute ϕ at the current plane *i*+1. Equation (10) involves both the density and contravariant velocity at the (*i*+1) plane, and both are functions of ϕ [Eq. (1)]. In order to write Eq. (10) in terms of ϕ will require only a local linearization procedure. This is done as follows:

$$(\rho U)_{i+1}\doteq(\rho U)_i+[(\rho U)_\phi]_i\Delta\phi+\dots \tag{11}$$

where

$$(\rho U)_\phi=\rho_\phi U+\rho U_\phi \quad\text{and}\quad \Delta\phi=\phi_{i+1}-\phi_i$$

Substituting for ρ_ϕ and U_ϕ into Eq. (11), and grouping various term,

$$(\rho U)_{i+1}\doteq\rho_i\left[\left(a_{11}-\frac{U^2}{a^2}\right)_i\frac{\partial(\Delta\phi)}{\partial\zeta}+\left(a_{12}-\frac{UV}{a^2}\right)_i\frac{\partial(\Delta\phi)}{\partial\eta}+\left(a_{13}-\frac{UW}{a^2}\right)_i\frac{\partial(\Delta\phi)}{\partial\xi}+U_i\right] \tag{12}$$

The above locally linearized equation involves only Δϕ as the unknown to be solved for. To maintain the conservative differencing, both $(\rho U)_{i+1}$ and $(\rho U)_i$ appearing in the first term of Eq. (10) will be linearized. That is, $(\rho U)_i$ will be linearized about (*i*−1) plane values. The upwind differencing of the ζ-derivative term as shown in Eq. (10) will produce a truncation term whose leading term is $\{1-(a^2 a_{11}/U^2)\}$ $U^2\phi_{\zeta\zeta\zeta}\Delta\zeta$. This will always represent a positive artificial viscosity as long as the marching condition dictated by the characteristic theory, Eq. (5), is satisfied.

C. Treatment of the Crossflow Term $(\rho V/J)_\eta$ in Eq. (1)

Similar to the treatment of the (ρU) term, the $(\rho V)_{i+1}$ will also be linearized as

$$(\rho V)_{i+1}=(\rho V)_i+[(\rho V)_\phi]_i\Delta\phi+\ldots$$
$$=\rho_i\left[\left(a_{21}-\frac{UV}{a^2}\right)_i\frac{\partial\Delta\phi}{\partial\zeta}+\left(a_{22}-\frac{V^2}{a^2}\right)_i\frac{\partial\Delta\phi}{\partial\eta}\right.$$
$$\left.+\left(a_{23}-\frac{VW}{a^2}\right)_i\frac{\partial\Delta\phi}{\partial\xi}+V_i\right]\tag{13}$$

The above linearized expression for $(\rho V)_{i+1}$ will be plugged inside the η-derivative term of Eq. (1). It involves only $\Delta\phi$ as the unknown variable. The finite-difference model for the $[\rho(V/J)]_\eta$ term will be dictated by the theory of characteristic signal propagation as described in Sec. II.A. When the eigenvalues of $A^{-1}B$ represent case 1 in Fig. 1 (one positive and one negative eigenvalue representing an elliptic type), then all of the terms in $[\rho(V/J)]_\eta$ will be central-differenced. For this case, $[a_{22}-(V^2/a^2)]$ is positive, and central differencing of the $[\rho(V/J)]_\eta$ term along with the backward differencing of the $[\rho(U/J)]_\zeta$ term as in Eq. (10) will preserve the diagonal dominance. For cases 2 and 3 of Fig. 1, the crossflow behaves like a hyperbolic type, and $[a_{22}-(V^2/a^2)]$ is negative. Then, central differencing of the terms in Eq. (13) is inappropriate, as it will destroy the diagonal dominance, and, in addition, will not provide the necessary artificial viscosity to avoid the formation of expansion shocks. Thus, when λ_1 and λ_2 are both positive or both negative (hyperbolic type), the terms in $[\rho(V/J)]_\eta$ should be upwind differenced depending on the direction of V. However, such an upwind differencing in the η direction will not give rise to a tridiagonal system and, in general, the overall system will be pentadiagonal in nature. In order to preserve the tridiagonal nature of the implicit scheme, rather than upwind differencing the ϕ derivatives, the density biasing concept[7,12] is implemented when the crossflow is hyperbolic.

The procedure is as follows:

$$\left(\rho\frac{V}{J}\right)_\eta\doteq\frac{\partial}{\partial\eta}\left\{\frac{\bar\rho}{J}(a_{21}\phi_\zeta+a_{22}\phi_\eta+a_{23}\phi_\xi)\right\}\tag{14}$$

Here, the density ρ has been replaced by $\bar\rho$ defined to be (referring to Fig. 2)

$$\bar\rho_{i+1,j+\frac{1}{2},k}=(1-\nu_{i,j+\frac{1}{2},k})\rho^*_{j+\frac{1}{2},k}$$
$$+\tfrac{1}{2}\nu_{i,j+\frac{1}{2},k}(\rho^*_{j+2m,k}+\rho^*_{j-1+2m,k})\tag{15}$$

where $m=0$ when $V_{i,j+\frac{1}{2},k}>0$, $=+1$ when $V_{i,j+\frac{1}{2},k}<0$. The artificial viscosity coefficient $\nu_{i,j+\frac{1}{2},k}$ is computed as follows:

$$\nu_{i,j+\frac{1}{2},k}=\mu\left(1-\frac{a_{22}a^2}{V^2}\right)_{i,j+\frac{1}{2},k}\tag{16}$$

where a is the local speed of sound and

$$\mu=0\ \text{for}\ \left(a_{22}-\frac{V^2}{a^2}\right)_{i,j+\frac{1}{2},k}>0\ \text{(elliptic crossflow)}$$
$$=1\ \text{for}\ \left(a_{22}-\frac{V^2}{a^2}\right)_{i,j+\frac{1}{2},k}<0\ \text{(hyperbolic crossflow)}$$

Thus, the density biasing is switched off smoothly when the eigenvalues λ_1 and λ_2 exhibit an elliptic crossflow. All the ϕ-derivative terms are central differenced in Eq. (14). Treatment of the density as represented by Eqs. (15) and (16) would always produce a positive artificial viscosity when the crossflow is hyperbolic. The local total velocity is always assumed to be greater than the speed of sound, otherwise the marching procedure would fail.

In Eq. (15), the evaluation of ρ^* depends on whether the flow is conical or nonconical. For conical flows, all ρ^* quantities are evaluated at the ith plane. For nonconical flows, at each nonconical marching plane, initially ρ^* is set to be the value at the ith plane and then subsequently iterated to convergence by setting ρ^* to the previous iterated value of ρ at the current $i+1$ plane.

A similar density biasing procedure is implemented for the $[\rho(W/J)]_\xi$ term in Eq. (1).

Activating the density biasing based on the eigenvalue structure of $A^{-1}B$ and $A^{-1}C$ has proven to be very efficient in predicting sharp shock profiles. The same concept can also be employed for transonic applications.

D. Implicit Factorization Algorithm

Combining the various terms of Eq. (1) as represented by Eqs. (10, 14, and 15) together with the terms arising from $[\rho(W/J)]_\xi$ will result in a fully implicit model. This is solved using an approximate factorization implicit scheme. After some rearrangement of the terms, the factored implicit scheme becomes

$$\left[1+\frac{A_3}{\beta\Delta\zeta}\frac{\partial}{\partial\xi}+\frac{1}{\beta}\frac{\partial}{\partial\xi}\left(\frac{\bar\rho}{J}\frac{a_{31}}{\Delta\zeta}\right)+\frac{1}{\beta}\frac{\partial}{\partial\xi}\frac{\bar\rho a_{33}}{J}\frac{\partial}{\partial\xi}\right]$$
$$\times\left[1+\frac{A_2}{\beta\Delta\zeta}\frac{\partial}{\partial\eta}+\frac{1}{\beta}\frac{\partial}{\partial\eta}\left(\frac{\bar\rho a_{21}}{J\Delta\zeta}\right)+\frac{1}{\beta}\frac{\partial}{\partial\eta}\frac{\bar\rho a_{22}}{J}\frac{\partial}{\partial\eta}\right]\Delta\phi=R\tag{17}$$

which has the form

$$L_\xi L_\eta(\Delta\phi)=R\tag{18}$$

and is implemented as

$$L_\xi(\Delta\phi)^*=R,\quad L_\eta(\Delta\phi)=(\Delta\phi)^*,\quad \phi=\phi_i+\Delta\phi\tag{19}$$

The various quantities appearing in Eq. (17) are given by

$$\beta=\frac{A_1}{(\Delta\zeta)^2},\quad A_1=\frac{\rho_i}{J}\left(a_{11}-\frac{U^2}{a^2}\right)_i,\quad A_2=\frac{\rho_i}{J}\left(a_{12}-\frac{UV}{a^2}\right)_i,$$
$$A_3=\frac{\rho_i}{J}\left(a_{13}-\frac{UW}{a^2}\right)_i\tag{20}$$

and the right-hand-side term R consists of various known quantities. The algorithm Eq. (19) requires only scalar tridiagonal inversions.

III. Grid System

The transformation of the physical space (x,y,z) to a body-fitted computational space (ζ,η,ξ) is performed numerically by using the elliptic grid generation technique of Ref. 11. The body geometry at every marching plane is prescribed along with a suitable outer boundary where freestream conditions are imposed. Since the equation is cast in a general coordinate system, the marching plane (constant ζ) can either be a constant x plane or a spherical (constant r) plane as long as the marching criterion [Eq. (5)] is satisfied. Given the geometry shape and the prescribed outer boundary, the following set of elliptic equations are solved to generate the interior grid.

$$\xi_{yy}+\xi_{zz}=P(\xi,\eta),\qquad \eta_{yy}+\eta_{zz}=Q(\xi,\eta)\tag{21}$$

The forcing terms P and Q are properly chosen to achieve two main desirable features: 1) to cluster grid points to a boundary, and 2) to force grid lines to intersect the boundary in a nearly orthogonal fashion.

Once the grid is generated, all the metric terms a_{ij} in Eq. (2) and the Jacobian J in Eq. (3) are computed by numerical differentiation. To subtract out any numerical truncation error in the freestream due to incomplete metric cancellation,[13] it is essential to add the term (especially for a high stretched nonorthogonal grid)

$$\frac{\partial}{\partial \zeta}\left(\frac{\rho_\infty U_\infty}{J}\right)+\frac{\partial}{\partial \eta}\left(\frac{\rho_\infty V_\infty}{J}\right)+\frac{\partial}{\partial \xi}\left(\frac{\rho_\infty W_\infty}{J}\right) \tag{22}$$

to the right-hand side of the finite-differenced model of Eq. (1). To be consistent with the implicit operator, Eq. (18), the linearization procedures given by Eqs. (12) and (14) are also applied in evaluating Eq. (22).

IV. Results

A series of calculations were performed for conical and nonconical geometries at various Mach numbers ($M_\infty \sim 2$-6) and angles of attack ($\alpha \sim 0$-10 deg) to validate the full-potential characteristic switch methodology and assess the feasibility of using numerical grid solvers for complex configurations. The results from this study are compared with experimental data and Euler simulation.

The generality of the formulation allows one to choose any ζ as the marching direction, provided the condition given by Eq. (5) is satisfied. Thus, depending on the geometry definition and the flowfield character, one could choose either a constant x-plane marching or constant r-plane spherical marching.

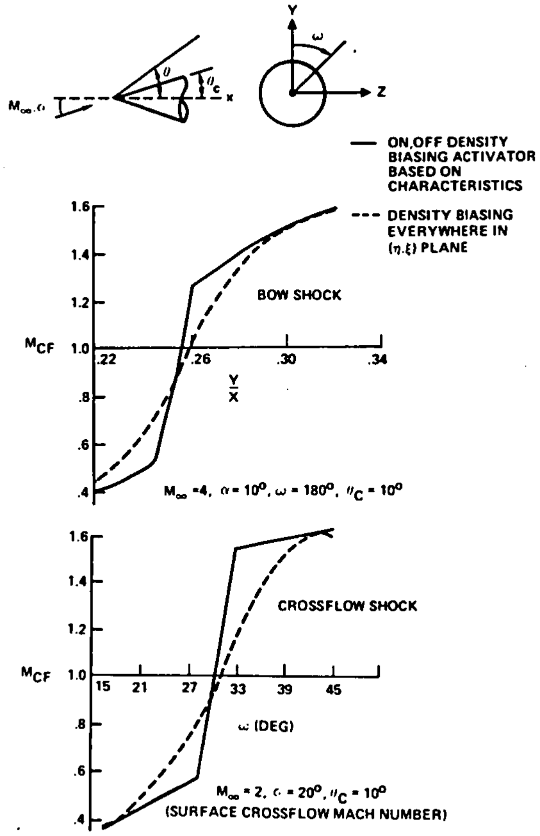

Fig. 3 Effect of density biasing activator on the crossflow Mach number distribution in the shock region.

The effect of on/off density biasing based on characteristic signals in the crossflow plane (η,ξ), described by Eq. (16), is demonstrated in terms of the crossflow Mach number (M_{CF}) distribution in the shock region in Fig. 3. When density

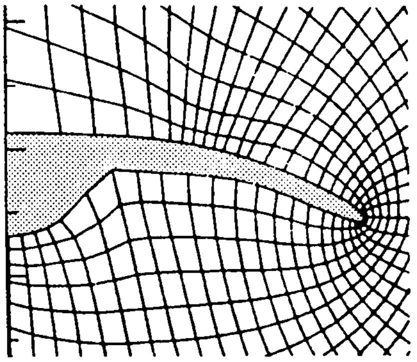

Fig. 4 Grid arrangement in the marching plane for a conically cambered wing-body combination.

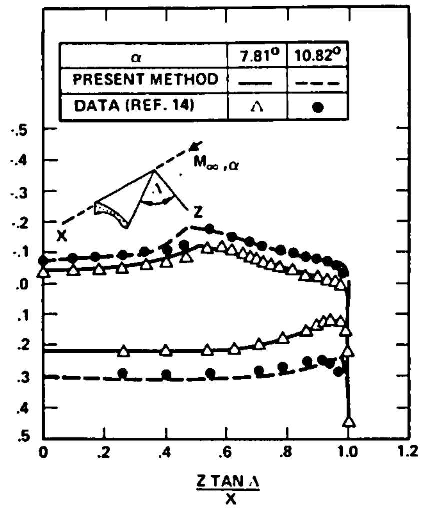

Fig. 5 Surface pressure distribution on a conically cambered wing-body combination, $M_\infty = 2$.

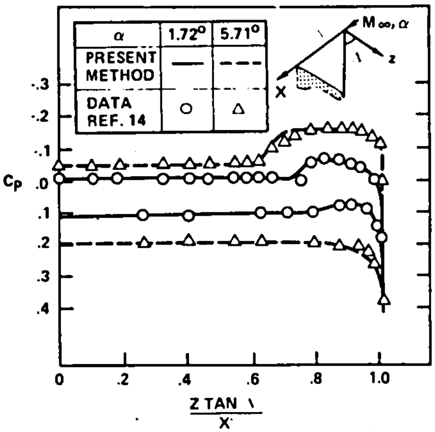

Fig. 6 Surface pressure distribution on a flat conical wing-body combination, $M_\infty = 2$.

biasing is applied everywhere,[7] including elliptic crossflow points, it introduces unnecessary artificial viscosity and tends to smear the discontinuities like shocks in the flowfield. This is seen by the dashed-line crossflow Mach number distribution across the bow shock and across the embedded shock on a cone surface in Fig. 3. When the density biasing is switched off at crossflow elliptic points, the shocks appear as a sharper discontinuity (usually within two mesh intervals), as shown by the solid line distribution in Fig. 3. All the calculations to be presented here were achieved using the second-order accurate implicit scheme [$\theta = 1$ in Eq. (10)], with on/off density biasing activator μ in Eq. (16).

Figure 4 shows the grid arrangement in the marching plane for a conically cambered wing-body combination. The elliptic grid solver with orthogonality constraints near the surface required 40-60 iterations to converge to within 10^{-8} error in the residual. Figure 5 shows the pressure distribution at $M_\infty = 2$ and angles of attack of 7.81 and 10.82 deg. The leading-edge sweep is moderate (57 deg), and spherical plane marching is implemented (instead of x-plane marching) to avoid low supersonic Mach number components along the x direction near the leading edge. The results are compared with experimental data given in Ref. 14. The comparison is excellent. The marching step size $\Delta\zeta$ is chosen by monitoring the eigenvalues and setting the Courant number to about 20. The numerical formulation, being a conservative form, predicts a stronger crossflow recompression on the leeward side than those seen in experiments. On a 20×49 (η, ξ) grid, the method requires about 1 min of CDC 7600 time. The conical flowfield is assumed to have converged when the change in root-mean-square density between two successive marching planes is reduced to less than 10^{-5}.

Figure 6 shows the surface pressure distribution on a flat conical wing-body (that is not designed to weaken the crossflow shock formation) at two different angles of attack (1.72 and 5.71 deg) and a Mach number of 2. The experimental data and the numerical prediction are in excellent agreement and clearly indicate the presence of an embedded crossflow shock.

Even though the full-potential theory is restricted by the isentropic assumption, one will be surprised to find that the

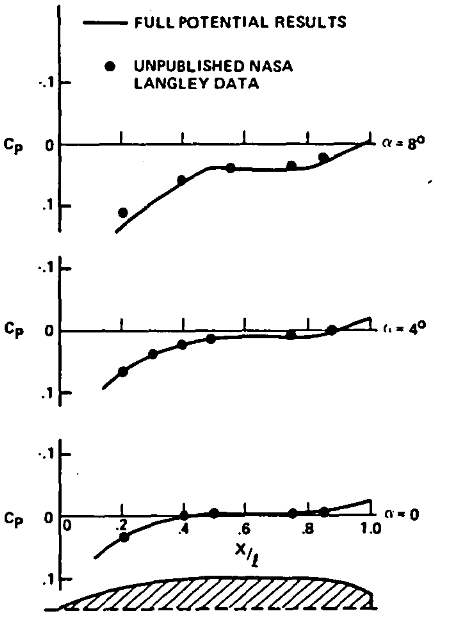

Fig. 7 Pressure distribution on Sears-Haack body at $M_\infty = 6$, windward plane of symmetry.

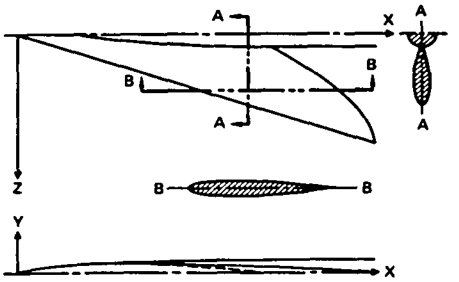

Fig. 8 Top and side views of a typical arrow wing-body configuration.

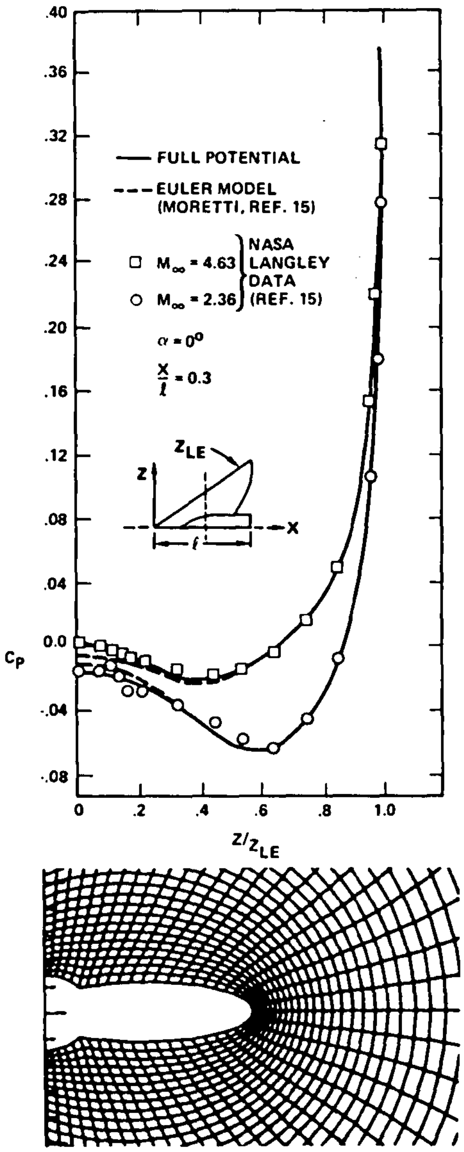

Fig. 9a Grid arrangement and surface pressure distribution for a symmetric arrow wing at $x/\ell = 0.3$.

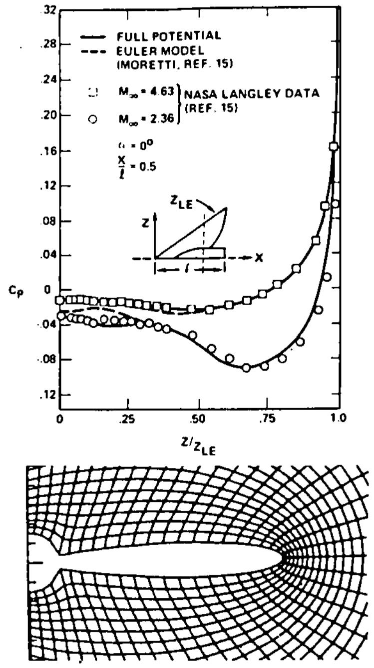

Fig. 9b Arrow wing pressure distribution at $x/\ell = 0.5$.

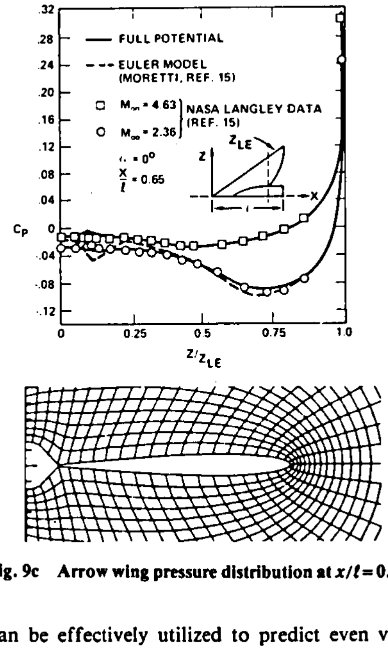

Fig. 9c Arrow wing pressure distribution at $x/\ell = 0.65$.

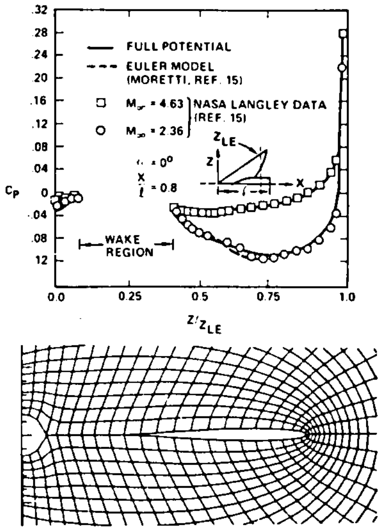

Fig. 9d Arrow wing pressure distribution at $x/\ell = 0.8$.

theory can be effectively utilized to predict even very high Mach number flows as long as $M\delta$ is less than or of the order of 1 ($M\delta \leq 1$). This is demonstrated in Fig. 7, which shows the results for a Sears-Haack body at $M_\infty = 6$ and different angles of attack (0, 4, and 8 deg). The numerical prediction is compared with unpublished NASA-Langley data, and the agreement is excellent. Constant x-plane marching is implemented for this configuration.

Figure 8 shows a schematic of a symmetric arrow wing-body configuration. The actual geometry shape is prescribed analytically as detailed in Ref. 15. A series of computer runs were made for this configuration at different Mach numbers and angles of attack and some results are presented here. First, an initial data plane near the nose region of the configuration is established by assuming a conical nose shape. The nonconical marching is then initiated. At each nonconical marching plane, the density is iterated to convergence [ρ^* in Eq. (15) usually takes 2-3 cycles to converge to 10^{-5} error tolerance] before proceeding to the next marching plane. The grid at each marching plane is generated using the elliptic grid solver. Figures 9a-d show a series of results at x/ℓ of 0.3, 0.5, 0.65, and 0.8, respectively. The full-potential results are compared with the experimental data and Euler simulation in Ref. 15. Figure 9a, which shows results for an x/ℓ of 0.3, clearly demonstrates the accuracy of the full-potential simulation. It is surprising to see that the present full-potential method compares with the experimental data even better than the Euler calculation, even at a high Mach number of 4.63. Similar excellent full-potential results are shown in Fig. 9b for an x/ℓ of 0.5 and compared with data from Ref. 15. The striking full-potential results are shown in Fig. 9c, where the unphysical oscillations experienced by the Euler simulation at $M_\infty = 2.36$ near the wing-body junction area are not seen in the present method, and comparison with experimental data is more dramatic. Figure 9d shows the pressure distribution at an x/ℓ of 0.8, where the wing is separated from the body. The wake is simulated by assuming a planar shape, and imposing pressure equality (in the present method, it will be density equality due to full-potential formulation) across the cut. Again, the full-potential results are in good agreement with the Euler solution and experimental data.

Figure 10 shows an angle-of-attack case, $M_\infty = 4.63$, $\alpha = 3$ deg for the same symmetric arrow wing-body configuration. The results are compared with the data of Ref. 15 at x/ℓ of 0.65, and the agreement is good even near the wing-body function region.

A typical arrow wing-body calculation using a 20×49 grid in the (η,ξ) plane and a marching step size Courant number of 3-5 [for a given Courant number, the predicted marching step size from Eq. (9) will decrease with decreasing freestream Mach number], required approximately 2-3 min of CPU time for the entire calculation. This includes the numerical grid generation at each plane and the conical initial data plane and represents an enormous savings in computer execution cost over other nonlinear methods, especially Euler solvers.

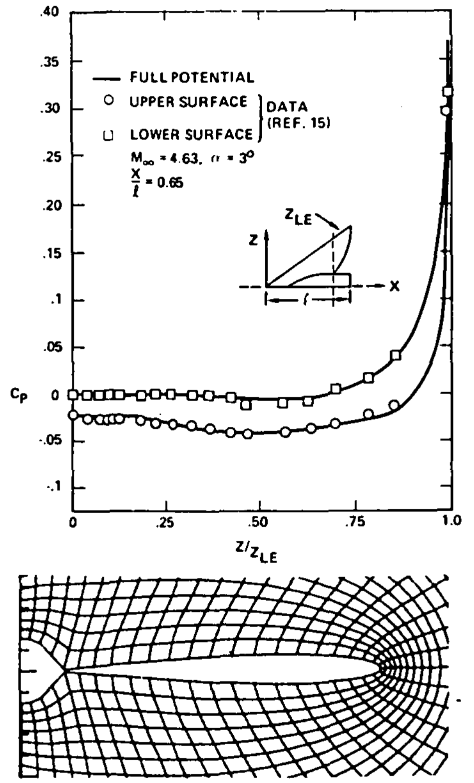

Fig. 10 Angle-of-attack solution for the arrow wing at $x/\ell = 0.65$.

V. Conclusions

A nonlinear full-potential aerodynamic prediction capability based on a sound mathematical theory of characteristic signal propagation has been developed. The method uses a general body-fitted coordinate system and numerical mapping techniques. The on/off density biasing activator in the crossflow plane has proved to be very effective in capturing sharp shock profiles. Results for conical and nonconical flows at various Mach numbers and angles of attack are shown to be in excellent agreement with experimental data and Euler results. The enormous savings in computational cost exhibited by the present approach makes it a very promising substitute for the less accurate linearized panel methods and expensive Euler solvers, for use as a preliminary design tool. Future work will involve automatic grid generation for wing-body-nacelle-canard configurations and better wake treatment.

Appendix—Derivation of the Marching Condition [Eq. (5)] for a Cartesian System

The Cartesian system analog of Eq. (4) is given by

$$Af_x + Bf_y + Cf_z = 0 \tag{A1}$$

where

$$A = \begin{bmatrix} (\rho u)_u & (\rho u)_v & (\rho u)_w \\ 0 & 1 & 0 \\ 0 & 0 & 1 \end{bmatrix}$$

$$B = \begin{bmatrix} (\rho v)_u & (\rho v)_v & (\rho v)_w \\ -1 & 0 & 0 \\ 0 & 0 & 0 \end{bmatrix}$$

$$C = \begin{bmatrix} (\rho w)_u & (\rho w)_v & (\rho w)_w \\ 0 & 0 & 0 \\ -1 & 0 & 0 \end{bmatrix}$$

$$f = \begin{bmatrix} u \\ v \\ w \end{bmatrix}$$

Equation (A1) is hyperbolic with respect to the x direction if 1) A^{-1} exist, and 2) A^{-1} $(\alpha B + \beta C)$ must have real eigenvalues for all α and β satisfying $\alpha^2 + \beta^2 = 1$.

Since A^{-1} is assumed to exist, the eigenvalues of A^{-1} $(\alpha B + \beta C)$ can be obtained by setting the following determinant to zero.

$$|\alpha B + \beta C - \lambda A| = 0 \tag{A2}$$

Substituting for A, B, and C from Eq. (A1) into Eq. (A2), the roots of the equation are obtained.

$$\lambda_{1,2} = \Bigg[-\frac{u}{a^2}(v\alpha + w\beta)$$

$$\pm \sqrt{\frac{u^2}{a^4}(v\alpha + w\beta)^2 - \left(1 - \frac{u^2}{a^2}\right)\left\{1 - \frac{(v\alpha + w\beta)^2}{a^2}\right\}}\Bigg] \Bigg/ \left(1 - \frac{u^2}{a^2}\right) \tag{A3}$$

Equation (A3) will have real values as long as the square root term is real. This implies the quantity inside the square root must be positive. Simplifying the quantity inside the square root, the condition becomes

$$\frac{u^2 + (v\alpha + w\beta)^2}{a^2} - 1 > 0 \tag{A4}$$

Let

$$\left.\begin{array}{l} \alpha = \cos\theta \\ \beta = \sin\theta \end{array}\right\} \Rightarrow \alpha^2 + \beta^2 = 1$$

$$v = \bar{q}\cos\bar{\theta}, \qquad w = \bar{q}\sin\bar{\theta}$$

where

$$\bar{q} = \sqrt{v^2 + w^2}, \qquad \tan\bar{\theta} = w/v$$

Substituting these into Eq. (A4) and simplifying results in

$$\frac{u^2 + \bar{q}^2\cos^2(\bar{\theta} - \theta)}{a^2} - 1 > 0 \tag{A5}$$

Since this condition must hold for all combinations of θ and $\bar{\theta}$, Eq. (A5) implies (for $\bar{\theta} - \theta = \pi/2$)

$$\boxed{\frac{u^2}{a^2} - 1 > 0} \quad \text{for } x \text{ to be the marching direction} \tag{A6}$$

Equation (A6) is a special case of Eq. (5) in Sec. II.

Acknowledgment

This work was supported in full by NASA-Langley Research Center under Contract NAS1-15820.

References

[1] Marconi, F., Salas, M., and Yeager, L., "Development of a Computer Code for Calculating the Steady Super/Hypersonic Inviscid Flow Around Real Configurations, Vol. I—Computational Techniques," NASA CR 2675, April 1976.

[2] Kutler, P., "Computation of Three-Dimensional, Inviscid Supersonic Flows," in *Lecture Notes in Physics 41*, Springer-Verlag, New York, 1975, pp. 287-374.

[3] Siclari, M. J., "Investigation of Cross Flow Shocks on Delta Wings in Supersonic Flow," *AIAA Journal*, Vol. 18, Jan. 1980, p. 85.

[4] Grossman, B., "Numerical Procedure for the Computation of Irrotational Conical Flows," *AIAA Journal*, Vol. 17, Aug. 1979, pp. 828-837.

[5] Grossman, B. and Siclari, M. J., "The Nonlinear Supersonic Potential Flow over Delta Wings," AIAA Paper 80-0269, Pasadena, Calif., Jan. 1980.

[6] Siclari, M. J., "Computation of Nonlinear Supersonic Potential Flow over Three-Dimensional Surfaces," AIAA Paper 82-0167, presented at the AIAA 20th Aerospace Sciences Meeting, Orlando, Fla., Jan. 1982.

[7] Shankar, V., "A Conservative Full Potential, Implicit, Marching Scheme for Supersonic Flows," *AIAA Journal*, Vol. 20, Nov. 1982, pp. 1508-1514.

[8] Carmichael, R. L. and Erickson, L. L., "Pan Air—A Higher Order Panel Method for Predicting Subsonic or Supersonic Linear Potential Flows about Arbitrary Configurations," AIAA Paper 81-1255.

[9] Jameson, A., "Transonic Potential Flow Calculations using Conservation Form," *AIAA Second Computational Fluid Dynamics Conference Proceedings*, 1975, pp. 148-155.

[10] Lax, P. D., "Weak Solutions of Nonlinear Hyperbolic Equations and Their Numerical Computation," *Communications on Pure and Applied Mathematics*, Vol. 7, No. 1, Jan. 1954, pp. 159-193.

[11] Steger, J. L. and Sorenson, R. L., "Automatic Mesh-Point Clustering Near a Boundary in Grid Generation with Elliptic Partial Differential Equations," *Journal of Computational Physics*, Vol. 33, No. 3, Dec. 1979, p. 405.

[12] Holst, T. L., "Fast, Conservative Algorithm for Solving the Transonic Full Potential Equation," *AIAA Journal*, Vol. 18, Dec. 1980, pp. 1431-1439.

[13] Steger, J. L. and Caradona, F. X., "A Conservative Implicit Finite Difference Algorithm for the Unsteady Transonic Full Potential Equation," FSI Rept. 79-04, Dec. 1979.

[14] Miller, D. S., Landrum, E. J., Townsend, J. C., and Mason, W. H., "Pressure and Force Data for a Flat Wing and a Warped Conical Wing Having a Shockless Recompression at Mach 1.62," NASA TP 1759, April 1981.

[15] Townsend, J. C., "Pressure Data for Four Analytically Defined Arrow Wings in Supersonic Flow," NASA TM 81835, Sept. 1980.

Treatment of Supersonic Flows with Embedded Subsonic Regions

V. Shankar, K.-Y. Szema, S. Osher

Reprinted from

AIAA Journal Volume 23, Number 1, January 1985, Page 41

AMERICAN INSTITUTE OF AERONAUTICS AND ASTRONAUTICS • 1633 BROADWAY • NEW YORK, N.Y. 10019

VOL. 23, NO. 1, JANUARY 1985 AIAA JOURNAL 41

Treatment of Supersonic Flows with Embedded Subsonic Regions

Vijaya Shankar* and Kuo-Yen Szema†
Rockwell International Science Center, Thousand Oaks, California

and

Stanley Osher‡
University of California, Los Angeles, California

A nonlinear method based on the full potential equation in conservation form, cast in an arbitrary coordinate system, has been developed to treat predominantly supersonic flows with embedded subsonic regions. This type of flow field occurs frequently near the fuselage/canopy junction area and wing leading-edge regions for a moderately swept fighter configuration. The method uses the theory of characteristics to accurately monitor the type-dependent flowfield. A conservative switching scheme is developed to handle the transition from the supersonic marching algorithm to a subsonic relaxation procedure, and vice versa. An implicit approximate factorization scheme is employed to solve the finite differenced equation. Results are shown for a few configurations, including a wing/body/wake realistic fighter model having embedded subsonic regions.

I. Introduction

NONLINEAR aerodynamic prediction methods based on the full potential equation are used regularly for treating transonic[1,2] and supersonic[3-5] flows over realistic wing/body configurations. The transonic algorithms[1,2] are designed to treat predominantly subsonic flows with pockets of supersonic regions bounded by sonic lines and shocks. The supersonic methods[3-5] are based on a marching concept and require the flow to remain supersonic in a given marching direction. Once the marching direction velocity becomes subsonic, the domain of dependence changes and a pure marching scheme[3-5] will violate the rules of characteristic signal propagation. The possibility of a marching velocity becoming subsonic in a supersonic flow is great, especially for low supersonic freestream Mach number flows ($M_\infty = 1.3 \sim 1.7$) over moderately swept fighter-like configurations (sweep angle $\Lambda = 45 \sim 50$ deg) and over forebody shapes having a sizeable fuselage/canopy junction region. *There is a strong need to construct a supersonic marching computer program that has built-in logics to detect and treat the embedded subsonic regions.*

The method of Ref. 5 is based on the characteristic theory of signal propagation and uses a generalized, nonorthogonal, curvilinear coordinate system. Compared to other nonlinear supersonic methods,[3] the method of Ref. 5 has no restrictions (limitations of the full potential theory hold) on its applicability to complex geometries and intricate shocked flowfields. It is a conservative formulation and uses numerical mapping techniques to generate the body-fitted system. The purpose of this paper is to describe an extension to the methodology of Ref. 5 to include the treatment of embedded subsonic regions in a supersonic flow.

The paper describes the characteristic theory involved in determining the condition for a marching direction to exist. Once that condition is violated, the marching scheme is transitioned to a relaxation scheme through a conservative switching operator. For marching condition violation, the total velocity q does not have to be subsonic. Even for a supersonic total velocity q, if the component in the marching direction is subsonic, a relaxation scheme is required. In order to properly produce the necessary artificial viscosity through density biasing, the paper defines two situations: 1) the total velocity q is supersonic, but the marching direction component is subsonic [defined as marching subsonic region (MSR)]; and 2) the total velocity q is subsonic [termed as total subsonic region (TSR)].

Results are presented for a few configurations that exhibit either the MSR or both the MSR and TSR flowfield. The paper also presents results from a wake model applied to a realistic wing/body fighter configuration.

The Appendix describes a flux biasing concept that will supersede the density biasing procedures currently in use.

The methodology of this paper is not restricted to the full potential equation alone. Currently, similar marching/relaxation methods are under development at Rockwell for application in parabolized Navier-Stokes (PNS) codes to treat the embedded subsonic regions or streamwise separated flows without having to use a time-dependent Navier-Stokes program.

II. Equation and Characteristic Theory

The conservative full potential equation cast in an arbitrary coordinate system defined by $\zeta = \zeta(x,y,z)$, $\eta = \eta(x,y,z)$, and $\xi = \xi(x,y,z)$, takes the form

$$\left(\rho \frac{U}{J}\right)_\zeta + \left(\rho \frac{V}{J}\right)_\eta + \left(\rho \frac{W}{J}\right)_\xi = 0 \tag{1}$$

where U, V, and W are the contravariant velocity components. Introducing the following notation for convenience:

$$U = U_1, \quad V = U_2, \quad W = U_3$$
$$x = x_1, \quad y = x_2, \quad z = x_3$$
$$\zeta = X_1, \quad \eta = X_2, \quad \xi = X_3$$

Received June 30, 1983; presented as Paper 83-1887 at the AIAA Computational Fluid Dynamics Meeting, Danvers, Mass., July 13-15, 1983; revision received March 19, 1984.

*Manager, Computational Fluid Dynamics Group. Associate Fellow AIAA.

†Member, Technical Staff. Member AIAA.

‡Professor, Department of Mathematics. Member AIAA.

the contravariant velocities and density are given by

$$U_i = \sum_{j=1}^{3} a_{ij} \phi_{X_j} \qquad i = 1, 2, 3$$

$$a_{ij} = \sum_{k=1}^{3} \frac{\partial X_i}{\partial x_k} \frac{\partial X_j}{\partial x_k} \qquad \begin{matrix} i = 1, 2, 3 \\ j = 1, 2, 3 \end{matrix} \quad \text{(transformation metrics)}$$

$$\rho = \left[1 - \left(\frac{\gamma - 1}{2} \right) M_\infty^2 \{ U\phi_\zeta + V\phi_\eta + W\phi_\xi - 1 \} \right]^{1/(\gamma-1)}$$

$$a = \text{speed of sound} = \sqrt{\rho^{(\gamma-1)}/M_\infty^2} \tag{2}$$

The Jacobian of the transformation J is represented by

$$J = \frac{\partial(\zeta, \eta, \xi)}{\partial(x, y, z)} = \begin{bmatrix} \zeta_x & \zeta_y & \zeta_z \\ \eta_x & \eta_y & \eta_z \\ \xi_x & \xi_y & \xi_z \end{bmatrix} \tag{3}$$

Equation (1) is in terms of a general coordinate system (ζ, η, ξ) and can accommodate any kind of mapping procedure, either analytical (conformal mapping) or numerical. The nature of Eq. (1) can be analyzed by studying the eigenvalue system of Eq. (1). Combining the irrotationality condition in the (ζ, η) and (ζ, ξ) plane and Eq. (1), one can write the following matrix equation:

$$Af_\zeta + Bf_\eta + Cf_\xi = 0 \tag{4}$$

where

$$A = \begin{bmatrix} \frac{1}{J}(\rho U)_{\phi_\zeta} & \frac{1}{J}(\rho U)_{\phi_\eta} & \frac{1}{J}(\rho U)_{\phi_\xi} \\ 0 & 1 & 0 \\ 0 & 0 & 1 \end{bmatrix}$$

$$B = \begin{bmatrix} \frac{1}{J}(\rho V)_{\phi_\zeta} & \frac{1}{J}(\rho V)_{\phi_\eta} & \frac{1}{J}(\rho V)_{\phi_\xi} \\ -1 & 0 & 0 \\ 0 & 0 & 0 \end{bmatrix}$$

$$C = \begin{bmatrix} \frac{1}{J}(\rho W)_{\phi_\zeta} & \frac{1}{J}(\rho W)_{\phi_\eta} & \frac{1}{J}(\rho W)_{\phi_\xi} \\ 0 & 0 & 0 \\ -1 & 0 & 0 \end{bmatrix}$$

$$f = \begin{bmatrix} \phi_\zeta \\ \phi_\eta \\ \phi_\xi \end{bmatrix}$$

The subscripts in Eq. (4) denote differentiation with respect to that variable.

The matrices A, B, and C appearing in Eq. (4) can now be analyzed to determine the character of that equation. In general, the following is true:

1) Equation (4) is *elliptic in the ζ direction* if the matrix $A^{-1}(\alpha B + \beta C)$ has complex eigenvalues for all combinations of α and β such that $\alpha^2 + \beta^2 = 1$.

2) Equation (4) is *hyperbolic in the ζ direction* if $A^{-1}(\alpha B + \beta C)$ has real eigenvalues for all α and β satisfying $\alpha^2 + \beta^2 = 1$.

The eigenvalue structure of $A^{-1}(\alpha B + \beta C)$ can be obtained by setting the determinant

$$|\alpha B + \beta C - \lambda A| = 0 \qquad \text{(assuming } A^{-1} \text{ exists)} \tag{5}$$

Substituting for A, B, and C from Eq. (4), the eigenvalues of Eq. (5) are given by solving the quadratic

$$\begin{aligned} &-\lambda^2(\rho U)_{\phi_\zeta} + \lambda\left[\alpha(\rho V)_{\phi_\zeta} + B(\rho W)_{\phi_\zeta} + \alpha(\rho U)_{\phi_\eta}\right. \\ &\left.+ \alpha(\rho U)_{\phi_\xi}\right] - \left\{\alpha^2(\rho V)_{\phi_\eta} + \beta^2(\rho W)_{\phi_\xi}\right. \\ &\left.+ \alpha\beta\left[(\rho W)_{\phi_\eta} + (\rho V)_{\phi_\xi}\right]\right\} = 0 \end{aligned} \tag{6}$$

Representing Eq. (6) in the form

$$\bar{A}\lambda^2 + \bar{B}\lambda + \bar{C} = 0 \tag{7}$$

the discriminant $(\bar{B}^2 - 4\bar{A}\bar{C})$ determines the character of Eq. (4):

1) If $(\bar{B}^2 - 4\bar{A}\bar{C})$ remains *positive* for all α and β satisfying $\alpha^2 + \beta^2 = 1$, then the eigenvalues of Eq. (4) are real and direction ζ is hyperbolic (marching scheme is valid).

2) If $(\bar{B}^2 - 4\bar{A}\bar{C})$ is *negative*, then the eigenvalues of Eq. (4) are complex and direction ζ is elliptic (requires a relaxation method).

To analyze when the eigenvalue solutions of Eq. (6) are real and when complex, the discriminant $(\bar{B}^2 - 4\bar{A}\bar{C})$ is rewritten in the following form using Eq. (2):

$$\begin{aligned} \bar{B}^2 - 4\bar{A}\bar{C} = {} & \alpha^2\left[\left(a_{21} - \frac{UV}{a^2}\right)^2 - \left(a_{11} - \frac{U^2}{a^2}\right)\left(a_{22} - \frac{V^2}{a^2}\right)\right] \\ & + 2\alpha\beta\left[\left(a_{21} - \frac{UV}{a^2}\right)\left(a_{31} - \frac{UW}{a^2}\right) - \left(a_{11} - \frac{U^2}{a^2}\right)\left(a_{23} - \frac{VW}{a^2}\right)\right] \\ & + \beta^2\left[\left(a_{31} - \frac{UW}{a^2}\right)^2 - \left(a_{11} - \frac{U^2}{a^2}\right)\left(a_{33} - \frac{W^2}{a^2}\right)\right] \end{aligned} \tag{8}$$

Using the properties of a positive definite quadratic form and the Schwarz inequality $(a_{ii}a_{jj} > a_{ij}^2)$, Eq. (8) can be shown to have the following results:

1) $(\bar{B}^2 - 4\bar{A}\bar{C})$ is positive if $[a_{11} - (U^2/a^2)]$ is less than zero. Then the ζ direction is hyperbolic (the marching algorithm of Ref. 5 is valid).

2) $(\bar{B}^2 - 4\bar{A}\bar{C})$ is negative if $[a_{11} - (U^2/a^2)]$ is greater than zero. Then the ζ direction is elliptic (requires a relaxation scheme).

Physical Interpretation

The physical interpretation of these results from the characteristic theory is illustrated in Fig. 1. Let q be the total velocity. The projection of q in the direction normal to the ζ = constant surface is given by

$$\vec{q} \cdot \vec{n} = (u\hat{i} + v\hat{j} + w\hat{k}) \frac{(\zeta_x\hat{i} + \zeta_y\hat{j} + \zeta_z\hat{k})}{\zeta_x^2 + \zeta_y^2 + \zeta_z^2} = U/\sqrt{a_{11}} \tag{9}$$

where u, v, and w are the Cartesian velocities and $\vec{n}$ the normal to the ζ = constant plane. Figure 1a shows the case when $U/\sqrt{a_{11}}$ is greater than the speed of sound $\{[a_{11} - (U^2/a^2)] < 0\}$. For this case, the characteristic cone of influence is behind the ζ = constant plane and marching along ζ is valid. Figure 1b illustrates the case for the $q > a$, but for the $U/\sqrt{a_{11}} < a$ situation, $[a_{11} - (U^2/a^2)] > 0$. For this case, a part of the characteristic cone of influence lies forward of the ζ = constant plane and marching along ζ is not possible. This case (Fig. 1b) is termed marching subsonic region (MSR) in this paper. Figure 1c shows the case when $q < a$ and $U/\sqrt{a_{11}} < a$, $[a_{11} - (U^2/a^2)] > 0$. This represents a pure subsonic flow and marching along ζ is not possible. This case is termed total subsonic region (TSR). For cases represented in Figs. 1b and 1c, a relaxation algorithm is required.

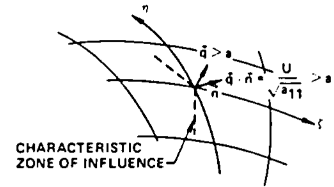

a) PURE SUPERSONIC REGION, $(a_{11} - \frac{U^2}{a^2}) < 0$.
MARCHING ALONG ζ IS VALID.

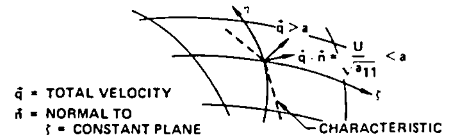

b) MARCHING SUBSONIC REGION (MSR), $(a_{11} - \frac{U^2}{a^2}) > 0, q > a$.
MARCHING ALONG ζ IS NOT VALID.

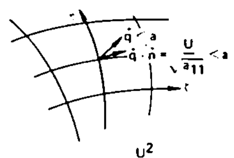

c) TOTAL SUBSONIC REGION (TSR), $(a_{11} - \frac{U^2}{a^2}) > 0$, $q < a$.
COMPLEX CHARACTERISTICS.

Fig. 1 Role of characteristics in defining supersonic region, marching subsonic region (MSR), and total subsonic region (TSR).

III. Numerical Method

Figure 2 shows the schematic of a fuselage/canopy forebody geometry with an embedded MSR and TSR present in a supersonic flow. To solve this problem, the marching scheme of Ref. 5 will be used when $[a_{11} - (U^2/a^2)]$ is negative and a relaxation scheme when $[a_{11} - (U^2/a^2)]$ is positive. First, march from the nose up to the plane denoted by (A-B) in Fig. 2, using the method of Ref. 5. Then, between (A-B) and (C-D), which embed the subsonic bubble (MSR and TSR), use a relaxation scheme and iterate until the subsonic bubble is fully captured. Then, resume the marching scheme from the plane (C-D), downstream of the body.

The purpose of this paper is to present a conservative algorithm that will automatically switch from a pure marching scheme of Ref. 5 to a relaxation method at the onset of an MSR formation and revert to the marching procedure when the flow becomes fully supersonic again. The entire flowfield can be classified into three types with respect to the marching direction ζ:

1) At a grid point, the marching direction is *hyperbolic* and the total velocity q is supersonic, $[a_{11} - (U^2/a^2)] < 0$, $q > a$. This point will use the algorithm of Ref. 5.

2) At a grid point, the marching direction ζ is *elliptic*, $[a_{11} - (U^2/a^2)] > 0$, but the total velocity q is supersonic, $q > a$ (MSR). This point will be treated by a transonic operator with a built-in density biasing based on the magnitude of $[1 - (a^2/q^2)]$.

3) At a grid point, the direction ζ is *elliptic* and the total velocity q is *subsonic*, $q < a$ (TSR). This point will be treated by a subsonic central differenced operator.

Treatment of $(\partial/\partial\zeta)[\rho(U/J)]$ in Eq. (1)

Refer to the computational molecule in Fig. 3.

$$\frac{\partial}{\partial\zeta}\left(\rho\frac{U}{J}\right) = \theta_i \underbrace{\frac{\overleftarrow{\partial}}{\partial\zeta}\left(\rho\frac{U}{J}\right)_{i+1}}_{\text{supersonic}} + (1 - \theta_{i+1}) \underbrace{\frac{\overrightarrow{\partial}}{\partial\zeta}\left(\tilde{\rho}\frac{U}{J}\right)_{i+1}}_{\substack{\text{marching}\\ \text{subsonic}}} \qquad (10)$$

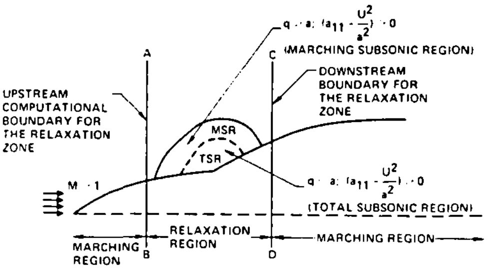

Fig. 2 Embedded subsonic bubble in a supersonic flow.

where

$\overleftarrow{\partial}$ refers to backward differencing

$\overrightarrow{\partial}$ refers to forward differencing

$$\theta_i = 1 \quad \text{if}\left(a_{11} - \frac{U^2}{a^2}\right) < 0$$

$$= 0 \quad \text{if}\left(a_{11} - \frac{U^2}{a^2}\right) > 0$$

In Eq. (10), the first term corresponds to the supersonic marching operator of Ref. 5 and the second term is the subsonic operator.

The backward difference operator in Eq. (10) is represented by

$$\frac{\overleftarrow{\partial}}{\partial\zeta}\left(\rho\frac{U}{J}\right)_{i+1} \doteq \frac{\overleftarrow{\partial}}{\partial\zeta}\rho_i\left[\left(a_{11} - \frac{U^2}{a^2}\right)\frac{\overleftarrow{\partial}}{\partial\zeta}\Delta\phi + \left(a_{12} - \frac{UV}{a^2}\right)\frac{\partial}{\partial\eta}\Delta\phi + \left(a_{13} - \frac{UW}{a^2}\right)\frac{\partial}{\partial\xi}\Delta\phi + U_i\right],$$

$$\Delta\phi = (\phi_{i+1} - \phi_i) \qquad (11)$$

The term $(\partial/\partial\zeta)(\Delta\phi)$ is backward differenced. Reference 5 gives more details on this supersonic marching operator.

The forward difference operator in Eq. (10) is represented by

$$\frac{\overrightarrow{\partial}}{\partial\zeta}\left(\tilde{\rho}\frac{U}{J}\right)_{i+1} \doteq \frac{\overrightarrow{\partial}}{\partial\zeta}\left[\frac{\tilde{\rho}^{n+1}_{i+1}}{J}\left(a_{11}\overleftarrow{\phi}_\zeta + a_{12}\phi_\eta + a_{13}\phi_\xi\right)_{i+1}\right] \qquad (12)$$

where

$$\tilde{\rho}^{n+1}_{i+1} = \rho^n_{i+1} - \nu(\rho^n_{i+1} - \rho^n_i), \qquad \text{for } U > 0$$

$$\nu = \max[0, 1 - (a^2/q^2)] \qquad (13)$$

The superscript $n + 1$ denotes the current relaxation cycle for a subsonic bubble calculation.

Note that in Eq. (12) the term ϕ_ζ is backward differenced such that $(\overrightarrow{\partial}/\partial\zeta)(\tilde{\rho}/J)a_{11}\overleftarrow{\phi}_\zeta$ will provide the central differencing needed for an elliptic (subsonic) point. The density biasing [Eq. (13)] is activated only when the total velocity q is greater than the speed of sound a. This will take place when a grid point is in the region denoted by MSR in Fig. 2. When $q < a$ (the TSR in Fig. 2), the density is not biased and the generation of artificial viscosity is turned off. The ϕ derivatives in Eq. (13) can be rewritten in terms of $\Delta\phi$, just as in Eq. (11).

Equation (10) can also be interpreted as

$$\frac{\partial}{\partial\zeta}\left(\rho\frac{U}{J}\right) = \underbrace{\frac{\overrightarrow{\partial}}{\partial\zeta}\left(\rho\frac{U}{J}\right)_{i+1}}_{\substack{\text{elliptic}\\ \text{operator}}} - \underbrace{\Delta\zeta\frac{\overleftarrow{\partial}}{\partial\zeta}\theta_{i+1}\frac{\overleftarrow{\partial}}{\partial\zeta}\left(\rho\frac{U}{J}\right)_{i+2}}_{\substack{\text{flux biasing to produce}\\ \text{the artificial viscosity}}} \qquad (14)$$

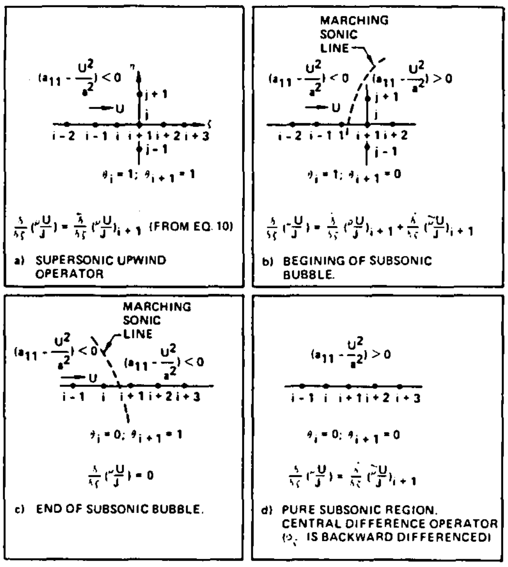

Fig. 3 Conservative type-dependent switching scheme for the treatment of subsonic bubble in a supersonic flow.

Figure 3 illustrates various possibilities that can be handled by Eq (10). It has both the shock point operator and the sonic operator required to treat the type-dependent flow. The only issue that philosophically affects the concept of a conservative scheme is that the definition of ρU for a supersonic operator in Eq. (11) is different from the definition for the subsonic operator of Eq. (12).

The evaluation of the subsonic operator in Eq. (12) requires velocity potential ϕ values at $i+1$ and $i+2$ planes from the previous n relaxation cycle to compute the density. The section on initial and boundary conditions below prescribes a method to start the first relaxation cycle of the subsonic bubble calculation.

Treatment of $(\partial/\partial\eta)[\rho(V/J)]$ in Eq. (1)

Referring to the Fig. 3a molecule,

$$\frac{\partial}{\partial\eta}\left(\rho\frac{V}{J}\right) = \theta_{i+1}\underbrace{\frac{\overleftarrow{\partial}}{\partial\eta}\left(\bar{\rho}\frac{V}{J}\right)_{j+\frac{1}{2}}}_{\text{supersonic}} + (1-\theta_{i+1})\underbrace{\frac{\overleftarrow{\partial}}{\partial\eta}\left(\bar{\bar{\rho}}\frac{V}{J}\right)_{j+\frac{1}{2}}}_{\substack{\text{marching}\\ \text{subsonic}}} \tag{15}$$

where

$$\theta_{i+1} = 1 \qquad \text{if}\left(a_{11} - \frac{U^2}{a^2}\right)_{i+1} < 0 \qquad \text{(supersonic point)}$$

$$\theta_{i+1} = 0 \qquad \text{if}\left(a_{11} - \frac{U^2}{a^2}\right)_{i+1} \geq 0 \qquad \text{(MSR)}$$

When $\theta_{i+1} = 1$, that is, the point is *supersonic* with respect to ζ, only the first term in Eq. (15) is used and the biased density $\bar{\rho}$ is defined by (for $V > 0$),

$$\bar{\rho}_{j+\frac{1}{2}} = \left(1 - \bar{\nu}_{j+\frac{1}{2}}\right)\rho^*_{j+\frac{1}{2}} + \tfrac{1}{2}\bar{\nu}_{j+\frac{1}{2}}\left(\rho^*_j + \rho^*_{j-1}\right) \tag{16}$$

where

$$\bar{\nu} = \max\left(0, 1 - a_{22}\frac{a^2}{V^2}\right)$$

In Eq. (16), the evaluation of ρ^* depends on whether the flow is conical or nonconical. For conical flows, all ρ^* quantities are evaluated at the ith plane. For nonconical flows, at each nonconical marching plane, initially ρ^* is set to be the value at the ith plane and then subsequently iterated to convergence by setting ρ^* to the previous iterated value of ρ at the current $i+1$ plane. Reference 5 provides more details on the density biasing procedure and the implicit treatment of $(\overleftarrow{\partial}/\partial\eta)[\bar{\rho}(V/J)]_{j+\frac{1}{2}}$ in Eq. (15).

When the point is *elliptic*, the density biasing is defined by

$$\bar{\bar{\rho}}^{n+1}_{j+\frac{1}{2}} = \left(1 - \bar{\bar{\nu}}_{j+\frac{1}{2}}\right)\rho^n_{j+\frac{1}{2}} + \tfrac{1}{2}\bar{\bar{\nu}}_{j+\frac{1}{2}}\left(\rho^n_j + \rho^n_{j-1}\right) \tag{17}$$

where $\bar{\bar{\nu}} = \max[0, 1 - (a^2/q^2)]$. As before, the superscript $n+1$ denotes the current relaxation cycle for a subsonic bubble calculation. Note the difference in the definition of $\bar{\nu}$ and $\bar{\bar{\nu}}$. The density biasing in the cross-flow direction η is turned off when the total velocity q is less than the speed of sound a, just as in the marching ζ direction [Eq. (13)]. The implicit treatment of V in the marching subsonic operator of Eq. (15) is the same as that of the supersonic part, explained in Ref. 5.

A similar procedure is implemented for the $[\rho(W/J)]_\xi$ term in Eq. (1).

Implicit Factorization Algorithm

Combining the various terms of Eq. (1) as represented by Eqs. (10)-(17) together with the terms arising from $[\rho(W/J)]_\xi$ will result in a fully implicit model. This is solved using an approximate factorization implicit scheme. After some rearrangement of the terms, the factored implicit scheme becomes

$$\left[1 + \frac{A_3}{\beta\Delta\zeta}\frac{\partial}{\partial\xi} + \frac{1}{\beta}\frac{\partial}{\partial\xi}\left(\frac{\hat{\rho}}{J}\frac{a_{31}}{\Delta\zeta}\right) + \frac{1}{\beta}\frac{\partial}{\partial\xi}\frac{\hat{\rho}a_{33}}{J}\frac{\partial}{\partial\xi}\right]$$
$$\times\left[1 + \frac{A_2}{\beta\Delta\zeta}\frac{\partial}{\partial\eta} + \frac{1}{\beta}\frac{\partial}{\partial\eta}\left(\frac{\hat{\rho}a_{21}}{J\Delta\zeta}\right) + \frac{1}{\beta}\frac{\partial}{\partial\eta}\frac{\hat{\rho}a_{22}}{J}\frac{\partial}{\partial\eta}\right]\Delta\phi = R \tag{18}$$

The density $\hat{\rho}$ appearing in Eq. (18) can be either $\bar{\rho}$ or $\bar{\bar{\rho}}$ depending on the sign of $[a_{11} - (U^2/a^2)]$ as illustrated in Eq. (15).

Equation (18) has the form

$$L_\xi L_\eta(\Delta\phi) = R \tag{19}$$

and it is implemented as follows:

$$L_\xi(\Delta\phi)^* = R \qquad L_\eta(\Delta\phi) = (\Delta\phi)^* \qquad \phi_{i+1} = \phi_i + \Delta\phi \tag{20}$$

The various quantities appearing in Eq. (18) are given by

$$\beta = \frac{1}{\Delta\zeta^2}\left[\theta_i A_1 - (1-\theta_{i+1})\frac{\Delta\zeta}{\Delta\zeta_0}\left(\frac{\tilde{\rho}a_{11}}{J}\right)_{i+1}\right]$$

$$A_1 = \frac{\rho_i}{J_{i+1}}\left(a_{11} - \frac{U^2}{a^2}\right)$$

$$A_2 = \theta_i\left[\frac{\rho_i}{J_{i+1}}\left(a_{12} - \frac{UV}{a^2}\right)\right] - (1-\theta_{i+1})\frac{\Delta\zeta}{\Delta\zeta_0}\left(\frac{\tilde{\rho}a_{12}}{J}\right)_{i+1}$$

$$A_3 = \theta_i\left[\frac{\rho_i}{J_{i+1}}\left(a_{13} - \frac{UW}{a^2}\right)\right] - (1-\theta_{i+1})\frac{\Delta\zeta}{\Delta\zeta_0}\left(\frac{\tilde{\rho}a_{13}}{J}\right)_{i+1}$$

$$\Delta\zeta_0 = \zeta_{i+2} - \zeta_{i+1}, \qquad \Delta\zeta = \zeta_{i+1} - \zeta_i \tag{21}$$

and the right-hand side term R consists of various known quantities.

If the flowfield does not contain an embedded MSR or TSR, the implicit factored algorithm of Eq. (18) performs a pure marching procedure starting from an initial known data plane. In this situation, there is no need to go back to the upstream starting plane and iterate the solution. However, if a subsonic bubble is present (between planes AB and CD in Fig. 2), then the solution procedure of Eq. (18) performs a relaxation method and iterates for the elliptic subsonic bubble to converge [superscript n in Eqs. (12), (13), and (17) refers to the relaxation cycle counter].

Initial and Boundary Conditions

Initial Conditions

For a pure supersonic flow, initial conditions need to be prescribed only at the starting plane. Usually, the starting plane is set close to the apex of the configuration to be solved and the conical solutions are prescribed.

Inside an MSR, as in Fig. 2, when Eq. (12) is applied at an $(i+1)$ grid point, information on ϕ_{i+2} is required to form the density $\tilde{\rho}$ and various derivative terms. For the first relaxation pass, an initial estimate for quantities in the $(i+2)$ plane is prescribed in the following manner:

$$\underbrace{\frac{\vec{\partial}}{\partial\zeta}\left(\rho\frac{U}{J}\right)_{i+1}}_{\text{MSR operator}} = \frac{1}{\Delta\zeta_0}\Bigg\{\underbrace{\left(\rho\frac{U}{J}\right)_{i+2}}_{\substack{\text{needs initial}\\ \text{estimate}}}$$

$$-\left(\frac{\rho}{J}\left(a_{11}\phi_\zeta + a_{12}\phi_\eta + a_{13}\phi_\xi\right)\right)\Bigg\}_{i+1} \tag{22}$$

In Eq. (22), sonic conditions are assumed at $(i+2)$ for the first relaxation pass,

$$\rho_{i+2} = \rho^*, \qquad U_{i+2} = q^*\sqrt{(a_{11})_{i+2}} \tag{23}$$

The sonic values ρ^* and q^* are purely a function of the freestream Mach number M_∞. Also, ρ_{i+1} in Eq. (22) is initialized to be ρ_i.

For the second relaxation cycle and onward $(n \geq 1)$, the conditions from the previous relaxation cycle are used,

$$\left(\rho\frac{U}{J}\right)^{n+1}_{i+2} \doteq \left(\rho\frac{U}{J}\right)^{n}_{i+2}, \qquad \rho^{n+1}_{i+1} \doteq \rho^{n}_{i+1} \tag{24}$$

Boundary Conditions

At a solid boundary, the contravariant velocity V is set to zero. Exact implementation of $V=0$ in the implicit treatment of Eq. (18) is described in Ref. 4.

The outer boundary is set away from the bow shock and the freestream velocity potential ϕ_∞ is imposed along that boundary. All discontinuities in the flowfield are captured. The precise density biasing activator ν, based on the characteristic theory, allows for sharp capturing of shocks in the flow.

Behind the trailing edge of a wing, a wake model is imposed. Figure 4 shows a schematic of a wake model. At a point P lying on the wake, the boundary condition is that there is no jump in the pressure across the wake, i.e., $(p_P - p_Q) = 0$. In the full potential (isentropic) formulation, this translates into the condition that the jump in density $(\rho_P - \rho_Q)$ is zero, or the jump in the total velocity q is zero $[(q_P - q_Q) = 0]$. The jump in q across the wake is set to zero in an approximate manner in the following way.

First, compute the jump in the potential ϕ at the trailing-edge point P' and maintain that jump constant along the line $P'P$ in Fig. 4. At the wake point P, Eq. (1) is not valid. Instead of solving Eq. (1), $\phi_{\eta\eta} = 0$ is satisfied at the wake point P to achieve the condition $(\phi_\eta)_P - (\phi_\eta)_Q = 0$. Incorporating a constant jump in ϕ along $P'P$ insures $(\phi_\zeta)_P - (\phi_\zeta)_Q \doteq 0$. The net effect is that $(q_P - q_Q)$ is approximately set to zero, yielding the necessary wake boundary condition. The following section presents a calculation performed for a realistic wing/body/wake fighter model and shows an excellent matching of the pressures across the wake, using the above wake boundary condition.

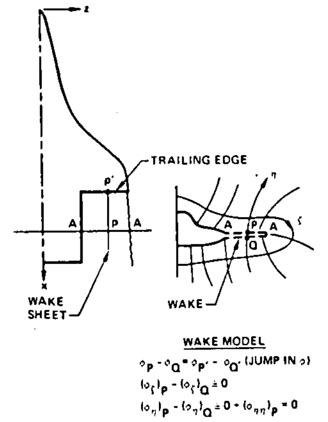

Fig. 4 Wake boundary condition.

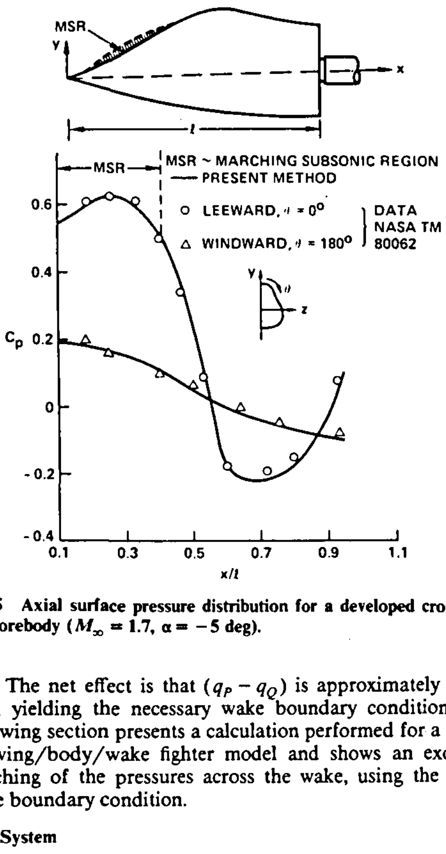

Fig. 5 Axial surface pressure distribution for a developed cross-section forebody ($M_\infty = 1.7$, $\alpha = -5$ deg).

Grid System

The transformation from the physical space (x, y, z) to a body-fitted computational space (ζ, η, ξ) is performed numerically at each constant ζ plane by using the elliptic grid generation technique of Ref. 6. Once the grid is generated, all the metric terms a_{ij} in Eq. (2) and the Jacobian J in Eq. (3) are computed by numerical differentiation. As described in Ref. 5, a freestream error subtraction is performed at each grid point to account for any improper metric cancellation.

Density Biasing Summary

This section summarizes in a tabular form the type-dependent density biasing procedures incorporated in this paper to generate the proper artificial viscosity. See Table 1.

Table 1 Summary to type-dependent density biasing procedure

Term	Total supersonic	Marching subsonic	Total subsonic
Definition	$[a_{11}-(U^2/a^2)]<0$, $q>a$	$[a_{11}-(U^2/a^2)]>0$, $q>a$	$[a_{11}-(U^2/a^2)]>0$, $q<a$
ρU in ζ direction	Upwind differencing, Eq. (11)	Density biasing based on $[1-(a^2/q^2)]$ in Eq. (13)	Shut off density biasing
ρV, ρW in η, ξ directions	Density biasing based on $[1-a_{22}(a^2/V^2)]$, $[1-a_{33}(a^2/W^2)]$ $\bar{\rho}$ in Eq. (16)	Density biasing based on $[1-(a^2/q^2)]$ $\bar{\rho}$ in Eq. (17)	Shut off density biasing

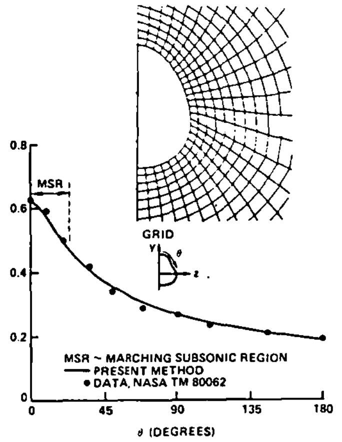

Fig. 6 Circumferential pressure distribution for a developed cross-section forebody (M_∞ = 1.7, α = −5 deg, x/l = 0.28).

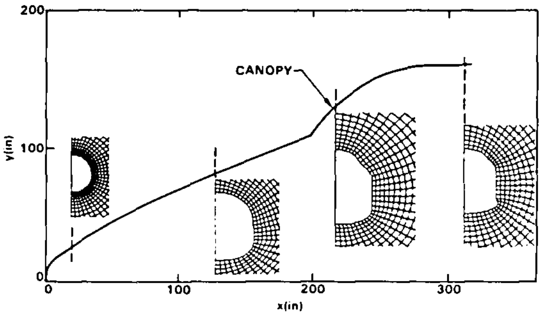

Fig. 7 Nose region geometry for Space Shuttle.

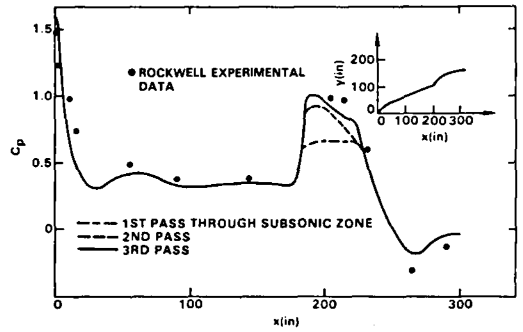

Fig. 8 Surface pressure distribution at leeward plane of symmetry.

IV. Results

As illustrated in Fig. 2, supersonic marching calculations are performed from the nose until an embedded MSR forms. In Fig. 2, the plane AB is the last supersonic marching plane preceding the subsonic bubble and forms the upstream computational boundary for the relaxation calculation. For the first relaxation pass through the subsonic bubble region, θ_{i+1} in Eq. (10) is set equal to θ_i and $(\rho U)_{i+2}=\rho^* q^*$. From the second relaxation cycle on, θ_{i+1}, θ_i, and $(\rho U)_{i+2}$ are computed according to their definitions. A typical supersonic flow with a subsonic bubble calculation required at most only four relaxation cycles (iterating back and forth between planes AB and CD) to obtain a converged location for the bubble. The initial guess, based on the sonic conditions $\rho^* q^*$, worked out very well for all the subsonic bubble cases presented in this paper. The (η,ξ) marching plane can be any arbitrary surface, but for convenience was chosen to be a constant x plane.

The step size in the marching direction ζ for the supersonic part $\{[a_{11}-(U^2/a^2)]<0,\ q>a\}$ was automatically chosen by setting the Courant number[5] to be around 5. Once the MSR forms, the eigenvalues become complex and the step size cannot be computed based on a specified Courant number. For marching planes containing the MSR/TSR, the step size was specified into the code depending on the geometry variation. When geometry changes were drastic (region of emergence of a wing from a fuselage), usually a smaller step size $\Delta\zeta$ was required (as small as 0.003 ~ 0.005 for a total length of one) to properly account for rapid changes in the flow. Once the MSR/TSR is fully captured and the flow becomes supersonic again, the step size selection once again becomes based on the Courant number. For a pure supersonic flow all the way, the entire calculation could be performed using 40 planes or less ($\Delta\zeta>0.025$). However, once an MSR or TSR is present, the total number of ζ planes in the calculation could go as high as 300.

Figure 5 shows the surface pressure distribution in the axial direction on the upper ($\theta=0$, lee side) and lower ($\theta=180$ deg, windward side) plane of symmetry for a developed cross-section forebody geometry reported in Ref. 7. At $M_\infty=1.7$ and $\alpha=-5$ deg, the lee side has an embedded MSR that required use of the relaxation operator in Eq. (10). A pure supersonic x marching for this case would have failed without the MSR treatment described in this paper.

Figure 6 shows the circumferential pressure distribution for the same developed cross-section forebody at $M_\infty=1.70$, $\alpha=-5$ deg, and $x/l=0.28$. The embedded MSR thickness is the largest at this axial station. The extent of the subsonic bubble is marked in Fig. 6. The results of Figs. 5 and 6 exhibit only MSR—TSR is not present.

To simulate both the MSR and TSR, the flow over the Shuttle orbiter at $M_\infty \doteq 1.4$ and $\alpha=0$ deg was considered. The side view, cross section, and grid in the fuselage/canopy region of the orbiter are shown in Fig. 7. At this Mach

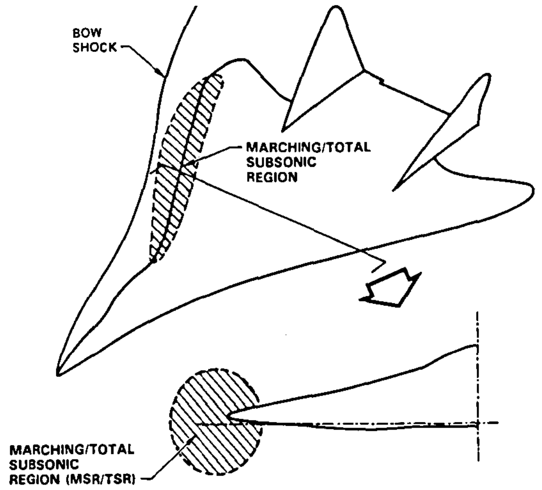

Fig. 9 Supersonic fighter with an embedded marching subsonic region near the leading edge.

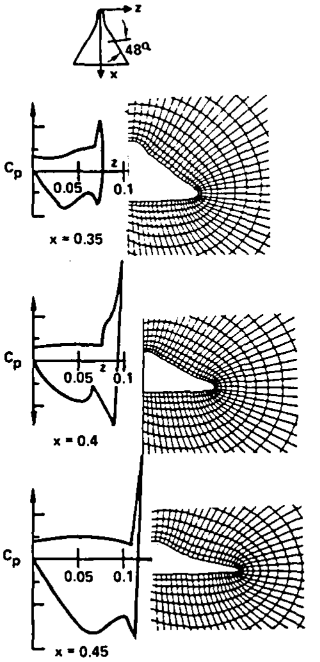

Fig. 10 Pressure distribution on a fighter-like configuration ($M_\infty = 1.6$, $\alpha = 5$ deg).

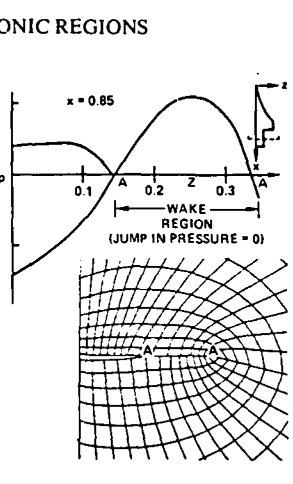

Fig. 11 Grid and pressure distribution in the wake region of a fighter-like configuration ($M_\infty = 1.6$, $\alpha = 5$ deg, $x = 0.85$).

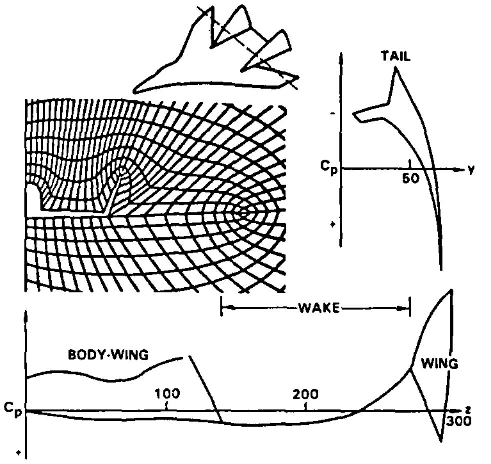

Fig. 12 Circumferential pressure distribution in the vertical tail and wing region of a fighter-like configuration ($M_\infty = 1.6$, $\alpha = 4.46$ deg, $x/l = 0.90$).

Table 2 Test cases for fighter-like configurations

α, deg	5	5	5	5
M_∞	1.6[a]	1.6[b]	1.4[b]	1.6[b]
Λ, deg	48	48	48	55
C_L				
Code	0.298	0.3016	0.3561	0.29186
Data[c]	0.277	0.295	0.342	0.3
C_D				
Code	0.0462	0.04916	0.04117	0.028129
Data[a]	0.0457	0.0493	0.0425	0.0301

[a] Tail off. [b] Tail on. [c] Rockwell data.

number, the fuselage/canopy junction exhibits a large MSR/TSR. Figure 8 shows the surface pressure distribution along the leeward plane of symmetry. At $x \cong 4.3$ m (170 in.), which is the beginning of the canopy, the pressure increases rapidly from $C_p \cong 0.3$ to 1.0 and an MSR/TSR is formed. It required three relaxation cycles to develop the solution. The comparison with the Rockwell experimental data is favorable. The blunt body initial solution for this Shuttle case was obtained from the unsteady full potential code of Ref. 8.

Figure 9 shows a supersonic fighter configuration with a wing sweep of around 48 deg. At a freestream Mach number of 1.6 and $\alpha = 5$ deg, the leading edge of the wing exhibits an MSR/TSR. To solve the flowfield over such a fighter configuration, one needs to use the embedded subsonic bubble treatment. Figure 10 shows the surface pressure at various axial stations along with respective grid distribution for the wing/body geometry. For this case, the MSR/TSR starts around $x = 0.4$. Figure 11 shows the pressure distribution for the fighter configuration of Fig. 9 at an axial station $x/l = 0.85$, where a wake sheet is present. The grid distribution goes around the wake sheet just like a wing/body case. The approximate wake model described in the paper seems to provide the correct zero pressure jump condition across the wake, as seen in Fig. 11. Figure 11 shows the simulation without the

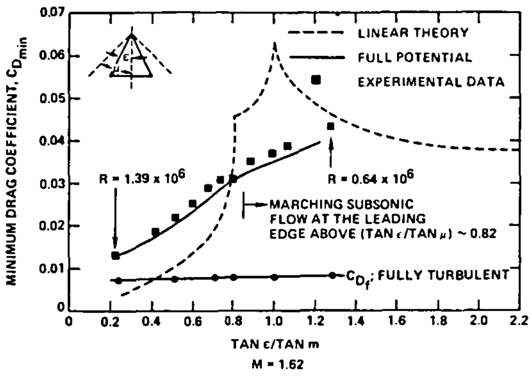

Fig. 13 Drag prediction for a double-wedge delta wing at $M_\infty = 1.62$, $\alpha = 0$ deg; for sweep angles less than 60 deg, the leading edge has a marching subsonic flow ($C_{D_{min}} = C_{D_f} + C_{D_{inviscid}}$).

vertical tails. Figure 12 shows the result for a different fighter model with a pronounced wing/body shape and a vertical tail. At this cross section, $x/l = 0.9$, the geometry is multiply connected with a wake sheet present between the tail and the wing. The circumferential pressure distribution on the wing/body/tail/wake and the gridding are shown in Fig. 12.

The lift and drag coefficients from the present calculation for a fighter model are given in Table 2. The comparison with Rockwell experimental data is excellent.

Figure 13 shows the drag prediction capability of the full potential code by demonstrating it on a double-wedge delta wing at $M_\infty = 1.62$. At this Mach number, the leading edge exhibited the presence of an MSR for sweep angles less than 60 deg. A pure supersonic marching code would not have worked for this case. The drag calculation from the full potential code compared very well with the experimental data available in the Princeton series.

V. Conclusions

A nonlinear full potential method has been developed to treat supersonic flows with embedded subsonic regions. A conservative switching scheme is employed to transition from the supersonic marching algorithm to a subsonic relaxation procedure. The theory of characteristic signal propagation plays a key role in activating various density biasing procedures to produce the necessary artificial viscosity. The method has been shown to produce results that were hitherto not possible using a pure supersonic marching scheme. The concept of density biasing will be modified in the future to a flux biasing procedure described in the Appendix.

Appendix: Flux Biasing Procedure

Based on the work of Hafez et al.,[9] it is possible to modify the density biasing concept to a flux biasing procedure.

Consider the term $(\partial/\partial\eta)[\tilde{\bar{\rho}}(V/J)]$ in Eq. (15). The density biasing procedure defines $\tilde{\bar{\rho}}$ to be

$$\tilde{\bar{\rho}}_{j+\frac{1}{2}} = (1-\nu)\rho_{j+\frac{1}{2}} + \tfrac{1}{2}\nu(\rho_j + \rho_{j-1}) \tag{A1}$$

where

$$\nu = \max\left[0; 1 - (a^2/q^2)\right]$$

In the flux biasing technique, it will be modified to

$$\frac{\overleftarrow{\partial}}{\partial\eta}\left(\tilde{\bar{\rho}}\frac{V}{J}\right)_{j+\frac{1}{2}} = \frac{\overleftarrow{\partial}}{\partial\eta}\left[\frac{V}{Jq}\left\{\rho q - \Delta\eta\,\overleftarrow{\partial}_\eta(\rho q)_-\right\}\right]_{j+\frac{1}{2}} \tag{A2}$$

where

$$\begin{aligned}(\rho q)_- &= 0 && \text{if } q \le a\\ &= (\rho q) - \rho^* q^* && \text{if } q > a,\end{aligned}$$

where ρ^* and q^* represent sonic conditions, a the local speed of sound, and (ρq) the flux. When the flow is purely subsonic, the flux biasing is turned off automatically.

Acknowledgment

This work was partially supported by NASA-Langley Research Center under Contract NAS1-15820.

References

[1] Jameson, A., "Transonic Potential Flow Calculations using Conservation Form," *AIAA Second Computational Fluid Dynamics Conference Proceedings*, AIAA, New York, 1975, pp. 148-155.

[2] Holst, T.L., "Fast, Conservative Algorithm for Solving the Transonic Full Potential Equation," *AIAA Journal*, Vol. 18, Dec. 1980, pp. 1431-1439.

[3] Siclari, M.J., "Computation of Nonlinear Supersonic Potential Flow over Three-Dimensional Surfaces," AIAA Paper 82-0167, Jan. 1982.

[4] Shankar, V., "A Conservative Full Potential, Implicit, Marching Scheme for Supersonic Flows," *AIAA Journal*, Vol. 20, Nov. 1982, pp. 1508-1514.

[5] Shankar, V. and Osher, S., "An Efficient Full Potential Implicit Method Based on Characteristics for Analysis of Supersonic Flows," *AIAA Journal*, Vol. 21, Sept. 1983, pp. 1262-1270.

[6] Shankar, V., Rudy, S., and Szema, K.-Y., "Application of a Two-Dimensional Grid Solver for Three-Dimensional Problems," *ASME Applied Mechanics, Bioengineering, and Fluids Engineering Conference*, Vol. No. G00222, ASME, New York, June 1983.

[7] Townsend, J.C., Howell, D.T., Collins, I.K., and Hayes, C., "Surface Pressure Data on a Series of Analytic Forebodies at Mach Numbers from 1.7 to 4.50 and Combined Angles of Attack and Sideslip," NASA TM 80062, June 1979.

[8] Shankar, V., "Implicit Treatment of the Unsteady Full Potential Equation in Conservation Form," AIAA Paper 84-0262, Jan. 1984.

[9] Hafez, M., Osher, S., and Whitlow, W. Jr., "Improved Finite Difference Schemes for Transonic Potential Calculations," AIAA Paper 84-0092, Jan. 1984.

Computation of Supersonic Flows over Three-Dimensional Configurations

K.-Y. Szema, W.L. Riba, V. Shankar, J.J. Gorski

Reprinted from
Journal of Aircraft Volume 22, Number 12, December 1985, Page 1079
AMERICAN INSTITUTE OF AERONAUTICS AND ASTRONAUTICS • 1633 BROADWAY • NEW YORK, N.Y. 10019

VOL. 22, NO. 12, DECEMBER 1985 J. AIRCRAFT 1079

Computation of Supersonic Flows over Three-Dimensional Configurations

Kuo-Yen Szema,* William L. Riba,* Vijaya Shankar,† and Joseph J. Gorski‡
Rockwell International Science Center, Thousand Oaks, California

An aerodynamic prediction technique based on the steady form of the full-potential equation has been applied to a variety of three-dimensional supersonic flow problems exhibiting embedded subsonic regions. A conservative switching scheme is employed to transition from the supersonic marching procedure to a subsonic relaxation algorithm, and vice versa. Numerical solutions are obtained for a number of complex configurations, including advanced tactical fighter, Langley canard-wing fighter configuration, isolated shuttle orbiter, and mated shuttle orbiter configuration with external tank. The computed results are in good agreement with available experimental data.

Nomenclature

a = speed of sound
a_{11} = transformation metric $\zeta_x^2+\zeta_y^2$
C_D = drag coefficient
C_L = lift coefficient
C_M = pitch-moment coefficient
C_p = pressure coefficient
i,j,k = streamwise, radial, and circumferential indices
J = Jacobian of transformation
M_∞ = freestream Mach number
q^+ = $[\rho^{*\gamma-1}/m_p^2]^{1/2}$, sonic condition
U,V,W = contravariant velocities
x,y,z = Cartesian coordinates
α = angle of attack
γ = ratio of specific heats
ζ,η,ξ = transformed coordinates
ρ = density
ρ^* = sonic density
ϕ = velocity potential
$(\hat{~})$ = wing sweep angle

Introduction

THE prediction of inviscid low supersonic Mach number flowfields about complex three-dimensional configurations is of great interest to both researchers and designers. For treatment of such flows, full-potential methods[1-3] based on a space-marching procedure offer the advantage of requiring only moderate computer resources (memory and time) while maintaining sufficient accuracy.

In the full-potential method of Refs. 1 and 2, the equation is transformed to a generalized, nonorthogonal, curvilinear coodinate system and is solved by a highly efficient, implicit, finite difference scheme based on the characteristic theory of signal propagation. A space-marching technique is used when the flow is supersonic in a given marching direction. If the velocity in the marching direction becomes subsonic, the domain of dependence changes and the marching scheme is modified to a relaxation-type method through a conservative switching operator.

The presence of subsonic pockets in a supersonic flow occurs very frequently near fuselage-canopy junction areas and wing leading-edge regions. In fact, future design of advanced fighter wings ($M_\infty = 1.2$-2.0, wing sweep ~ 48 deg) will purposely incorporate subsonic regions near the leading edge to benefit from the leading-edge suction peak associated with subsonic flows.

In Ref. 1, a numerical mapping technique is used to generate the body-fitted coordinate system at a marching plane. The key advantage of this method is that it has no restrictions on its applicability to complex geometries and intricate shocked flowfields. In contrast to the general coordinate formulation of Ref. 1, the method of Ref. 3 is based on a spherical plane marching technique and its application to general three-dimensional geometries is yet to be demonstrated.

The main purpose of this study is to investigate the usefulness of the methodology of Ref. 1 in treating supersonic flows with large embedded subsonic regions over complex geometries, including realistic fighter configurations, shuttle orbiter, and multibody configurations (orbiter on top of the external tank/solid rocket boosters) at low supersonic Mach numbers ($M_\infty = 1.2$ to 2.0).

Analysis

The physical and computational coordinate systems are shown in Fig. 1. As discussed in Refs. 1 and 2, the entire flowfield is divided into three regions (see Fig. 2): 1) the pure supersonic region, 2) the marching subsonic region (MSR), and 3) the total subsonic region (TSR). The basic governing equations and boundary conditions are essentially the same as in Ref. 2 and, therefore, only a brief discussion of the method is presented here.

Governing Equation

The conservative form of the full-potential equation cast in an arbitrary coordinate system defined by $\zeta=\zeta(x,y,z)$, $\eta=\eta(x,y,z)$, and $\xi=\xi(x,y,z)$ can be written as

$$\left(\rho\frac{U}{J}\right)_\zeta+\left(\rho\frac{V}{J}\right)_\eta+\left(\rho\frac{W}{J}\right)_\xi=0 \tag{1}$$

where the density is given by

$$\rho=\left[1-\frac{(\gamma-1)}{2}M_\infty^2\left\{U\phi_\zeta+V\phi_\eta+W\phi_\xi-1\right\}\right]^{1/(\gamma-1)} \tag{2}$$

and M_∞ is the freestream Mach number, U, V, and W are the contravariant velocity components, and J is the Jacobian of

---

Presented as Paper 85-0272 at the AIAA 23rd Aerospace Sciences Meeting, Reno, NV, Jan. 14-17, 1985; received March 14, 1985; revision received Sept. 10, 1985.

*Member Technical Staff. Member AIAA.

†Manager, Computational Fluid Dynamics Department. Associate Fellow AIAA.

‡Senior Technical Associate. Member AIAA.

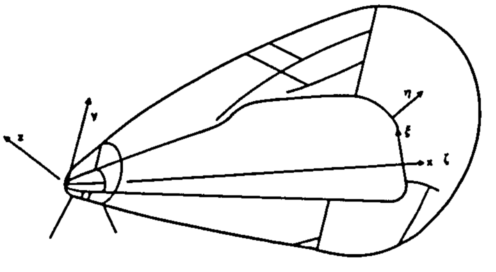

Fig. 1 Computational coordinate system.

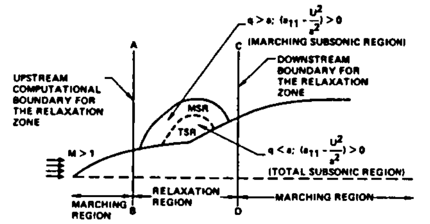

Fig. 2 Embedded subsonic bubble in a supersonic flow.

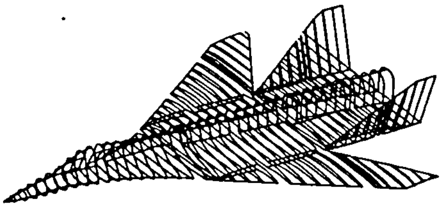

Fig. 3 Fighter-like configuration (ATF).

the transformation. The treatment of each term in Eq. (1), including the density biasing procedure and the implicit approximate factorization algorithm, can be found in Refs. 1 and 2.

Initial Conditions

Supersonic Flow Region

For a pure supersonic flow, initial conditions are required at the starting plane. For sharp-nosed configurations, conical solutions are prescribed, and for a blunt-nosed configuration, the axisymmetric, unsteady, full-potential solver of Ref. 4 is used to obtain the detached bow shock flowfield in the forebody region.

Embedded Subsonic Flow Region

When Eq. (1) is applied at the $(i+1)$ plane within an embedded subsonic region, information on the flux ρU at the $(i+2)$ plane is required. For the first relaxation pass, sonic conditions are assumed at $(i+2)$

$$\rho_{i+2} = \rho^* = \left(\frac{2}{\gamma+1} + \frac{\gamma-1}{\gamma+1} M_\infty^2\right)^{1/\gamma-1} \tag{3}$$

$$U_{i+2} = q^* \sqrt{a_{11_{i+2}}}$$

where

$$q^* = [\rho^{*\gamma-1}/M_\infty^2]^{1/2}$$

Sonic values ρ^* and q^* are purely a function of the freestream Mach number M_∞. The quantity a_{11} is a transformation metric term.

Table 1 Test cases

	Case 1 (Fig. 3)	Case 2 (Fig. 10)	Case 3 (Fig. 12)	Case 4 (Fig. 17)
M_∞	1.6, 1.4	2.0	1.4	1.4
α	See Table 2	4.0	0 deg, −1.94 deg	0 deg

Boundary Conditions

In order to solve the full-potential equation, it is essential to specify appropriate boundary conditions on the body surface and along the outer boundary.

Body Surface

At a solid boundary, the contravariant velocity V is set to zero. Exact implementation of $V=0$ in the implicit treatment of Eq. (2) is described in Ref. 1.

Outer Boundary

The outer boundary is outside the bow shock where the freestream velocity potential ϕ_∞ is imposed. All discontinuities in the flowfield are captured. The precise density biasing activator of Ref. 1, based on the characteristic theory, allows for sharp capturing of shocks in the flow.

Swept Trailing-Edge Wake Treatment

In order to treat the region behind the trailing edge, an artificial cut is created, and the pressure jump $[p]$ across this cut is imposed to be zero as a boundary condition. The full-potential equation is not solved at grid points on the wake cut. Instead, $\phi_{\eta\eta} = 0$ is solved to provide $[p] = 0$ across the wake cut. A complete discussion of this is given in Ref. 2.

Method of Solution

Figure 2 shows the schematic of a fuselage-canopy forebody geometry with an embedded MSR and TSR present in a supersonic flow. To solve this problem, the marching scheme of Ref. 1 is used when $(a_{11} - U^2/a^2)$ is negative, and a relaxation scheme is used when $(a_{11} - U^2/a^2)$ is positive.

First, march from the nose up to the plane denoted by A-B in Fig. 2, using the method of Ref. 1. Then, between planes A-B and C-D, which embed the subsonic bubble (MSR and TSR), use a relaxation scheme and iterate until the subsonic bubble is fully captured. Finally, resume the marching scheme from the plane C-D downstream of the body.

Geometry and Grid System

The geometry of a configuration is prescribed at discrete points in a cross plane (usually x = constant planes) at various axial locations. These geometry input points are usually obtained from a geometry package such as GEMPAK[5] or CDS.[6] The input points are then divided into several patches, and at each patch a key-point system is established. The geometry at a marching plane is then obtained by joining appropriate key points for each patch. Using a cubic spline passing through the key points, a desired grid-point distribution (clustering) is set up on the body surface. Then, by choosing an appropriate outer boundary, the grid for the flowfield calculation is generated by using an elliptic grid generator. More discussions can be found in Ref. 2.

Results

Results for the following five different configurations are presented to demonstrate the versatility and robustness of the code in handling a wide variety of nonlinear flows:

Case 1: Advanced tactical fighter configuration (Fig. 3).
Case 2: Langley canard-wing fighter configuration (Fig. 8).
Case 3: Isolated shuttle orbiter (Fig. 12).
Case 4: Multibody configuration: shuttle orbiter with external tanks/solid rocket boosters (Fig. 17).

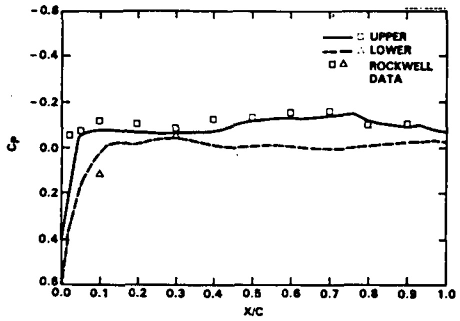

Fig. 4 ATF chordwise pressure distribution; $M_\infty = 1.6$, $\alpha = 1.24$, $Z = 183$ in.

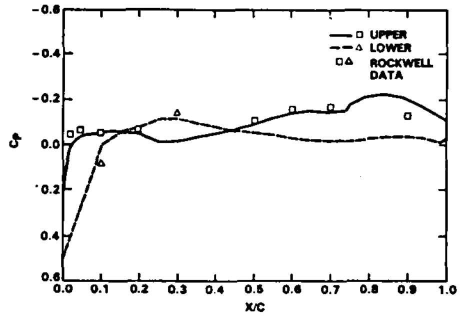

Fig. 5 ATF chordwise pressure distribution; $M_\infty = 1.6$, $\alpha = 1.24$, $Z = 245$ in.

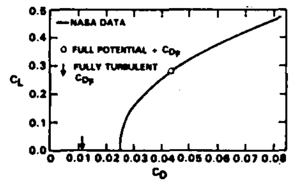

a) DRAG COEFFICIENT (WING SWEEP ANGLE Λ = 48°)

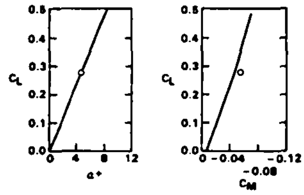

b) LIFT AND PITCH MOMENT COEFFICIENT (WING SWEEP ANGLE Λ = 48°)

Fig. 6 Comparison of measurement and full-potential prediction at $M = 1.6$ for 48 deg sweep linear multipoint design wing.

Table 2 Test cases for the advanced tactical fighter configuration

α		5°	4.5°	5°	4.5°
M_∞		1.6[a]	1.6[b]	1.4[b]	1.6[b]
Λ		48°	48°	48°	55°
C_L	Code	0.298	0.3016	0.3561	0.29186
	Data	0.277	0.295	0.342	0.283
C_D	Code	0.0482	0.04916	0.04117	0.0404
	Data	0.0457	0.0493	0.0426	0.0396

[a] Without vertical tail. [b] With vertical tail. Λ = wing sweep angle.

The test conditions for each of these cases are summarized in Table 1.

Case 1

Figures 4 and 5 show the chordwise pressure distribution on the upper and lower surfaces at 60% (183 in.) and 80% (245 in.) span stations, respectively. The results show that the present predictions are in very good agreement with Rockwell's experimental data.

Figure 6 shows the comparison of overall forces and moments in terms of C_L, C_D, and C_M. The full-potential results compare very well with NASA data. The drag calculation C_D includes the skin-friction and base drag. The computed viscous drag was for a fully turbulent condition at the test unit Reynolds number of 2×10^6. The 48-deg wing sweep results of Fig. 6 correspond to a supersonic leading-edge condition of 3.3 deg. The lift and drag coefficients from the present calculations for this fighter model, at different Mach numbers, are summarized in Table 2. The results are in excellent agreement with experimental data.

Figure 7 shows the grid and pressure contours for the same fighter geometry with a nacelle mounted on the undersurface of the wing. Only the exterior of the nacelle is modeled as part of the wing-body combination. At an axial marching station immediately preceding the inlet face, initial conditions are generated by interpolation from the flowfield without the nacelle. The shock formed around the nacelle near the inlet face (see Fig. 7) is diffused at downstream stations.

Case 2

Figure 8 shows a fighter model tested at NASA Langley that has a canard and a fuselage-mounted flow-through nacelle. The actual computational geometry and the surface grid employed in this study are shown in Fig. 9. Computations were performed for this configuration at $M_\infty = 2$ and $\alpha = 4$ deg. Figure 10 shows results of cross-flow streamlines, surface pressures, pressure contours, and cross-flow velocity vectors at an axial station where the fuselage, wing, canard wake, and nacelle are all presented. The nodal singularity in pressure contour present at lower wing-body junction regions corresponds to a saddle singularity of cross-flow streamlines, as shown in Fig. 10. Note the pressure match along the canard wake cut. The upper and lower center plane pressure contours at $M_\infty = 2.0$ and $\alpha = 4.0$ deg are shown in Fig. 11. The bow shock, canopy shock, nacelle shock, and expansion wave are all nicely presented in this figure.

Case 3

Figures 12-16 give the geometry, the gridding, and the corresponding flowfield solutions of the isolated shuttle orbiter at $M_\infty = 1.4$, $\alpha = 0$, and -1.94 deg. The chordwise pressures on the upper surface are shown in Fig. 13, and they compare very well with the experimental data. Figure 14 shows the circumferential pressure distribution for the orbiter at $x = 1200$ in. It is noted that the pressure along the vertical tail and the

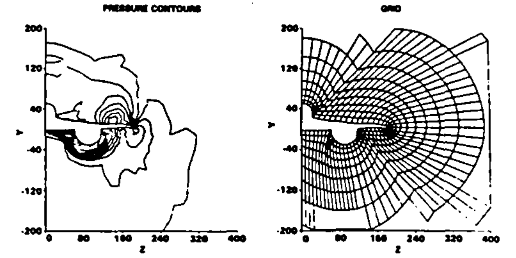

Fig. 7 Pressure contour and grid of ATF with nacelle; $M_\infty = 1.6$, $\alpha = 5$ deg at $x = 375$ in.

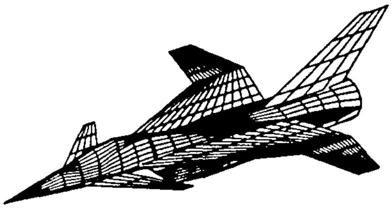

Fig. 8 Langley canard-wing fighter configuration.

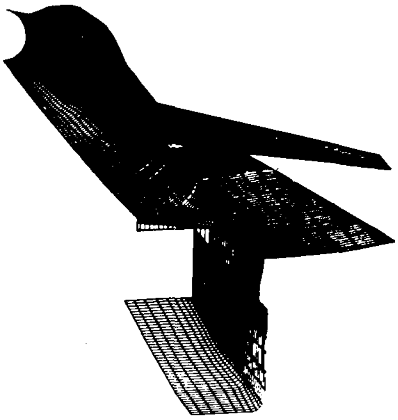

Fig. 9 Computational geometry and surface gridding for Langley fighter configuration.

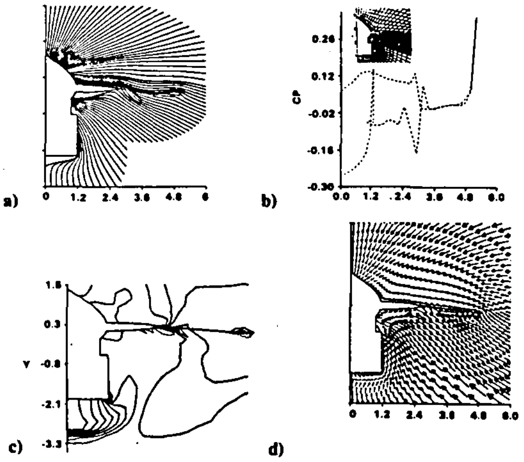

Fig. 10 Solution for Langley figher configuration, $M_\infty = 2.0$, $\alpha = 4.0$, $x = 14.0$; a) Streamline. b) Surface pressure coefficient. c) Pressure contour. d) Velocity vector.

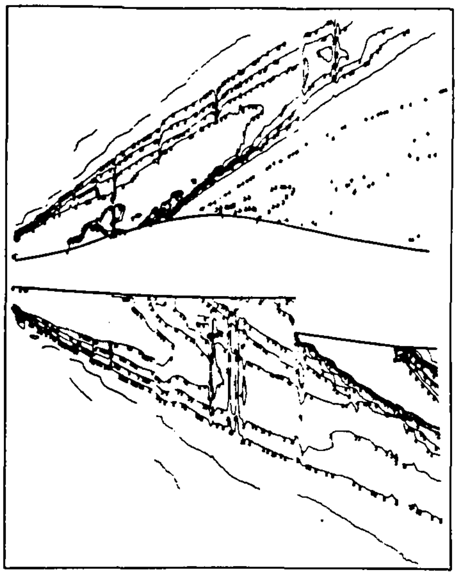

Fig. 11 Upper and lower centerplane pressure contour for Langley fighter configuration; $M_\infty = 2.0$, $\alpha = 4.0$.

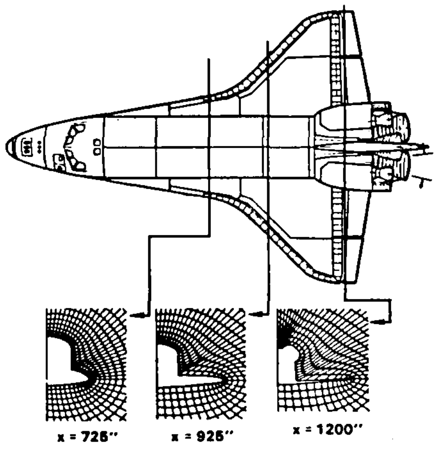

Fig. 12 Shuttle orbiter configuration.

orbital maneuvering subsystem (OMS) pods are well predicted.

Figure 15 shows the details of the orbiter geometry as modeled in this study. The OMS pod is clearly seen in Fig. 15. Figure 16 presents a series of isobar plots at different x locations. The onset of the OMS pod shock formation is clearly seen. The OMS pod shock is formed around $x = 1065$ in., then grows, and finally hits the upper wing surface at approximately $x = 1090$ in. The foot of the OMS pod shock moves further away from the fuselage for increasing x along the orbiter. The trace of the shock foot on the upper surface is also shown in Fig. 16, and a comparison between the experimental shock and the numerical prediction is made. It should be mentioned that, since the present method is valid for supersonic flow with an embedded subsonic region, it allows one to treat the actual shuttle orbiter without having to make any modifications in geometry.

Case 4

Figure 17 schematically illustrates the multibody interaction problem of the shuttle orbiter in a mated configuration with the external tank (ET) and solid rocket boosters (SRBs) present. Figure 18 shows a perspective view of the complicated multibody problem as modeled by this full-potential code. It is found that the external tank has no effect on the upper wing surface and only a small effect on the lower wing surface of the shuttle orbiter. The high pressure present on the lower surface of the orbiter wing is caused by the aft attach struts that connect the orbiter to the external tank. The presence of the aft attach struts is modeled by a wedge blockage effect and the ET and SRBs are modeled by an elliptic cross-section exter-

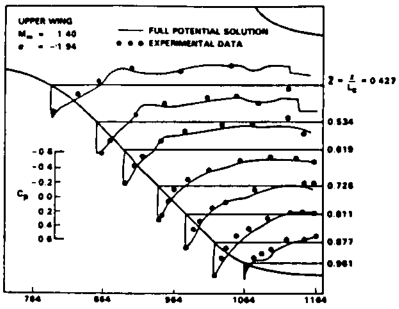

Fig. 13 Shuttle orbiter upper surface pressure distribution.

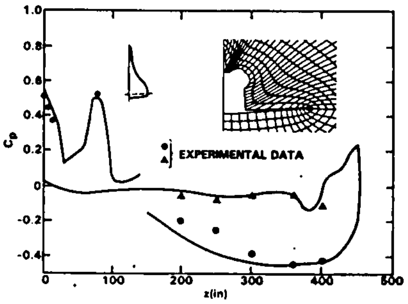

Fig. 14 Circumferential pressure distribution for the orbiter at $x = 1200$ in., $M_\infty = 1.4$, $\alpha = 0$.

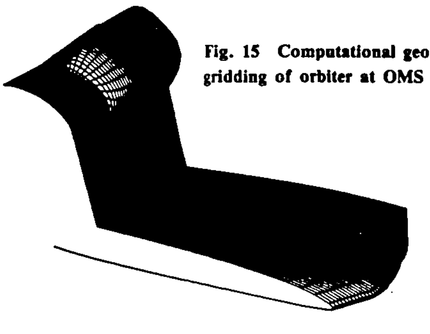

Fig. 15 Computational geometry and gridding of orbiter at OMS pod region.

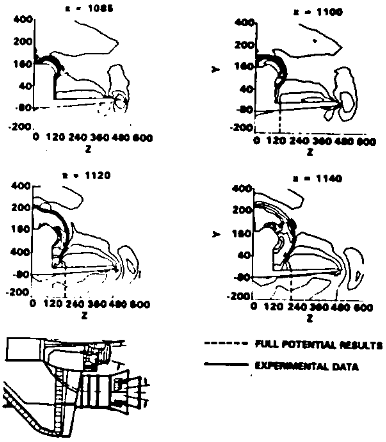

Fig. 16 Trace of OMS pod shock on the upper surface; $M_\infty = 1.4$, $\alpha = 1.94$.

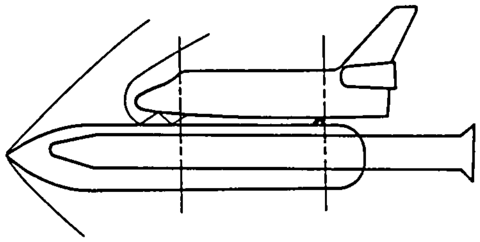

Fig. 17 Orbiter with external tank and SRB.

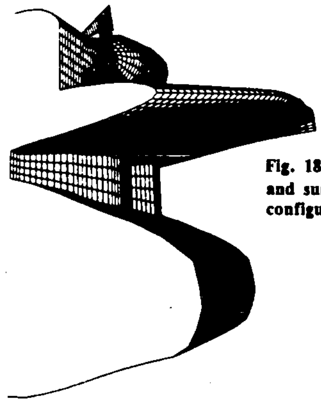

Fig. 18 Computational geometry and surface gridding for mated configuration.

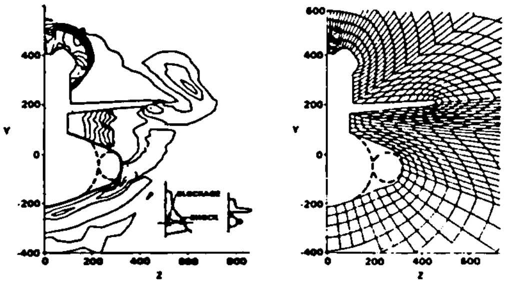

Fig. 19 Gridding and pressure contours for the mated configuration; $M_\infty = 1.4$, $\alpha = 0.0$.

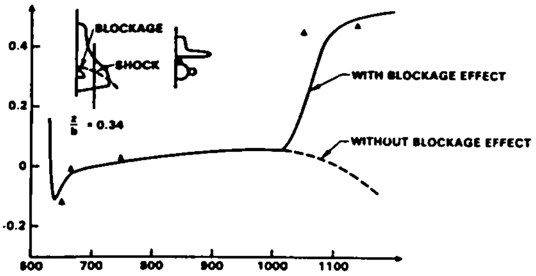

Fig. 20 Orbiter lower surface chordwise pressure distribution; $M_\infty = 1.4$, $\alpha = 0$ deg.

nal tank. Figure 19 shows the gridding and the isobar plot for this multibody problem at an axial station where the wedge blockage effect is present. The detached bow shock formed by the blockage is clearly shown in this figure. Chordwise pressure distribution of the orbiter lower surface at $\bar{z}=0.34$, with and without the blockage, is given in Fig. 20. The result with the blockage effect included shows a very good comparison with the experimental data.

Conclusion

The main objective of this study is to illustrate the versatility and usefulness of a recently developed nonlinear aerodynamic prediction capability based on the full-potential equation. Results are shown for a variety of complex configurations, including a multibody problem. Comparison of results with available experimental data are in good agreement. The fully vectorized version of this code takes about 4 to 5 min of CPU time for analysis of typical fighter-like configurations on the CYBER 176 computer and about 25-30 s on the CRAY-XMP for a marching plane grid of 70 × 25.

Acknowledgments

This work was partially supported by NASA Langley Research Center under Contract No. NAS1-15820 and by Rockwell International Space Division under IDWA No. M22178, Contract No. NAS9-14000.

References

[1] Shankar, V., Szema, K. Y., and Osher, S., "A Conservation Type-Dependent Full Potential Method for the Treatment of Supersonic Flow with Embedded Subsonic Region," AIAA Paper 83-1887, July 1983.

[2] Szema, K. Y. and Shankar, V., "Nonlinear Computation of Wing-Body-Vertical Tail-Wake Flows at Low Supersonic Speeds," AIAA Paper 84-0427, Jan. 1984.

[3] Siclari, M. J., "The NCOREL Computer Program for 3D Nonlinear Supersonic Potential Flow Computations," NASA CR-3694, Aug. 1983.

[4] Shankar, V., "Implicit Treatment of the Unsteady Full Potential Equation in Conservation Form," AIAA Paper 84-0262, Jan. 1984.

[5] Stack, S. H., Edwards, C. L. W., and Small, W. J., "GEMPAK: An Arbitrary Aircraft Geometry Generator," NASA TP-1022, Dec. 1977.

[6] Tice, S. E., Zolon, J. L., and Repic, R. A., "SVCDS—An Evolutionary CDS for Preliminary Space Vehicle Design, Analysis and Simulation," AIAA Paper 84-2393, Oct. 1984.

AIAA'85

AIAA-85-1703

AN EULER SOLVER FOR THREE-DIMENSIONAL SUPERSONIC FLOWS WITH SUBSONIC POCKETS

S.R. CHAKRAVARTHY and K.Y. SZEMA,
ROCKWELL INTERNATIONAL SCIENCE CENTER,
THOUSAND OAKS, CA

AIAA 18th Fluid Dynamics and Plasmadynamics and Lasers Conference

July 16-18, 1985 / Cincinnati, Ohio

AN EULER SOLVER FOR THREE-DIMENSIONAL SUPERSONIC FLOWS WITH SUBSONIC POCKETS

Sukumar R. Chakravarthy* and Kuo-Yen Szema*
Rockwell International Science Center, Thousand Oaks, California

Abstract

A new finite-difference scheme has been developed to efficiently solve the Euler equations for three-dimensional inviscid supersonic flows with subsonic pockets. The technique utilizes planar Gauss-Seidel relaxation in the marching direction and approximate factorization in the cross-flow plane. It is a unified formulation based on the unsteady Euler equations: an 'infinitely large' ('infinitely small' reciprocal of) time step is used in parts of the flow-field where the component of velocity in the marching direction is supersonic—here the Gauss-Seidel sweeps are restricted to the forward direction only and the procedure reduces to simple space-marching; a finite time step is used in parts of the flow-field where the marching component of velocity is subsonic—here backward and forward Gauss-Seidel sweeps are employed to allow for upstream and downstream propagation of signals, and a time-asymptotic steady state is obtained. The discretization formulae are based on finite-volume implementations of high accuracy (up to third order) Total Variation Diminishing formulations. The fully general coordinate treatment used permits the use of arbitrary marching fronts (rather than just planes perpendicular to an axis, spherical fronts, etc.). Results are presented for an analytically defined forbody, a twisted-cone inlet spike, a realistic fighter configuration, and the Space Shuttle.

1.0 Introduction

For fully supersonic flows, an efficient strategy for obtaining numerical solutions is to employ space-marching techniques. Realistic high speed flight vehicle configurations often give rise to subsonic pockets even though they fly at supersonic speeds. For such predominantly supersonic flows, a hybrid approach is suitable: a space marching technique for the supersonic parts and a relaxation technique for the subsonic parts. Such a hybrid approach has been developed for potential flows by Shankar, Szema et al[1,2,3]. For the Euler equations, however, the hybridization is conventionally achieved by coupling separate space-marching and time-marching codes, each with disparate grid systems, etc. Here, we present a unified approach for efficiently solving the Euler equations for three-dimensional supersonic flows with subsonic pockets. The aim is to develop an Euler solver as versatile as the potential flow solvers[1,2,3] in treating complex and realistic aircraft, space shuttle, and other types of flight vehicle configurations. By solving the Euler equations, however, we hope to be able to compute a wider range of flows with stronger shocks, rotational slip streams, etc. which void the irrotationality assumptions built into the potential flow simulations.

The new approach utilizes finite-volume implementations of high accuracy (up to third order) Total Variation Diminishing (TVD) discretizations and are thus expected to be more accurate and reliable than other Euler space-marching and time-marching techniques based on central difference approximations. In contrast to these latter methods, there are no parameters in our approach for fine-tuning numerical dissipation for every case. Numerical oscillations are, for the most part, eliminated by using TVD scheme based discretizations.

The new approach is based on the unsteady Euler equations. However, in the supersonic parts of the flow (where the velocity component normal to the cross-flow plane that identifies the local marching direction is supersonic) an 'infinitely large' time step (which implies an 'infinitely small' reciprocal of time step) is employed. This makes the transient terms of the discretized unsteady equations vanish. In subsonic parts of the flow, a finite time step is employed and the steady-state is approached as a time-asymptote.

The new solution approach is based on a planar Gauss-Seidel relaxation method coupled to approximate factorization in the cross-flow plane. In supersonic parts of the flow-field, the Gauss-Seidel method is restricted to forward sweeps and thus the solution procedure reduces to a simple marching technique. In subsonic parts, both forward and backward sweeps are used along with the finite time steps mentioned earlier. Stability of such an approach is guaranteed by the diagonal dominance resulting from using TVD discretizations in the marching direction in the transonic parts of the flow-field. This is a crucial difference between conventional hybrid Euler solvers and the new approach. In conventional approaches, space-marching and time-marching techniques must be applied in overlapping regions for stability. In the new unified approach, there is no need for overlap.

In the following sections, we describe the new method in detail. We first cast the equations in finite-volume discrete conservation law form. Then we explain how the volume and the metrics are evaluated. This essentially completes the treatment of geometry and we proceed next to the details of the algorithm. TVD discretizations are explained first. Then the marching/relaxation procedure is described. This covers the use of approximate factorization in the cross-flow plane, the reduction of the Gauss-Seidel procedure to a marching procedure in supersonic zones, etc. The boundary point treatment is also explained briefly.

In the results section, calculations for an analytically defined forebody are presented first to illustrate some features of the new algorithm. Results for many conical flow cases have also been obtained but are presented elsewhere[4]. Next, results for a twisted-cone inlet spike are shown. Then,

---

* Member Technical Staff
Computational Fluid Dynamics Department
Member, AIAA

results are presented for a realistic fighter aircraft configuration with fuselage, canopy, wing, nacelle and vertical tail. Finally, we conclude by presenting results for the Space Shuttle Orbiter configuration.

2.0 Finite-Volume Framework

In this section, we describe the finite-volume framework chosen to implement the algorithm. We start by introducing the semi-discrete conservation law form and associating it with a finite-volume formulation of the geometry. Then we provide detailed formulae for the evaluation of the cell volume and cell-face normals.

2.1 Semi-discrete Conservation Law

We begin with the conservation law form of the unsteady Euler equations in the Cartesian coordinates x, y, z, and time t

$$Q_t + E_x + F_y + G_z = 0 \qquad (2.1a)$$

where the dependent variable vector Q, and the fluxes E, F, and G are given by

$$Q = \begin{pmatrix} e \\ \rho \\ \rho u \\ \rho v \\ \rho w \end{pmatrix}, E = \begin{pmatrix} (e+p)u \\ \rho u \\ \rho u^2 + p \\ \rho v u \\ \rho w u \end{pmatrix},$$
$$F = \begin{pmatrix} (e+p)v \\ \rho v \\ \rho u v \\ \rho v^2 + p \\ \rho w v \end{pmatrix}, G = \begin{pmatrix} (e+p)w \\ \rho w \\ \rho u w \\ \rho v w \\ \rho w^2 + p \end{pmatrix}. \qquad (2.1b)$$

In the above, pressure is p, density is ρ, Cartesian x, y, z velocity components are u, v, w, and the total energy per unit volume is e computed from $e = p/(\gamma - 1) + \rho(u^2 + v^2 + w^2)/2$.

Assuming a time invariant grid, under the transformation of coordinates implied by

$$\tau = t, \qquad (2.2)$$
$$\xi = \xi(x, y, z), \quad \eta = \eta(x, y, z), \quad \varsigma = \varsigma(x, y, z),$$

Eq. 2.1 can be recast into the conservation form given by

$$\overline{Q}_\tau + \overline{E}_\xi + \overline{F}_\eta + \overline{G}_\varsigma = 0 \quad , \qquad (2.3a)$$

where

$$\overline{Q} = \frac{Q}{J} \quad ,$$
$$\overline{E} = \frac{\xi_x}{J}E + \frac{\xi_y}{J}F + \frac{\xi_z}{J}G \quad ,$$
$$\overline{F} = \frac{\eta_x}{J}E + \frac{\eta_y}{J}F + \frac{\eta_z}{J}G \quad , \qquad (2.3b)$$
$$\overline{G} = \frac{\varsigma_x}{J}E + \frac{\varsigma_y}{J}F + \frac{\varsigma_z}{J}G \quad ,$$

where, in turn, J is the Jacobian of the transformation

$$J = \partial(\xi, \eta, \varsigma)/\partial(x, y, z) \qquad (2.3c)$$

Associating the subscripts j, k, l with the ξ, η, ς directions, a numerical approximation to Eq. 2.3a may be expressed in the semi-discrete conservation law form given by

$$\begin{aligned}(\hat{Q}_{j,k,l})_\tau &+ (\hat{E}_{j+1/2,k,l} - \hat{E}_{j-1/2,k,l}) \\ &+ (\hat{F}_{j,k+1/2,l} - \hat{F}_{j,k-1/2,l}) \\ &+ (\hat{G}_{j,k,l+1/2} - \hat{G}_{j,k,l-1/2}) = 0\end{aligned} \qquad (2.4)$$

where $\hat{E}, \hat{F}, \hat{G}$ are numerical or representative fluxes at the bounding sides of the cell for which discrete conservation is considered, and $\hat{Q}_{j,k,l}$ is the representative conserved quantity (the numerical approximation to $\overline{Q}$) considered conveniently to be the centroidal or cell-average value. The half-integer subscripts denote cell sides and the integer subscripts the cell itself or its centroid. In Fig. 1, the eight vertices of one computational hexahedral cell are identified by numerals 1 through 8. These must be associated with the appropriate j, k, l triplets:

$$\begin{aligned}1 &\equiv j-1/2, k-1/2, l-1/2 \\ 2 &\equiv j+1/2, k-1/2, l-1/2 \\ 3 &\equiv j-1/2, k+1/2, l-1/2 \\ 4 &\equiv j-1/2, k-1/2, l+1/2 \\ 5 &\equiv j+1/2, k+1/2, l-1/2 \\ 6 &\equiv j-1/2, k+1/2, l+1/2 \\ 7 &\equiv j+1/2, k-1/2, l+1/2 \\ 8 &\equiv j+1/2, k+1/2, l+1/2\end{aligned} \qquad (2.5)$$

In the following, subscripts easily understood by implication will be dropped for brevity.

The semi-discrete conservation law given by Eq. 2.4 may be regarded as representing a finite-volume discretization if the following associations are made:

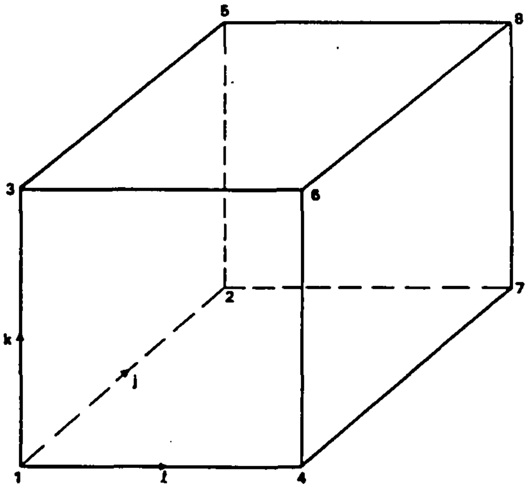

Fig. 1 Computational finite-volume cell

$$\widehat{Q}_{j,k,l} = QV_{j,k,l} \tag{2.6a}$$

where V is the volume of the cell under consideration;

$$\begin{aligned}
&\left(\frac{\xi_{x,y,z}}{J}\right)_{j\pm 1/2} = \\
&n_{x,y,z}\{(k-1/2,l-1/2),(k+1/2,l-1/2), \\
&\qquad (k+1/2,l+1/2),(k-1/2,l+1/2)\}_{j\pm 1/2} \quad , \\
&\left(\frac{\eta_{x,y,z}}{J}\right)_{k\pm 1/2} = \\
&n_{x,y,z}\{(j-1/2,l-1/2),(j-1/2,l+1/2), \\
&\qquad (j+1/2,l+1/2),(j+1/2,l-1/2)\}_{k\pm 1/2} \quad , \\
&\left(\frac{\zeta_{x,y,z}}{J}\right)_{l\pm 1/2} = \\
&n_{x,y,z}\{(j-1/2,k-1/2),(j+1/2,k-1/2),, \\
&\qquad (j+1/2,k+1/2),(j-1/2,k+1/2)\}_{l\pm 1/2} \quad .
\end{aligned} \tag{2.6b}$$

In the above, $n_{x,y,z}$ are the x, y, z components of the representative normals to the surface formed by the four points a, b, c, d implied in $n_{x,y,z}(a, b, c, d)$. Four points do not necessarily lie in one plane and therefore the components $n_{x,y,z}$ refer to representative values for an equivalent single plane.

The evaluation of the volume and metrics (cell-face normals) are now presented in the following subsections. The evaluation of the representative flux is presented in the next major section.

2.2 Computation of Cell Volume

First, the volume of a tetrahedron denoted by its vertices a, b, c, d is evaluated from

$$\begin{aligned}
&V^{tet}(a,b,c,d) = \\
&|x_a[y_b(z_c-z_d) - y_c(z_b-z_d) + y_d(z_b-z_c)] \\
&-x_b[y_a(z_c-z_d) - y_c(z_a-z_d) + y_d(z_a-z_c)] \\
&+x_c[y_a(z_b-z_d) - y_b(z_a-z_d) + y_d(z_a-z_b)] \\
&-x_d[y_a(z_b-z_c) - y_b(z_a-z_c) + y_c(z_a-z_b)]|/6.0
\end{aligned} \tag{2.7}$$

Then, referring to Fig. 1 again, the volume of the hexahedron is computed as a sum of the six individual tetrahedra that constitute it.

$$\begin{aligned}
V = {} & V^{tet}(1,2,5,7) + V^{tet}(1,7,5,8) \\
& + V^{tet}(1,3,5,8) + V^{tet}(1,3,8,6) \\
& + V^{tet}(1,7,8,6) + V^{tet}(1,4,7,6)
\end{aligned} \tag{2.8}$$

It is of interest to note that such a formula will result in the proper evaluation of volume even when some of the faces of the hexahedron collapse to a line or a point.

2.3 Computation of Cell-Face Metrics (Normals)

In Eq. 2.6b, cell-face normals were introduced. Each cell face is identified by four vertices not all of which are necessarily on a single plane (three points being sufficient for defining a plane). In our approach, we allow for this and also for some of the faces to collapse to an edge or even a point. Computationally, we will always identify a face by its four vertices a, b, c, d expressed in the j, k, l subscript system. Physically, some or all of the four vertices may lie at the same x, y, z location.

The cell-face normals are evaluated as

$$\begin{aligned}
n_x(a,b,c,d) &= (dy_{ba}dz_{cb} - dy_{cb}dz_{ba})/2 \\
&\quad + (dy_{dc}dz_{ad} - dy_{ad}dz_{dc})/2 \\
n_y(a,b,c,d) &= (dz_{ba}dx_{cb} - dz_{cb}dx_{ba})/2 \\
&\quad + (dz_{dc}dx_{ad} - dz_{ad}dx_{dc})/2 \\
n_z(a,b,c,d) &= (dx_{ba}dy_{cb} - dx_{cb}dy_{ba})/2 \\
&\quad + (dx_{dc}dy_{ad} - dx_{ad}dy_{dc})/2
\end{aligned} \tag{2.9a}$$

where

$$ds_{12} = s_1 - s_2 \tag{2.9b}$$

where, in turn, s corresponds to x or y or z, and 1 and 2 correspond to a or b or c or d. The first term in each of the definitions is respectively one half of the x, y, or z component of the cross product of the vector from a to b with the vector from b to c. The second term in each definition is correspondingly one half of the x, y, or z component of the cross product of the vector from c to d with the vector from d to a. A cross product of two vectors lies along the direction of the normal to the two vectors. In the present situation, the two vectors are connected. Therefore, such a normal also defines the direction of the normal to the plane containing the two vectors. One half of the cross product of connected vectors also has a magnitude equal to the area of the three dimensional triangular planar shape defined by the two vectors. Thus, while $\xi_{x,y,z}/J, \eta_{x,y,z}/J, \zeta_{x,y,z}/J$ define the x, y, z components of the normals (not unit normals) to the local tangent plane to the constant ξ, η, ζ surfaces respectively, the associated quantities $(n_{x,y,z})_{j,k,l}$ define the components of the normals to the local constant j, k, l planes.

3.0 TVD Discretization

In the last section, the numerical or representative fluxes $\widehat{E}, \widehat{F}, \widehat{G}$ were introduced. These fluxes are so named because they approximate the real fluxes $\overline{E}, \overline{F}, \overline{G}$ to the required order of accuracy. The actual fluxes appearing in the governing partial differential equations depend on the metrics $\xi_{x,y,z}/J, \eta_{x,y,z}/J, \zeta_{x,y,z}/J$ and correspondingly, we allow the numerical fluxes to depend on the numerical metrics (the cell-face normals). In the last section we did point out the link between the metrics and the components of the cell-normals, but the numerical flux was not defined there. The latter task is the subject of this section.

We employ an upwind-biased scheme in our approach in such a fashion as to essentially eliminate numerical or spurious (unphysical) oscillations while, at the same time, achieving high accuracy. In order to describe this type of discretization, we first mention the underlying upwind scheme used in terms of the corresponding approximate Riemann Solver, and then expand upon how high accuracy and the TVD property are built in. More details on these and related topics may be found in Refs. 5 and 6 and in references cited therein.

3.1 Roe's Approximate Riemann Solver

The Riemann Solver is a mechanism to divide the flux difference between neighboring states (between Q_m and Q_{m+1} for e.g.) into component parts associated with each wave field. These can in turn be divided into those that correspond to positive and negative wave speeds. When we compute the numerical flux at the cell face at $m+1/2$ using various combinations of fluxes and positive and negative flux differences, in the finite-volume formulation, we will only use the cell-face normals defined at $m+1/2$ in all the terms contributing to that representative flux. The actual fluxes $\overline{E}, \overline{F}, \overline{G}$, when evaluated with the metrics equated to cell-face normals, can all be written in the same functional form given by

$$\overline{E}, \overline{F}, \overline{G} = f(Q, n_x, n_y, n_z) = f(Q, N) \qquad (3.1)$$

where the appropriate values of n_x, n_y, n_z are used and N denotes the set of those normals. Using such notation, it is possible to present the necessary algebra very concisely.

Let us first denote the Jacobian matrix of the flux f with respect to the dependent variables Q by $\partial f/\partial Q$. This Jacobian can also be called the coefficient matrix. Let us denote the eigenvalues of the coefficient matrix by λ^i and the corresponding left and right eigenvectors by ℓ^i and r^i, respectively. The matrix formed by the left eigenvectors as its rows is then called the left eigenvector matrix L and the matrix of right eigenvectors comprising right eigenvectors as its columns is R. For our purposes, we choose an orthonormal set of left and right eigenvectors which implies that $LR = RL = I$, the identity matrix. In the above, the superscript i has been used to denote the association of the i-th eigenvalue with its corresponding eigenvector. Each eigenvalue is also associated with its own wave field.

The underlying upwind scheme is based upon Roe's approximate Riemann solver[7]. In this approach, cell interface values of density, velocities, and enthalpy ($h = \gamma p/((\gamma - 1)\rho) + (u^2 + v^2 + w^2)/2$) are computed using a special averaging procedure:

$$\begin{aligned}
\rho_{m+1/2} &= \frac{\rho_{m+1}\sqrt{\rho_{m+1}} + \rho_m\sqrt{\rho_m}}{\sqrt{\rho_{m+1}} + \sqrt{\rho_m}} \\
(u, v, w)_{m+1/2} &= \frac{(u, v, w)_{m+1}\sqrt{\rho_{m+1}} + (u, v, w)_m\sqrt{\rho_m}}{\sqrt{\rho_{m+1}} + \sqrt{\rho_m}} \\
h_{m+1/2} &= \frac{h_{m+1}\sqrt{\rho_{m+1}} + h_m\sqrt{\rho_m}}{\sqrt{\rho_{m+1}} + \sqrt{\rho_m}}
\end{aligned} \qquad (3.2)$$

where $m = j$ or k or l. From the above, the speed of sound can be computed from

$$c_{m+1/2} = \sqrt{\{h_{m+1/2} - (u^2 + v^2 + w^2)/2\}(\gamma - 1)} \qquad (3.3)$$

Knowing $(u, v, w, c)_{m+1/2}$, the eigenvalues and orthonormal set of left and right eigenvectors corresponding to a cell face can be computed. These may be denoted by

$$\begin{aligned}
\lambda^i_{m+1/2} &= \lambda^i_{m+1/2}(Q_{m+1/2}, N_{m+1/2}), \\
\ell^i_{m+1/2} &= \ell^i_{m+1/2}(Q_{m+1/2}, N_{m+1/2}), \\
r^i_{m+1/2} &= r^i_{m+1/2}(Q_{m+1/2}, N_{m+1/2}).
\end{aligned} \qquad (3.4)$$

At each cell face, the positive and negative projections of the eigenvalues may be defined by

$$\lambda^{i\pm} = \frac{(\lambda^i_{m+1/2} \pm |\lambda^i_{m+1/2}|)}{2} \quad , i = 1, \cdots, 5 \quad . \qquad (3.5)$$

In order to help Roe's Riemann Solver avoid expansion shocks, only at sonic rarefactions ($\lambda^i(Q_m, N_{m+1/2}) < 0 < \lambda^i(Q_{m+1}, N_{m+1/2})$), the corresponding positive and negative projections are redefined as

$$\begin{aligned}
\lambda^{i\pm}_{m+1/2} &= \lambda^{i\pm}_{m+1/2} \\
&\pm \frac{(\lambda^i(Q_{m+1}, N_{m+1/2}) - \lambda^i(Q_m, N_{m+1/2}))}{4}
\end{aligned} \qquad (3.6)$$

For the sake of completeness, detailed formulae for the eigenvalues and the eigenvector matrices are now presented. Defining the contravariant velocity by

$$\overline{U} = n_x u + n_y v + n_z w \quad , \qquad (3.7)$$

the eigenvalues are given by

$$\begin{aligned}
\lambda^1 &= \overline{U} - c\sqrt{n_x^2 + n_y^2 + n_z^2} \\
\lambda^{2,3,4} &= \overline{U} \\
\lambda^5 &= \overline{U} + c\sqrt{n_x^2 + n_y^2 + n_z^2}
\end{aligned} \qquad (3.8)$$

Defining

$$\hat{n}_{x,y,z} = n_{x,y,z}/\sqrt{n_x^2 + n_y^2 + n_z^2} \qquad (3.9)$$

and

$$\vartheta = (u^2 + v^2 + w^2)/2 \quad , \qquad (3.10)$$

the left and the right eigenvector matrices are given in Table 3.1 and Table 3.2 respectively.

3.2 High-Accuracy TVD Schemes

We can construct upwind-biased schemes of varying accuracies using the basic ingredients given in the last subsection. Here, we present a family of schemes based on the *preprocessing* approach[6]. Let us now define some convenient variables as an intermediate step before defining the numerical flux corresponding to a high-accuracy TVD scheme. First, we define α parameters which are a measure of the change in dependent variables across the corresponding wave family and therefore are a measure of the slope between neighboring states. In the following, the superscript i corresponds, as usual, to the i-th eigenvalue and i-th eigenvector. The subscripts 1, 2, and 3 are just labels to differentiate between the three different types of α parameters.

$$\begin{aligned}
\alpha^i_{1,m+1/2} &= \ell^i_{m+1/2}(Q_m - Q_{m-1}), \\
\alpha^i_{2,m+1/2} &= \ell^i_{m+1/2}(Q_{m+1} - Q_m), \\
\alpha^i_{3,m+1/2} &= \ell^i_{m+1/2}(Q_{m+2} - Q_{m+1}).
\end{aligned} \qquad (3.11)$$

$\left[\frac{\gamma-1}{c}\right]/\sqrt{2}$	$\left[\frac{\gamma-1}{c}\vartheta+\hat{n}_x u + \hat{n}_y v+\hat{n}_z w\right]/\sqrt{2}$	$\left[-\frac{\gamma-1}{c}u - \hat{n}_x\right]/\sqrt{2}$	$\left[-\frac{\gamma-1}{c}v - \hat{n}_y\right]/\sqrt{2}$	$\left[-\frac{\gamma-1}{c}w - \hat{n}_z\right]/\sqrt{2}$
$-\frac{\gamma-1}{c}\hat{n}_y$	$-\frac{\gamma-1}{c}\hat{n}_y\vartheta+\hat{n}_y c -\hat{n}_z u+\hat{n}_x w$	$\frac{\gamma-1}{c}\hat{n}_y u +\hat{n}_z$	$\frac{\gamma-1}{c}\hat{n}_y v$	$\frac{\gamma-1}{c}\hat{n}_y w -\hat{n}_x$
$-\frac{\gamma-1}{c}\hat{n}_z$	$-\frac{\gamma-1}{c}\hat{n}_z\vartheta+\hat{n}_z c +\hat{n}_y u-\hat{n}_x v$	$\frac{\gamma-1}{c}\hat{n}_z u -\hat{n}_y$	$\frac{\gamma-1}{c}\hat{n}_z v +\hat{n}_x$	$\frac{\gamma-1}{c}\hat{n}_z w$
$-\frac{\gamma-1}{c}\hat{n}_x$	$-\frac{\gamma-1}{c}\hat{n}_x\vartheta+\hat{n}_x c +\hat{n}_z v-\hat{n}_y w$	$\frac{\gamma-1}{c}\hat{n}_x u$	$\frac{\gamma-1}{c}\hat{n}_x v -\hat{n}_z$	$\frac{\gamma-1}{c}\hat{n}_x w +\hat{n}_y$
$\left[\frac{\gamma-1}{c}\right]/\sqrt{2}$	$\left[\frac{\gamma-1}{c}\vartheta-\hat{n}_x u - \hat{n}_y v-\hat{n}_z w\right]/\sqrt{2}$	$\left[-\frac{\gamma-1}{c}u + \hat{n}_x\right]/\sqrt{2}$	$\left[-\frac{\gamma-1}{c}v + \hat{n}_y\right]/\sqrt{2}$	$\left[-\frac{\gamma-1}{c}w + \hat{n}_z\right]/\sqrt{2}$

Table 3.1 The left eigenvector matrix L

Next, we define the slope-limited values given by

$$\begin{aligned}
\widetilde{\widetilde{\alpha}}^i_{1,m+1/2} &= \text{minmod}[\alpha^i_{1,m+1/2}, b\,\alpha^i_{2,m+1/2}],\\
\widetilde{\alpha}^i_{2,m+1/2} &= \text{minmod}[\alpha^i_{2,m+1/2}, b\,\alpha^i_{1,m+1/2}],\\
\widetilde{\widetilde{\alpha}}^i_{2,m+1/2} &= \text{minmod}[\alpha^i_{2,m+1/2}, b\,\alpha^i_{3,m+1/2}],\\
\widetilde{\alpha}^i_{3,m+1/2} &= \text{minmod}[\alpha^i_{3,m+1/2}, b\,\alpha^i_{2,m+1/2}].
\end{aligned} \tag{3.12}$$

In the above, the compression parameter b is to be taken as the following function of the accuracy parameter ϕ which is explained shortly.

$$b = \frac{3-\phi}{1-\phi} \tag{3.13}$$

The "minmod" slope-limiter operator is

$$\text{minmod}[x,y] = \text{sign}(x)\ \max[0, \min\{|x|, y\,\text{sign}(x)\}] \tag{3.14}$$

In Eq. 2.4, we introduced numerical fluxes $\widehat{E}, \widehat{F}, \widehat{G}$. Based on the concise notation of using f to represent either $\overline{E}$ or $\overline{F}$ or $\overline{G}$, let us use $\widehat{f}$ to denote the numerical fluxes $\widehat{E}$ or $\widehat{F}$ or $\widehat{G}$. We can then write down a family of TVD schemes as follows in terms of the previously defined α parameters (with the subscript $m+1/2$ dropped from these for convenience):

$$\begin{aligned}
\widehat{f}_{m+1/2} = h_{m+1/2}&\\
&+\sum_i\left(\frac{1+\phi}{4}\widetilde{\alpha}^i_2+\frac{1-\phi}{4}\widetilde{\widetilde{\alpha}}^i_1\right)\lambda^{i+}_{m+1/2}r^i_{m+1/2}\\
&-\sum_i\left(\frac{1+\phi}{4}\widetilde{\widetilde{\alpha}}^i_2+\frac{1-\phi}{4}\widetilde{\alpha}^i_3\right)\lambda^{i-}_{m+1/2}r^i_{m+1/2}
\end{aligned} \tag{3.15}$$

The first term on the right hand side of Eq. 3.15 defines a first-order numerical flux and is constructed from

$$\begin{aligned}
h_{m+1/2} &= \frac{1}{2}\left[f(Q_{m+1}, N_{m+1/2}) + f(Q_m, N_{m+1/2})\right]\\
&\quad -\frac{1}{2}\left[\sum_i\left(\lambda^{i+}_{m+1/2}-\lambda^{i-}_{m+1/2}\right)\alpha^i_2 r^i_{m+1/2}\right]\\
&= f(Q_m, N_{m+1/2}) + \sum_i \lambda^{i-}_{m+1/2}\alpha^i_2 r^i_{m+1/2}\\
&= f(Q_{m+1}, N_{m+1/2}) - \sum_i \lambda^{i+}_{m+1/2}\alpha^i_2 r^i_{m+1/2}
\end{aligned} \tag{3.16}$$

The remaining terms on the right hand side of Eq. 3.15 define correction terms that upgrade the accuracy. For use in the next subsection, we define

$$df^{i\pm}_{m+1/2} = \lambda^{i\pm}_{m+1/2}\alpha^i_{2,m+1/2}r^i_{m+1/2} \quad . \tag{3.17}$$

It is interesting to note that in all the above formulae used to define the numerical flux at $m+1/2$, the eigenvectors and eigenvalues are only necessary at the corresponding cell interface. Therefore, the only geometry information used corresponds to the cell-face normals at $m+1/2$. The solution variables Q are sampled between the centroidal points $m-1, m, m+1, m+2$ when the various α parameters are defined.

The parameter ϕ defines schemes of varying accuracy. The notations $\widetilde{\alpha}^i$ and $\widetilde{\widetilde{\alpha}}^i$ have been used to define slope-limited values of the α parameters. If we replace these by their unlimited values, we obtain schemes whose truncation error in one-dimensional steady-state problems on uniform grids is given by

$$TE = -\left(\frac{\phi-\frac{1}{3}}{4}\right)(\Delta x)^2\frac{\partial f}{\partial Q}\frac{\partial^3 Q}{\partial x^3} \quad . \tag{3.18}$$

$\left[\frac{\vartheta}{c} + \frac{c}{\gamma - 1} - \hat{n}_x u - \hat{n}_y v - \hat{n}_z w\right] / \sqrt{2}$	$\frac{\vartheta}{c}\hat{n}_y + \hat{n}_z u - \hat{n}_x w$	$\frac{\vartheta}{c}\hat{n}_z - \hat{n}_y u + \hat{n}_x v$	$\frac{\vartheta}{c}\hat{n}_x - \hat{n}_z v + \hat{n}_y w$	$\left[\frac{\vartheta}{c} + \frac{c}{\gamma - 1} + \hat{n}_x u + \hat{n}_y v + \hat{n}_z w\right] / \sqrt{2}$
$\left[\frac{1}{c}\right] / \sqrt{2}$	$\frac{\hat{n}_y}{c}$	$\frac{\hat{n}_z}{c}$	$\frac{\hat{n}_x}{c}$	$\left[\frac{1}{c}\right] / \sqrt{2}$
$\left[\frac{u}{c} - \hat{n}_x\right] / \sqrt{2}$	$\frac{u}{c}\hat{n}_y + \hat{n}_z$	$\frac{u}{c}\hat{n}_z - \hat{n}_y$	$\frac{u}{c}\hat{n}_x$	$\left[\frac{u}{c} + \hat{n}_x\right] / \sqrt{2}$
$\left[\frac{v}{c} - \hat{n}_y\right] / \sqrt{2}$	$\frac{v}{c}\hat{n}_y$	$\frac{v}{c}\hat{n}_z + \hat{n}_x$	$\frac{v}{c}\hat{n}_x - \hat{n}_z$	$\left[\frac{v}{c} + \hat{n}_y\right] / \sqrt{2}$
$\left[\frac{w}{c} - \hat{n}_z\right] / \sqrt{2}$	$\frac{w}{c}\hat{n}_y - \hat{n}_x$	$\frac{w}{c}\hat{n}_z$	$\frac{w}{c}\hat{n}_x + \hat{n}_y$	$\left[\frac{w}{c} + \hat{n}_z\right] / \sqrt{2}$

Table 3.2 The right eigenvector matrix R

Here, the truncation error refers to the difference between the centroidal value of the numerical solution and the average value of the exact solution in that cell. The choice of $\phi = 1/3$ results in a TVD scheme based on an underlying third-order scheme. The choice of $\phi = -1$ results in a TVD scheme based on the fully upwind second-order accurate formulation. Fromm's scheme arises when $\phi = 0$.

3.3 TVD Schemes and Diagonal Dominance

In the next section, a procedure is presented to solve the finite difference equations resulting from the TVD discretization of the space differencing terms. In supersonic zones, the method reduces to a simple marching scheme, while in subsonic zones it becomes a relaxation approach and both forward and backward sweeps are employed along the marching direction. In order for such a relaxation approach to be stable, a sufficient condition is the diagonal dominance of the underlying finite difference scheme. This diagonal dominance can be shown to exist for TVD discretizations. For more details, the reader is referred to Ref. 8.

4.0 The Solution Procedure

We begin this section by considering an implicit time discretization coupled with the TVD space discretization discussed earlier in terms of the corresponding numerical flux terms.

$$\begin{aligned}\frac{\hat{Q}^{n+1} - \hat{Q}^n}{\Delta\tau} &+ \left(\hat{E}_{j+1/2} - \hat{E}_{j-1/2}\right)^{n+1} \\ &+ \left(\hat{F}_{k+1/2} - \hat{F}_{k-1/2}\right)^{n+1} \\ &+ \left(\hat{G}_{l+1/2} - \hat{G}_{l-1/2}\right)^{n+1} = 0\end{aligned} \tag{4.1}$$

Here, n is the index in time and $\Delta\tau$ is the time step. In what follows, we will consider the linearization of the above nonlinear set of finite difference equations. Then we will simplify the algebraic solution procedure by approximately factorizing the implicit operator in the cross-flow plane (which is a plane in only computational coordinates—constant j plane). The marching direction is along j. We will further specialize the scheme for the two cases of supersonic and subsonic velocity components in the marching direction.

4.1 Linearization

Let us linearize Eq. 4.1 about a known state $Q = q^s$ using a Newton procedure to obtain a better approximation q^{s+1} to Q^{n+1}. Here, s is a subiteration index. Defining

$$\begin{aligned}\Delta^s q &= q^{s+1} - q^s \\ \Delta_j \hat{E} &= \hat{E}_{j+1/2} - \hat{E}_{j-1/2} \\ \Delta_k \hat{F} &= \hat{F}_{k+1/2} - \hat{F}_{k-1/2} \\ \Delta_l \hat{G} &= \hat{G}_{l+1/2} - \hat{G}_{l-1/2} \quad ,\end{aligned} \tag{4.2}$$

we can describe the Newton procedure by

$$\begin{aligned}&\left[\frac{V}{\Delta\tau} I + \frac{\partial}{\partial q}(\Delta_j \hat{E} + \Delta_k \hat{F} + \Delta_l \hat{G})\right] \Delta^s q = \\ &\left[\frac{V}{\Delta\tau}(q^s - Q^n) + \Delta_j \hat{E}(q^s) + \Delta_k \hat{F}(q^s) + \Delta_l \hat{G}(q^s)\right] \quad .\end{aligned} \tag{4.3}$$

We next simplify the left hand side by defining an approximation to the true linearization. Towards this goal, we consider only a first-order accurate scheme (based on the first-order numerical flux h) for the left hand side while we include the full high-accuracy scheme on the right hand side. Even so, when the subiterations converge, the right hand side is satisfied to the desired degree. Next we assume that the eigenvalues and eigenvectors are not functions of q. Finally, we observe that

$$\begin{aligned}&\sum_{m=j,k,l} h_{m+1/2} - h_{m-1/2} = \\ &\qquad \sum_{m=j,k,l} \sum_i df^{i+}_{m-1/2} + \sum_{m=j,k,l} \sum_i df^{i-}_{m+1/2}\end{aligned} \tag{4.4}$$

because, in expanding Eq. 4.4 using Eq. 3.16, we find that

$$\begin{aligned}\sum_{m=j,k,l} [(n_x)_{m+1/2} - (n_x)_{m-1/2}] &= 0 \\ \sum_{m=j,k,l} [(n_y)_{m+1/2} - (n_y)_{m-1/2}] &= 0\end{aligned} \tag{4.5}$$

$$\sum_{m=j,k,l} [(n_x)_{m+1/2} - (n_x)_{m-1/2}] = 0$$

when the cell-face normals are evaluated using the formulae given in Eq. 2.9. Using the above, Eq. 4.3 is simplified to

$$\begin{aligned}
&\frac{V}{\Delta\tau}\Delta^s q \\
&+A^+_{j-1/2}(\Delta^s q_j - \Delta^s q_{j-1}) + A^-_{j+1/2}(\Delta^s q_{j+1} - \Delta^s q_j) \\
&+B^+_{k-1/2}(\Delta^s q_k - \Delta^s q_{k-1}) + B^-_{k+1/2}(\Delta^s q_{k+1} - \Delta^s q_k) \\
&+C^+_{l-1/2}(\Delta^s q_l - \Delta^s q_{l-1}) + C^-_{l+1/2}(\Delta^s q_{l+1} - \Delta^s q_l) \\
&=\text{Right Hand Side of Eq. 4.3}
\end{aligned} \tag{4.6}$$

where

$$\begin{aligned}
A^\pm_{j\pm 1/2} &= R_{j\pm 1/2}\Lambda^\pm_{j\pm 1/2}L_{j\pm 1/2} \\
B^\pm_{k\pm 1/2} &= R_{k\pm 1/2}\Lambda^\pm_{k\pm 1/2}L_{k\pm 1/2} \\
C^\pm_{l\pm 1/2} &= R_{l\pm 1/2}\Lambda^\pm_{l\pm 1/2}L_{l\pm 1/2} \quad .
\end{aligned} \tag{4.7}$$

Here,

$$\Lambda^\pm = (\Lambda + |\Lambda|)/2 \tag{4.8}$$

in which Λ is the diagonal matrix whose diagonal elements are λ^i and $|\Lambda|$ is the diagonal matrix whose diagonal elements are $|\lambda^i|$.

4.2 Planar Gauss-Seidel Relaxation

Even after the many simplifications leading to Eq. 4.6, it is obvious that more algebraic simplification is needed before a computationally feasible and efficient solution procedure is obtained. This is because Eq. 4.6 signifies a system of equations which links every point j, k, l with its six neighbors $j+1, j-1, k+1, k-1, l+1, l-1$ in such a fashion that the left hand side of Eq. 4.6, when considered for all grid points, is a huge (even though sparse) matrix whose bandwidth is also very large. Of course, for supersonic flows, a fully upwind difference approximation arises in the j direction and the dimensionality is reduced because the left hand side does not link j with $j+1$. However, with our expressed aim of developing a method for subsonic pockets also, it is necessary to consider the case when j is linked with both its neighbors $j-1$ and $j+1$. In such a case, a direct Gaussian elimination procedure for the matrix system of equations would be unacceptably expensive. Therefore, instead of a direct elimination procedure, we seek to obtain an efficient relaxation solution to Eq. 4.6. We choose a planar Gauss-Seidel procedure by retaining all terms of the left hand side except the off-diagonal terms in j (those terms that multiply $\Delta^s q_{j\pm 1}$). That such a procedure will be stable for TVD discretizations was discussed in Section 3.3 and in the references cited therein.

The planar Gauss-Seidel procedure can be written as

$$\begin{aligned}
&[\frac{I}{\Delta\tau} + \frac{1}{V}A^+_{j-1/2} + \frac{1}{V}A^-_{j+1/2}]\Delta^s q_j \\
&+ \frac{1}{V}B^+_{k-1/2}(\Delta^s q_k - \Delta^s q_{k-1}) \\
&+ \frac{1}{V}B^-_{k+1/2}(\Delta^s q_{k+1} - \Delta^s q_k) \\
&+ \frac{1}{V}C^+_{l-1/2}(\Delta^s q_l - \Delta^s q_{l-1}) \\
&+ \frac{1}{V}C^-_{l+1/2}(\Delta^s q_{l+1} - \Delta^s q_l) \\
&= \frac{1}{V}[\text{Right Hand Side of Eq. 4.3}] \quad .
\end{aligned} \tag{4.9}$$

Denoting

$$\widehat{A} = \frac{I}{\Delta\tau} + \frac{1}{V}A^+_{j-1/2} + \frac{1}{V}A^-_{j+1/2} \quad , \tag{4.10}$$

we can rewrite Eq. 4.9 as

$$\begin{aligned}
&\Big[I + \frac{1}{V}\widehat{A}^{-1}\Big\{B^+_{k-1/2}\Delta_{k-1/2} + B^-_{k+1/2}\Delta_{k+1/2} \\
&\qquad\qquad +C^+_{l-1/2}\Delta_{l-1/2} + C^-_{l+1/2}\Delta_{l+1/2}\Big\}\Big]\Delta^s q \\
&= \frac{1}{V}\widehat{A}^{-1}[\text{Right Hand Side of Eq. 4.3}] \quad .
\end{aligned} \tag{4.11}$$

Of course, when the relaxation cycles denoted by superscript s converge to the desired extent, $\Delta^s q = 0$, and the full accurate formulae of the right hand side will be satisfied to a corresponding degree.

4.3 Approximate Factorization in the Plane

While Eq. 4.11 defines an algebraic set of equations whose dimensionality is one order less than that of Eq. 4.9, it is still too huge to be tackled by an elimination algorithm. Therefore, we will now further reduce the dimensionality by approximately factorizing the left hand side of Eq. 4.11 to result in

$$\begin{aligned}
&\Big[I + \frac{1}{V}\widehat{A}^{-1}\Big\{B^+_{k-1/2}\Delta_{k-1/2} + B^-_{k+1/2}\Delta_{k+1/2}\Big\}\Big] \\
&\Big[I + \frac{1}{V}\widehat{A}^{-1}\Big\{C^+_{l-1/2}\Delta_{l-1/2} + C^-_{l+1/2}\Delta_{l+1/2}\Big\}\Big]\Delta^s q \\
&= \frac{1}{V}\widehat{A}^{-1}[\text{Right Hand Side of Eq. 4.3}] \quad .
\end{aligned} \tag{4.12}$$

The actual sequence of steps to solve Eq. 4.12 can be chosen so that $\widehat{A}^{-1}$ need not actually computed and only $\widehat{A}$ is needed. For this purpose, we solve, in order, the equations

$$\begin{aligned}
&\Big[\widehat{A} + \frac{1}{V}\Big\{B^+_{k-1/2}\Delta_{k-1/2} + B^-_{k+1/2}\Delta_{k+1/2}\Big\}\Big]\overline{q} \\
&= \frac{1}{V}[\text{Right Hand Side of Eq. 4.3}]
\end{aligned} \tag{4.13a}$$

and

$$\begin{aligned}
&\Big[\widehat{A} + \frac{1}{V}\Big\{C^+_{l-1/2}\Delta_{l-1/2} + C^-_{l+1/2}\Delta_{l+1/2}\Big\}\Big]\Delta^s q \\
&= \widehat{A}\overline{q} \quad .
\end{aligned} \tag{4.13b}$$

with $\overline{q}$ being a temporary storage variable.

Let us summarize the solution procedure developed in Eq. 4.13 for just one constant j plane. Equation 4.13a must be solved for all k-varying lines (for all l). Then Eq. 4.13b must be solved for all l-varying lines (for all values of k). However, each k-varying or l-varying line is associated with only a one-dimensional block-tridiagonal system of algebraic equations whose block matrices are 5×5. These two steps only constitute one cycle of the Gauss-Seidel iterations and that too for only one constant j plane. The planar Gauss-Seidel procedure requires that one constant j plane is updated at a time. When the neighboring j plane is updated next, the latest available values of the update variables q are used in the right and left hand sides. The j sweep strategy will be specialized for supersonic and subsonic flow regions in what follows.

4.4 Programming Notes

We store grid information at two planes (grid-planes 2 and 3) which describe the j boundaries ($j-1/2, j+1/2$) of one plane of cells. Let the centroids of these cells be denoted as solution-plane 3. Array storage is provided for dependent variable planes (solution-planes) 1,2,3,4,5. As the solution is marched, the contents of the grid-plane and solution-plane arrays are updated by replacing them with neighboring values or by the planar Gauss-Seidel algorithm.

Let us consider the very first marching sweep now. We begin by initializing the two grid planes and the dependent variables at solution-planes 1 and 2. We are interested in updating the solution at plane 3. We first set the solution at planes 3, 4 and 5 to be equal to the values at solution-plane 3. After one or more subiterations for solution-plane 3, we shift our attention to the next j-plane. Grid-plane 2 is replaced with the contents of grid-plane 3. Grid-plane 3 nodal values are stored on auxiliary storage for later use. New values for grid-plane 3 are generated by grid generation procedures or read in from auxiliary storage initialized previously. Similarly, solution-plane 3 is saved on auxiliary storage for subsequent processing. Solution-plane 1 is replaced by contents of solution-plane 2, and plane 2 is then replaced by contents of plane 3. Solution-planes 4 and 5 are set to the values at plane 3 and the marching proceeds.

If more than one subiteration is to be performed in the first marching sweep, the grid information is not updated for the subsequent subiterations. Solution-planes 4 and 5 are reset to values at solution-plane 3 after the previous subiteration and the next subiteration is processed. Solution-plane 3 values are not set to solution-plane 2 values for the second and subsequent subiterations.

For fully supersonic flows, a fully-upwind, not-flux-limited differencing scheme is used. Thus, the values set for solution-planes 4 and 5 are actually not used at all. Forward marching is enough. Even first-order upwind scheme in the j-direction and one subiteration per marching plane are also often enough. A small value is input for the reciprocal of time step. Accuracy of approximate factorization for any time step size is maintained due to reasonable marching step size (distance between j grid planes).

Subsonic regions could develop as a result of gradual compression (for e.g., around canopies) or abrupt transition through a shock wave (for e.g., in front of a blunt nosed object in an oncoming supersonic flow). In such regions, a larger value is chosen for the reciprocal of time step. The solution is marched forward using one or more (usually a maximum of two) subiterations by conforming to the procedure outlined above for the first marching sweep. Then, a backward marching sweep (or even another forward marching sweep) is performed. For all sweeps (forward or backward) after the first, solution planes are filled with previous sweep solution values before updating using subiterations. Shifted replacements of solution-plane values of dependent variables are not used. For subsonic regions (subsonic pockets in supersonic flow), a TVD formulation of the desired accuracy is used enabling even strong shocks to be captured routinely.

For very small pockets of subsonic flow caused by gradual compression, one forward sweep followed by one reverse sweep is enough. Even the reverse sweep is usually redundant in this case. For larger subsonic zones, a few (tens) of sweeps usually suffice. Residues are monitored for convergence.

5.0 Boundary Point Treatment

Only an outline of the boundary point treatment will be presented here due to lack of space. The boundary method used is fully compatible with the interior point differencing. It is based on considering a Riemann Initial and Boundary Value Problem at the boundary to construct the boundary point discretization. In this, it is similar in spirit to the correspondence between interior point discretization and the Riemann Initial Value Problem. The implementation is specifically tailored to approximately factored implicit schemes. Linear boundary conditions (such as surface tangency) are exactly satisfied after every marching step. Corner points are also properly treated. More details on the new treatment used here including theoretical background and implementation details for explicit and other implicit methods are available in Ref. 9. A brief description of the type of boundary condition techniques used here can also be found in Ref. 5. Another approach to boundary condition procedures which can be applied to implicit schemes for the Euler equations is presented in Ref. 10. The importance of proper and accurate boundary condition procedures is demonstrated in Ref. 4.

6.0 COMPUTATIONAL EXAMPLES

The preceding sections have described an Euler Marching Technique for Accurate Computations (EMTAC) and we now present many computational results obtained using the EMTAC code. The first set of results are for an analytically defined forebody geometry and these results are compared with experimental data. The next case considered is the supersonic flow over a twisted-cone spike of a hypothetical aircraft inlet and the results are compared with numerical results obtained using a full potential marching code. The third set of results are for a realistic fighter configuration and once again most of the comparisons for this case are with the full potential marching code. The last set of results are for a Shuttle Orbiter configuration and the numerical results are compared with experimental data for this case.

6.1 Analytic Forebody

Figure 2a shows the developed cross-section of a forebody geometry reported in Ref. 11. The surface pressure distributions in the axial direction on the upper ($\theta = 0°$, leeward side) and lower ($\theta = 180°$, windward side) planes of symmetry at $M_\infty = 2.5, \alpha = 0°$ are given in Fig. 2b. The grid and circumferential pressure distribution on the body surface at $x/\ell = 0.22$ and $x/\ell = 0.34$ for the same free-stream conditions are presented in Figs. 2c and 2d respectively. Figure 2e shows the circumferential pressure distribution on the same geometry for $M_\infty = 1.7, \alpha = -5°$ at $x/\ell = 0.278$. It is noted that a small subsonic pocket develops, for this second case, on the lee side and two global marching sweeps are enough for the present numerical method to give a very good converged solution. The experimental data[11] are also presented in these figures. The comparisons show that the present numerical predictions are in excellent agreement with experimental data.

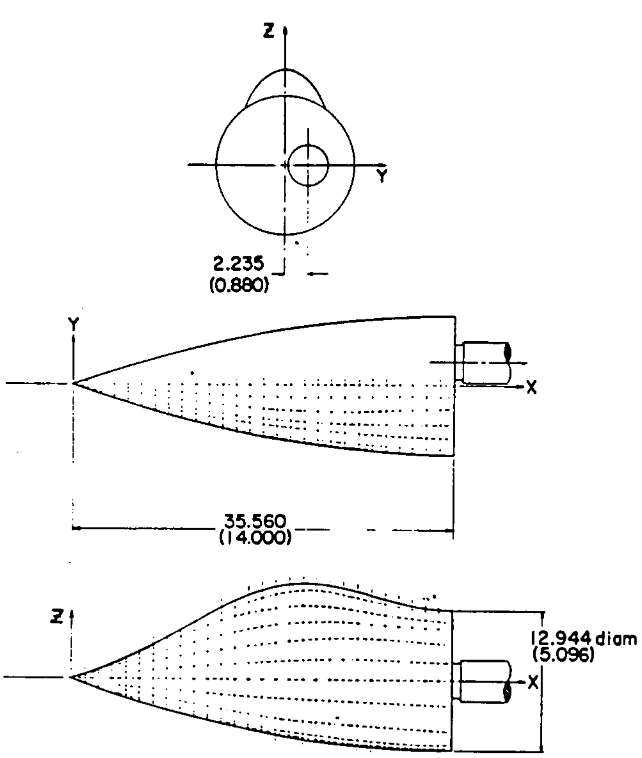

Fig. 2a Forebody geometry

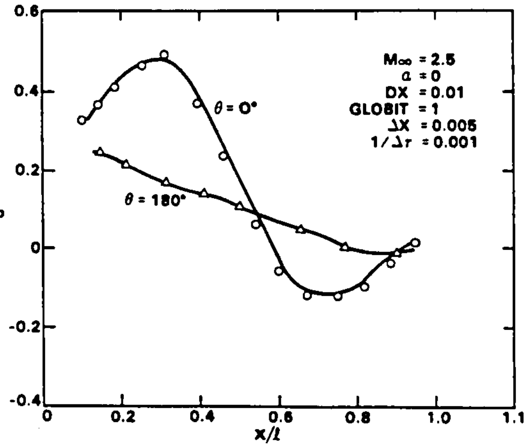

Fig. 2b Axial pressure distribution

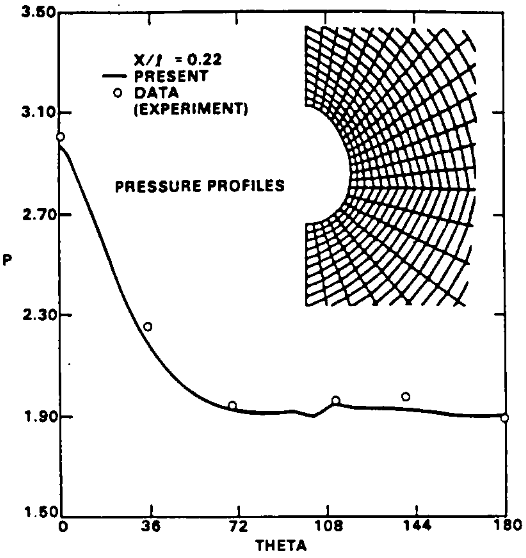

Fig. 2c Circumferential pressure distribution at $x/\ell = 0.22$

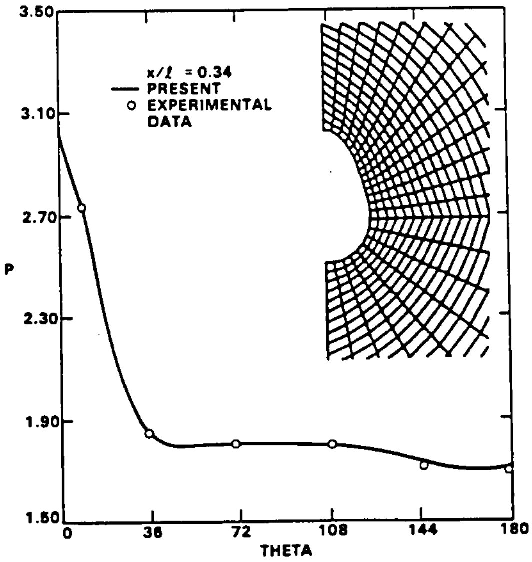

Fig. 2d Circumferential pressure distribution at $x/\ell = 0.34$

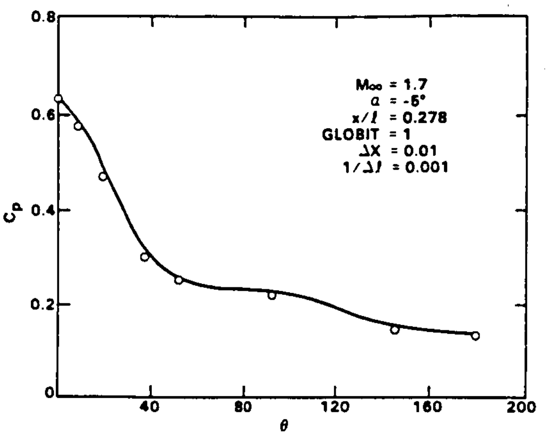

Fig. 2e Circumferential pressure distribution at $M_\infty = 1.7, x/\ell = 0.34$

6.2 Twisted-Cone Inlet Spike

Figure 3a presents the geometry of a twisted-cone inlet spike. At $M_\infty = 2.5$, the pressure contours at various x locations are given in Fig. 3b. The circumferential pressure at $x = 40$ is compared with results obtained using a full potential solver (SIMP, described in Refs. 1-3) in Fig. 3c. As expected, the full potential method predicts a higher pressure on the upper surface where a strong nonisentropic shock is formed for the case considered. This shows the importance of using an Euler solver rather than a full potential solver for supersonic flow computations which must capture strong shock waves.

6.3 Realistic Fighter Configuration

Figure 4a shows the geometry and surface gridding of a realistic fighter-type configuration which includes a nacelle and a vertical tail. To illustrate the important features of the present analysis method, results have been obtained for the free-stream condition $M_\infty = 1.6, \alpha = 4.94°$. The results are compared with those obtained using the SIMP full potential solver. Figures 4b and 4c present the surface pressure at the upper and lower symmetry plane. The results show the excellent agreement between the predictions of these two codes. Circumferential pressure distributions and pressure contours at two different x locations which include the nacell, vertical-tail, wake and wing are presented in Figs. 4d-e. The comparison shows very good agreement except at the lower surface of the wing in the vicinity of the wake region. A higher pressure is predicted by the Euler (EMTAC) code. It is also noted that the wake treatment in both methods provides the correct zero pressure jump across the wake.

Table 6.1 shows the comparison of overall forces in terms of C_L, C_D and C_L/C_D. The drag calculation includes skin friction drag estimated using a boundary layer technique and an estimate of the base drag. Both the full potential and Euler results agree very well with Rockwell experimental data with the Euler results being closer to the data.

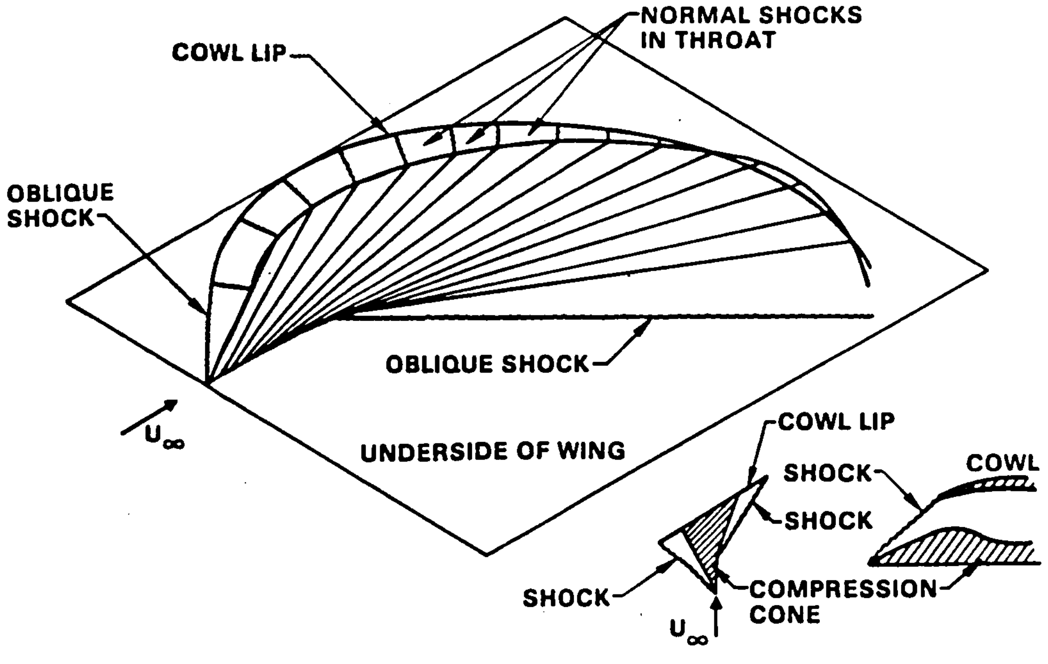

Fig. 3a Spiral inlet-cone geometry

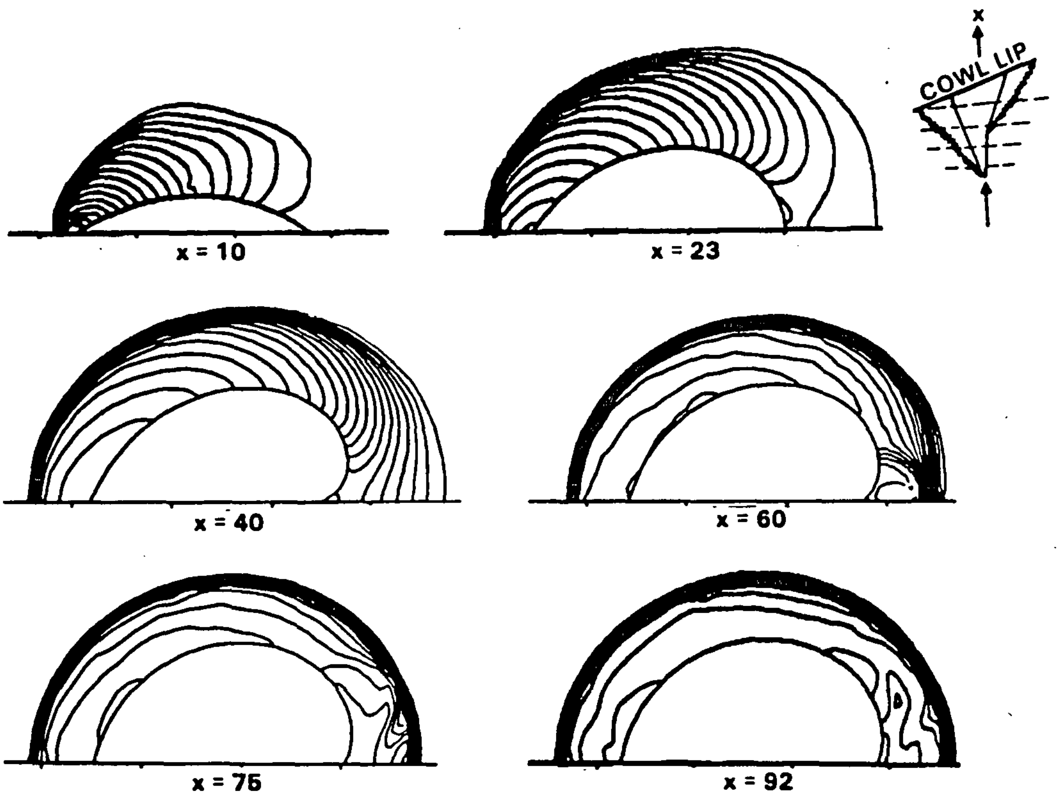

Fig. 3b Pressure contours - evolution of inlet compression cone shock pattern

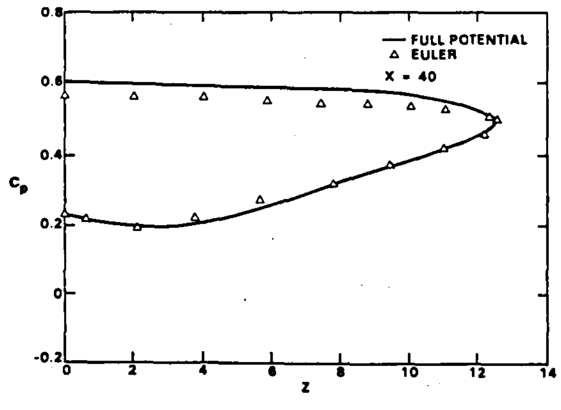

Fig. 3c Circumferential pressure distribution

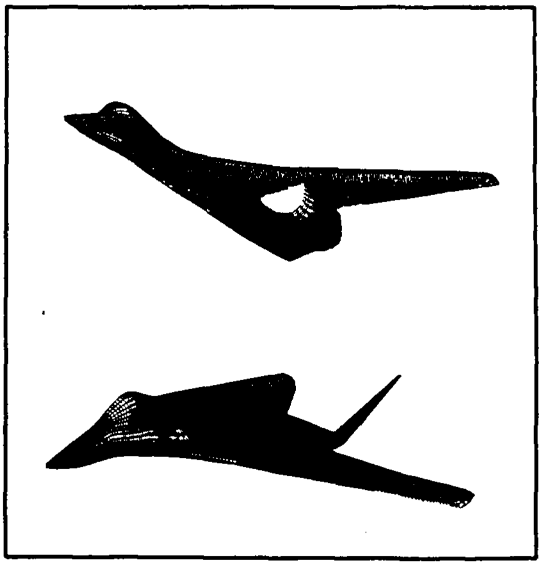

Fig. 4a Geometry and surface grid for realistic fighter-type configuration

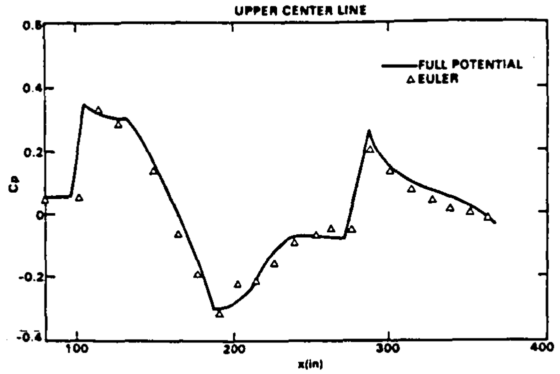

Fig. 4b Surface pressure distribution along upper symmetry plane

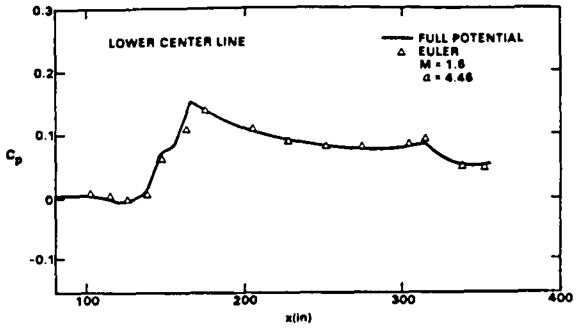

Fig. 4c Surface pressure distribution along lower symmetry plane

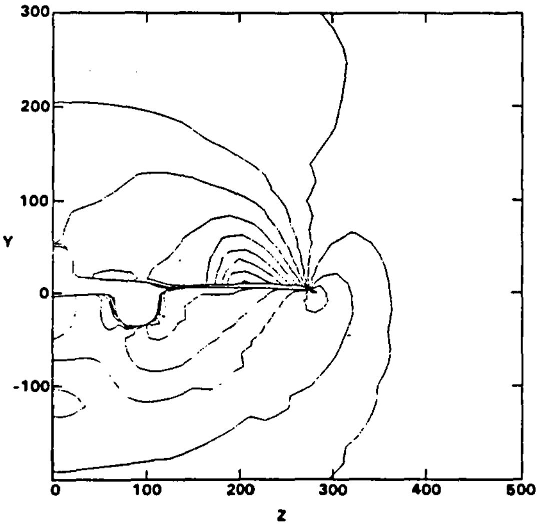

Fig. 4d Pressure contours at $x = 550$ in.

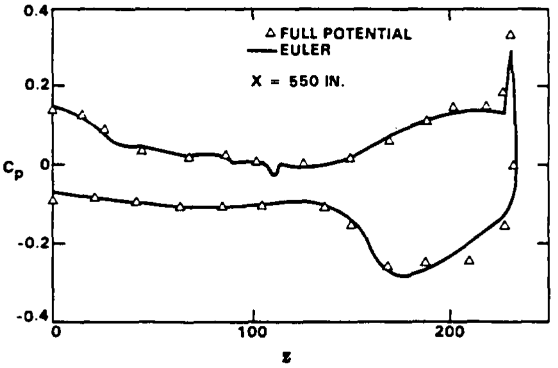

Fig. 4e Circumferential pressure distribution

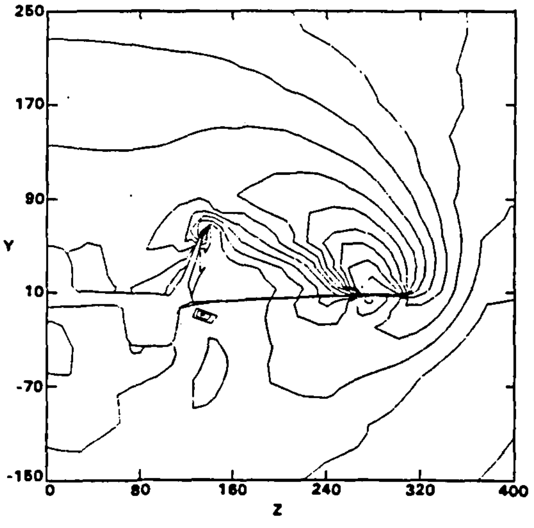

Fig. 4f Pressure contours at $x = 688$ in.

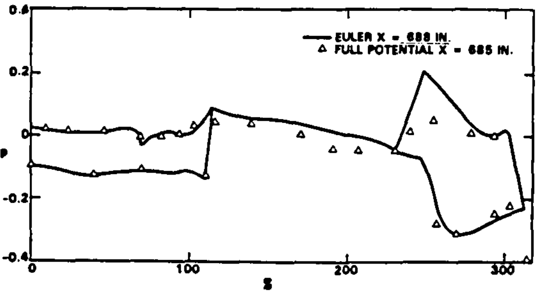

Fig. 4g Circumferential pressure distribution

	SIMP	EMTAC	DATA
C_L	0.30588	0.3017	0.303
C_D	$0.032458 + 0.013$ $= 0.045458$	$0.03433 + 0.013$ $= 0.04733$	0.0475
C_L/C_D	6.72	6.38	6.42

Table 6.1 Comparison of Potential, Euler and and experimental data for $C_L, C_D, C_L/C_D$

6.4 Space Shuttle Orbiter

Figures 5a-5g give the geometry, gridding and corresponding flow-field solutions for an isolated Space Shuttle Orbiter flying at $M_\infty = 1.4, \alpha = 0°$. The EMTAC code is applied to compute the flow field about the entire orbiter, from nose to tail. Multiple (uni- or bi-directional sweeps are used in the nose region to capture the detached bow shock and the subsonic region behind it. After this subsonic region transitions by expansion, over the shoulder region of the nose, into a supersonic flow-field, a simple forward-marching technique is employed. Multiple relaxation sweeps are also used in the canopy and OHMS pod regions to compute the locally subsonic regions.

The surface pressure distribution along the leeward plane of symmetry in the nose region is presented in Fig. 7b. At x = 170 in., which is the beginning of the canopy, the pressure increases rapidly from C_p = 0.3 to ≈ 1.0. An embedded subsonic pocket is formed in the canopy region and required three relaxation marching sweeps to develop

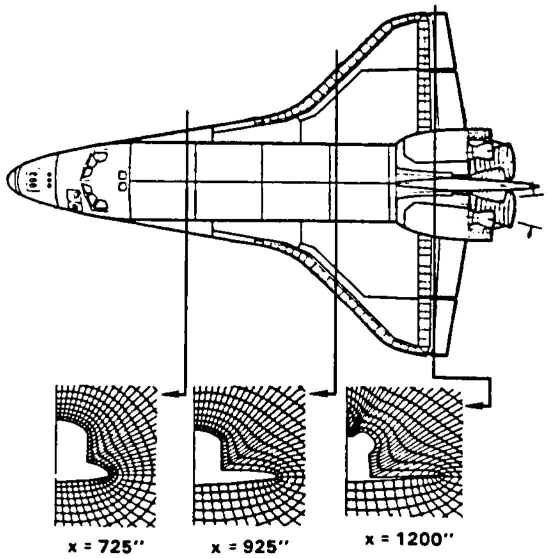

Fig. 5a Shuttle Orbiter configuration and sample grids.

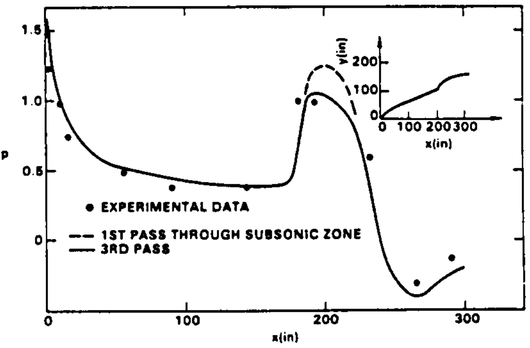

Fig. 5b Surface pressure distribution along upper symmetry plane

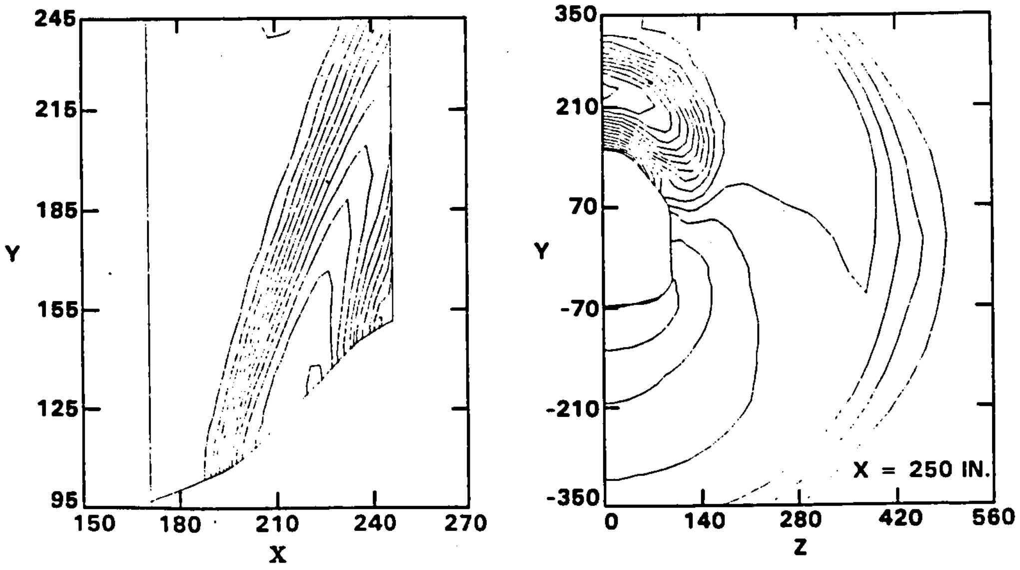

Fig. 5c Canopy region pressure contours for $x - y$ and $z - y$ sectional cuts

the solution. The results show that the present prediction is in excellent agreement with data. Pressure contours on the upper symmetry plane and on the marching plane cross-sectional views are shown in Fig. 5c. The shock and expansion waves induced by the canopy can be clearly seen in this figure.

Figure 5d shows the details of the orbiter geometry in the OMS pod region as modeled in this study. A detached OMS pod shock and a large subsonic pocket are formed in this region. Since the subsonic pocket is big and the Mach number is almost zero near the root of the OMS pod, a total of 30 relaxation marching sweeps (forward only) are required to give a good, converged result. Figure 5e presents the pressure and Mach number contours as obtained in this region. The cross-sectional pressure contours at $x = 1080$ in. and $x = 1125$ in. are given in Fig. 5f. The OMS pod shock is formed around $x = 1050$ in., then grows and finally hits the upper wing surface at $x \approx 1095$ in.. The chordwise pressure distributions on the upper surface of the wing at several span stations are compared with experimental data in Fig. 5g. It is seen that the present calculation agrees with the experimental data very well over the entire upper surface including in the region where the OMS pod shock interacts with the wing surface.

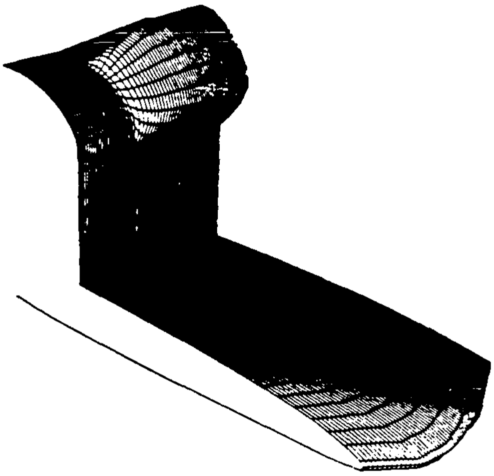

Fig. 5d Computational surface geometry of Orbiter at OMS pod region

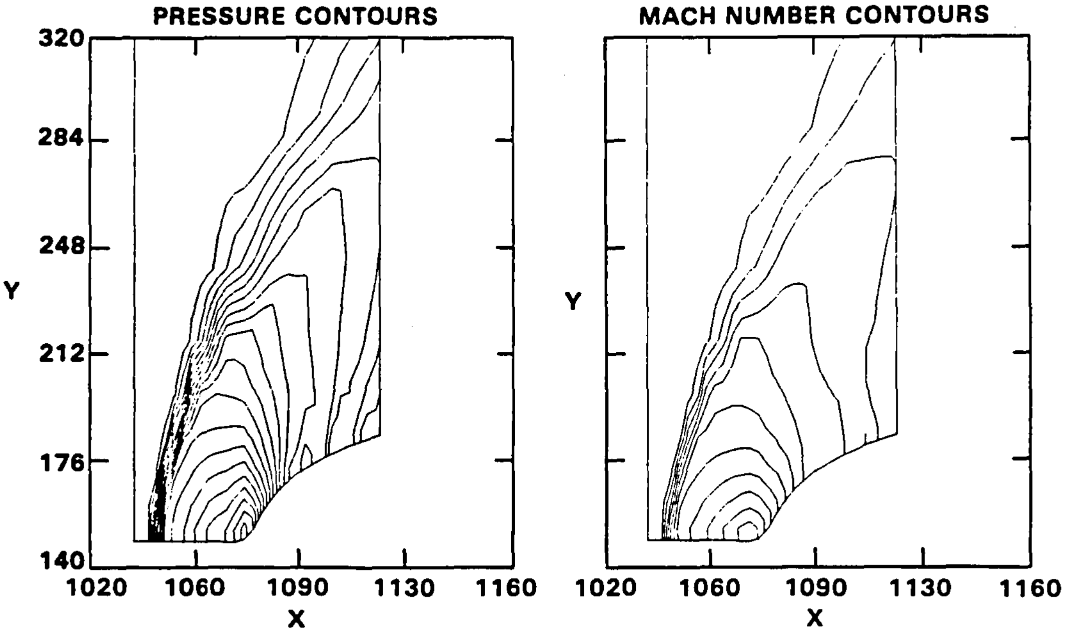

Fig. 5e Pressure and Mach number contours at OMS pod region: $x - y$ section

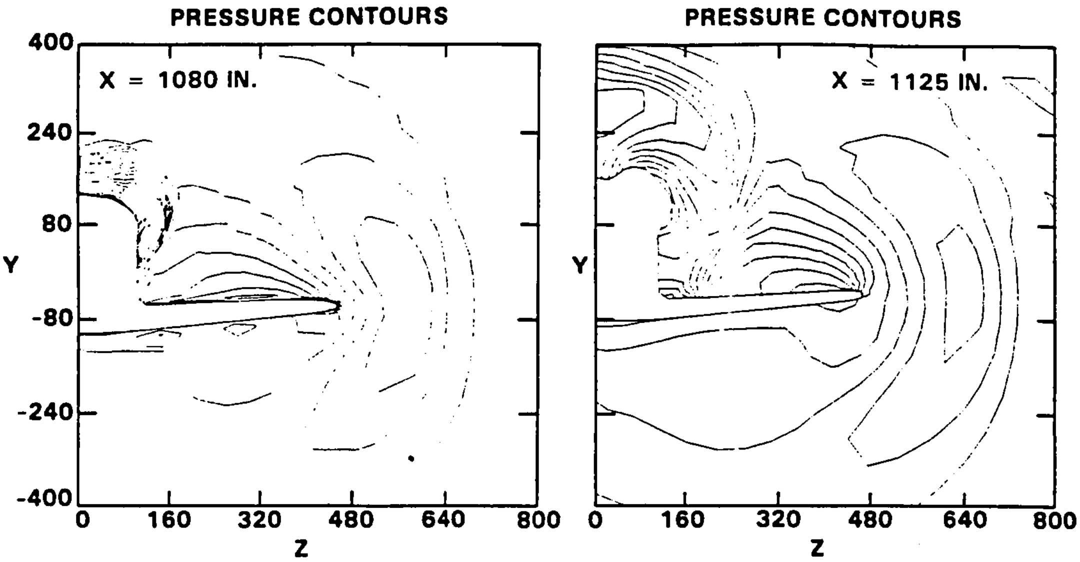

Fig. 5f Pressure contours at OMS pod region: $z - y$ section

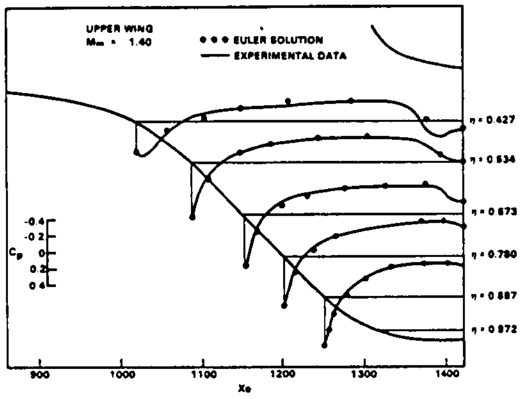

Fig. 5g Orbiter upper surface pressure distribution

7.0 CONCLUDING REMARKS

A new computational procedure has been devised to solve the Euler equations for three-dimensional supersonic inviscid flows with subsonic pockets. The method is akin to a simple marching procedure in portions of the flow field where the component of velocity normal to the local marching plane is supersonic. When this local velocity is subsonic (in subsonic pockets for example), a relaxation approach is used. The marching and relaxation strategies are both but variations of a unified approach to the development of finite difference methods for this class of problems. This approach is based on a planar Gauss-Seidel procedure coupled with approximate factorization in the plane. Being an expository paper, detailed formulae are presented to aid the reader who would like to program the method independently.

It is of interest to note the following observations: The method presented is not only applicable to supersonic flows with subsonic pockets, but is also applicable to all compressible inviscid flow regimes including entirely subsonic, transonic (subsonic flow with supersonic pockets), and entirely supersonic flows. By iterating in just one marching plane, a computer program based on the method presented can be used to also solve problems that are two-dimensional or that can be reduced to two dimensions. Conical flows are examples of the latter. The same computer program can also be used to solve three-dimensional (and two-dimensional) unsteady flows. Thus, the unified approach taken is really greater in scope and applicability than what the title of this paper might suggest. Of course, the method is eminently suitable for the case of supersonic flows with subsonic pockets.

The use of TVD discretisations results in a highly reliable method with no artificial parameters such as coefficients of numerical smoothing to be provided by the user. Spurious oscillations and expansion shocks are also eliminated.

The relaxation approach used can also be used to solve the Navier-Stokes equations[12]. By following the unified methodology used to derive the present algorithm for the Euler equations, a unified scheme can also be derived for the Navier-Stokes equations. Parabolized forms of the Navier-Stokes equations may be solved in regions where there is little upstream propagating influence upon the boundary layer and when the flow external to the boundary layer is supersonic. In regions of separation, etc. where there is an appreciable effect of the downstream upon the upstream flow, and/or where the external flow is subsonic, the relaxation approach may be used. Such methods can provide superior replacements to current Parabolized Navier-Stokes solvers and can be the subject of research by us or by other investigators.

ACKNOWLEDGEMENT

This study was partially supported by NASA Langley Research Center under Contract Number NAS 1-17492 awarded to Rockwell International Science Center.

REFERENCES

[1] V. Shankar, K. Y. Szema, and S. Osher, "A Conservative Type-Dependent Full Potential Method for the Treatment of Supersonic Flow with Imbedded Subsonic Region," AIAA Paper No. 83-1887, July 1983.

[2] K. Y. Szema and V. Shankar, "Nonlinear Computation of Wing-Body-Vertical Tail-Wake Flows at Low Supersonic Speed," AIAA Paper No. 84-0427, Jan. 1984.

[3] K. Y. Szema, W. L. Riba, V. Shankar, and J. J. Gorski, "Full Potential Treatment of Flows Over 3-D Geometries Including Multi-body Configurations," AIAA Paper No. 85-0272, Jan. 1985.

[4] S. R. Chakravarthy and D. K. Ota, "Numerical Issues in Computing Inviscid Supersonic Flow Over Conical Delta Wings," in preparation.

[5] S. R. Chakravarthy and S. Osher, "A New Class of High Accuracy TVD Schemes for Hyperbolic Conservation Laws," AIAA Paper 85-0363.

[6] S. R. Chakravarthy and S. Osher, "Computing With High-Resolution Upwind Schemes for Hyperbolic Equations", to appear in the Proceedings of the 1983 AMS-SIAM Summer Seminar on Large-Scale Computations in Fluid Mechanics, published by American Mathematical Society in *Lectures in Applied Mathematics*, Volume 22, 1985.

[7] P. L. Roe, "Approximate Riemann Solvers, Parameter Vectors, and Difference Schemes," *Journal of Computational Physics*, Vol. 43, 1981, pp. 357-372.

[8] S. R. Chakravarthy, "Relaxation Methods for Unfactored Implicit Upwind Schemes," AIAA Paper 84-0165, 1984; also to appear in the AIAA Journal.

[9] S. R. Chakravarthy, "Numerical Implementation of Boundary Conditions for Hyperbolic Systems of Conservation Laws," in preparation.

[10] S. R. Chakravarthy, "Euler Equations—Implicit Schemes and Boundary Conditions," AIAA Journal, Volume 21, Number 5, May 1983, pp. 699-706.

[11] J. C. Townsend, D. T. Howell, I. K. Collins, and C. Hayes, "Surface Pressure Data on a Series of Analytic Forebodies at Mach Numbers from 1.7 to 4.5 and Combined Angles of Attack and Sideslip," NASA TM 80062, June 1979.

[12] S. R. Chakravarthy, K. Y. Szema, J. J. Gorski, U. C. Goldberg, and S. Osher, "Application of a New Class of High Accuracy TVD Schemes to the Navier-Stokes Equations," AIAA Paper No. 85-0165, January 1985.

1. Report No.
NASA CR-3982

2. Government Accession No.

3. Recipient's Catalog No.

4. Title and Subtitle
FULL POTENTIAL METHODS FOR ANALYSIS/DESIGN OF COMPLEX AEROSPACE CONFIGURATIONS

5. Report Date
May 1986

6. Performing Organization Code

7. Author(s)
Vijaya Shankar, Kuo-Yen Szema, and Ellwood Bonner

8. Performing Organization Report No.

9. Performing Organization Name and Address
Rockwell International Corporation
Los Angeles, CA 90009

10. Work Unit No.

11. Contract or Grant No.
NAS1-15820

12. Sponsoring Agency Name and Address
National Aeronautics and Space Administration
Washington, DC 20546

13. Type of Report and Period Covered
Contractor Report

14. Sponsoring Agency Code
505-61-71-05

15. Supplementary Notes
Langley Technical Monitors: Noel A. Talcott, Jr., and Kenneth M. Jones

16. Abstract

The steady form of the full potential equation, in conservative form, is employed to analyze and design a wide variety of complex aerodynamic shapes. The nonlinear method is based on the theory of characteristic signal propagation coupled with novel flux biasing concepts and body-fitted mapping procedures. The resulting codes are vectorized for the CRAY-XMP and the VPS-32 supercomputers.

Use of the full potential nonlinear theory is demonstrated for a single-point supersonic wing design and a multipoint design for transonic maneuver/supersonic cruise/maneuver conditions. Achievement of high aerodynamic efficiency through numerical design is verified by wind tunnel tests. Other studies reported here include analyses of a canard/wing/nacelle fighter geometry.

17. Key Words (Suggested by Author(s))
Aerodynamics
Numerical Methods
Aircraft Design/Analysis
Potential Theory

18. Distribution Statement
FEDD Distribution

Subject Category 02

19. Security Classif. (of this report)
Unclassified

20. Security Classif. (of this page)
Unclassified

21. No. of Pages
160

22. Price

Available: NASA's Industrial Applications Centers

End of Document